Univariate and Dynamic Multivariate Analysis of Functional MRI Data

by

Hao Jia

A dissertation submitted to the Graduate Faculty of
Auburn University
in partial fulfillment of the
requirements for the Degree of
Doctor of Philosophy

Auburn, Alabama
May 4, 2014

Keywords: Functional MRI, Awake animal imaging, Functional connectivity, Effective connectivity, Clustering, Support vector machine

Approved by

Gopikrishna Deshpande, Chair, Assistant Professor, Department of Electrical & Computer Engineering
Thomas Denney, Director, Auburn University MRI Research Center
Jeffrey Katz, Alumni Professor, Department of Psychology Auburn University
Prathima Agrawal, Professor, Department of Electrical & Computer Engineering

Abstract

Functional magnetic resonance imaging (fMRI) has been increasingly used in the past decade for inferring brain function in both healthy and clinical populations. In this dissertation, we demonstrate fMRI data analysis strategies using both univariate and multivariate models. We demonstrate the utility of mass univariate general linear regression models in a novel context wherein we analyzed fMRI data of conscious dogs to investigate their olfactory system at the cognitive level. We investigated the modulation of olfactory related activity in the canine brain as a function of odorant concentration and dogs' consciousness state (lightly anesthetized or fully conscious). Besides, we conducted experiments with zinc nanoparticles added to the odorant to investigate their enhancement effect on olfactory perception, with pure odorant and odorant + gold nanoparticles as control conditions. The major finding was that olfactory bulb and piriform lobes were commonly activated in both awake and anesthetized dogs, while the frontal cortex and cerebellum were activated mainly in conscious dogs. Comparison of responses to low and high odorant concentrations showed differences in both the intensity and spatial extent of activation in the olfactory bulb, piriform lobes, cerebellum, and frontal cortex. Zinc nanoparticles conspicuously enhanced activations of olfactory bulb and olfactory cortex for anesthetized dogs and frontal areas for conscious dogs, compared to pure odorant and odorant + gold nanoparticles. On the other hand, multivariate regression models of fMRI data were employed to investigate connectivity between different regions of the brain. We used human resting state fMRI data to calculate four types of connectivities: static & dynamic functional connectivity (FC), and static

& dynamic effective connectivity (EC). For dynamic connectivities, we used adaptive evolutionary clustering algorithm to cluster brain network states, correlated FCs with behavioral metrics, and linked EC network patterns to real world functionalities. We found several major patterns of brains states alternating with each other in a quasi-stable way, featuring the default mode network (DMN) in FC patterns and temporal-parietal-frontal interactions in EC patterns. Also, connectivity dynamics were testified to have more power in explaining behavior as compared to the static counterparts. Finally, connectivity dynamics were compared with connectivity statics with an application to classify patients with post-traumatic stress disorder (PTSD) and healthy individuals. We found that the temporal variability of connectivities had more sensitivity in predicting the diagnostic label of a novel subject than connectivity statics.

Acknowledgments

I would like to thank my advisor, Dr. Gopikrishna Deshpande, for his prominent instructiveness in analyzing data, great patience in reviewing and modifying manuscripts, sparkling ideas and exquisite insight in trouble shooting during data processing. I would like to thank Oleg Pustovyy, Paul Waggoner, Ronald Beyers, John Schumacher, Chester Wildey, Jay Barrett, Edward Morrison, Nouha Salibi, Thomas Denney and Vitaly Vodyanoy for their cooperation and great help in conducting dog fMRI experiments, especially Ronald Beyers for his guidance in operating fMRI scans and Vitaly Vodyanoy for providing *in vitro* data of electro-olfactogram measurement and suggestions on analysis of dog fMRI data about zinc nanoparticles' effect. Next, I would like to thank my friends in MRI center for their great help and encouragement, especially Pruthviraj Kyathanahally and Karthik Sreenivasan for help in software troubleshooting. Also, I would like to thank Prof. Xiaoping Hu for his precious feedback on projects about human data. For projects in Chapter 2 and Chapter 3, I acknowledge funding support from Auburn University Intramural Level-3 research grant from the Office of the Vice President for Research, Auburn University, and support by the Defense Advanced Research Projects Agency (government grant/contract number W911QX-13-C-0123). For project in Chapter 4, data were provided by the Human Connectome Project, WU-Minn Consortium (Principal Investigators: David Van Essen and Kamil Ugurbil; 1U54MH091657).

Table of Contents

List of Tables

List of Figures

Chapter 1 Introduction

1.1 MRI & Functional MRI

Magnetic resonance imaging (MRI) is a medical imaging technique used in radiology, biomedical research, and clinic diagnostics to visualize internal structures of the body in detail [1]. MRI is a noninvasive technique which uses magnetic field and electro-magnetic waves as probe to detect tissues and organs inside the body. It makes use of the property of nuclear magnetic resonance (NMR) of atoms for imaging [2] [3]. Body tissue contains lots of water, and hence protons, which can get aligned with a larger magnetic field. When people lie inside a MRI scanner, large static magnetic field (produced by a superconducting magnet) makes protons aligned with the direction of the field. A gradient magnetic field (produced by gradient magnet coil) is often added to select the proper layer or location of the body that is to be imaged. Then a transient radio frequency current pulse (produced by radio frequency coil) is transmitted to the body, with the frequency corresponds to the static magnetic field strength of the layer selected, such that a resonance of precession results. After the electromagnetic wave is turned off, the precession of protons relaxes and bulk magnetization becomes re-aligned to the static magnetic field. During this course, a radio frequency electromagnetic wave is generated from the imaged layer and received by coils for imaging. By using different gradient magnetic field design, it can be made magnetizations at different spatial locations precess in different patterns, which enables different k-space encoding of spatial information [4]. Also in this way, 2D images or 3D volumes can be obtained in any arbitrary orientation. Using inverse Fourier transformation, k-space information is transformed into image domain, recovering the spatial information of scanned area.

Protons in different tissues return to their equilibrium state at different relaxation rates. Different tissue has different proton density, T1 and T2 relaxation times (for T1 and T2 relaxation mechanism, please see [3]), which can be utilized to construct images of different contrast. Images of different contrast can reflect different properties of scanned area, and thus have different applications, such as those of functional MRI and diffusion tensor MRI.

Hitherto, MRI is the imaging technique known that can provide the most amount of imaging modalities and best image quality: good contrast between different tissues and high resolution. Thus, it has broad prevalence in brain imaging, muscles, heart, and cancer imaging, over other medical imaging techniques like X-rays and computed tomography (CT) [5] [6]. A schematic of MRI scanner is illustrated in Fig.1.1.

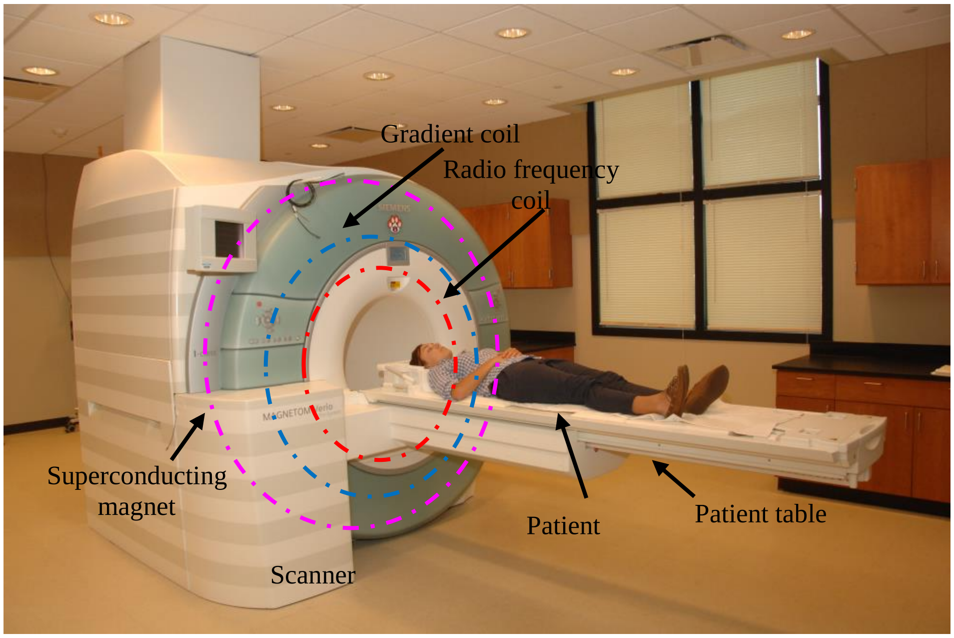

Figure 1.1 Schematic of a MRI scanner

Functional magnetic resonance imaging (fMRI) is now a primary tool to study the organization of a working brain, and relevant clinical applications are growing exponentially [7] [8] [9] [10]. Since the early 1990s, fMRI has become to dominate brain mapping research because this non-invasive technique does not require people to undergo shots, surgery, or to ingest substances, or be exposed to radiation. So it is relatively ecologically safe. FMRI technique measures the blood oxygenation level dependent signal (BOLD) in the brain, based on which the neuronal activity in the brain can be inferred [11]. There is an intrinsic physiological agent that signifies blood susceptibility: deoxyhemoglobin (dHb). Deoxyhemoglobin is paramagnetic and thus changes the susceptibility of blood. As local blood becomes more deoxygenated, the MR (magnetic resonance) signal drops. The brain does not store glucose which is the primary source of its energy. When neurons go active, getting them back to their original (polarized) state requires actively pumping ions back and forth across the neuronal cell membranes. The energy for these motor pumps is produced from glucose. More blood flows in to transport more glucose, also bringing in more oxygen in the form of oxygenated hemoglobin molecules in red blood cells. This is from both a higher rate of blood flow and an expansion of blood vessels. The blood-flow change is localized to within 2 or 3 mm of where the neural activity is. Usually the oxygen brought in is more than the oxygen consumed for burning glucose, and this causes a net decrease in dHb in that brain area's blood vessels [12] [9]. In a word, neuronal activity and cerebral blood flow are coupled in such a way that when neuron fires, the demand of energy and thus metabolism rate around the firing place increase, leading to the increase of regional blood flow and decrease of capillary and venous dHb concentrations. As a consequence, an increase in magnetic spin-spin relaxation times T_2* and T_2 occurs, resulting in an increase of intensity in T_2*- and T_2-weighted MR images [3]. Such a complicated relationship between neuronal activity and BOLD signal reflects as the hemodynamic response (HDR). The HDR normally starts about 1 to 2 seconds after the triggering of neuronal activity, and then rises up to a peak at about 5 seconds thereafter. Then, it falls till below the baseline, forming a small "undershoot", and finally goes back to the baseline. If the neuron keeps firing, the peak would spread to a flat plateau [9] [10].

Functional MRI takes snapshots of brain consecutively in time in order to track functionality of the brain (Fig.1.2). Therefore, the temporal resolution is of great importance. Nowadays, the temporal resolution can reach to as small as 200ms, but the BOLD signal has intrinsic limitation of temporal resolution, which prevents the temporal resolution from further increasing. This blockage can be overcome by deconvolution technique [13].

Although functional MRI has relatively poor temporal resolution compared with underlying neuronal signals, it does have a relatively high spatial resolution when compared with other imaging techniques. The spatial resolution of fMRI is measured by size of voxels, which is determined by scanning parameters like slice thickness and in-plane matrix resolution. Normally, the spatially resolution ranges from 1mm to 5mm. A full brain scan uses larger voxels, while a region of interest (ROI) study within the brain typically uses smaller voxels. To offset the shortage of temporal resolution and draw on its strength of spatial resolution, fMRI can be and has been combined with other modalities of brain physiology imaging such as electroencephalograph (EEG) and magnetoencephalogram (MEG) [10]. Meanwhile new techniques which improve both spatial and temporal resolutions are being researched [14].

For every time of repetition (TR), a 3D volume image is generated by the scanner. All 3D images generated during the scan can be put together to form a 4D volume image. Since fMRI is designed to track the change of brain BOLD signal and one volume should be imaged timely fast, the signal-to-noise ratio (SNR) cannot be very high and corruption from noise is not negligible. The statistical post-processing is often employed to suppress noise and extract the underlying true signal or true activation. A statistical activation means the signal in one region passes the statistical hypothetical testing and the null assumption is rejected. The activation map can be displayed graphically by color-coding the strength of activation. Currently the activation map can be localized to within millimeter scope.

Pertaining to clinic applications, physicians use fMRI to assess brain healthy condition, provide reference for surgery or invasive treatment, and get insights into how a normal, diseased or injured brain is functioning. A mapping of brain regions to real world functionalities such as speaking, walking, and smelling offers valuable information for diagnostics. Clinicians also use fMRI to inspect the anatomy of the brain and detect tumors, stroke, lesion, or atrophy [15].

An example of fMRI volume image acquired at one TR is illustrated in Fig.1.2.

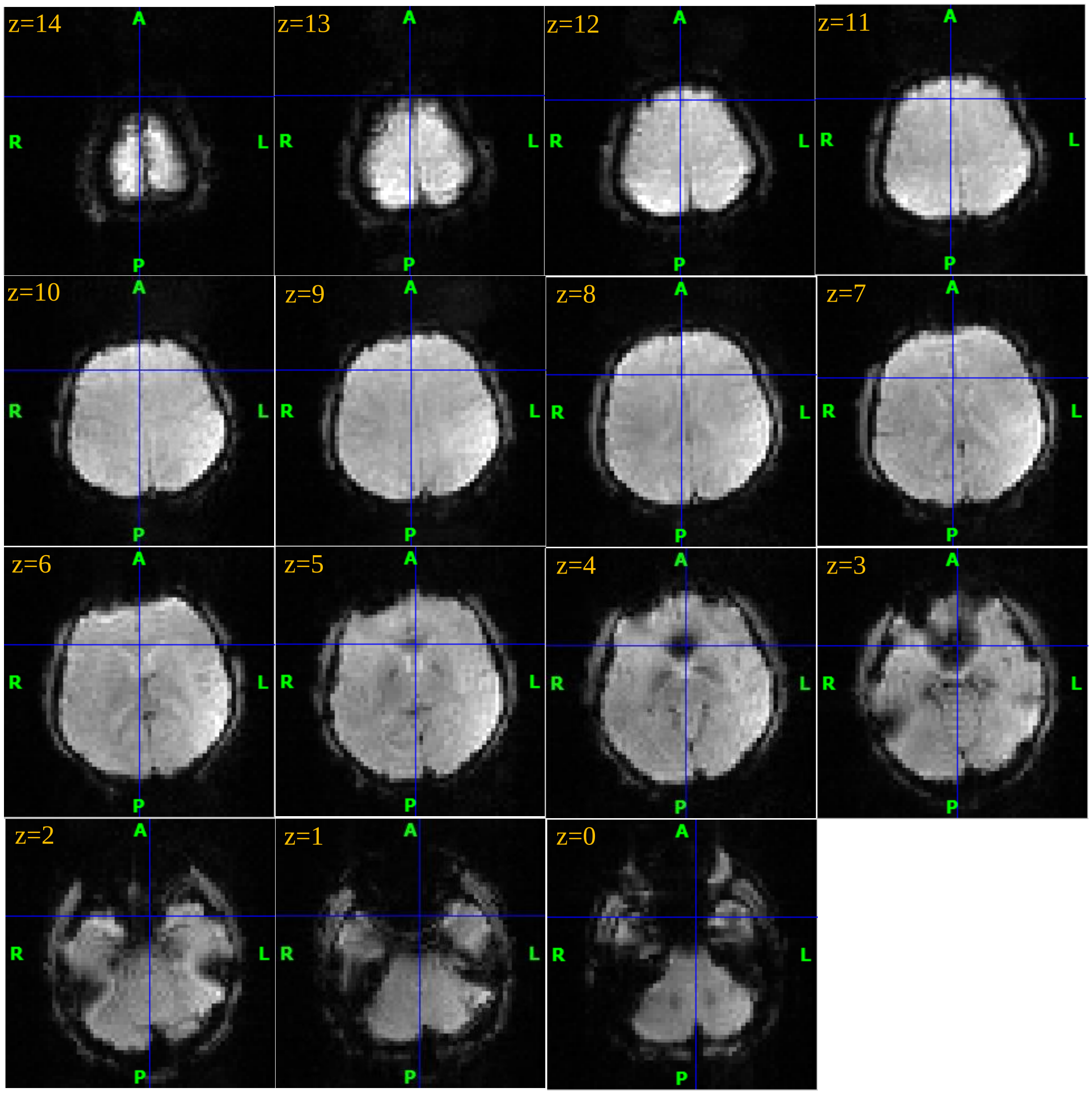

Figure 1.2 An example of functional MRI volume image acquired at one TR. This functional volume of EPI (echo-planar imaging) images acquired at one TR is comprised of 14 axial slices of a resting human brain. All axial slices are sequentially shown with each slice's z coordinate (slice number) shown at top left corner. (A: anterior, P: posterior, L: left, R: right)

1.2 FMRI Data Preprocessing

Raw fMRI data cannot be directly used for brain functionality analysis, since there exist noise, head motion, field non-uniformity, acquisition asynchrony and so on [10]. Normally, a standard preprocessing pipeline of raw fMRI data includes slice timing correction, realignment, reslice, coregistration/normalization, temporal filtering, white matter and cerebrospinal fluid (CSF) signal removal, and spatial smoothing. Some preprocessing pipelines may include grand mean normalization.

1.2.1 Slice Timing Correction

Slice timing correction is to align each slice in temporal domain. Since the slices at different z positions have staggered acquisition time, the data on one slice will represent a point in time as far removed as 1/2 the TR from an adjacent slice (in the case of an interleaved sequence). Slice timing correction performs interpolation such that all slices appear to be acquired at the same instant. This is accomplished by a simple shift of the phase of the sines that make up the signal. The shifted signal is typically resampled using sinc-interpolation.

1.2.2 Realignment & Reslice

While slice timing performs alignment of images in the temporal domain, realignment does it in the spatial domain. Due to head motion during the scanning which is inevitable, and even physiological noise such as breathing and heartbeat, the images acquired at different time instants cannot be perfectly matched. Thus a spatial realignment of all images is needed. The motion effect can be accounted for by rigid body translations in 3 directions and rotations in 3 directions. A reference image (normally the first image or the mean image) is set as to calculate the rigid body transformation parameters between the reference image and the image to be realigned. Then the rigid body transformation is imposed on each image so that all images are aligned to each other. The 6 parameters (3 translations and 3 rotations) are calculated under least square sense.

After realignment, the function “reslice” performs resampling a series of registered images such that they are on the same volume of slices and match each other voxel-by-voxel. During this procedure, interpolation is effected for which there are many algorithms including nearest neighbor method, trilinear and spline methods. Normally the B-spline method is preferred over others.

1.2.3 Coregistration & Normalization

Coregistration and normalization [16] serve to jiggle about one or a bunch of images to best match the reference image, which we call it the template. Spatial coregistration or normalization is necessary because we need to accumulate fMRI data of different sessions and different subjects for statistical analysis, in order to boost statistical power. However, different subjects have different head shapes and sizes, even the same subject, when in different sessions, may have slight difference in head profile. Therefore, to perform group-level analyses, we need to normalize all fMRI images to a standard template. Coregistration and normalization differ in the transformation algorithm, with the former using affine transformation to register images, and the latter using non-linear transformation for registration. The criteria for both transformations is to optimize some cost function, which can be the mutual information, entropy correlation coefficient, or sum of squared difference plus membrane energy of the deformation field. For humans, several extant standard template atlases such as MNI (Montreal Neurological Institute) template [17] are available for this registration.

1.2.4 Temporal Filtering

Temporal filtering is intended since there are unwanted noise and artifacts mingled with the signal of usefulness. These noise and artifacts come from thermal noise, physiological noise from heartbeat and breathing, and magnetic field shifting, etc. One common characteristic among them is normally their power is limited within a certain frequency band. Thus, if we use lowpass/highpass/bandpass filters to remove their power from corresponding frequency band, we make the signal purged.

1.2.5 White Matter and Cerebrospinal Fluid Signal Removal

Sometimes the gray matter signal is the only signal of interest, so we hope to remove, or regress out the white matter and CSF signal from original signal. Normally this is done by using white matter mask and CSF mask to extract only the white matter portion and CSF portion of the brain, taking the mean signal within the mask, and regressing out this signal from time series of all voxels.

1.2.6 Spatial Smoothing

Spatial smoothing, also called spatial filtering, is the idea of averaging the intensities of nearby voxels to produce a smooth spatial map of intensity across the image. This operation aims to suppress spatial noise, facilitating statistical inference afterwards. The averaging is often done by convolution with a smoothing kernel, usually a Gaussian kernel. If the true spatial extent of activation matches the width of the kernel used, this process improves the signal-to-noise ratio since signal power adds in in-phase manner while noise cancels out. It also makes the noise for each voxel more approximately follow the Gaussian distribution. This is intended since the statistical analysis thereafter is normally based on the assumption that noise follows Gaussian distribution, both temporally and spatially.

Grand mean normalization is also recruited in preprocessing by a lot of studies. It is in nature the normalization of mean intensity of each fMRI image volume acquired at each TR, i.e., to make the mean intensity of each fMRI image volume equal to each other. This is intended to eliminate the disruptive effect caused by grand mean signal intensity bias of each fMRI image volume. This step often goes before spatial normalization step.

There are also some other preprocessing issues that need to be taken account of, though not often encountered, such as distortion corrections for field nonuniformities. For this issue, one method is to use shimming coils and another one is to recreate a field map of the main field by acquiring two images with differing echo times. If the field were uniform, the differences between the two images also would be uniform. Bias field can be estimated using some mathematical model of the noise from distortion and used for correction.

1.3 Organization of This Dissertation

This first chapter gives introduction of relevant background knowledge, briefly expounding MRI, fMRI and its preprocessing procedures. Other chapters are organized as follows. The second and third chapters deal with univariate analysis of fMRI data with two projects. Chapter 2 investigates the olfactory system in canines using fMRI, and compares activation maps between low and high concentration of odorant stimuli, as well as between lightly sedated and fully conscious dogs. Chapter 3 is about the fMRI investigation of zinc nanoparticles' enhancement effect on canines' olfactory perception, and comparisons are made with pure odorant, as well as gold nanoparticles + odorant as controls. Similar to Chapter 2, another comparison is made on activation maps between lightly sedated and fully conscious dogs. Chapter 4, 5 and 6 demonstrate (dynamic) multivariate analysis of fMRI data. In Chapter 4, we use the multivariate metric: dynamic functional connectivity, to cluster brain network states, and correlate this metric and its static counterpart with behavioral measures. In Chapter 5, another two multivariate metrics: static and dynamic effective connectivity are researched. With dynamic effective connectivity and the similar clustering strategy as in Chapter 4, human resting state fMRI data is explored to find brain effective connectivity network patterns. Also, the relationship from these patterns to real world functionalities is inspected. In Chapter 6, the dynamics of connectivities are compared with static connectivities in terms of performance on discriminating patients with mental disorders from healthy controls, with an application to classify between post-traumatic stress disorder (PTSD) patients and healthy controls. The classification is realized via support vector machine. In the end, the entire dissertation is concluded with Chapter 7. The information on published and submitted papers is in Chapter 8.

Chapter 2 Univariate Analysis:

Functional MRI of the Olfactory System in Conscious Dogs

Univariate analysis technique has been introduced into fMRI processing for a long time. Its realization in fMRI processing is based on the assumption that, each voxel is independent of other voxels. We process the time series for a given voxel only using its own information, and assume information from other voxels has no contribution to the time series of the voxel being investigated. The variable of interest is calculated usually by mass univariate general linear regression model. A comprehensive elaboration on univariate analysis can be found in Ref. [18] and its characterization in fMRI can be found in Ref. [19]. The work in this chapter is based on this assumption and our main contribution is that we constructed a novel dog fMRI olfactory system, used it to acquire dog fMRI data and analyzed the data of anesthetized and conscious dogs to investigate their olfactory system at the cognitive level.

2.1 Introduction

The properties of the dog's olfactory system result from physical and biochemical events that occur at the olfactory epithelium of its nasal cavity where olfactory receptor neurons interact with odorants. Based on previous reports involving *in vitro* studies and *in vivo* studies in canines and other species (mainly humans), we can construct the following hypothesis about the cerebral architecture of the canine olfactory system. Olfaction begins with sniffing, which transports odorant molecules into the nose and delivers them to the mucus layer covering the olfactory epithelium [20]. The binding of the odorant by a receptor protein initiates an intracellular cascade of signal transduction events, including the G-protein-dependent production of second messenger molecules, leading to opening of ion channels and passing of ion currents. This process triggers an action potential in the axon of the olfactory receptor neuron that projects directly to the olfactory bulb (OB) [20] [21]. The OB generally functions as a filter and has three non-exclusive functions: discriminating among odors, enhancing sensitivity of odor detection and filtering out background odors to enhance the transmission of selected odors. OB neurons then transmit signals to pyramidal neurons in the olfactory cortex that is composed of the anterior olfactory cortex, piriform cortex, periamygdaloid cortex and entorhinal cortex. The anterior olfactory cortex detects and stores correlations between olfactory features, creating representations (gestalts) for particular odorants and odorant mixtures, as shown by Haberly in humans [22]. Piriform cortex carries out functions that detects and learns correlations between olfactory gestalts formed in anterior olfactory cortex and a large repertoire of behavioral, cognitive and contextual information to which it has access through reciprocal connections with frontal, entorhinal, and periamygdaloid areas [22]. The periamygdaloid area participates in emotional processing of olfactory stimuli and facilitates memory encoding, as shown by Zald et al with human PET (positron emission tomography) data [23], and entorhinal cortex functions as a hub for memory network and navigation [22]. The pathway then projects to the hippocampal formation and thalamus, which relays information to neocortical areas such as the medial and orbitofrontal cortex where the olfactory signal is interpreted [24] (see Fig.2.1 for schematic). The medial and orbital parts of the frontal cortex are known to be involved in cognitive integration of all sensory stimuli in relation to prior experiences, as shown using functional neuroimaging in humans [25]. The hippocampal formation is involved in recognition memory of odors [22]. The thalamus' involvement in olfaction as a relaying hub is still under debate, however its involvement in odor thresholding has been acknowledged, at least in humans [26]. Also, previous studies have shown that dogs possess much more olfactory receptors per square centimeter of the olfactory epithelium as compared to humans [27]. This clearly demonstrates the dogs' advantage over humans in sensory transduction at the cellular level. However, how this advantage is carried forward higher into the odorant detection chain remains unexplored.

While much is known about the canine olfactory system at the *in vitro* cellular level [28] [29] [30] [31] [32] [33] and behavioral level [34] [35], little work has been done at the cognitive level, which is an important and largely unexplored link in the series of events leading to odor detection. It is critical to bridge the gap between cellular findings and systemic behavioral observations by investigating the sense of smell at the cognitive level. For example, an increase in the concentration of odorant will induce a change in response at the cellular level according to Weber's law [36]. How this change in response translates to a change in odorant detection *in vivo*, however, is unknown, and could potentially be explored by using fMRI, which allows noninvasive mapping of brain function without the administration of an exogenous contrast agent [37] [7].

In this study, we characterized the cognitive response in dogs' brain to odorants of different concentrations using dogs that were fully conscious, and compared the response to that of lightly sedated dogs. Awake animal fMRI studies are methodologically challenging but more valuable because the data reflect the brain activity under more ecologically valid conditions. Anesthesia affects the neural activity as well as the regulation of cerebral circulation significantly [38] [39]. Only a small amount of animal fMRI studies have been published under awake conditions due to the difficulty of restricting motion effect [38] [39] [40]. Here, awake dog imaging was made possible by using an optical head motion tracking system [41] for retrospectively correcting for artifacts created by head motion. FMRI provides for the apparatus to investigate the dog olfactory system *in vivo* and noninvasively, and has been used to study the neural basis of olfaction in humans [42] [43], monkeys [44] and rodents [45]. But, to our knowledge, there has been no investigation of the olfactory system in dogs (either awake or sedated) using fMRI or any other imaging modality. Dog imaging techniques developed in this study measure activity in the olfaction-related brain areas and quantify concomitant changes with different odorant concentrations. We believe that the techniques we report here will serve as a seminal noninvasive method for the exploration of the dog's olfactory system at the cognitive level.

The broader impacts of this endeavor are multifold. Currently, we depend upon the olfactory abilities of dogs for what are considered highly specialized and critical tasks such as detecting explosive devices, hazardous chemicals, and illicit substances. The societal importance of such tasks has increased efforts to enhance the technological sophistication by which canine olfaction is employed. To support such enhancement, greater emphasis has been placed on understanding fundamental olfactory function and capacities. Non-invasive imaging techniques such as fMRI, coupled with animal psychophysics based techniques, hold significant promise for advancing the understanding of fundamental olfactory function and associated cognitive processing of odor sensory information. A mechanistic understanding of canine odorant detection is not only important from a basic science perspective but also to understand how canine detection capabilities change with different odorants and operating environments. Federal agencies in United States (Federal Aviation Administration, Department of Homeland Security and Department of Defense) have invested millions of dollars to support research into basic science of canine odor detection and training because of the increase in terrorism threats, domestic and foreign narcotics trafficking.

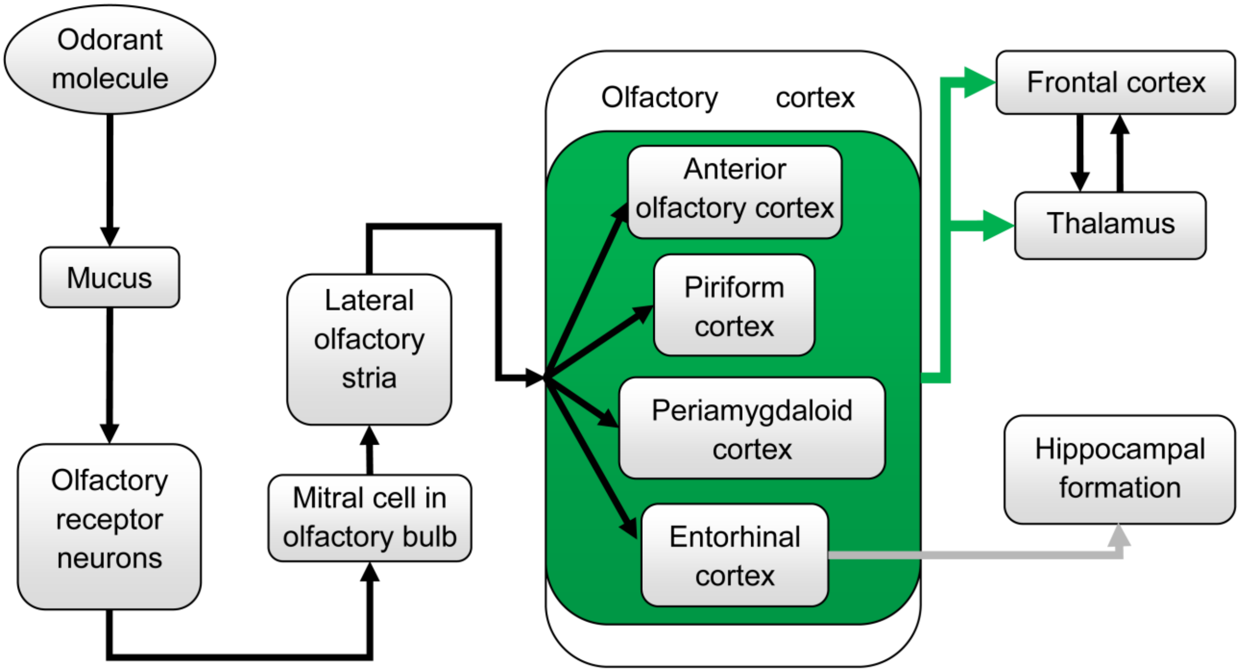

Figure 2.1 A schematic of the olfactory pathway in canines. Arrows indicate the olfactory signal flow. Anterior olfactory cortex, piriform cortex, periamygdaloid cortex, and entorhinal cortex are contained in a green box and the green arrows extending from this green box indicate the olfactory signal from them go to frontal cortex and thalamus. The gray arrow from entorhinal cortex to hippocampal formation indicates the olfactory signal to hippocampus comes only from the entorhinal cortex. For functions of each site, please refer to [20] [21] [22] [23] [25] [26].

2.2 Material and Methods

Ethics Statement: Approval was obtained from the Auburn University Institutional Animal Care and Use Committee for performing this study.

2.2.1 Overview of the Dog FMRI Olfactory Imaging System

The components of the dog fMRI olfactory imaging system are shown in Fig.2.2. First, the dogs were trained to insert and keep their heads as still as possible inside the human knee coil when being scanned (Fig.2.2 (A)). This was achieved by positive reinforcement training techniques using a target stick and bridging stimulus (i.e., clicker) for head placement maintained by delivery of edible treats for emission of desired responses. Second, a custom-built odor applicator was used for controlled delivery of odorant stimulus (Fig.2.2 (B)). Third, the scanner system consisted of a 3T Siemens Verio scanner and a human knee coil which perfectly fit into the role of a dog head coil. Fourth, an optical head motion tracking system was employed for tracking dog head motion during fMRI (Fig.2.2 (B), (C)), and consisted of an infrared (IR) camera, an IR illuminator, a video monitor, and a data recording palmtop. A schematic of the interlinking and triggering among them is shown in Fig.2.3. Finally, post-processing of functional data was performed with SPM8 (statistical parametric mapping) [46].

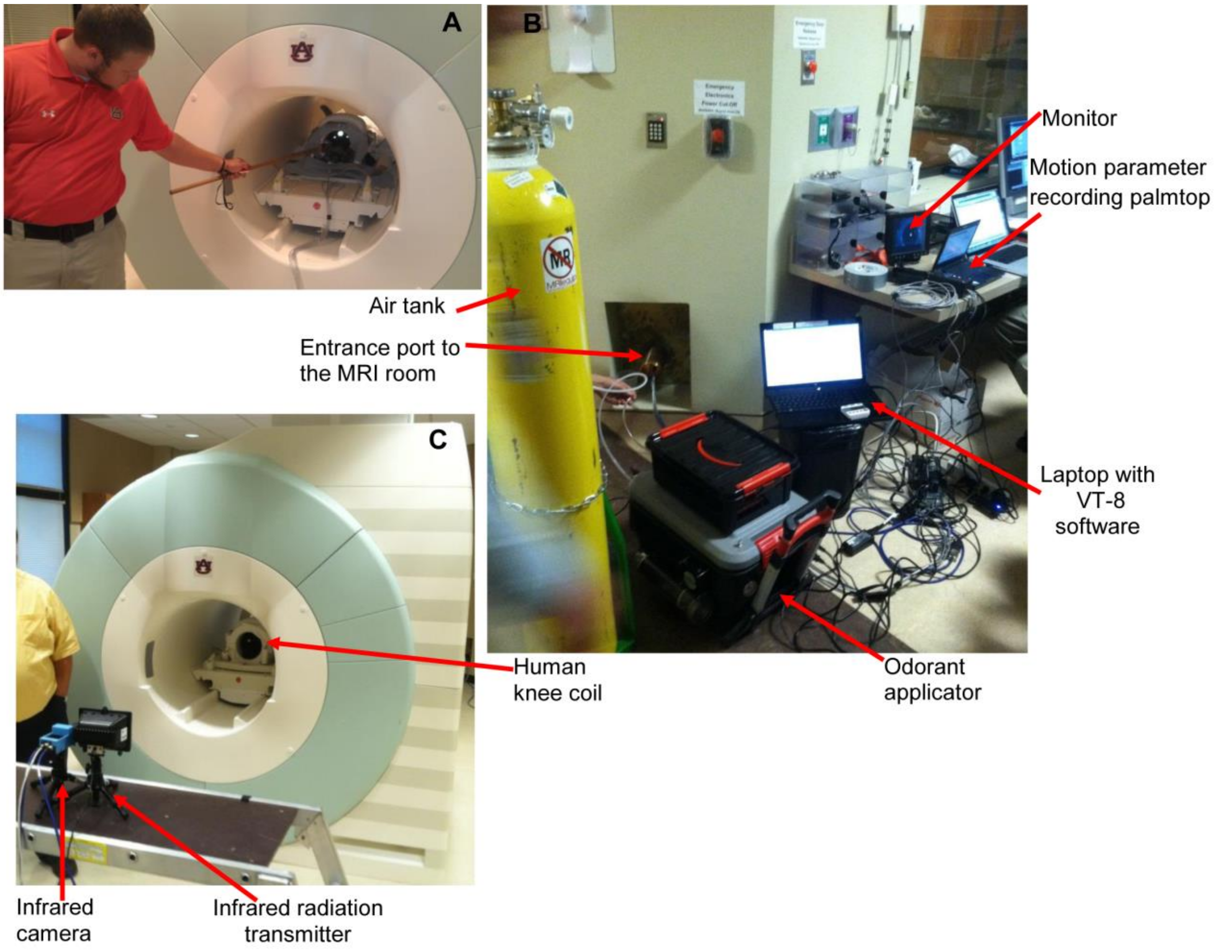

Figure 2.2 Components of the dog fMRI olfactory imaging system. (A) dog training to insert and keep their heads as still as possible inside the human knee coil using positive reinforcement learning (a black dog can be seen inside the coil); (B) components of imaging system outside the MRI room showing odorant applicator, air tank, motion parameter recording palmtop, video monitor, laptop with VT-8 software (see Section 2.2.3), and the entrance port to the MRI room; (C) components of imaging system inside the MRI room, showing human knee coil, infrared camera and infrared radiator.

Figure 2.3 The interlinked trigger system. Arrows denote the triggering direction. A laptop with VT-8 software [47] provided the interface to trigger the odorant applicator. The VT-8 software is a platform that can be used to design and display sequence of odorant flow and clearance, and provides communication and control to odorant applicator to generate the expected experimental sequence. Once the odorant applicator started to give odorant stimulus, it sent a signal to the trigger synchronizer, which then triggered the scanner and sent a signal to the manual trigger. The manual trigger, as the name suggests, was manually set for switching between two states. One was waiting for signals from trigger synchronizer, and the other was waiting for signal from a hand-pressed button. In our experiment, the first state was used for data collection and the second was used only for testing. Upon receiving the signal, it triggered the infrared radiation transmitter to give off infrared rays, and the infrared camera to start recording infrared reflections from the dog's head, and the motion parameter recording palmtop to start calculating displacement parameters. When the camera was triggered, it sent the signal to the monitor for display.

2.2.2 Dog Training and Preparation

We recruited six Labrador Retriever dogs (five males) from the Auburn University Canine Detection Research Institute with ages in the range of 12 to 60 months. For anesthetized imaging, dogs were sedated with intramuscularly administered xylazine (2.2 mg/kg) and lightly anesthetized with ketamine HCl (11mg/kg). For awake imaging, the dogs were trained to move to the correct position within the scanner, insert their heads within a human knee coil, and remain still for the required duration of imaging using positive reinforcement behavior shaping procedures.

All training used positive reinforcement to obtain the desired performance by the dogs. Prior to training for fMRI scanning, the dogs were trained to follow, touch, and remain touching the end of a “target-stick” (3/8 inch diameter, 36 inch long, wooden dowel with red tape as target on one end) with their nose using small bits of commercial dog food treats as rewards to shape and maintain this response. Concomitantly, a tin clicker was established as a conditioned reinforcer by pairing the click with the delivery of food treats for correctly touching and holding their nose to a touch-stick. Such a conditioned reinforcer is also known as a “bridge” because it provides an immediate signal to the animal that the desired response has been emitted and bridges the gap in time until a food treat can be delivered. This sort of target-stick and bridging signal training is a common practice in pet animal as well as professional husbandry with animals in zoos to train them to present themselves for medical monitoring and treatment, conduct educational/entertainment animal shows, and to generally reduce the dangers associated with managing animals. The use of the clicker allows more precise delivery of a rewarding stimulus to shape (i.e., build, develop) a desired response. Establishing the target-stick repertoire to a proficiency level adequate for moving onto training for fMRI took from 30 minutes to an hour for each dog.

The first round of training for awake, unrestrained fMRI of the dogs took place outside of the actual scanning using a fixture to replicate the human knee coil (i.e., 2.5 gal plastic bucket with the bottom cut out) affixed to one end of a table that approximated the height and width of the MRI table. The dogs were prompted to jump up on the table or, if unable to easily jump on the table, place their front paws upon the edge of the table so they could be easily lifted upon the table by one person. The previously established clicker and target-stick repertoire was used to train the dog to place its head within the simulated MRI coil and position its nose within the olfactory stimulus delivery mask, which was affixed inside the simulated human knee coil. The dogs were trained to hold their heads relatively motionless within the simulated coil by clicking the clicker only when their head was in the correct position and held still. The amount of time that a dog had to hold its head still in the correct position to receive the click followed by a food treat was gradually increased. Meanwhile, throughout this process, a recording of the sound from the operation of the MRI was played through a portable stereo, the volume of which was gradually increased until similar in intensity to that of being in the actual scanning. The final training performance was the dog holding its head relatively motionless in the correct position while the MRI sounds were played at approximately the same intensity as that of being in the actual MRI for 5 minutes and repeating this performance several times across the course of an hour-long training session. This training phase took, on average, about 20, 1-hour training sessions across a 4-week period for each dog.

The second round of training was performed inside the real scanner with the human knee coil and with running of the functional and structural sequences. The dogs were acclimated and transitioned to performing the head positioning response in the actual MRI scanner in one, approximately hour-long session each. The dog trainer always accompanied and monitored it (see Fig.2.2 (A)) in the scanning room. The dog was prompted onto the MRI table, into the MRI core, to place its head within the human knee coil, and position its nose in the olfactory stimulus delivery mask. Starting with a relatively short duration of holding its head in position and relatively motionless with the fMRI intermittently operating, the time requirement for receiving a click followed by a food treat was variably and rapidly increased until the dog reliably executed the performance for one fMRI sequence to be used in the experiment. The click was presented at the end of the sequence followed by delivery of the food treat from the hand of the trainer to the dog. A recent paper demonstrated a similar training approach for imaging the reward system in awake dogs [48]. However, even with training, some head movement was inevitable (e.g. respiratory repositioning). Therefore, we used a single camera optical head motion tracker to monitor the motion of the dog's head and retrospectively correct for motion effect.

2.2.3 Olfactory Stimulus Device

Odorant delivery

The accurate delivery of odor stimulus is very important in olfactory physiological experiments. When used with fMRI, demanding additional constraints are placed on olfactometers [49] [50] [51] [52]. The most obvious one is the absence of any magnetized material in the MRI room. Other features of the instrument include computer control and odorant presentation of accurate and reproducible duration of a preselected sequence with no additional stimulation (e.g., tactile, auditory) [49] [53].

We built a custom device for the precise computer-controlled delivery of pre-determined quantities of odorants over a precise time interval (Fig.2.4). The device provided for the flow of air under pressure through a series of filters, valves, and manifolds to sweep the headspace over containers into a mask, for the precise quantitative delivery of odorants to the nasal cavity of dogs. A vacuum suction then cleared the odorant after a precise amount of time. In this manner, the device controlled the precise extent and time of exposure of substances to olfactory tissue. The moisture content of the air was controlled to a constant humidity using a drierite type air filter. The drierite type air filter is a purifier that is specially designed for gas chromatography and other applications requiring pure and dry gas. It dries, purifies, and filters gases used for chromatography and spectrometry.

During the fMRI experiment, the air tank, odorant applicator, and computer were positioned outside the MRI room in the close proximity from the utility entrance port into the MRI room. Six 6-mm plastic tubes were passing through the entrance port for connection with the animal mask. Each tube, channel, and bottle was used only for the particular odorant sample to avoid cross contamination. Valve 2 and pressure regulator (PR) (see Fig.2.4) were purged and cleaned after each experimental session. All materials and components used in this device were chemically stable and are not odoriferous.

As illustrated in Fig.2.4, the computer (PC) used VT-8 software [47] to send a signal to the VT-8 Warner Valve Timer (indicated as "Timer" in Fig.2.4) that in turn communicated with the VC-8 Warner Valve Controller (Controller) to open one of six Oxygen Clean 2-way normally closed electronic valves (EV1) installed in the 6-port Oxygen Clean Manifold (Clippard Instrument Laboratory, Manifold 1). When EV1 was open, the corresponding LED (light emitting diode) control light was on, and air entered from the Air Tank into the Miniature Clippard Air Flow Control Valve (Valve 1). Then through the W.A. Hammond Drierite Laboratory Gas Drying Unit (Filter1) the air went to the open EV1, the first Clippard Unidirectional Valve (VU1), the head space of 100mL bottle, and then the second Clippard Unidirectional Valve (VU2). After that, it followed through the corresponding normally open channel of the Clippard Manifold 2 and via the second Miniature Clippard Air Flow Control Valve (Valve 2) to the Clippard Pressure Regulator (PR), with air pressure measured by DT-8890CEM Ruby-electronics Digital Differential Air Vapor Pressure Meter Gauge Manometer

(Manometer). Finally, the air with odorant exited the odor applicator and entered the SurgiVet Pet Oxygen Mask (Mask) [54] via the 6-mm tubing.

At the end of activation time (10 s) the Controller closed EV1 in the Manifold 1 and simultaneously opened the Oxygen Clean 2-way normally closed electronic valve (EV2) and the vacuum pump (AM6BS Metropolitan Vacuum) (VP) in the applicator exhaust path. The air with odorant was cleared from Mask, Valve 2, open channel of Manifold 2, EV2, and W.A. Hammond Carbon Filter (Filter 2). After the clearance of odorant (10 s) the EV2 and the vacuum pump were shut off and the system rested 20 s before a new activation began. The full cycle of the odor applicator, therefore, was typically composed of 10 s of odor application and 30 s of no odor. The no odor time was composed of 10 s clearance of odorant and 20 s rest time.

The pressure pulses were measured by Manometer and sent to computer (PC). The odor applicator was synchronized with MRI by the Timer signal sent to MRI computer. A cooling fan (CF) helped to maintain the temperature of odorants and device components. We used a known odorant mixture of ethyl butyrate, eugenol, and (+) and (–) carvone in water at concentrations of 0.016mM (low concentration) and 0.16mM (high concentration) each [55].

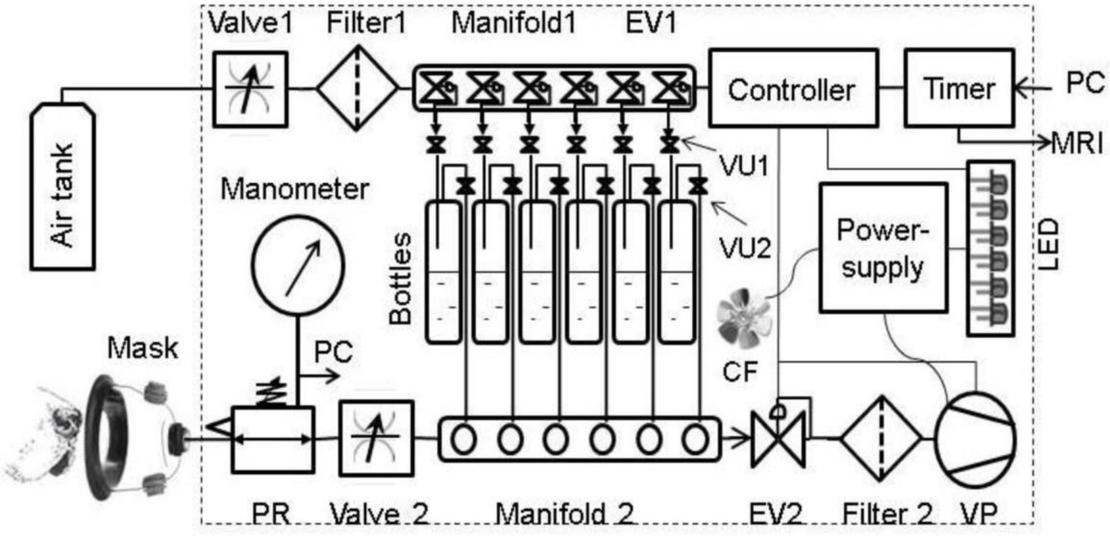

Figure 2.4 Diagrammatic representation of the olfactory stimulation device. The device consists of inflow & clearance air paths and an electronic control system. The inflow air/odorant path consists of a tank, flow control Valve 1, dry-rite type air Filter 1, Manifold 1 (6 isolated channels with electronically controlled valves), an electronic valve (EV1), 6 unidirectional pressure controlled valves (VU1, VU2), 6 odor bottles, Manifold 2 (6 flow-through isolated channels), flow control Valve 2, pressure regulated valve (PR), and electronic Manometer. The clearance path includes vacuum pump (VP), charcoal Filter 2, and electronic valve (EV2). The electronic control system consists of a 6-channel valve Timer, 6-channel valve Controller; Power-supply (feeds the VP, the visual LED control pane, and the cooling fan (CF)). Power for the Timer and Controller comes from the personal computer (PC). The protocols of timing and sequencing are stored and directed by the PC connected to the Timer. The Timer is synchronized with MRI. The experimental air pressure directed to the Mask are measured by the electronic Manometer and recorded by PC.

Plastic caps were modified for air-tight connection with the bottles containing odor solutions. The removable platform for bottles containing odorants, LED assembly and various clamps for positioning the parts were custom built. The odor applicator was controlled by the Warner VT-8 software [47] and was programmed to generate the experimental sequence of odorant flow and clearance (Fig.2.5). Since the odorant airstream was unwarmed and introduced at room humidity, excessive flow rate was not desirable. Also, animals subjected to continuous un-humidified flows could have nasal drying and discomfort. High air flow can present air flow turbulence, impacting rise times [56]. Because the mask had two valves that supported unrestricted exhaling and inhaling, the incoming air flow was limited to 1 l/min based on American Animal Hospital Association (AAHA) guidelines [56].

Mask

A SurgiVet Pet Oxygen Mask [54] was used in our experiments. This mask is made of polycarbonate and has two valves that aid unrestricted exhaling and inhaling, and a port to which the tube for odorant delivery and evacuation was attached. The mask was mounted on the frame of the knee coil such that when the dog placed its nose in the mask, its head was correctly positioned within the coil for imaging (Fig.2.6).

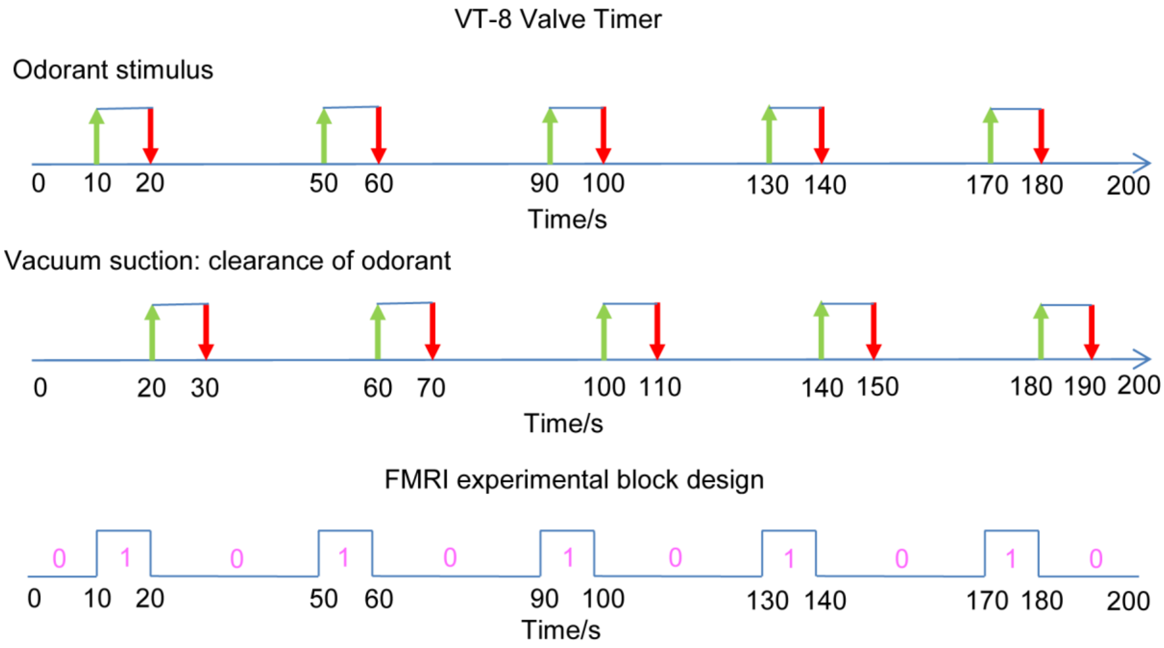

Figure 2.5 Odorant applicator sequences controlled by VT-8 Warner Timer software and fMRI experimental block design. For the first sequence, green arrows indicate the onset time of the odorant stimulus and red arrows indicate when the stimulation ends. For the second one, green arrows indicate the onset of clearance of odorant, and red arrows indicate when it ends. The third sequence shows the fMRI block design in this work, matching the first sequence. “0” and “1” denote the odor “on” and “off” conditions.

Figure 2.6 A black dog positioned with muzzle in mask for odorant delivery. The dot reflector is mounted to dog's head for motion tracking, the knee coil encompasses the dog's head and the mask is mounted on the front frame of the knee coil.

2.2.4 Optical Head Motion Tracking

Head movement is a critical issue for all modalities of brain imaging, especially for fMRI. Excessive movement results in image ghosting and blurring. Because head movement is a significant obstacle in imaging studies of conscious animals, and some cognitive processes such as olfaction are impossible to comprehensively study in anesthetized animals [38] [39] [40], we have adopted an approach involving both dog training and optical head motion tracking. Even the best trained dogs will inevitably make slight, sometimes jerky, head movement. In the present case, the dogs would sometimes pant, which is a physiologically mediated response that is difficult to reliably control through positive reinforcement procedures. Such motions are difficult to remove using post-hoc image transformations. Therefore, the ability to compensate or reduce motion artifacts is one of the most challenging difficulties while acquiring MR images from a conscious animal. To solve this problem, two approaches have been tried in the past. First, the head of the animal can be immobilized [57] using external constraints. But this method makes the animal uncomfortable and hence the data collected is not fully ecologically valid;

furthermore, such restraint is aversive and considered to be a higher level of invasiveness from an animal welfare point of view. The second approach is to independently record motion parameters during the scan, and then retrospectively use it to correct for motion or as a regressor of no interest in the activation analysis. This method is more ecologically valid, so in our experimental setting, we utilized an optical head motion tracking system [41] [58] based on a single camera to monitor and record motion parameters. However, originally this system was not specially designed for dog imaging, and thus can be adopted for general use. The advantages of single camera system over multi-camera systems are as follows [41]. First, the former does not need calibration of the angle and settings between the cameras, which must be routinely and repeatedly established in the daily function of the MRI facility. Second, the former avoids the technical difficulty of mounting multi-camera systems in-bore. Third, many MRI bores limit the field of view of cameras and this narrow aperture hinders the placement and efficacy of the second camera.

The single camera optical head motion tracking system was an MRRA Inc. model HT-1000 comprised of an IR (infrared) illuminator, an optical IR camera with a built-in DSP (digital signal processing) processor, a dot reflector, a video monitor and a palmtop computer. The IR illuminator provided an IR source that was reflected by the dot reflector mounted on the dog’s head; the IR camera picked up the reflected IR light from the dot reflector and aided in calculating the change in dot position. Specifically, the image taken by the IR camera was binarized so that the round dot reflector was clearly separated from the background. The binarized image, the x, and y displacement of the centroid of the dot reflector as well as its area calculated by the DSP processor in the IR camera were digitally transmitted to the video monitor and palmtop computer. The sampling rate was 1 kHz. By doing so, we obtained the time series of the x, y coordinates and the area in units of millimeter and mm^2, respectively. Then, these time series were downsampled to fMRI temporal resolution of TR = 1s, and the relative displacements of x(t), y(t) with respect to x(0), y(0), which were the x, y coordinates corresponding to the first fMRI volume, were obtained and used as a regressor of no interest ($Q_i(t)$ as in Eqn.2.3 of "General Linear Modeling and Statistical Testing" section which is explained later) in the activation analysis, after correcting for motion using image transformation based realignment. The dot reflector was a one-inch diameter disk of engineering grade-10 retro-reflective tape (3M Corp.) attached by adhesive to the forehead of the dog. The video monitor allows the operator to check for proper image framing.

It is noteworthy that the system described above was only capable of 2-dimensional tracking, i.e. x and y directions, anterior-posterior direction missing. However, with a properly designed 3D target [41] and scanner interface, prospective online motion correction could potentially be performed with animals which cannot be trained to minimize head movement.

2.2.5 Stimulation Paradigm

Each run consisted of 5 blocks of odor stimulation of 10s duration, with a fixed resting (no odor) interval of 30s between the end of one block and the start of the next, as illustrated in the fMRI block design sequence in Fig.2.5. The order of low and high concentration runs were randomized for both awake and anesthetized dogs. The no-odor interval was thrice the duration of the odor stimulation interval in order to prevent the adaptation of the dog's olfactory system to the odorant. Previously it was shown that repetitive brief odorant pulses ($\leq$10 s) can evoke activity in the rat olfactory bulb measurable through fMRI [59]. The choice of 10 s for odor stimulation and 30 s for baseline was motivated by previous studies showing that such a paradigm is effective for eliciting measurable neural response and at the same time, prevent habituation [60] [61]. In an fMRI analysis of the rat olfactory bulb, odorant stimulation for 4.8 minutes failed to show a reduction in activation [62]. Within a much longer stimulation (27.6 min) the activation declined, displaying habituation. Extra- and intracellular recordings of the main olfactory bulb of the rat support these results, showing just a small reduction in activation when a long stimulus of 50 s was given [63].

2.2.6 Data Acquisition

T_2*-weighted functional images were acquired using a single-shot gradient-recalled echo-planar imaging (EPI) [64] sequence for blood oxygenation level dependent (BOLD) contrast on a Siemens 3 Tesla Verio scanner. Two hundred temporal volume repetitions of 14 axial slices with 3 mm thickness were acquired using the following parameters: repetition time (TR)=1000 ms, echo time (TE)=29 ms, field of view (FOV)=192 $\times$192 mm^2, flip angle (FA)=90 degree, in-plane resolution 3$\times$3 mm, in-plane matrix 64$\times$64, and whole brain coverage. A total of 34 low and 34 high concentration runs were obtained from anesthetized dogs whereas a total of 32 low and 32 high concentration runs were obtained from awake dogs. However, 4 runs of low and 4 runs of high concentration obtained from awake dogs were excluded due to excessive motion. The exclusion criterion was: >10 mm displacement between two consecutive acquisition time points in x, y or z direction. Also, in the z direction, if there was 10mm total displacement between any two acquisition time points in one run, it meant that the dog's nose was not fully inserted in the mask at some time. This would have jeopardized the odorant effect at that time point. Therefore, any runs with > 10mm total displacement between any two acquisition time points in the z direction were also discarded. Anatomical images were acquired using magnetization-prepared rapid gradient echo (MPRAGE) [65] sequence for overlay and localization, with parameters as:

TR=1550 ms, TE=2.64 ms, voxel size: $0.792 \times 0.792 \times 1 \text{mm}^3$, FA=9°, and in-plane matrix 192×192, FOV=152×152 mm^2, number of slices: 104.

2.2.7 Image Processing

Image processing was performed using SPM8 [46] and consisted of slice timing correction, realignment to the first functional image, spatial normalization to a template, spatial smoothing, and general linear modeling (GLM) analysis. For spatial normalization, we adopted a customized strategy to deal with dog data as described below. For spatial smoothing, a Gaussian smoothing kernel with full width half maximum (FWHM) of $4 \times 4 \times 4$ mm^3 was employed. Considering that the dog's brain is smaller than that of humans, the FWHM employed by us was smaller than a FWHM of $8 \times 8 \times 8$ mm^3 usually employed with human data.

Spatial Normalization

Spatial normalization [16] is necessary because dogs have different head shapes and sizes. Therefore, to perform group-level analyses, we need to normalize them to a standard template. For human as well as monkey and rodent imaging, a standard template is available (for example, the MNI template for humans and MNI monkey atlas) [66]. Unlike human anatomical templates such as MNI which are derived using data from hundreds of subjects, the existing dog anatomical templates are derived from less than 10 dogs and hence do not capture the entire spectrum of head size variability [67]. Therefore, we adopted a more principled two-step approach. First, since for the normalization step to produce a good estimate of the spatial transformation, the modality of images should be similar, it was inappropriate to directly normalize all functional images of different dogs to one anatomical template. As a substitute, we chose a good quality anatomical image from the pool of anatomical images, obtained from an anesthetized dog, as the template. This choice was motivated by the fact that movement is negligible when dogs were anesthetized, and hence the quality of anatomical images obtained were superior. Then we chose one functional image from the same session as that of the anatomical template, and normalized it to the chosen template. Since both images were obtained from the same anesthetized dog in the same session, the normalization was relatively accurate and reliable. In the subsequent step, we used this transformed functional image as a template to normalize functional images obtained from other sessions (involving both anesthetized and conscious dogs). Since the images involved in this step were of the same modality, the normalization was relatively accurate. Note that by "session", we mean the period during which we performed a number of runs for one dog. For example, in a session for one dog, we performed 1 structural run, 2 low concentration runs, 2 high concentration runs, and 2 resting state runs. So, one session included one subject with several consecutive runs in one day. The schematic of the proposed approach is shown in Fig.2.7 and each step of the proposed normalization procedure was realized in SPM with the following parameters: 1. Template smoothing: 8 mm FWHM for step-1 and 4 mm FWHM for step-2. Since the structural image had higher resolution than the functional, we could afford to use higher smoothing in step-1 compared to step-2. 2. Source image smoothing: 4mm FWHM for both steps. 3. Interpolation: 4th B spline. 4. Voxel sizes: [2 2 2] mm.

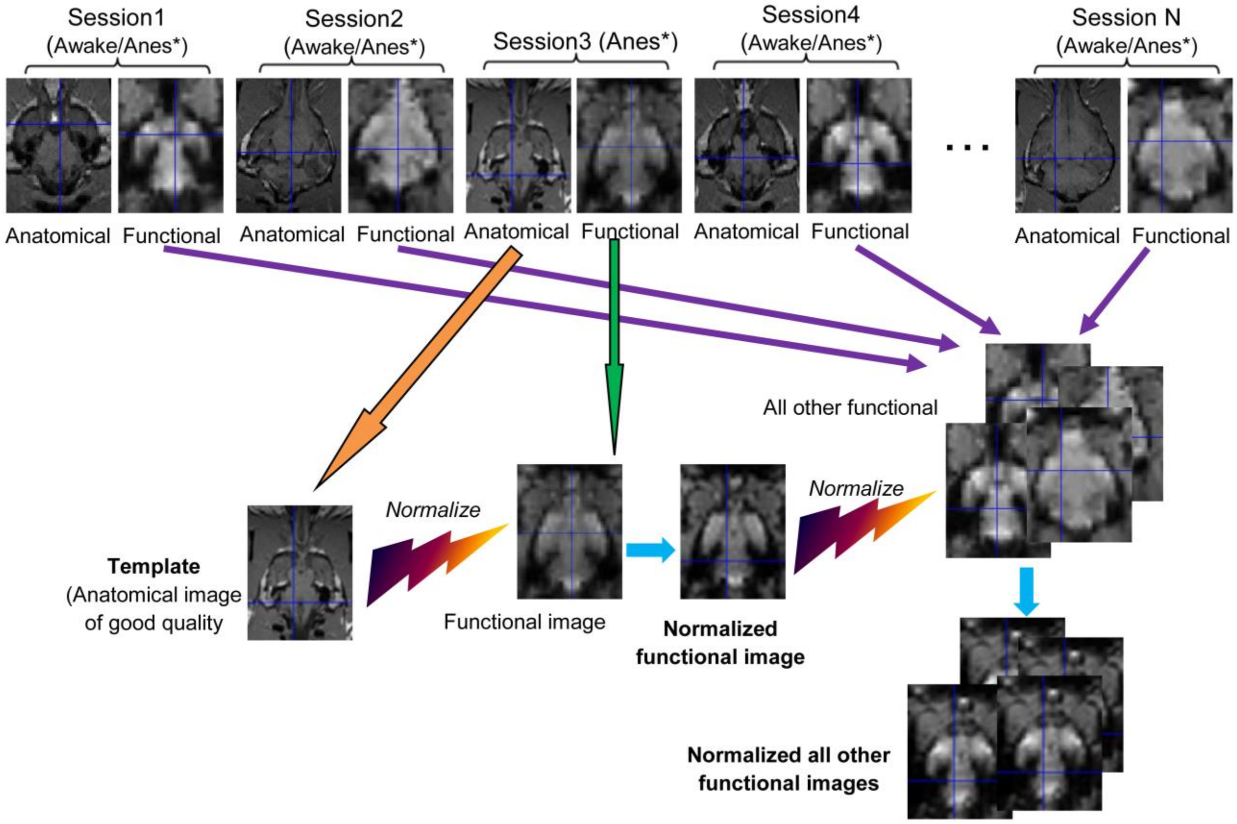

Figure 2.7 Flow chart of proposed spatial normalization procedure. A good quality anatomical image of an anesthetized dog was chosen as the template from Session 4 (4, being just an example). Then one functional image from the same session (Session 4) was chosen and normalized to the template. Subsequently, this transformed functional image was used as a template to normalize other functional images of other sessions. (*Anes: Anesthetized)

2.2.8 General Linear Modeling and Statistical Testing

Modeling the contrast of low/high odor concentration vs. rest condition

The pre-processed data was fed into a GLM for regression analysis and statistical testing of the effects of interest. The general linear equation can be briefly formulated as below.

$$Y_j = \beta_1 X_{j1} + \beta_2 X_{j2} + \cdots + \beta_N X_{jN} + \varepsilon_j \qquad j = 1 \ldots M \qquad (2.1)$$

Where Y_j is the response variable (fMRI time series at each voxel), j=1… M indexes the observation; each X_{jk} is an explanatory variable, k=1… N, β_k, k=1… N are parameters to be regressed, under least square sense. In practice, the independent identically distributed (i.i.d.)

normal distribution assumption for the error term is violated, but as long as we gather sufficient amount of data, the deviation from this assumption is deemed trivial. In our case, as indicated by the third sequence in Fig.2.5, a block design for task conditions was employed, so a boxcar function corresponding to each of the two conditions (odor ON condition and odor OFF condition) was generated such that

$$b(t) = \begin{cases} 1, \ odor\ on \\ \hline 0, \ odor\ off \end{cases} \tag{2.2}$$

The boxcar function was then convolved with a standard hemodynamic response function (HRF) *hrf*(*t*) used in SPM so as to obtain a vectorial explanatory variable X_1(t)=$b(t) \otimes hrf(t)$. This HRF was not measured directly from dogs, but in order to model the variability of HRF in experimental data, we included time derivatives and dispersion derivatives of the HRF as regressors X_2(t) and X_3(t) in the GLM. Also, in order to regress out motion effects, the 6 rigid body transformation motion parameters P_i(t), *i*=1,…,6 resulting from realignment, and camera tracking parameters Q_i(t), *i*=1, 2 corresponding to head motion captured by the camera in *x* and *y* directions, were also added in the GLM as regressors. The resulting GLM equation is as follows.

$$Y(t) = \beta_1 X_1(t) + \beta_2 X_2(t) + \beta_3 X_3(t) + \sum_{i=1}^{6} \gamma_i P_i(t) + \sum_{i=1}^{2} \delta_i Q_i(t) + \varepsilon(t) \tag{2.3}$$

Where β, γ, δ, s are the coefficients and $Y(t)$ is the observed fMRI signal at the given voxel. We tested for the statistical significance of β_1, which represents the main contrast of odor versus rest, using a t-test and obtained corresponding activation maps.

Modeling the parametric modulation of the BOLD signal by low and high odor concentrations

We will use “parametric modulation” for short when referring to “parametric modulation of the BOLD signal by odor concentration” in the following sections. To test the effect of concentration modulation, parametric modulators were included in the GLM based on the following considerations. As is well known, the intensity of odor perception *I*, as a function of odorant concentration *C*, can be described by the Weber-Fechner law [36]:

$$I = a \times \ln C + b \tag{2.4}$$

Where *I* is the perceived psychological intensity, *a* is the Weber-Fechner coefficient, and *b* is a constant. The experimental values of *a* and *b* measured for many odorants are approximately equal to 1.3 and 0.5, respectively. Thus, the change in perception due to a 10-fold increase in odorant concentration is equal to $1.3 \times \ln(10) \approx 3$ [31]. *In vitro* data recently reported by our group showed elegant agreement with this, i.e., a 10-fold increase in odorant concentration resulted in approximately 3-fold increase of the electro-olfactogram (EOG) signal [33], under the assumption that amplitudes of EOG signals elicited by various odorants *in vitro* correlate with perception of odor intensity. If we assume the fMRI signal has the same correlation with perception of odor intensity, a parametric modulation of the fMRI signal with a ratio of 1:3 for increasing the odorant concentration by 10 times is suggested. Therefore, we concatenated one run of low concentration and one run of high concentration from the same session to form one observed variable. We constructed a parametric modulator *M* with a value of 1 for representing low concentration, and 3 for representing high concentration, and then included it into the GLM. So Eq.2.3 changes to Eq.2.5 as below.

$$\begin{bmatrix} Y_{low}(t) \\ Y_{high}(t) \end{bmatrix} = \beta_{1mod} \begin{bmatrix} X_1(t) \\ X_1(t) \end{bmatrix} .\times M + \beta_{2mod} \begin{bmatrix} X_2(t) \\ X_2(t) \end{bmatrix} .\times M + \beta_{3mod} \begin{bmatrix} X_3(t) \\ X_3(t) \end{bmatrix} .\times M$$

$$+ \sum_{i=1}^{6} \gamma_{imod} \begin{bmatrix} P_{low}(t) \\ P_{high}(t) \end{bmatrix} + \sum_{i=1}^{2} \delta_{imod} \begin{bmatrix} Q_{low}(t) \\ Q_{high}(t) \end{bmatrix} + \begin{bmatrix} \varepsilon_{low}(t) \\ \varepsilon_{high}(t) \end{bmatrix} \tag{2.5}$$

Here, .× means array multiplication, and subscripts “low” and “high” indicate corresponding regressors in Eq.2.5 obtained from low or high concentration runs, with corresponding coefficients named $\beta_{1\text{mod}}$, $\beta_{2\text{mod}}$, $\beta_{3\text{mod}}$, γ_{imod}, i=1:6, and δ_{imod}, i=1:2.

After solving Eq.2.5 with regression coefficients as unknowns, a t-test was conducted for the significance of the parametric modulator $\beta_{1\text{mod}}$. The numerical value of $\beta_{1\text{mod}}$ represents the effect of the concentration modulation, meaning that the brain area with significant nonzero $\beta_{1\text{mod}}$ showed three times the response for high concentration as opposed to low concentration.

Correction for multiple comparisons

To account for the false positive activations, we used a multiple comparison correction procedure called AlphaSim algorithm [68] [69] [70]. AlphaSim provides a means of estimating the overall significance level (the probability of a false detection) for an entire 3D functional image. This is accomplished by Monte Carlo simulation of the process of image generation, spatial correlation of voxels, voxel intensity thresholding, masking, and cluster identification. Based on the combination of individual voxel probability thresholding and minimum cluster size thresholding, the probability of a false positive detection per image is determined from the frequency count of cluster sizes. The underlying principle is that true regions of activation will tend to occur over contiguous voxels, whereas noise has much less of a tendency to form clusters of activated voxels. Therefore, the presence of clustering can be used as one criterion to distinguish between signal and noise. We used the dog brain mask created by ourselves as the image within which the activation was of interest to us and fed it into this algorithm. And we set the number of iterations to be 1000, the individual voxel probability threshold as p=0.05, and consequently the minimum cluster size threshold was calculated to be equal to 15 voxels, corresponding to false positive detection probability = 0.05 for the entire image.

2.3 Results

2.3.1 Spatial Normalization

Figure 2.8 shows one representative set of images before and after the spatial normalization using the procedure described in Figure 2.7. It can be seen that the functional image (Fig.2.8 (B)) is normalized well to its own anatomical (Fig.2.8 (A)). The mismatch between functional images from different dogs is conspicuous before normalization (Fig.2.8 (B) and (C)). After the second normalization step, they look similar (Fig.2.8 (B) and (D)).

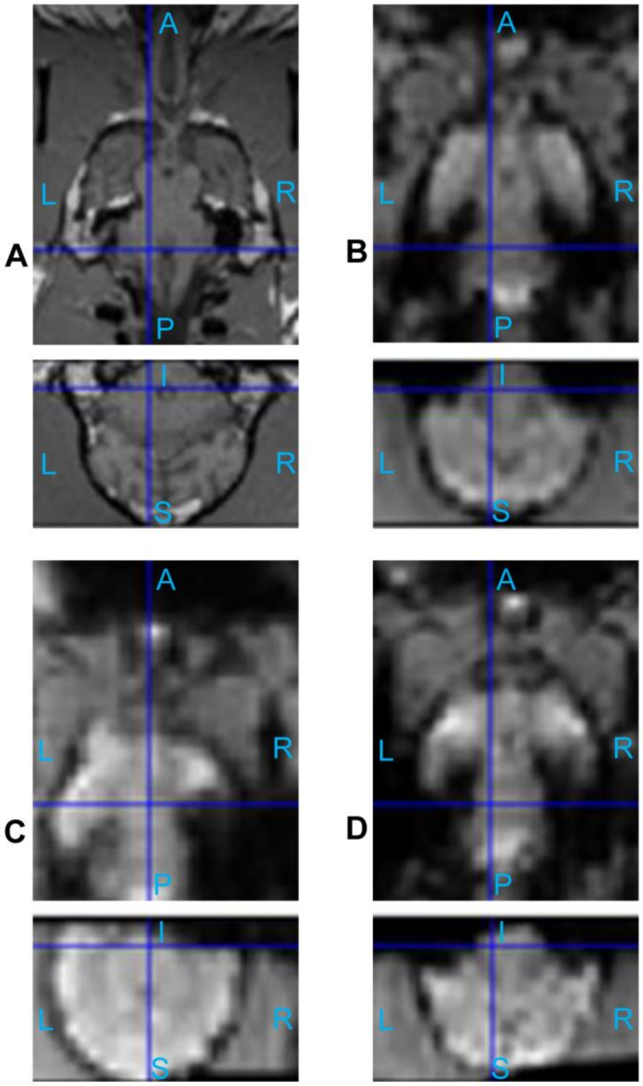

Figure 2.8 Normalization of functional images to anatomical template. The image (A) is the chosen anatomical template, its functional counterpart acquired in the same session is normalized to this template, which is shown in (B). The image (C) is a functional image of another dog. After normalization to the functional image (B), it becomes the image (D). (A: Anterior, P: posterior, S: superior, I: inferior, L: left, R: right)

2.3.2 Low and High Odor Concentration in Anesthetized and Conscious Dogs

The statistical activation maps shown in Figs.2.9, 2.10, and 2.11 were obtained using a t-contrast, cluster size threshold of 15 voxels calculated from AlphaSim algorithm applied to account for multiple comparisons, and individual voxel probability threshold p=0.05 (the t threshold corresponding to this p value is 1.645). It is noteworthy that humans normally lie in the scanner facing up (i.e. head first-supine), but in our scenario, dogs were in “head first-prone” position in the scanner. Therefore, there is a difference in orientations between Fig.2.8, 2.9, 2.10, 2.11 and 2.14 in this paper and the routinely reported human images. The names of activated areas were identified by Professor Edward Morrison and Vitaly Vodyanoy who have vast experience with dog neuroanatomy and olfactory physiology. They based their conclusions on visual comparison of activation images with published dog brain atlases [71]. Figure 2.9 shows activation maps obtained from anesthetized dogs for low odor concentration (Fig.2.9 (A)), and for high odor concentration (Fig.2.9 (B)). Corresponding cluster-level activation statistics are summarized in Table 2.1 and Table 2.2. Figure 2.10 illustrates the activation maps for low (Fig.2.10 (A)) and high odor concentration (Fig.2.10 (B)) in conscious dogs. Tables 2.3 and 2.4 show corresponding cluster-level activation statistics for conscious dogs. For both awake and anesthetized dogs, we observed expected strong activation in the olfactory bulb and bilateral piriform lobes, including anterior olfactory cortex, piriform cortex, periamygdala, and entorhinal cortex for both low and high odor concentration. The ventro-posterior location of the activation in the olfactory bulb is in agreement with previous studies in rats [72]. Visual comparison of the maps obtained from low odor vs. rest and high odor vs. rest contrasts reveals that the spatial extent and intensity of activations are larger for high odor concentration as compared to low concentration in both anesthetized (see Tables 2.1 and 2.2) and awake dogs (see Tables 2.3 and

2.4). A visual comparison of activation maps of anesthetized and conscious dogs shows dramatic differences in the spatial localization of activation. Activations in cognition-related areas such as medial, superior and orbital frontal cortices, and cerebellum are mainly found in conscious dogs.

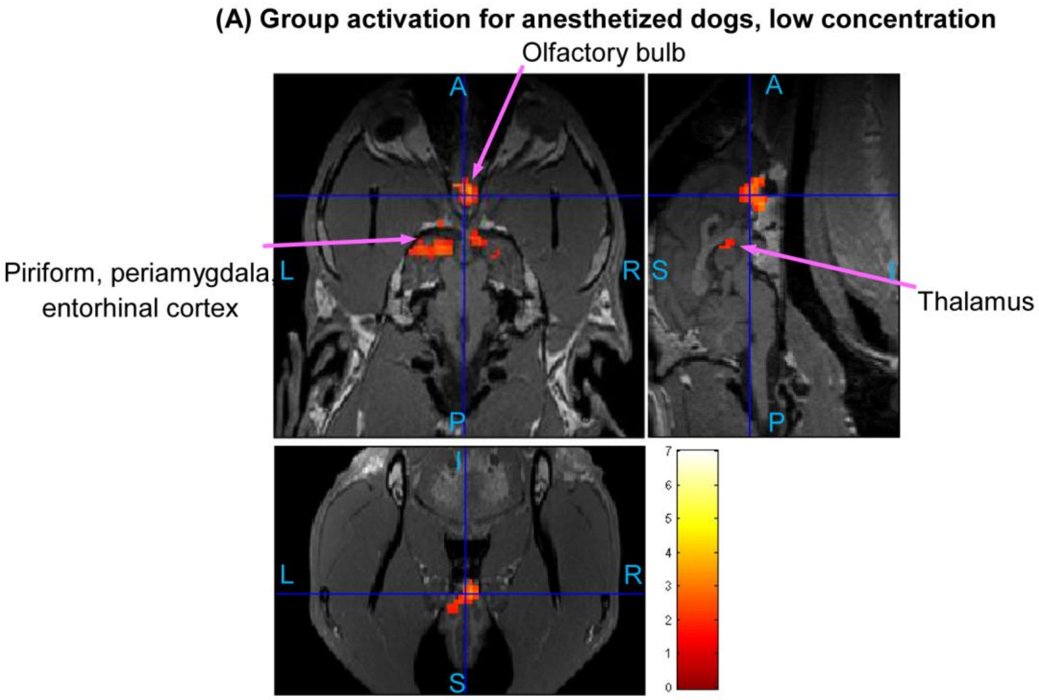
(A) Group activation for anesthetized dogs, low concentration

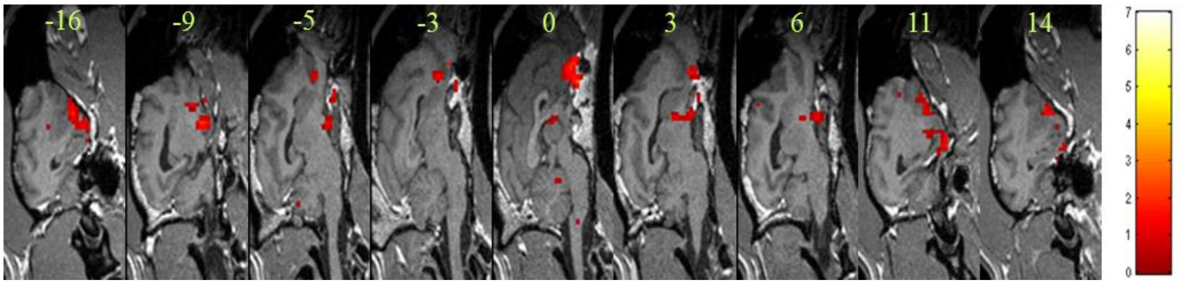

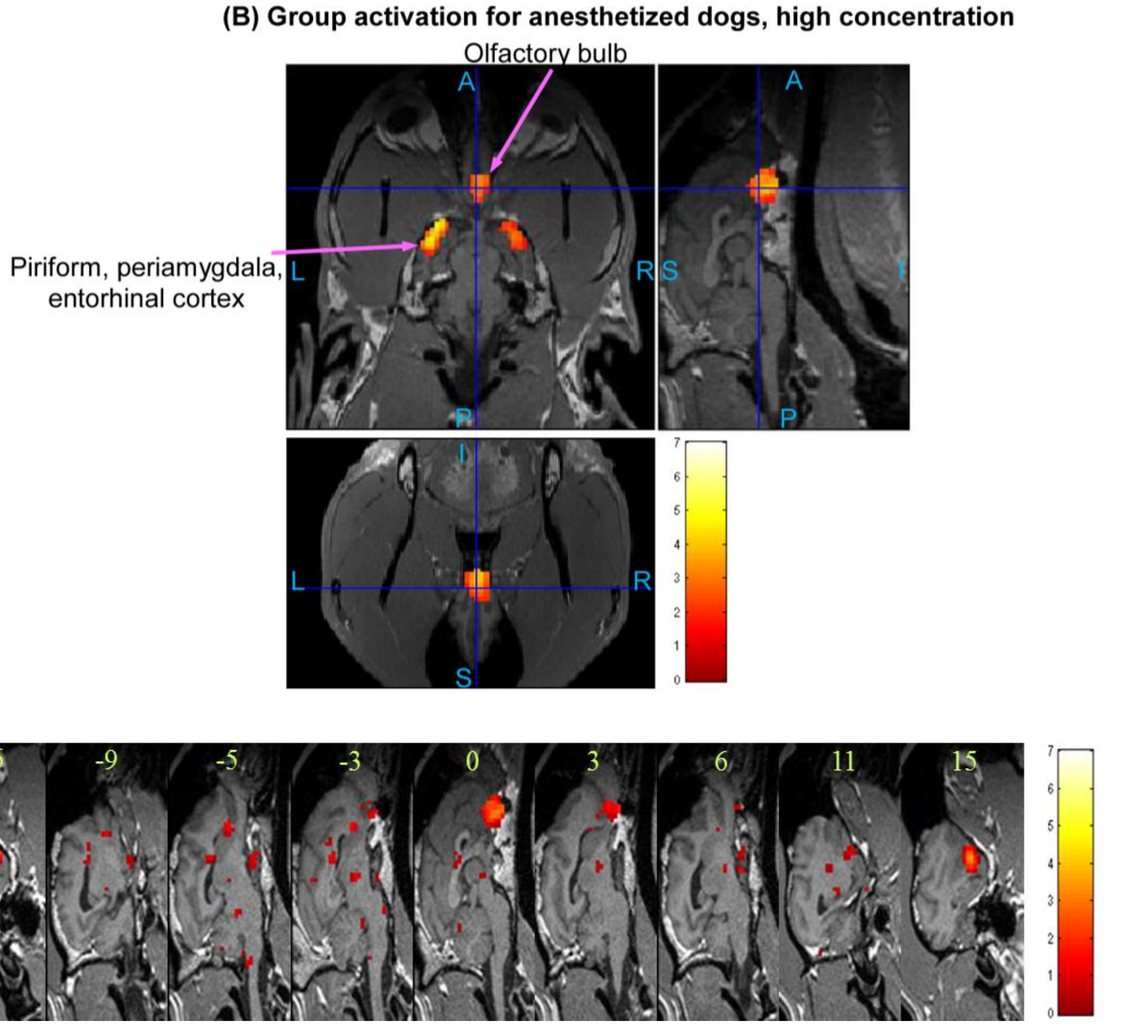

Figure 2.9 Group activation maps for anesthetized dogs. (Overall FDR=0.05, cluster threshold =15 voxels using AlphaSim, t-contrast) Three orthogonal views are shown above and key sagittal slices are shown below for each subfigure. Hot colormap is used for activation intensity, and important areas are indicated by arrows with labels. Subfigure (A) corresponds to low concentration odorant (0.016mM), subfigure (B) corresponds to high concentration odorant (0.16mM). (A: Anterior, P: posterior, S: superior, I: inferior, L: left, R: right) The image order in sagittal slices is from left to right hemisphere, with coordinate labels shown atop.

(A) Group activation for awake dogs, low concentration

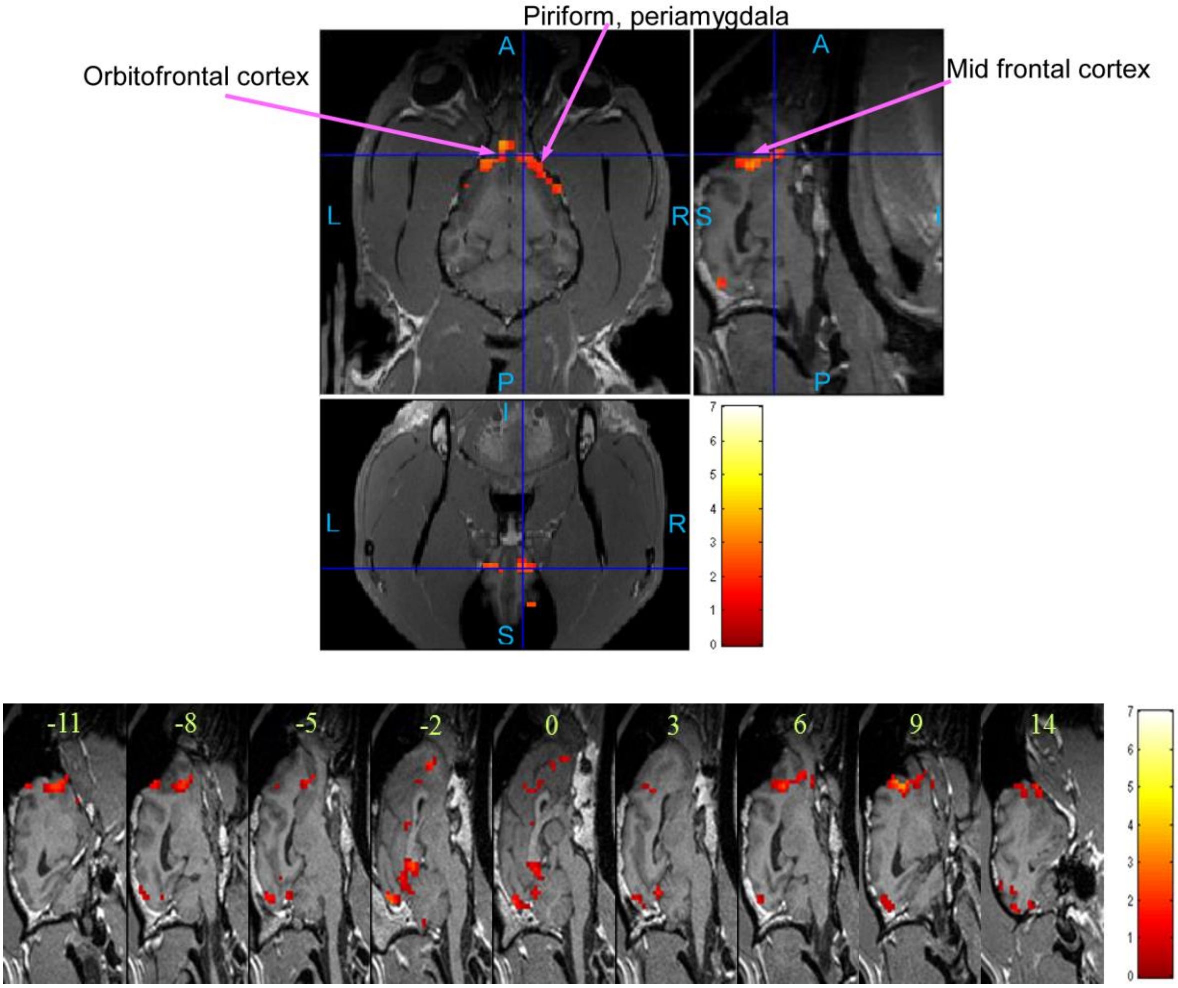

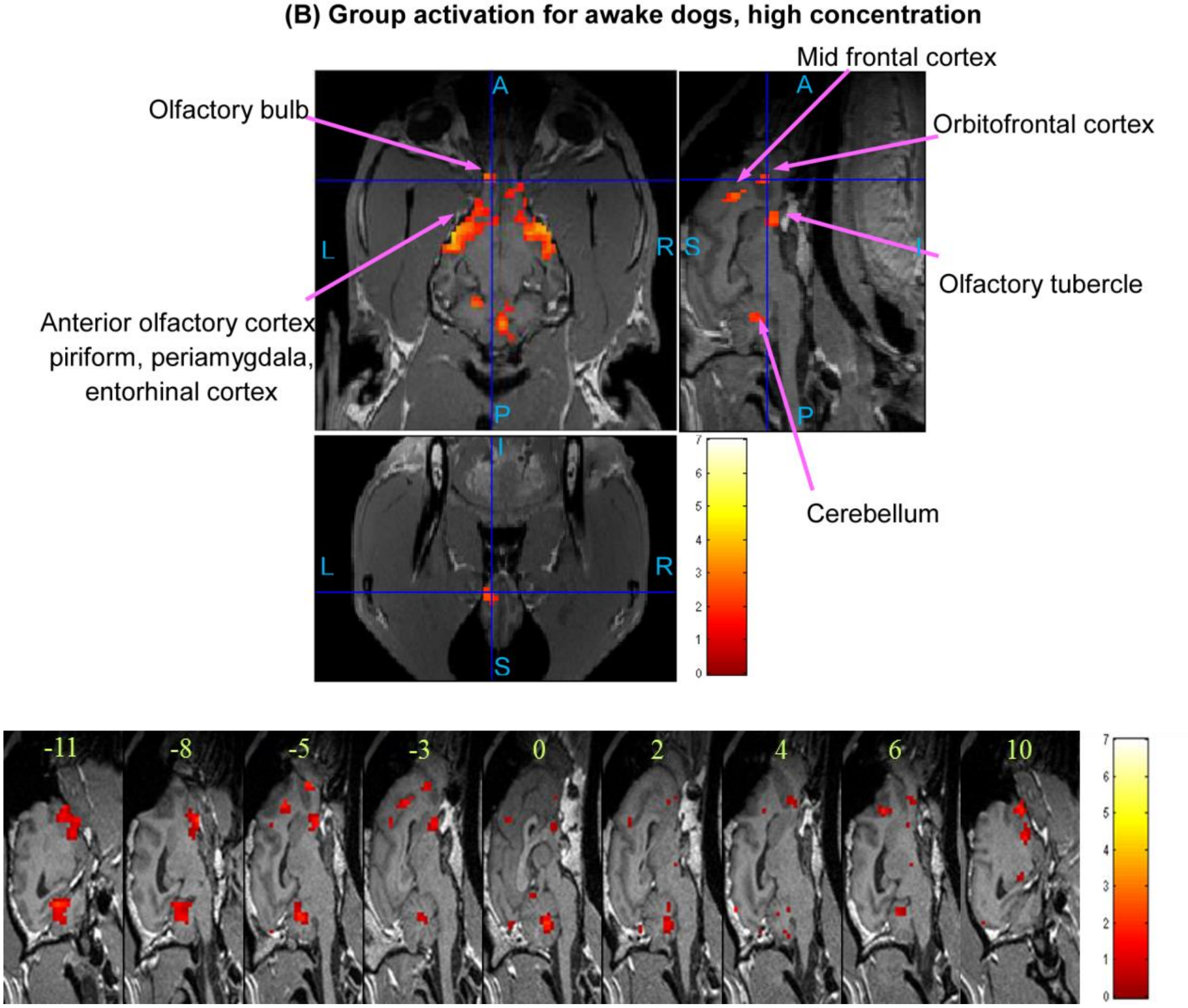

Figure 2.10 Group activation maps for awake dogs. (Overall FDR=0.05, cluster threshold =15 voxels using AlphaSim, t-contrast) Three orthogonal views are shown above and key sagittal slices are shown below for each subfigure. Hot colormap is used for activation intensity, and important areas are indicated by arrows with labels. Subfigure (A) corresponds to low concentration odorant (0.016mM), subfigure (B) corresponds to high concentration odorant (0.16mM). The activation in olfactory bulb for low concentration is not visible in this view; please refer to Table 2.3 for activation statistics with regard to this region. (A: Anterior, P: posterior, S: superior, I: inferior, L: left, R: right) The image order in sagittal slices is from left to right hemisphere, with coordinate labels shown atop.

Table 2.1 Cluster-level statistics of activations for anesthetized dogs, low concentration of odorant.*

Number of activated clusters: 4, total number of activated voxels: 365			
Cluster	Anatomical areas included	Number of activated voxels	Peak T value
#1	**olfactory bulb**	105	3.53
#2	**left anterior olfactory cortex, left**	146	3.05

	piriform cortex, left periamygdaloid cortex, left entorhinal cortex		
#3	thalamus, hypothalamus	89	2.95
#4	**right anterior olfactory cortex, right piriform cortex, right periamygdaloid cortex**	25	2.64

*: ROIs shown in bold face were commonly activated for low and high (Table.2.2) odor concentration, as well as parametric modulation by odor concentration (Table.2.5)

Table 2.2 Cluster-level statistics of activations for anesthetized dogs, high concentration of odorant. *

Number of activated clusters: 5, total number of activated voxels: 424			
Cluster	Anatomical areas included	Number of activated voxels	Peak T value
#1	**left anterior olfactory cortex, left piriform cortex, left periamygdaloid cortex, left entorhinal cortex**, left frontal cortex	159	5.16
#2	**right anterior olfactory cortex, right piriform cortex, right periamygdaloid cortex**, right entorhinal cortex	97	4.16
#3	**olfactory bulb**	113	4.00
#4	**left piriform cortex**	24	2.75
#5	mid-cingulate	31	2.43

*: ROIs shown in bold face were commonly activated for low (Table.2.1) and high odor concentration, as well as parametric modulation by odor concentration (Table.2.5)

Table 2.3 Cluster-level statistics of activations for awake dogs, low concentration of odorant. *

Number of activated clusters: 3, total number of activated voxels: 379			
Cluster	Anatomical areas included	Number of activated voxels	Peak T value
#1	right superior frontal, right mid-frontal, right orbito-frontal cortex, right piriform cortex, right periamygdaloid cortex, right entorhinal cortex	124	4.15
#2	occipital cortex, **cerebellum**	172	3.75
#3	**Olfactory bulb**, left mid-frontal, left and central orbito-frontal cortex, left piriform cortex, left periamygdaloid cortex, left entorhinal cortex	83	3.35

*: ROIs shown in bold face were commonly activated for low and high (Table.2.4) odor concentration, as well as parametric modulation by odor concentration (Table.2.6)

Table 2.4 Cluster-level statistics of activations for awake dogs, high concentration of odorant. *

Number of activated clusters: 7, total number of activated voxels: 759			
Cluster	Anatomical areas included	Number of activated voxels	Peak T value
#1	bilateral anterior olfactory cortex, bilateral piriform cortex, bilateral periamygdaloid cortex, bilateral entorhinal cortex, medial and lateral olfactory stria, olfactory tubercle, left and right prefrontal, mid-frontal cortex	430	5.15
#2	**right cerebellum**	57	3.88
#3	**cerebellum**	185	3.64
#4	**olfactory bulb**	18	2.90
#5	left mid-frontal cortex	19	2.84
#6	left orbito-frontal cortex	27	2.81
#7	thalamus	23	2.58

***:** ROIs shown in bold face were commonly activated for low (Table.2.3) and high odor concentration, as well as parametric modulation by odor concentration (Table.2.6)

2.3.3 Parametric Modulation of BOLD Signal by Odor Concentration

The differential response to odor concentration in terms of intensity can be quantified by using parametric modulators in GLM analysis as discussed before. The activated regions shown in Fig.2.11 corresponding to anesthetized (Fig.2.11 (A)) and conscious dogs (Fig.2.11 (B)), respectively, have higher amplitude of activation in response to high as compared to low odorant concentration. Cluster-level activation statistics for parametric modulation are summarized for anesthetized and awake dogs in Tables 2.5 and 2.6, respectively. For anesthetized dogs, the regions showing parametric modulation are in the olfactory bulb, olfactory tubercle, piriform lobes, and part of brain stem, while those regions for conscious dogs are mainly in the olfactory bulb and cerebellum (see Tables 2.5 and 2.6).

While Fig.2.11 shows the spatial localization of regions parametrically modulated by odor concentration, Figs 2.12 and 2.13 show their temporal profile. Figure 2.12 gives a comparison of the fitted time series for low and high concentration in anesthetized dogs. The fitted time series were derived from the GLM and were mean time series for region of interests (ROIs) within anatomical areas which were activated by both low and high concentrations, as well as the parametric modulator. These anatomical areas were the olfactory bulb, left and right piriform lobes for anesthetized dogs. In each of the anatomical areas, the ROI was determined by a 2 mm radius sphere centered at the location of highest activation of parametric modulation. Fig.2.13 gives a comparison of the fitted time series for low and high concentrations in conscious dogs. The anatomical areas were the olfactory bulb and cerebellum. These fitted time series demonstrate higher activation intensity for high, as compared to low, odor concentration, suggesting the modulation of response by odor intensity in these ROIs. It is noteworthy that the fitted time series for awake dogs in ROIs approximately follow the 1:3 ratio in accordance with Weber’s law [36] whereas in anesthetized dogs, it is approximately 1:2.

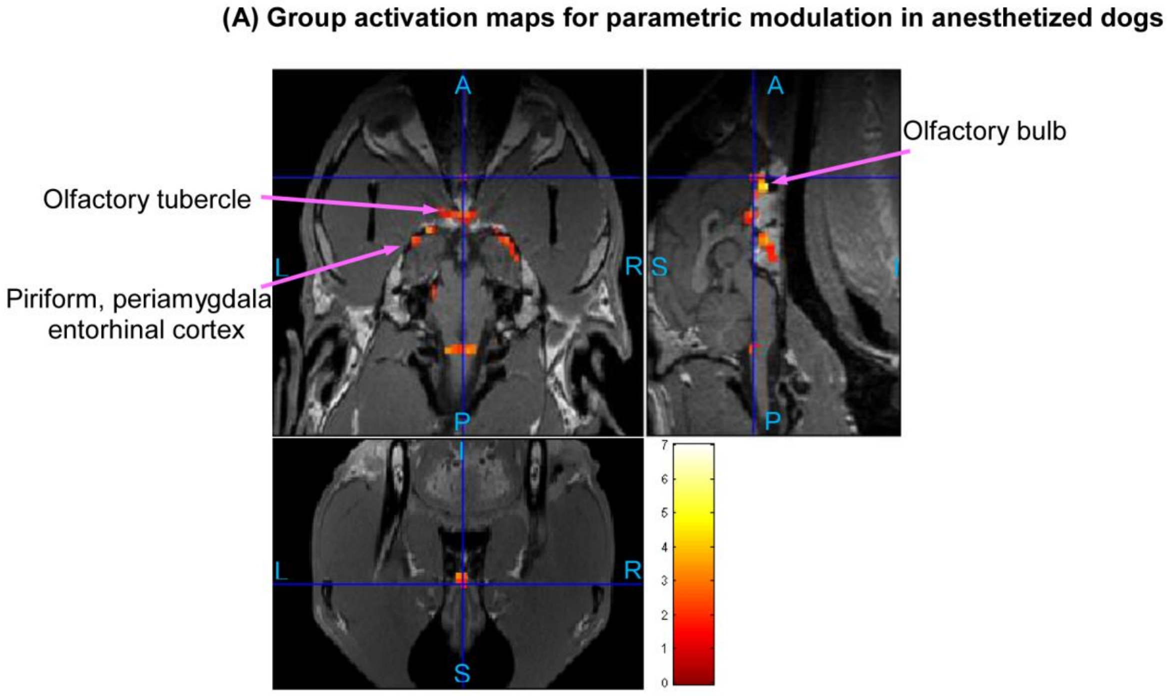

(A) Group activation maps for parametric modulation in anesthetized dogs

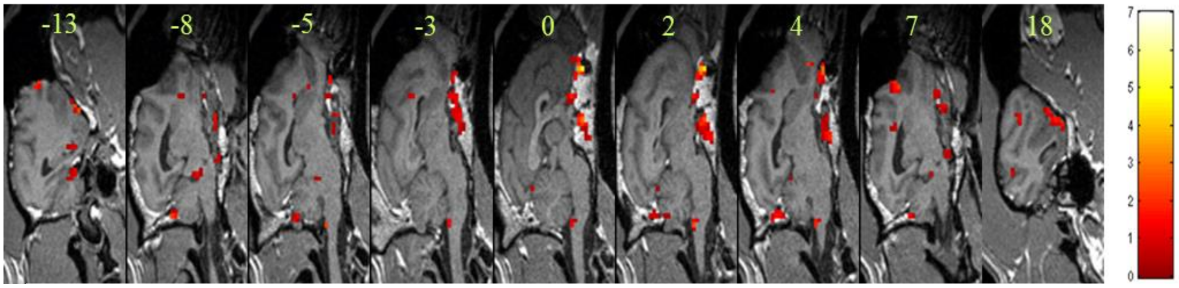

(B) Group activation maps for parametric modulation in awake dogs

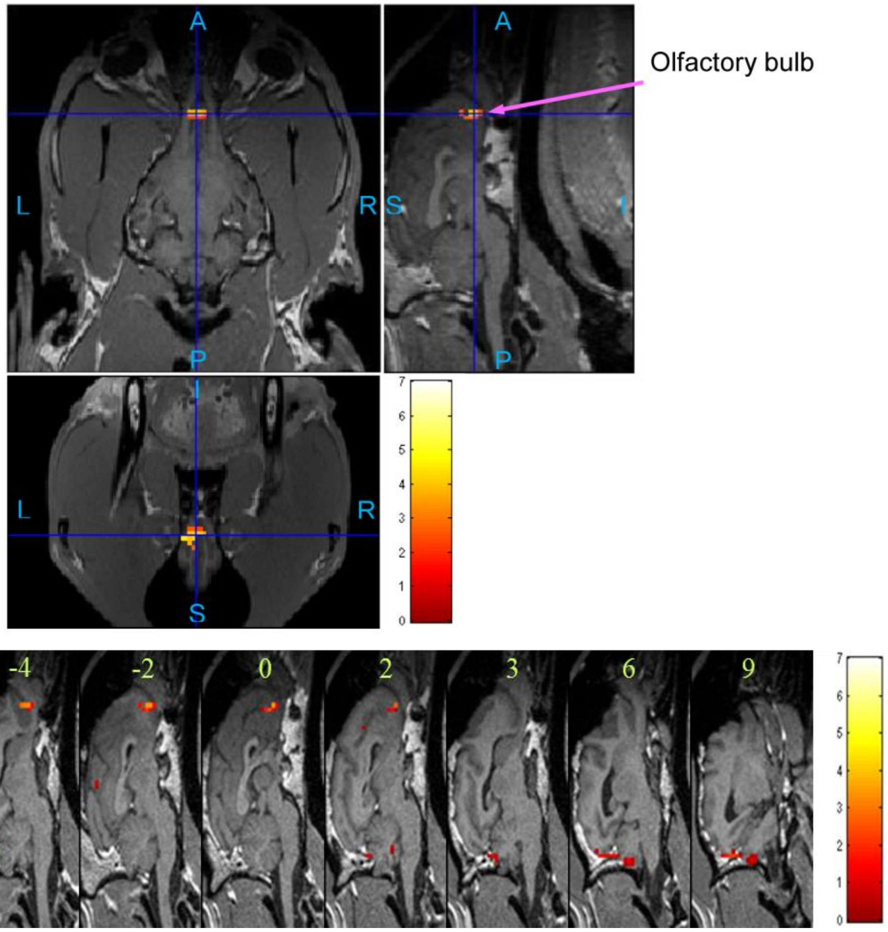

Figure 2.11 Group activation maps for parametric modulation in anesthetized dogs (A) and awake dogs (B). (Overall FDR=0.05, cluster threshold =15 voxels using AlphaSim, t-contrast). Three orthogonal views are shown above and key sagittal slices are shown below for each subfigure. Hot colormap is used for activation intensity, and important areas are indicated by arrows with labels. (A: Anterior, P: posterior, S: superior, I: inferior, L: left, R: right) The image order in sagittal slices is from left to right hemisphere, with coordinate labels shown atop.

Table 2.5 Cluster-level statistics of activations for parametric modulation of anesthetized dogs.*

Number of activated clusters: 8, total number of activated voxels: 345

Cluster	Anatomical areas included	Number of activated voxels	Peak T value
#1	**olfactory bulb**	42	5.49
#2	medial and lateral olfactory stria, olfactory tubercle,	112	3.77
#3	right superior frontal cortex	35	3.49
#4	**right anterior olfactory cortex, right piriform cortex, right periamygdaloid cortex,** right entorhinal cortex	61	3.36
#5	brain stem	15	3.36
#6	**left anterior olfactory cortex, left piriform cortex, left periamygdaloid cortex, left entorhinal cortex**	26	3.26
#7	mid-occipital cortex	18	2.80
#8	left cerebellum	36	2.55

*: ROIs shown in bold face were commonly activated for low (Table.2.1) and high (Table.2.2) odor concentration, as well as parametric modulation by odor concentration.

Table 2.6 Cluster-level statistics of activations for parametric modulation of awake dogs.*

Number of activated clusters: 2, total number of activated voxels: 52			
Cluster	Anatomical areas included	Number of activated voxels	Peak T value
#1	**olfactory bulb**	24	4.53
#2	right occipital cortex, **cerebellum**	28	3.51

*: ROIs shown in bold face were commonly activated for low (Table.2.3) and high (Table.2.4) odor concentration, as well as parametric modulation by odor concentration.

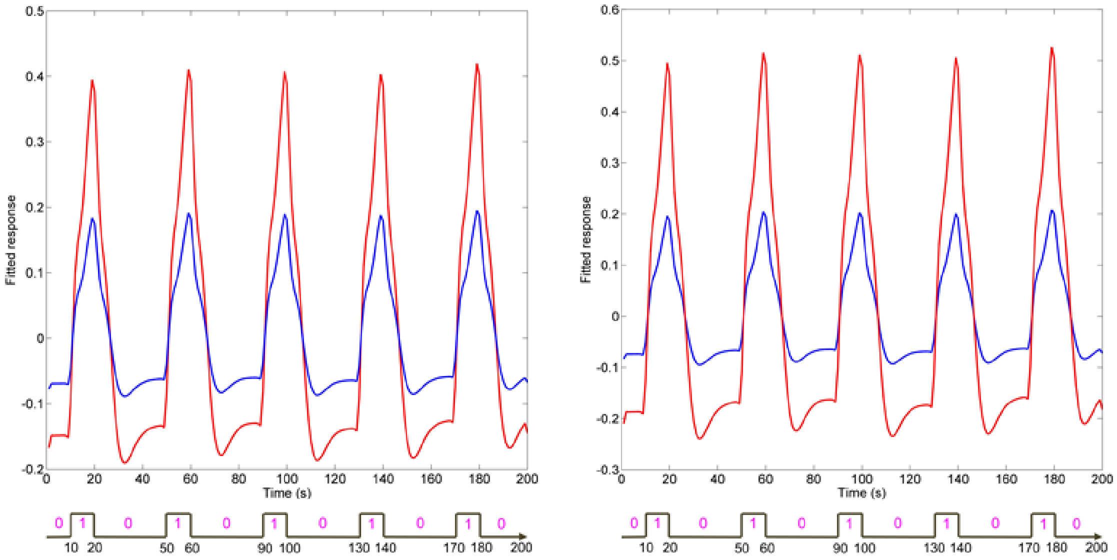

(A) Olfactory bulb

(B) Left piriform lobe

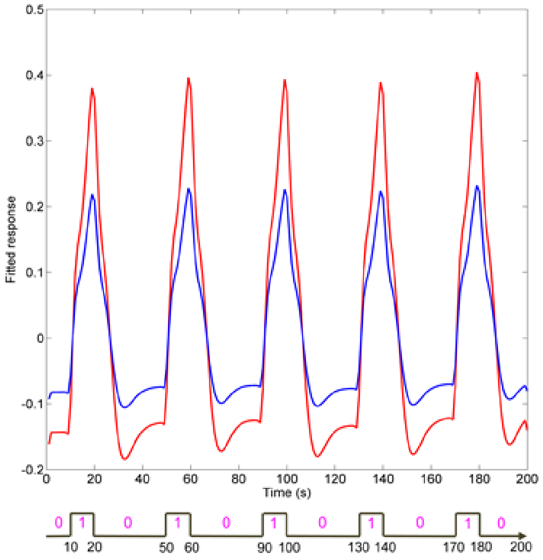

(C) Right piriform lobe

Figure 2.12 Comparisons of fitted time series obtained from the GLM for ROIs in anesthetized dogs. The ROIs are in brain regions that were activated by low and high odor concentration, as well as parametric modulation by odor intensity in anesthetized dogs. These regions are olfactory bulb and bilateral piriform lobes, which are shown in bold face in Tables 2.1, 2.2, and 2.5. In each of these regions, the ROI was determined by a sphere which centers at the peak activation of parametric modulation and has a radius of 2mm. Fitted time series for low concentration are shown in blue, and high concentration in red.

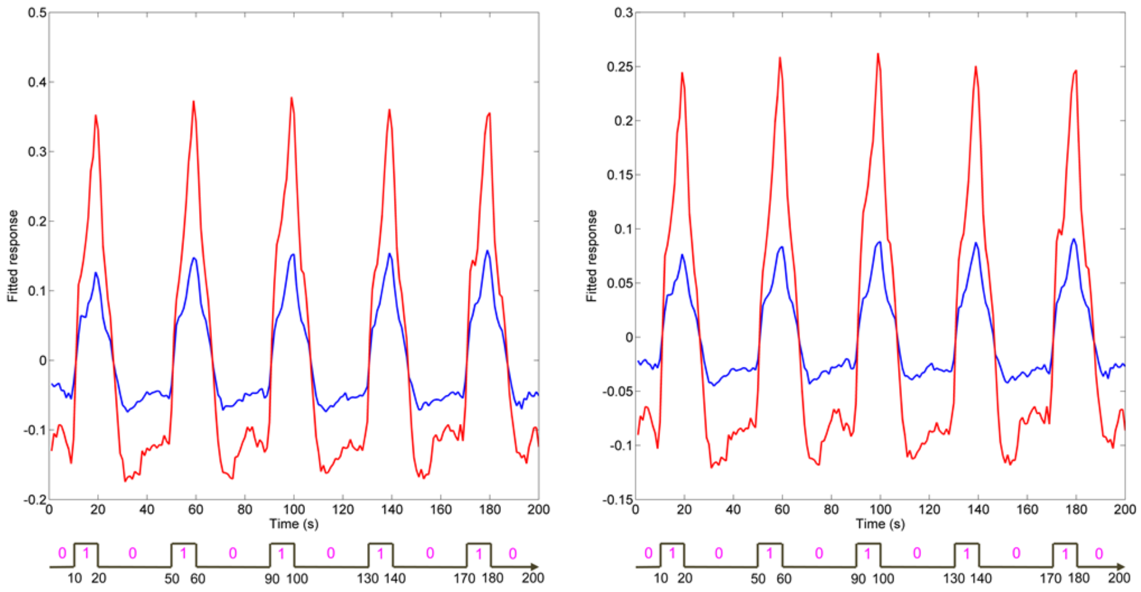

(A) Olfactory bulb

(B) Cerebellum

Figure 2.13 Comparisons of fitted time series obtained from the GLM for ROIs in awake dogs. The ROIs are in brain regions that were activated by low and high odor concentration, as well as parametric modulation by odor intensity in awake dogs. These regions are olfactory bulb and cerebellum, which are shown in bold face in Tables 2.3, 2.4, and 2.6. In each of these regions, the ROI was determined by a sphere which centers at the peak activation of parametric modulation and has a radius of 2mm. Fitted time series for low concentration are shown in blue, and high concentration in red.

2.3.4 Effect of Motion

Figure 2.14 shows a comparison of the activation maps obtained with only realignment parameters obtained from rigid body transformations performed in SPM used as regressors in the GLM versus using both camera motion tracking and SPM realignment parameters as regressors in the GLM. It can be seen that, many activated areas can be identified using either methods, but there are non-trivial differences. We can see apparent additional activation in olfaction-related areas such as the orbitofrontal cortex and right piriform lobe when using motion parameters obtained from the camera as regressors in the GLM. This shows that jerky movements cannot be solely accounted for by SPM realignment and hence optical head motion tracking is valuable for imaging awake dogs.

Each subfigure in Figure 2.15 shows 6 realignment parameters obtained by using SPM for anesthetized or awake dogs. The realignment was referenced to the first functional image for each run, so all curves have zero values at the first time point, the basis point. Figures 2.15 (A) and (B) show mean and standard deviation time series of affine parameters for anesthetized dogs, respectively, while (E) and (F) show mean and standard deviation time series for awake dogs, respectively. (C) and (D) show affine parameters for the worst and best performing dogs, respectively, under anesthesia. Likewise, (G) and (H) show affine parameters for the worst and best performing awake dogs, respectively. Note that the worst performing awake dog was not included in the analysis. As expected, the motion for anesthetized dogs is significantly smaller, i.e. much smaller than the size of a single voxel, than that for awake dogs. Also, for awake dogs, we can observe jerky movements in Fig.2.15. It is difficult to correct for such jerky movements using the realignment procedures based on rigid body transformations. Therefore, it is advisable to use optical head motion tracking to account for these jerky movements.

Additionally, we examined the proportion of variance in the signal explained by motion for the low/high concentration vs. rest condition contrast in awake dogs. For the proportion of signal variance explained by motion parameters in Eqn.2.3, we found the mean power (variance) of $\delta_1 Q_1(t)$ to be 1.58 (since the fMRI signal does not have specific units, no units can be assigned to the power as well) and that of $\delta_2 Q_2(t)$ to be 1.25. The powers of $\beta_i X_i(t)$, i=1:3 were 9.9, 4.6, and 2.6. Similarly, the powers of $\gamma_i P_i(t)$, i=1 to 6, were 0.43, 0.35, 0.21, 0.18, 0.20, 0.31, wherein the first three values corresponded to x, y, z translations and last three corresponded to 3 rotations. So, the proportion of variance in the signal explained by camera motion parameters was (1.58+1.25)/(9.9+4.6+2.6+1.58+1.25+0.43+0.35+0.21+0.18+0.2+0.31)=0.131, i.e. 13%, and the proportion of variance explained by SPM realignment parameters was

(0.43+0.35+0.21+0.18+0.2+0.31)/(9.9+4.6+2.6+1.58+1.25+0.43+0.35+0.21+0.18+0.2+0.31)=0.078, i.e. about 8%. Both were not very large. Hence this verified that retrospective motion correction sufficed.

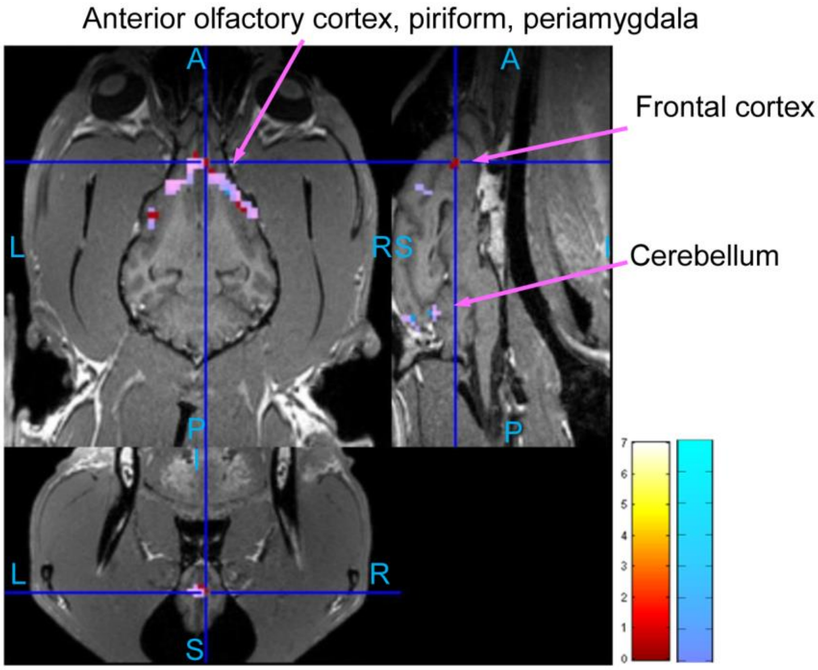

Figure 2.14 Comparison of activation maps with and without camera motion tracking parameters as regressors. (Overall FDR=0.05, cluster threshold =15 voxels using AlphaSim, t-contrast) The activtion maps were for low concentration (0.016mM) in awake dogs. The activation map obtained with only SPM realignment parameters as regressors is shown in cool colormap. The activation map with camera motion tracking parameters and SPM realignment parameters as regressors is shown in hot colormap. The common areas are overlaid such that they appear as purple. We found 3 clusters, 379 voxels in cool-colored map (same as in Table 2.3); 3 clusters, 396 voxels in hot-colorred map, and 3 clusters, 340 voxels in the common area. (A: Anterior, P: posterior, S: superior, I: inferior, L: left, R: right)

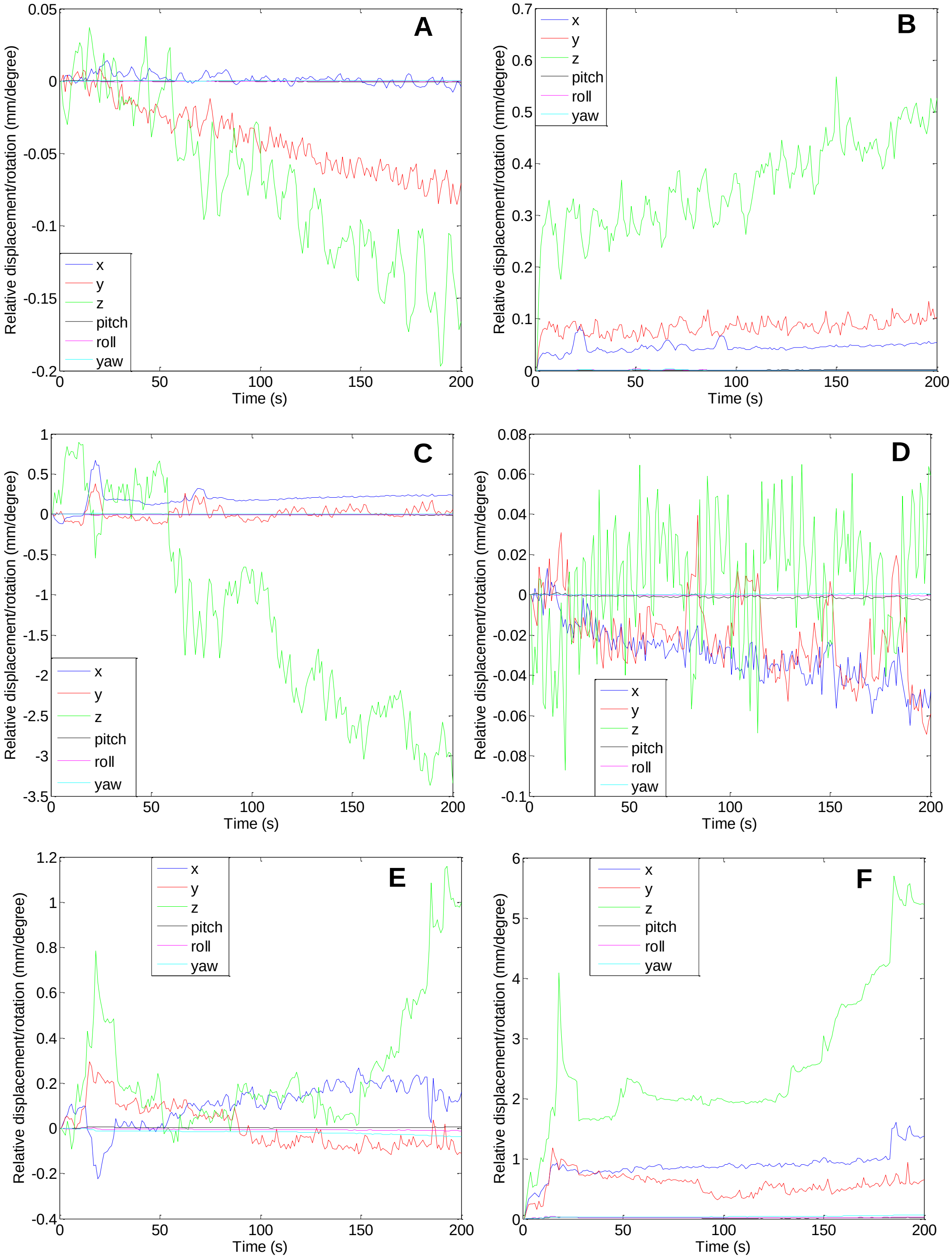
A
0.05
0
-0.05
-0.1
-0.15
-0.2
0
50
100
150
200
Time (s)
Relative displacement/rotation (mm/degree)
x
y
z
pitch
roll
yaw
B
0.7
0.6
0.5
0.4
0.3
0.2
0.1
0
0
50
100
150
200
Time (s)
Relative displacement/rotation (mm/degree)
x
y
z
pitch
roll
yaw
C
1
0.5
0
-0.5
-1
-1.5
-2
-2.5
-3
-3.5
0
50
100
150
200
Time (s)
Relative displacement/rotation (mm/degree)
x
y
z
pitch
roll
yaw
D
0.08
0.06
0.04
0.02
0
-0.02
-0.04
-0.06
-0.08
-0.1
0
50
100
150
200
Time (s)
Relative displacement/rotation (mm/degree)
x
y
z
pitch
roll
yaw
E
1.2
1
0.8
0.6
0.4
0.2
0
-0.2
-0.4
0
50
100
150
200
Time (s)
Relative displacement/rotation (mm/degree)
x
y
z
pitch
roll
yaw
F
6
5
4
3
2
1
0
0
50
100
150
200
Time (s)
Relative displacement/rotation (mm/degree)
x
y
z
pitch
roll
yaw

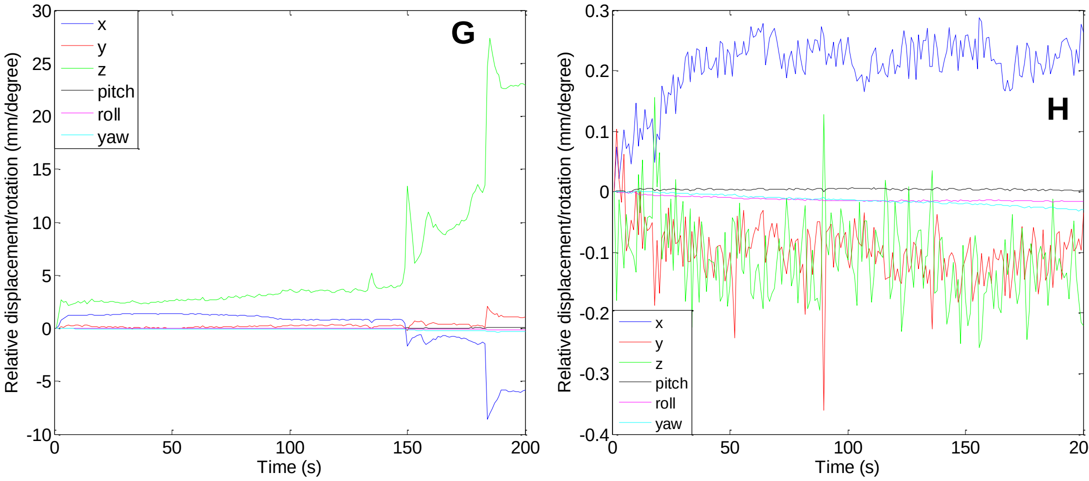

Figure 2.15 Affine parameters relative to the first functional image volume calculated by SPM realignment procedure. (A) mean time series of 6 affine parameters for anesthetized dogs; (B) standard deviation time series of 6 affine parameters for anesthetized dogs; (C) The time series of 6 affine parameters for the worst performing dog run at anesthetized state; (D) The time series of 6 affine parameters for the best performing dog run at anesthetized state; (E) mean time series of 6 affine parameters for awake dogs; (F) standard deviation time series of 6 affine parameters for awake dogs; (G) The time series of 6 affine parameters for the worst performing dog run at awake state (not included in the analysis); (H) The time series of 6 affine parameters for the best performing dog run at awake state.

2.4 Discussion

Canine detection is one of the most efficient and effective tools used by law enforcement agencies to locate and identify a wide range of explosives and illicit substances. Despite the legendary accomplishment of the canine detector, a full understanding of its olfactory system is lacking. This study is the first to our knowledge to explore the canine olfactory system at *in vivo* cognitive level using fMRI. Previous studies explored the canine olfactory system either at *in vitro* cellular level, at the behavior level, or at the anatomical level. For example, at the cellular level, distribution of putative neurotransmitter amino acids in the dog olfactory bulb [28], anisole binding protein in dog olfactory epithelium [29] and changes of dog olfactory system with age [30] have been studied. Electrophysiological responses from the olfactory epithelium to odorant mixtures have been investigated to characterize the relationship between odorant stimulation and olfactory response at the cellular level [31] [32] [33]. Psychophysical studies regarding the dog's olfactory sensitivity [73] [74] and discrimination [75] [76], as well as behavioral assessments of trained detector dog performance characteristics have been performed [34] [35]. However, the neural substrates connecting the cellular level findings with behavior have been rarely explored. From our understanding of other sensory systems, the cognitive link is critical. For example, in the visual system, neurons in the primary visual cortex contain a faithful representation of the visual field [77]. However, the behavior of the organism is driven by different aspects in the visual field which are filtered through attention and higher level cognitive integration [78]. It is this contextual “understanding” of the visual field which drives behavior, rather than the entire visual field. By analogy, the olfactory map in the olfactory bulb is projected onto neocortical areas where an “understanding” of what the olfactory cue means to the organism at that moment is constructed, which drives behavior. Therefore, it is not possible to map cellular recordings in the olfactory bulb directly onto behavior unless a cognitive-level understanding is obtained.

This study is the first attempt to propose a framework to bridge this gap by performing noninvasive functional imaging of conscious and anesthetized dogs. We found activations in the olfactory bulb, anterior olfactory cortex, piriform cortex, periamygdala and entorhinal cortex for both awake and anesthetized dogs, and they were modulated by odor concentrations. The cerebellum and cognition-related areas such as superior, medial, and orbital parts of the frontal cortex were activated mainly in the awake dogs. However, only the activations in the cerebellum and olfactory bulb were parametrically modulated by odor concentration in awake dogs. These activations are consistent with known anatomical projections from the olfactory cortex [79] [80] [81]. It is noteworthy that mainly unilateral activations in low concentration condition in awake dogs became bilateral in the high concentration condition, in agreement with previous reports of such findings in human data [81]. Other structures, such as the hippocampus, which have structural connectivity with the olfactory cortex, did not have enough activated voxels to pass the cluster size threshold imposed by us for correcting for multiple comparisons. In addition, activation of higher order structures in conscious dogs is consistent with the role of homologous structures in other species (such as humans) as reported previously. For example, it has been shown in humans that the medial and orbital parts of the frontal cortex are involved in cognitive integration of all sensory stimuli in relation to prior experiences [25] and the cerebellum is implicated in sniffing and odorant threshold detection [82]. This shows that the olfactory stimulus is not being processed in higher cognitive structures in anesthetized dogs to the extent that it is in conscious dogs, thus justifying the need for awake dog imaging.

Our interpretation regarding the parametric modulation of the BOLD signal in 1:3 ratio for a ratio of 1:10 for odor concentration is based on the assumption that the scaling of EOG signal by odorant concentration can be extrapolated to the BOLD signal. Admittedly, the latter is not solely and linearly coupled with neural electrical activity. Rather, the latter is linked to neural activity through the convolution with HRF, or more accurately, the Volterra kernel of HRF [83]. Therefore, it is remarkable that we indeed used the same scaling with BOLD as with EOG to identify olfactory related areas which are parametrically modulated. However, there is need for cautious interpretation of these results till they can be replicated by other studies.

The utility of a practical method for assessing the cognitive processing of olfactory information in awake dogs is significant. Clinically, degradation of the sense of smell is a sentinel condition, particularly for neurodegenerative diseases such as Alzheimer’s. The dog is recommended as a particularly good model of human age-related neurological disease as its brain shows neuro-pathologies and its behavior displays attendant cognitive deficits that are similar to that of humans [84]. Understanding normal cognitive processing of olfactory information may allow for identification of abnormalities of such processing well before it manifests in detectable alteration in sensory capabilities. Furthermore, the method may allow for elucidation of mechanisms underlying such olfactory degeneration that inform the etiology of such diseases.

The method described may allow for important enhancements in the use of dogs for detection of hazardous substances. The trained detector dog is widely regarded as the most versatile and capable tool for the detection of hazardous materials such as explosive devices [85]. However, there are many unresolved issues regarding how best to select, train, and employ dogs for such tasks [85]. The method described may allow for identification of olfactory processing characteristics of individual dogs indicative of exhibiting superlative performance in performing detection tasks. Thus, it may provide a means to select breeding stock for more efficient and effective production of working dogs. Description of the perceptual odor space (i.e., the physical dimensions responsible for the degree of similarity/difference of the perceptual experience of different odorants) through behavioral psychophysical methods has proven difficult and amenable to only relatively simple variation between individual chemical compounds [86]. Description of the perceptual space of olfaction relative to typical substances that are the targets of detector dogs, which are often composed of complex mixtures of chemical compounds, could significantly enhance detector dog technology. Detector dog technology could be greatly enhanced by the ability to examine the variation in cognitive processing of odorants that vary across different chemical dimensions, such as odorants to which a dog has been trained to detect vs. neutral odorants, through fMRI imaging of awake dogs. A cognitive processing model of the perceptual odor space could provide insights in explaining and ameliorating the occurrence of false alerts to particular non-target materials and misses of target materials within particular odor contexts. Phenomena such as the masking or overshadowing of target odors by other odors as well as the enhancement or disturbance of olfactory capability by the presence of particular substances could be examined using the awake fMRI imaging. Additionally, the ability to map cognitive olfactory processing could prove to be a valuable tool in characterizing the mechanism underlying the learning of odor discriminations. It is noteworthy that all of the dogs used in the current study had previous explosive odor detection training and their experience ranged from a few months of detector dog work in research projects to operational employment as a working detector dog. However, the odor detection experience of the dogs was not guided by any experimental design implications, rather, they were chosen because of their availability and because they are representative of the size and general disposition of dogs that are used as working detector dogs; hence allowing us to demonstrate the feasibility of this technique for future studies of such dogs. For the current study, none of the dogs had previous experience in detecting the specific odorants used in this study. We purposefully used odorant mixture with which the dogs had no learning history in order to not confound brain activity related to olfactory perception or the effects of previous learning history on perceptual processing of the odor stimulus. At the same time, the odorant mixture we have used is related to explosives and is recognized by dogs [87]. We intend to examine brain activity related to “learned” odors in future work by controlling the amount of exposure and training with specific odors, but in this first experiment, our intention was to confine our investigation to odors with which the dogs had no prior experience.

Apart from specific implications for the use of canine capabilities for detecting hazardous substances, our results also have implications for the advancement of dog non-invasive cognition and neurophysiology research in general. Previously researchers have made the case that physiological measures of canine cognition are required to complement behavioral studies, and have used non-invasive electroencephalography (EEG) to measure neural responses to auditory stimulus discrimination [88] and visual stimuli (specifically dog and human faces) [89, 90]. This work follows in their footsteps by incorporating fMRI as a non-invasive measure of brain function. Given the complementary strengths of EEG and fMRI, our work is likely to advance the cause of exploring the functions of deeper brain structures in canines. Further, the conclusions of this study have general implications for olfactory and sensory research in other animals.

In addition to the scientific contributions and implications discussed above, this work is likely to advance technical knowledge in the field of olfactory fMRI. First, head movement is a critical issue for fMRI. Excessive movement will corrupt the data and has been one of the barriers for imaging awake animals, though it is very well accepted that some cognitive processes are very difficult to study in anesthetized animals [38] [39] [40]. Specifically in the case of olfaction in dogs, we have demonstrated that different brain regions are recruited in awake and anesthetized dogs. In addition to passively studying cognition, even simple sensory acquisition may involve an active process which cannot be executed during anesthesia. For example, awake dogs can sniff but anesthetized dogs cannot, and hence jeopardizing the sensory acquisition process [91].

Though the case for awake animal imaging is strong, the technical challenges for achieving it are enormous. Some approaches used by previous researchers include the use of external constraints to limit motion [57] and head motion tracking using dual optical cameras in-bore [92] or external to the scanner [93]. Our proposed approach comprised of a combination of training and optical head motion tracking during awake dog imaging. The training part was employed to restrict large-scale movements which cannot be compensated retrospectively, while the optical head motion tracking part can account for jerky movements. In addition, our optical head tracking system was detached from the scanner, thus not suffering the problems caused by mount-in-bore camera systems. The results with integration of optical head tracking parameters showed the same basic activation pattern obtained by using only SPM realignment parameters, but also additional areas of activation in the orbitofrontal cortex and piriform lobe. This verifies the efficacy of the optical head tracking system. It is to be noted though, that constructing an appropriate target for the dog as done for humans before [41], could potentially allow the optical head motion system to track head movements in all six degrees of freedom thereby not requiring SPM realignment altogether. We will concentrate our future endeavors in this direction.

Next, the functional and anatomical data obtained from all dogs must be spatially normalized into one space for cross-subject comparison and group-level inference. We have proposed a strategy wherein we first chose one anatomical image with good image quality as a template, chose one functional image from the same session to normalize to the chosen anatomical, and the resulting functional image was then used as a template to normalize other functional images. This strategy was superior to directly normalizing all functional images to one anatomical template because, unlike human anatomical templates such as MNI which are derived using data from hundreds of subjects, the existing dog anatomical templates are derived from less than 10 dogs and hence do not capture the entire spectrum of head size variability [67].

Finally, the simultaneous delivery of odorants such that it is synchronized with fMRI data acquisition requires additional features in olfactometers. The most obvious one is that the components of the olfactometer which will be within the scanner's magnetic field be free of any metallic components. The desirable features of the device include computer control and odorant delivery of precise and reproducible duration at selected times, without any added stimulation (e. g., tactile, auditory) [49]. Our custom built device met all these specifications. Additionally, since it is portable, it can be used for both electrophysiological and fMRI studies.

Chapter 3 Univariate Analysis:

Enhancement of Odor-induced Activity in the Canine Brain by Zinc Nanoparticles: A Functional MRI Study in Conscious Dogs

The work in this chapter is a continuation of the work in Chapter 2. In Chapter 2, we construct the dog fMRI olfactory system and use it to acquire dog fMRI data and compare the effect of low concentration of odorant with that of high concentration of odorant. In this chapter, we continue to use this system (including fMRI scanning, dog training, odorant stimulus and optical motion tracking subsystems) to further investigate dog olfactory processing at the cognitive level. Our main contribution is that we conducted experiments with zinc nanoparticles added to the odorant and compared their enhancement effect on olfactory perception of dogs at the cognitive level, with pure odorant and odorant + gold nanoparticles as control conditions.

3.1 Introduction

It is well known that dogs possess extraordinary olfactory senses compared to humans. The human society relies heavily on the superior olfactory capabilities of dogs for detecting threats such as explosives arising from terrorism, narcotics trafficking, hazardous chemicals and other illicit substances. In many operating environments (e.g. airports, warzones, border crossings), the concentration of such odorants can be extremely low. Specifically, detecting explosives buried in soil or otherwise camouflaged is extremely difficult. Physical and chemical explosive detection methods work relatively well in the laboratory but serious challenges exist for detection in the field [76]. Sniffer dogs have been the most effective explosive detectors [85], but even trained dogs are limited because most plastic explosive materials have very low vapor pressures and their detection is therefore difficult. Therefore techniques which are capable of enhancing detector dogs' olfactory capabilities have received attention in the past decade. In this vein, previous studies [33] [94] have demonstrated that a dose-dependent addition of zinc metal nanoparticles to odorants can strongly increase the *in vitro* responses of olfactory sensory neurons as measured by electro-olfactogram (EOG). Through intracellular or extracellular perfusion, zinc nanoparticles will approximately locate at the interface between the guanine nucleotide-binding protein and the receptor proteins, and are engaged in triggering signals at the start of olfactory cascade. Further, it was demonstrated that zinc nanoparticles alone without odorants, or Zn^{2+} ions with or without odorants cannot produce such enhancement effects. Also, it was shown that gold, silver, and copper nanoparticles produced mildly stronger response than pure odorants which faded away rapidly and did not produce as much an increase in response as compared to zinc nanoparticles. Importantly, zinc nanoparticles are nontoxic to the dogs for the concentrations used [95] and it does not significantly alter the operating environment. Therefore, introduction of zinc nanoparticles into the operating environment could lead to a potential approach for the enhancement of canine olfactory detection capabilities.

Most of the previous investigations of the canine olfactory system, regarding the effect of zinc nanoparticles have been carried out at the cellular level [33] [94] [96]. This, however, presents challenges for translating these findings on *in vitro* olfactory enhancement effects into a method deployable in the field. Specifically, the *in vivo* cognitive mechanisms underlying olfactory enhancement by zinc nanoparticles in canines and corresponding behavioral modifications [75] need to be investigated. The former part is the subject of our investigation in this work. Specifically, we employed fMRI to investigate the *in vivo* effect of zinc nanoparticles on olfaction-related brain regions in awake dogs.

Since its advent, fMRI has become a very powerful tool to non-invasively investigate the cognitive and neuroscientific mechanisms of brain functions [37] [7]. Specifically with respect to olfaction, Savic et al and Zald et al investigated the cognitive basis of olfaction in humans [42] [43], while Boyett-Anderson et al. and Mori et al have reported similar work in monkeys [44] and rodents [45], respectively. Chapter 2 demonstrates the use of fMRI for investigating the cognitive basis of odor processing in fully conscious and unrestrained dogs. Specifically, we built a computer-controlled odorant applicator capable of delivering specified amount of odors at specified intervals of time to the dog inside the scanner, enabling a block design fMRI paradigm. In order to address motion-related issues in awake dogs, optical motion tracking of the dog's head was employed using external cameras. Further, the camera and odor applicator were synchronized with acquisition of fMRI data. In this work, we demonstrate the utility of this experimental framework for non-invasively investigating the *in vivo* effect of zinc nanoparticles on olfaction in the dog brain. We test the hypothesis that enhancement of cellular response in olfactory receptor neurons by zinc nanoparticles will lead to corresponding increase in activity in olfaction-related and higher order brain areas of the canine brain. We will employ odorant without zinc nanoparticles and with gold nanoparticles as control conditions to test the above hypothesis.

A brief overview of the olfactory cascade in the dog brain would facilitate the elucidation of our hypothesis. Please refer to the introduction section in Chapter 2 for details about olfactory processing chain inside the dog brain. To facilitate, a graphic illustration of the olfactory pathway rendered on dog brain surface is in Fig 3.1. We hypothesize that all regions inside the brain displayed in Fig.3.1 will show up-regulated activity in the presence of zinc nanoparticles mixed with odorant.

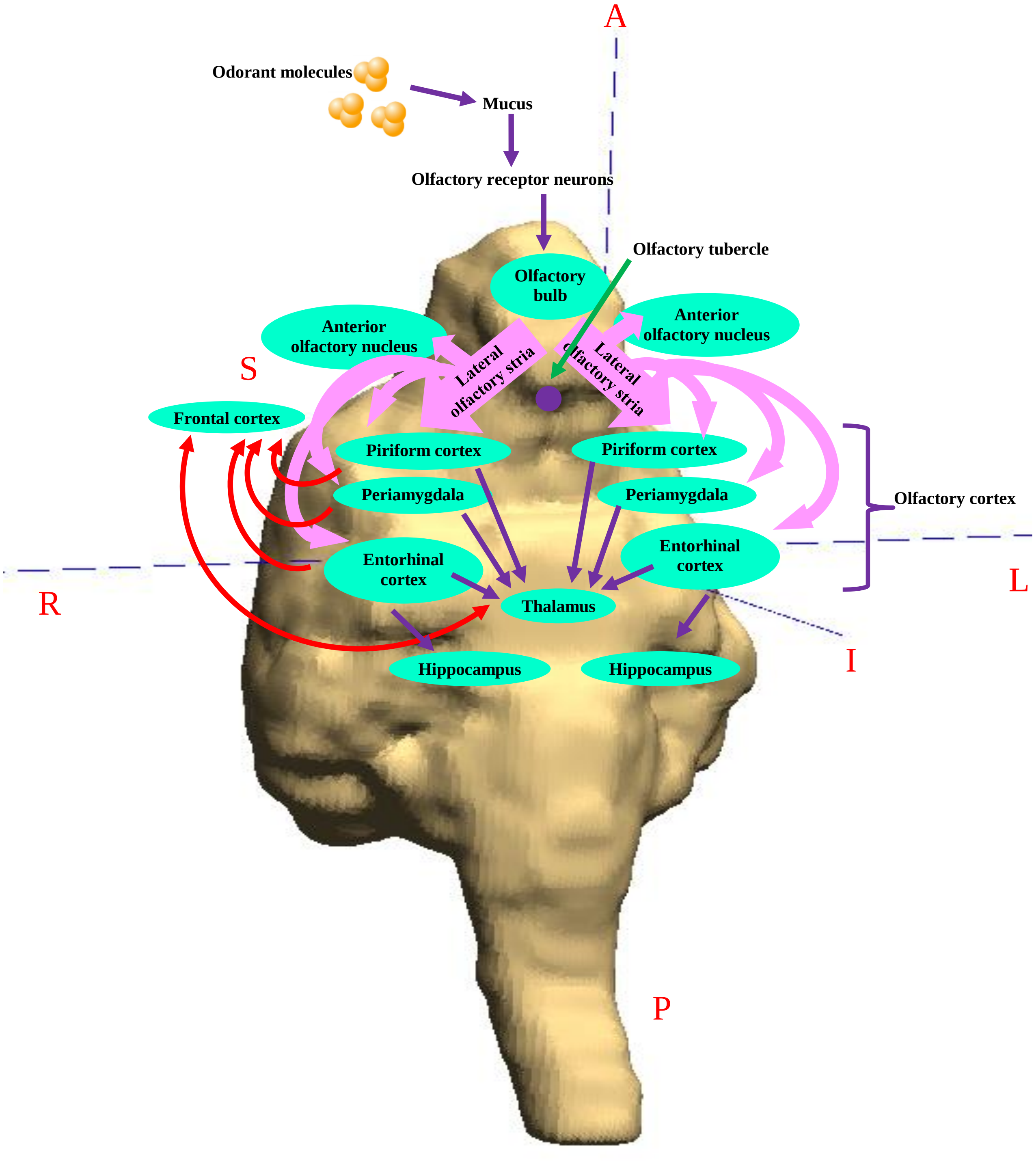

Figure 3.1 Olfactory pathway in canines rendered on inflated canine brain surface. Arrows indicate the olfactory signal flow. (A: anterior, P: posterior, L: left, R: right, S: superior, I: inferior)

This study consists of three aspects. First, we compared the effect of zinc nanoparticles in the up-regulation of activity in olfaction-related brain areas with pure odorant, i.e., no metal nanoparticles added, and gold nanoparticles + odorant as control conditions. The second aspect of this study was to compare olfactory responses for dogs in lightly anesthetized state with that in fully conscious state. As illustrated in Chapter 2, sedated dogs cannot sniff and remain unconscious, thus the activation pattern in the brain for anesthetized dogs can be quite different from awake dogs. We explored this aspect again here in the context of zinc nanoparticles. Third, the validity of optical motion tracking system [41] for imaging awake dogs had been verified in Chapter 2, therefore we continued to use this system to retrospectively correct for head motion for awake dogs. This method proved to be ecologically valid and imposed nearly no restrictions on the dog being scanned.

3.2 Material and Methods

3.2.1 Dog Preparation

The same six Labrador Retriever dogs as in Chapter 2 raised in the Auburn University Canine Detection Research Institute, with ages between 12 to 60 months, were recruited. Ethical approval for the study was obtained from the Auburn University Institutional Animal Care and Use Committee. Institutional and national guidelines for the care and use of laboratory animals were followed. It is noteworthy that, zinc nanoparticles were nontoxic to the dogs for the concentrations used [95] and hence their use was not unethical in this study. For anesthetized dog imaging, subjects were sedated with intramuscularly administered xylazine (2.2 mg/kg) and lightly anesthetized with administered ketamine HCl (11mg/kg,). For imaging of conscious dogs, a first set of experiments were conducted wherein they were trained to lie prone on the scanner bed, insert their heads into a human knee coil which elegantly acted as a dog head coil, and remain still during a specified length of scanning period. Positive reinforcement behavior shaping procedures was used to keep them as still as possible and desensitize them to loud scanner noise. The second round of experiments was conducted for data acquisition with both structural and functional sequences.

3.2.2 Odorant

The odorant was the mixture of ethyl butyrate, eugenol, and (+) and (–) carvone in water at a concentration of 0.016mM. This odorant mixture and the training procedure were the same as in Chapter 2. It is noteworthy that the odorant concentration (0.016mM) used was the low concentration in Chapter 2, for which the activation of olfaction related areas in the dog's brain can be detected. However, we were able to detect increased activation when a higher concentration (0.16 mM) was used in this previous study. This indicates that by using a low concentration of 0.016 mM in the current study, there is sufficient latitude for zinc nanoparticles to take effect to enhance olfaction related activation in the brain without saturating the brain responses.

The metal nanoparticles (zinc and gold) were prepared in the following way and then mixed with odorant. We used colloidal zinc and gold suspensions from Purest Colloids, Inc., and Indigenous Products as sources of zinc and gold nanoparticles. The suspensions were processed by filtering through 0.22-micrometer Fisherbrand Syringe Filters and centrifuged at 40,000 × g for 90 min at 18^{o}C. The metal concentration in the suspension was surveyed by atomic absorption spectra (GTW Analytical Services). Then, aliquots of the suspension were dried onto coated grids, and the particles were counted in dark field transmission electron microscope images [97] [33]. Finally, the suspensions of nanoparticles were mixed with odorant solutions at a particle concentration of 5 nM.

3.2.3 Dog FMRI Olfactory Imaging System

The dog fMRI olfactory imaging system was the same as in Chapter 2. Here we put this system and data processing pipeline together to show a complete picture of the project process in Fig.3.2. Please refer to Chapter 2 for details about optical motion tracking system and odorant stimulus devices.

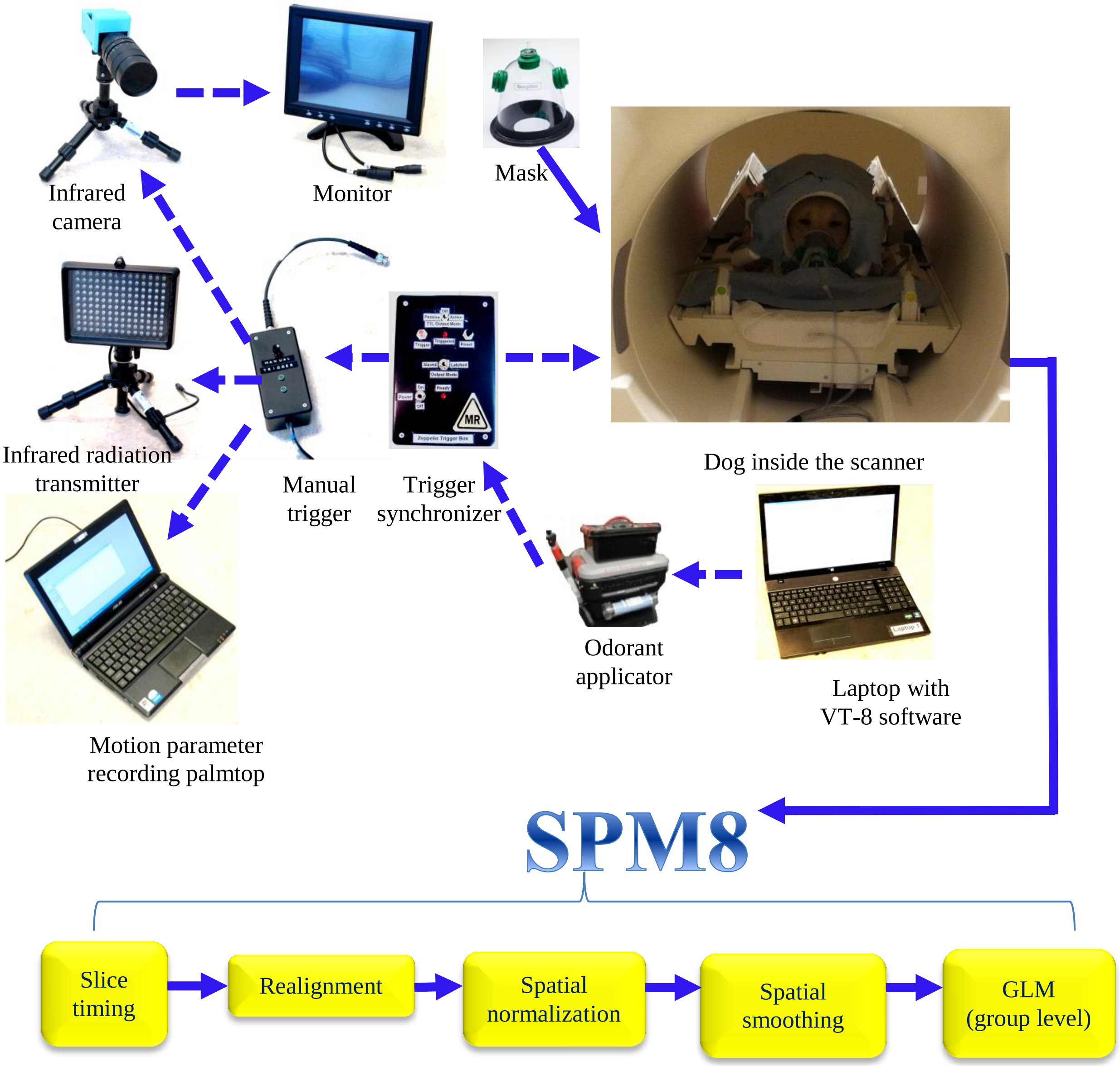

Figure 3.2 Schematic of dog fMRI olfactory imaging system and post processing procedures. The dashed arrows indicate triggering directions, and the solid arrows indicate flow of procedures.

3.2.4 Data Acquisition

Functional data were acquired using T_2*-weighted single-shot gradient-recalled echo-planar imaging (EPI) [64] on a Siemens 3 Tesla Verio scanner. Imaging parameters were set as: 200 volumes, 14 axial slices with 3 mm thickness and 0.75 mm gap, repetition time (TR)/ echo time (TE) =1000/29 ms, field of view (FOV)=192×192 mm, flip angle (FA)=90°, in-plane resolution of 3×3 mm, and in-plane matrix of 64×64. Dogs were scanned once per week, but data were gathered only every other week, alternating with mock scanning (used for the purpose of training). For each dog, one scanning session generally included 1 run of structural scan, 2 runs of functional scans involving odor stimulation without metal nanoparticles, 2 runs of functional scans involving odor stimulation with zinc nanoparticles, 2 runs of functional scans involving odor stimulation with gold nanoparticles. The order of the functional scans was randomized. The final dataset used for post-processing included 22 anesthetized dog sessions consisting of 110 runs including 34 runs for pure odorant, 38 runs for zinc nanoparticles, and 38 runs for gold nanoparticles; and 25 awake dog sessions consisting of 122 runs including 42 runs for pure odorant, 40 runs for zinc nanoparticles, and 40 runs for gold nanoparticles. 2 runs with zinc nanoparticles and 2 runs with gold nanoparticles were excluded from post processing because of excessive motion which could not be corrected even from motion parameters obtained from the camera. The exclusion criterion was: >10 mm displacement between any two consecutive acquisition time points in x, y or z direction (x: left ↔ right; y: up ↔ down; z: front ↔ back). Also, in the z direction, if there was 10mm total displacement between any two acquisitions in one run (not necessarily consecutive), it meant that the dog’s nose was not fully inserted in the mask at some time. This would have jeopardized the odorant effect at that time point. Therefore, any runs with > 10mm total displacement between any two acquisition time points in the z direction were also discarded. Structural images were acquired with magnetization-prepared rapid gradient echo (MPRAGE) sequence [65] to provide a template for spatial normalization, localization, and overlay. The imaging parameters for MPRAGE were set as follows: TR/TE=1550/2.64ms, voxel size of $0.792\times0.792\times1\text{mm}^3$, FA=9°, in-plane matrix 192×192, FOV=152×152 mm^2, and 104 axial slices of 1mm thickness.

3.2.5 Experimental Paradigm

The experimental paradigm was the same as that in Chapter 2. So we brief it as follows for convenience. For details, please refer to Chapter 2. Each functional run with odorant stimulus had 5 blocks with each block consisting of 10s of odorant stimulation and 30s of rest. The paradigm started with a 10s resting condition in order to allow the scanner to enter steady state and for dogs to adjust themselves to the context. The odorant stimulation paradigm and the fMRI block design sequence are illustrated in Fig. 3.3.

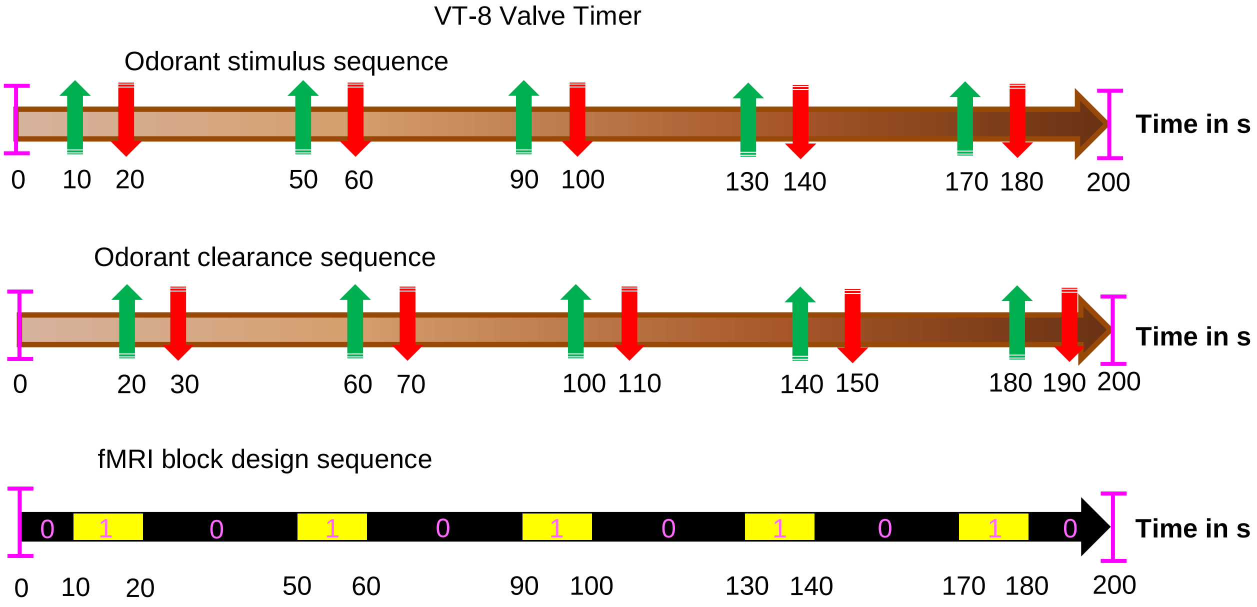

Figure 3.3 Odorant applicator sequences controlled by VT-8 Warner Valve Timer and the corresponding fMRI experimental block design. Top: odorant stimulus sequence, wherein

green arrows indicate the onset time of the odorant stimulus in the three conditions (pure odorant, odorant + zinc nanoparticles, and odorant + gold nanoparticles) and red arrows indicate the time when the stimulation ends. Middle: odorant clearance sequence, with green arrows indicating the onset of clearance of odorant, and red arrows indicating when it ends. Bottom: fMRI block design sequence used in this work, which matches with the odorant stimulus sequence on the top row. “0” denotes the odor “on” condition and “1” denotes the odor “off” condition.

3.2.6 Post Processing

The post-processing of fMRI data was performed using SPM8 toolbox [46] including slice timing correction, realignment to the first functional image, spatial normalization to one structural template of good quality with $2\times2\times2$ mm resampling and 4th order B-spline interpolation, spatial smoothing with full width half max (FWHM) $=4 \times 4 \times 4$ mm^3 Gaussian kernel, general linear modeling (GLM) and statistical testing. A schematic illustrating this is shown at the bottom of Fig.3.2.

It is noteworthy that for spatial normalization [16], as aforementioned in Chapter 2, currently there is no standard and comprehensive brain atlas for dogs. Existing dog brain atlases cannot cover the full spectrum of all dog brain shapes and sizes across different canine breeds [67]. On the other hand, data from different human brains can be spatially normalized into existing templates such as MNI [66] which are derived from a large number of subjects so as to capture the full spectrum of head size and shape variability. Since such a template is currently not available for canines, we adopted the normalization strategy as demonstrated in Chapter 2 to spatially normalize all functional runs to a chosen structural image acquired by us. For details and graphic illustration of this procedure, please see Section 2.2.7 in Chapter 2.

Then, the processed fMRI data were input to a GLM for obtaining voxels in the canine brain which were activated by each of the three odor conditions (pure odorant, odorant + zinc nanoparticles, and odorant + gold nanoparticles) as compared to no odor. In order to account for the variability of the hemodynamic response, time and dispersion derivatives were used in the design matrix. In addition, similar to our previous study in Chapter 2, motion parameters (3 translations in x, y, and z directions and 3 rotations about x, y, and z axes) obtained from rigid body registration in SPM as well as x and y motion parameters calculated from optical head motion tracking camera device were used as nuisance regressors in the design matrix of the GLM. The results from GLM were passed through statistical F test to find activation maps.

Correction for multiple comparisons

The multiple comparison correction step is the same as in Chapter 2. We applied the parameters obtained via AlphaSim algorithm to both the study in Chapter 2 and the study in this chapter. We had: individual voxel probability threshold was p=0.05, minimum cluster size threshold was equal to 15 voxels, and false positive detection probability of the entire image was 0.05.

3.3 Results

The group level statistical activations for anesthetized dogs are shown in Fig.3.4. The functional activations are overlaid on the structural template which was used to spatially normalize other functional images. Fig.3.4 (A) corresponds to the activation map with pure odorant stimulus. Fig.3.4 (B) corresponds to the activation map obtained from odorant stimulus with zinc nanoparticles added, and Fig.3.4 (C) corresponds to the activation map obtained from odorant stimulus with gold nanoparticles added. Cluster level statistics of the activations and corresponding anatomical areas are summarized in Tables 3.1-3.3. The anatomical labels of activated areas were identified based on visual comparison of activation images with published dog brain atlases [71]. We can observe that for anesthetized dogs, with no nanoparticles added to the odorant, all activations have low intensity, and the activated areas mainly include olfactory bulb, periamygdala, entorhinal cortex and anterior cingulate cortex. The anterior cingulate has been proved to be connecting to prefrontal area activated during odor-processing [98]. It also has been shown to be activated for pleasant and unpleasant odors [99]. By contrast, very strong activation (both in terms of intensity and spatial extent) is observed for odorant with zinc nanoparticles. Clearly, the activation pattern in the axial view in Fig.3.4 (B) has a shape similar to the profile of olfactory processing pathway shown in Fig.3.1. Other clusters of activations can be found in orbitofrontal cortex, superior frontal cortex, visual cortex, mid cingulate and cerebellum. The regions activated by the odorant stimulus with gold nanoparticles are the olfactory bulb, orbitofrontal cortex, bilateral piriform cortices, periamygdala, entorhinal cortices, and parietal cortex (Fig.3.4 (C)). Compared with the result obtained from zinc nanoparticles, the activations for the gold nanoparticle are weaker both in terms of intensity and spatial extent. Overall, the results indicate that the activations for odorant with gold nanoparticles are generally greater than that for odorant with no nanoparticles and less than that for odorant with zinc nanoparticles. This is in agreement with results obtained from *in vitro* cellular EOG data [33] [94].

Activation maps for awake dogs are shown in Fig.3.5 and corresponding cluster level statistics are summarized in Tables 3.4, 3.5, and 3.6. Fig.3.5 (A) corresponds to the activation map with pure odorant stimulus. Fig.3.5 (B) corresponds to the activation map obtained from odorant stimulus with zinc nanoparticles added, and Fig.3.5 (C) corresponds to the activation map obtained from odorant stimulus with gold nanoparticles added. All these activation maps are overlaid on the same structural image as used for anesthetized dogs in Fig.3.4. The activation map in Fig.3.5 (A) includes areas of olfactory bulb, superior frontal cortex, and mid cingulate. The cingulate cortex receives inputs from the thalamus and the frontal cortex, and projects to the entorhinal cortex via the cingulum [100]. It acts as a bridge for communications between entorhinal cortex on the one hand and thalamus and frontal cortex on the other. As shown by Savic et al [101], the cingulate cortex is engaged in odor processing in humans. In contrast, the activations in Fig.3.5 (B) involve areas of olfactory bulb, bilateral periamygdala and entorhinal cortices, hippocampus, medial and posterior frontal cortex, superior frontal cortex, cerebellum, visual cortex, posterior cingulate cortex, as well as thalamus. Many more olfaction related areas are activated in the presence of zinc nanoparticles than without, especially in the piriform lobes and hippocampus. Also, higher order cortical areas such as medial frontal cortex, which are involved in cognition, are strongly activated in terms of both intensity and spatial extent, as compared to Fig.3.5 (A). This suggests that enhanced olfactory response at olfactory receptor neurons is transmitted into this higher order cognitive area. During odorant stimulation with gold nanoparticles, the activations in olfactory bulb and piriform lobes are much less than that for zinc nanoparticles as evident from Fig.3.5 (C). While we expected the olfactory bulb to be activated by odorant with gold nanoparticles, such activation did not survive corrections for multiple comparisons. The activated areas include superior frontal cortex, anterior cingulate cortex, cerebellum, visual cortex, posterior cingulate cortex, thalamus, right periamygdala and right entorhinal cortex. Generally, the piriform lobes, and hippocampus have stronger activations in Fig.3.5 (B) than Figs.3.5 (A) and (C). Also, the cerebellum, posterior cingulate cortex, visual cortex, mid frontal cortex and thalamus, are activated more in terms of both intensity and spatial extent for odorant with zinc and gold nanoparticles than with no nanoparticles.

(A) Group activation for anesthetized dogs for pure odorants

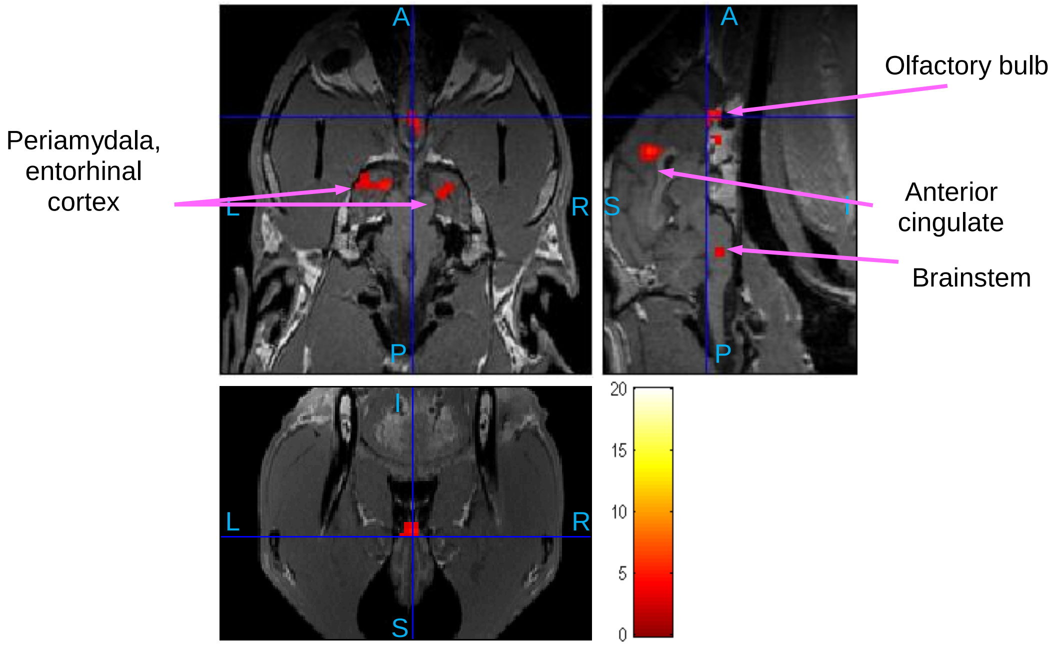

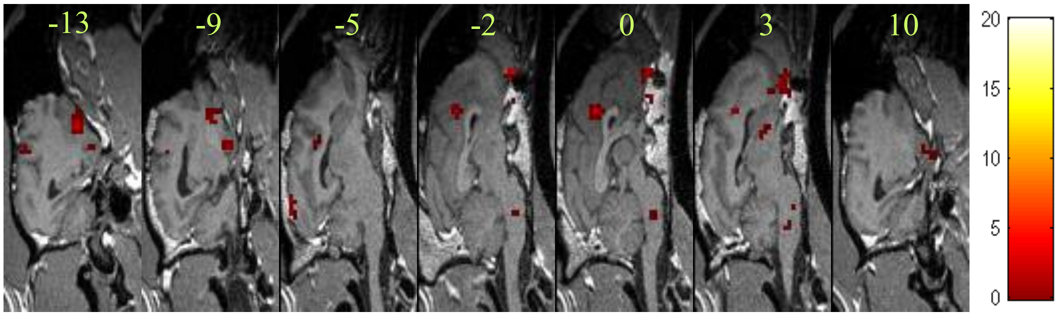

(B) Group activation for anesthetized dogs for odorants + zinc nanoparticles

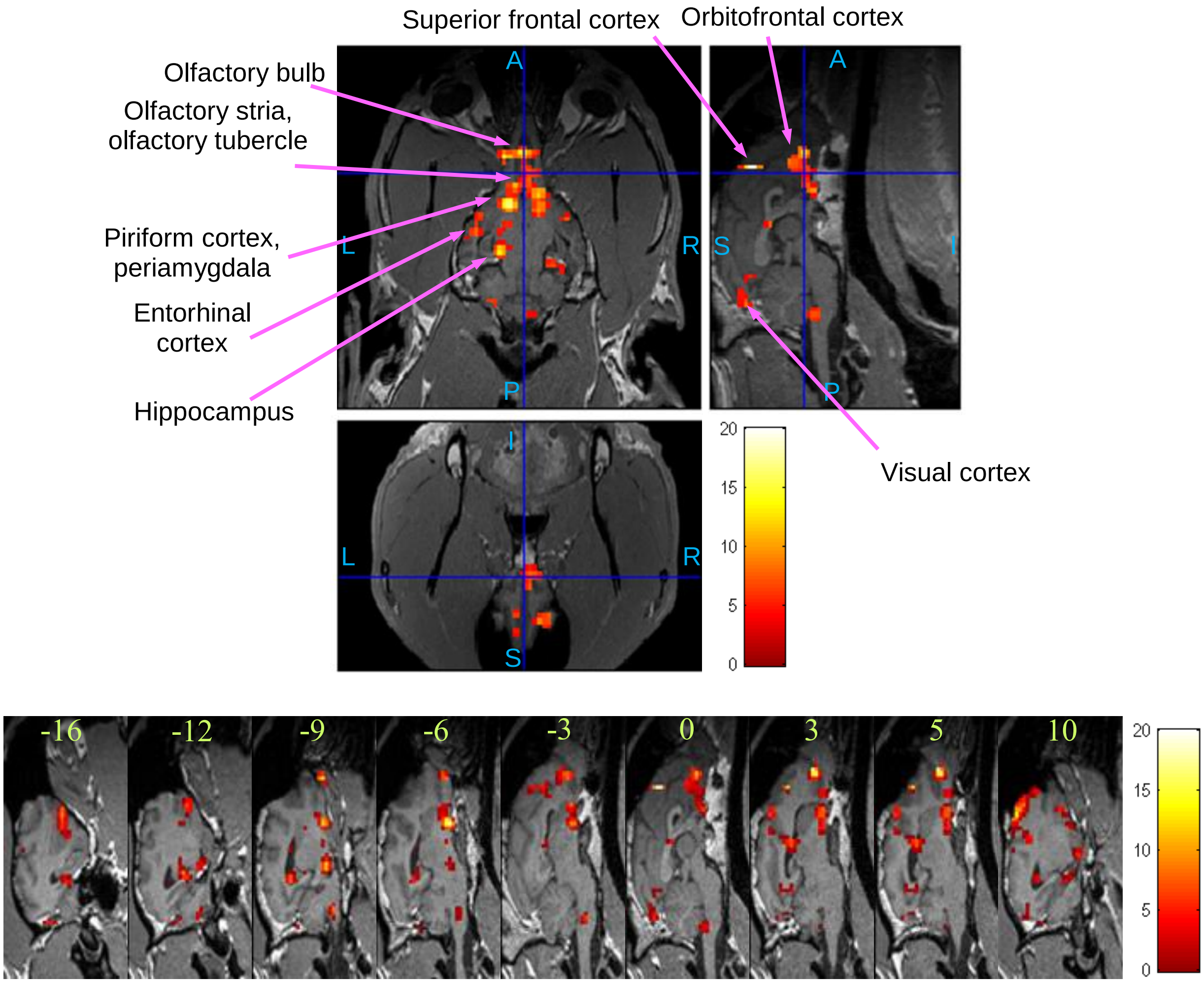

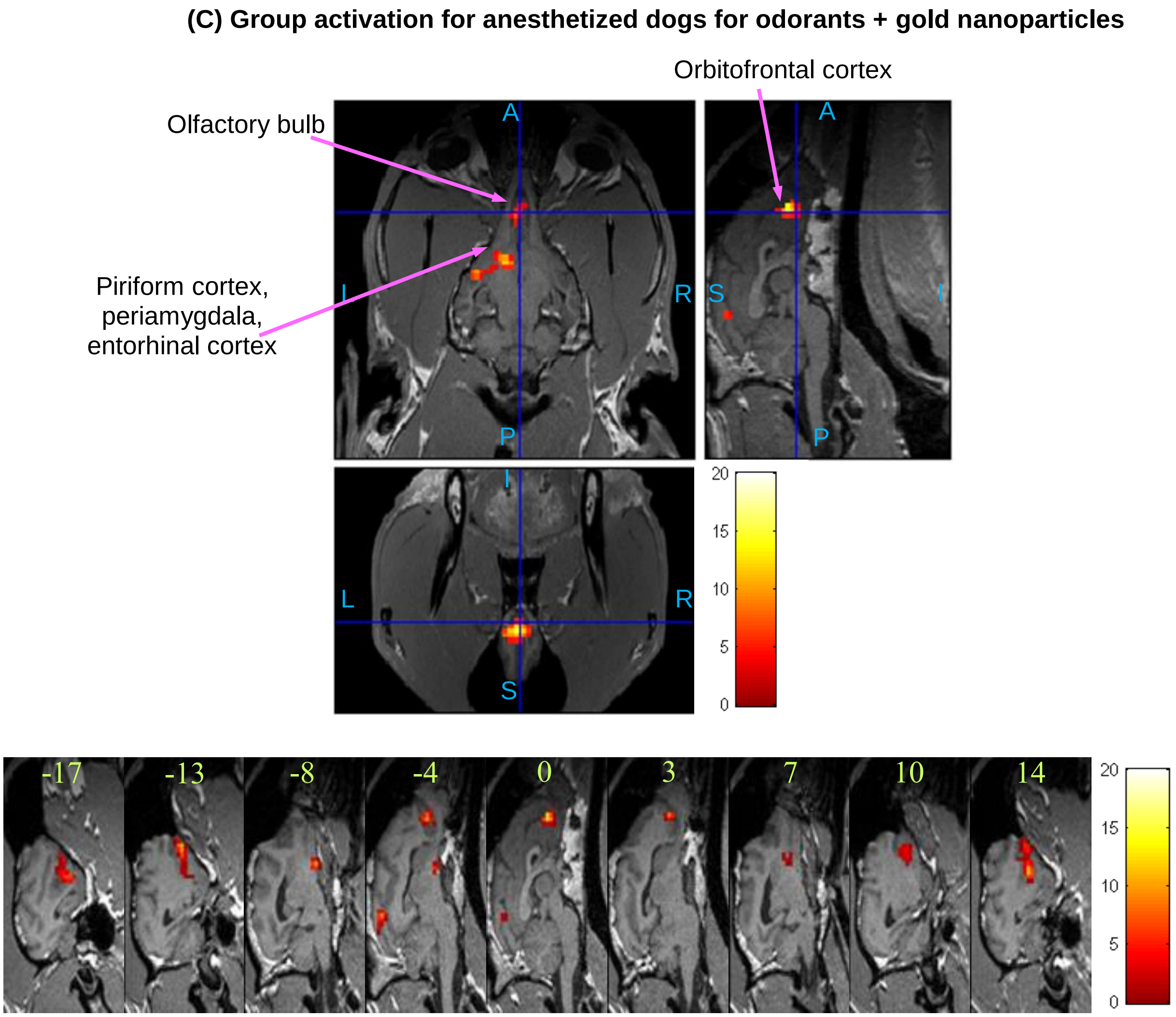
(C) Group activation for anesthetized dogs for odorants + gold nanoparticles

Figure 3.4 Group activation maps for anesthetized dogs (F test, p-value threshold (FDR corrected) =0.05, cluster threshold =15 voxels using AlphaSim). Subfigure (A) corresponds to odorants with no nanoparticles added; subfigure (B) corresponds to odorant with zinc nanoparticles added; and subfigure (C) corresponds to odorant with gold nanoparticles added. Three orthogonal views are shown above and key sagittal slices are shown below for each subfigure. The image order in sagittal slices is from left to right hemisphere, with coordinate labels shown atop. Hot color map is used for activation intensity, and important areas are indicated by arrows with labels. (A: Anterior, P: posterior, S: superior, I: inferior, L: left, R: right)

(A) Group activation for awake dogs for pure odorants

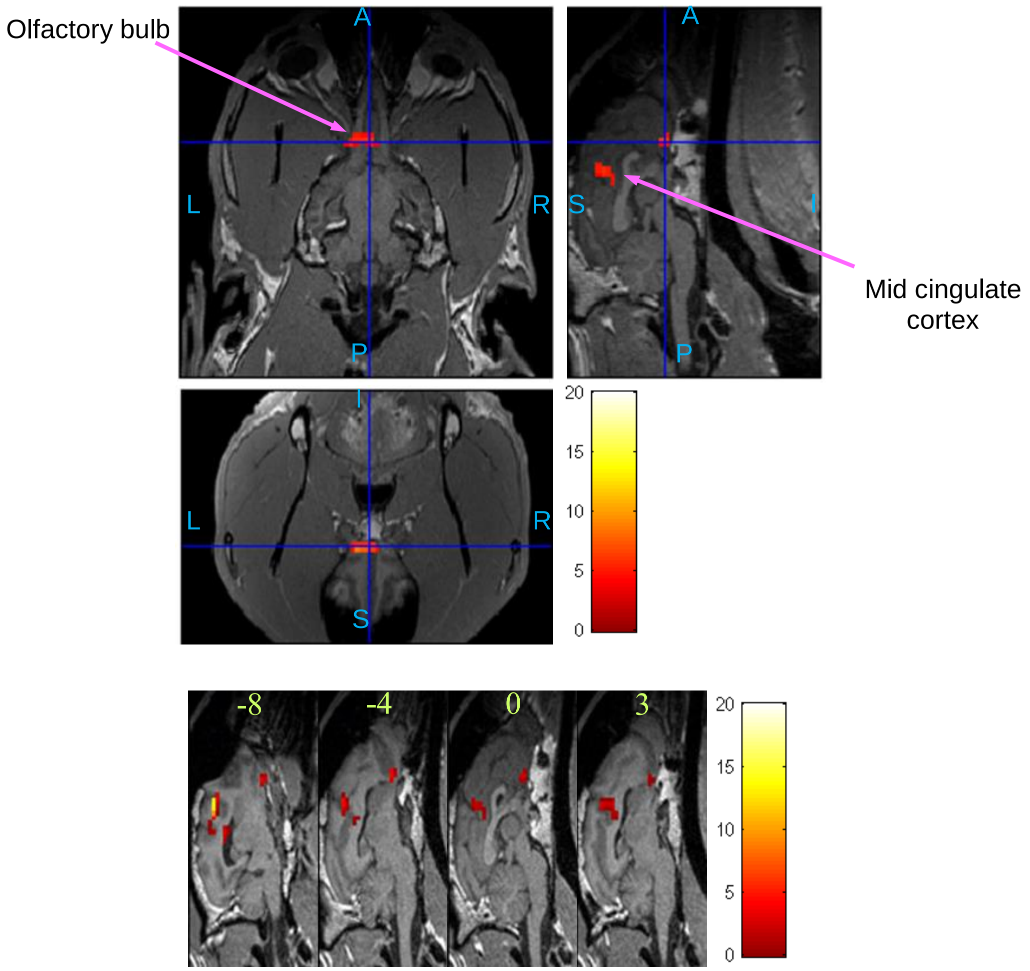

(B) Group activation for awake dogs for odorants + zinc nanoparticles

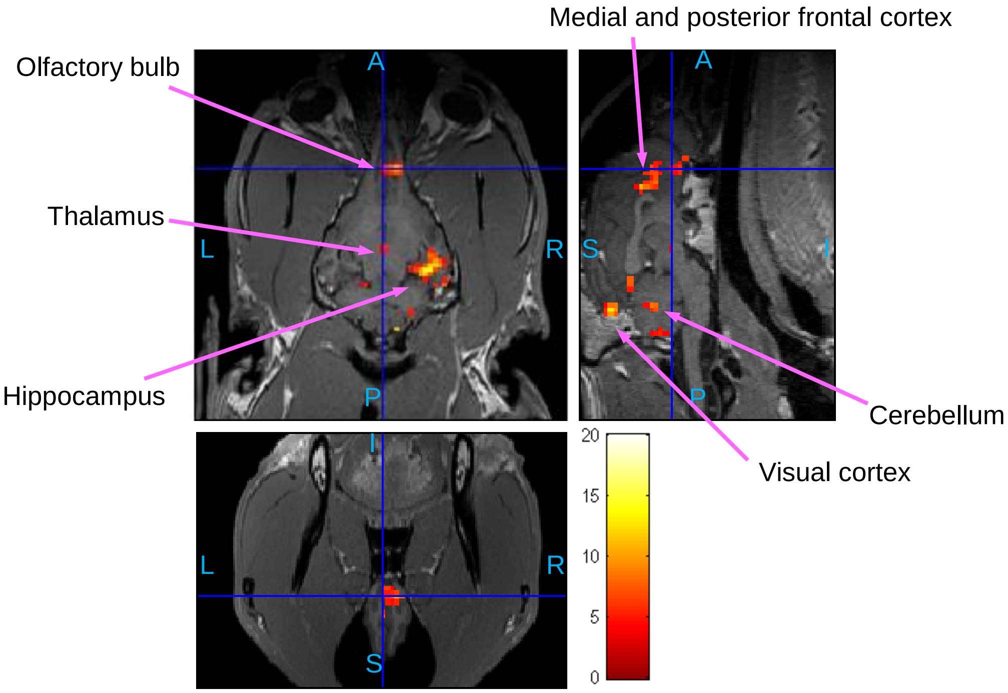

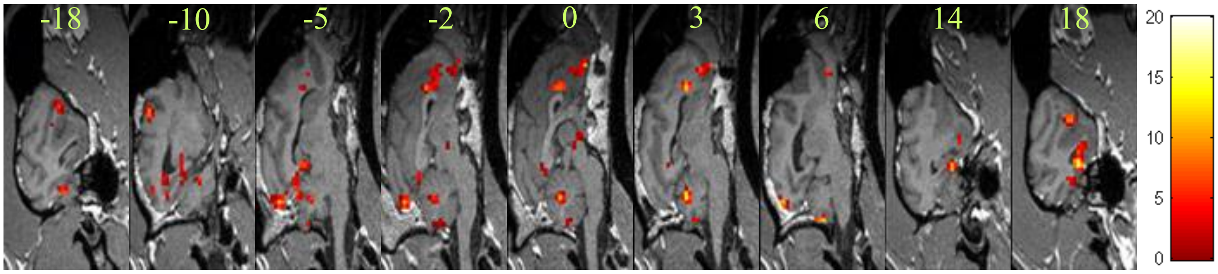

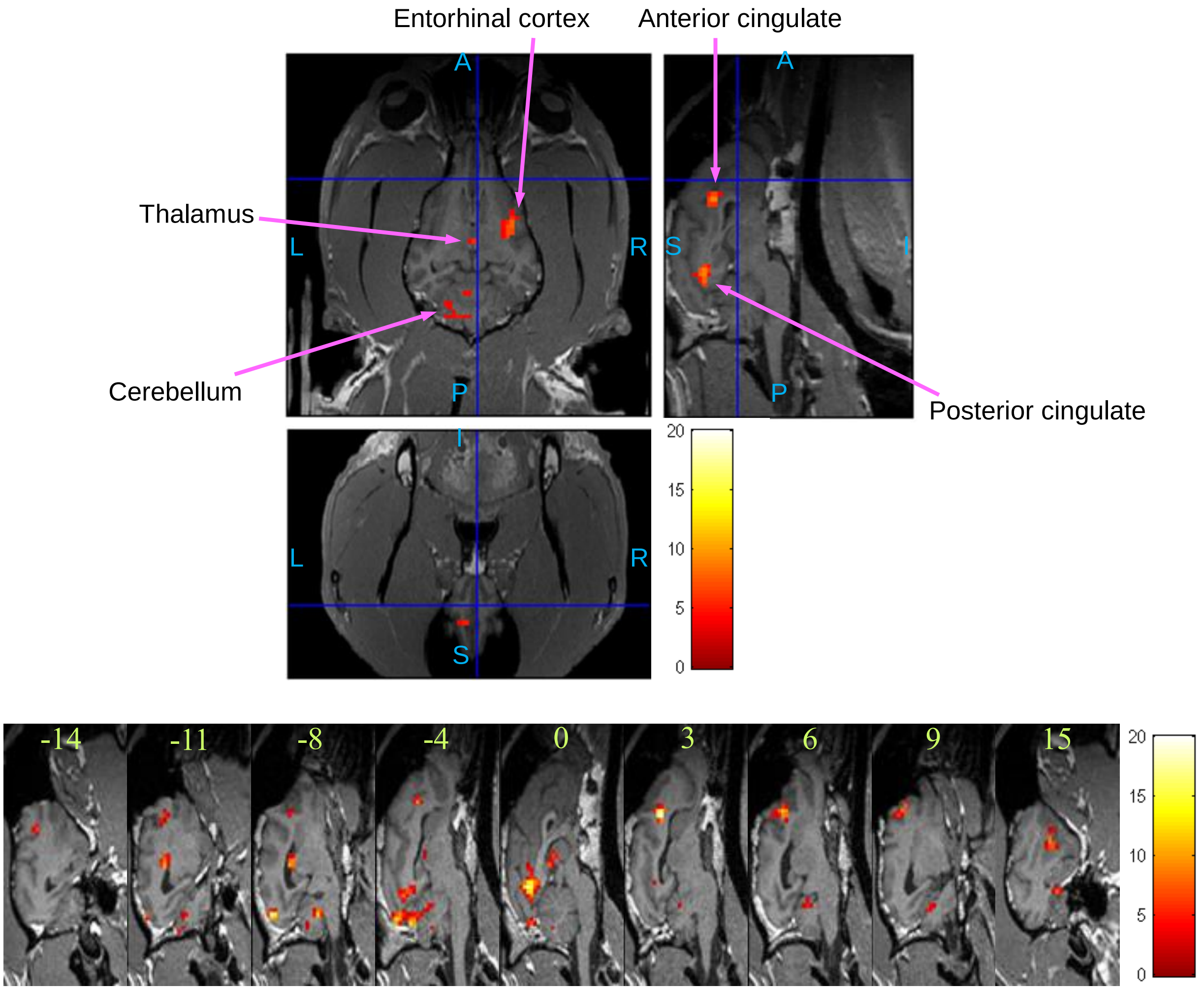
(C) Group activation for awake dogs for odorants + gold nanoparticles

Figure 3.5 Group activation maps for awake dogs (F test, p-value threshold (FDR corrected) =0.05, cluster threshold =15 voxels using AlphaSim). Subfigure (A) corresponds to odorants with no nanoparticles added; subfigure (B) corresponds to odorant with zinc nanoparticles added; and subfigure (C) corresponds to odorant with gold nanoparticles added. Three orthogonal views are shown above and key sagittal slices are shown below for each subfigure. The image order in sagittal slices is from left to right hemisphere, with coordinate labels shown atop. Hot color map is used for activation intensity, and important areas are indicated by arrows with labels. (A: Anterior, P: posterior, S: superior, I: inferior, L: left, R: right)

Table 3.1 Cluster-level statistics of activations for anesthetized dogs for odorant with no nanoparticles

Number of activated clusters: 6, total number of activated voxels: 171			
Cluster	Anatomical areas included	Number of activated voxels	Peak F value
#1	olfactory bulb	34	6.19
#2	anterior cingulate cortex	25	5.85
#3	left piriform cortex, left	42	5.68

	periamygdaloid cortex		
#4	brainstem	16	4.73
#5	left periamygdaloid cortex, left entorhinal cortex	35	4.70
#6	right periamygdaloid cortex, right entorhinal cortex	19	4.44

Table 3.2 Cluster-level statistics of activations for anesthetized dogs for odorant with zinc nanoparticles.

Number of activated clusters: 12, total number of activated voxels: 1033			
Cluster	Anatomical areas included	Number of activated voxels	Peak F value
#1	medial and right superior frontal cortex, mid cingulate	233	19.42
#2	olfactory bulb, left and right anterior olfactory cortex, left piriform cortex, left periamygdaloid cortex, right piriform cortex, right periamygdaloid cortex, medial and lateral olfactory stria, olfactory tubercle, left entorhinal cortex, orbitofrontal cortex	410	18.31
#3	left hippocampus	46	13.85
#4	right superolateral frontal cortex	51	12.52
#5	right entorhinal cortex	49	12.13
#6	left hippocampus	42	11.24
#7	right hippocampus	30	10.91
#8	left cerebellum, brainstem	48	10.89
#9	left caudate tail	21	10.62
#10	left cerebellum	20	9.19
#11	right caudate tail	15	8.92
#12	right cerebellum, right and mid occipital cortex	68	8.58

Table 3.3 Cluster-level statistics of activations for anesthetized dogs for odorant with gold nanoparticles.

Number of activated clusters: 4, total number of activated voxels: 317			
Cluster	Anatomical areas included	Number of activated voxels	Peak F value
#1	olfactory bulb, orbitofrontal cortex	60	15.44
#2	left anterior olfactory cortex, left piriform cortex, left periamygdaloid cortex, left lateral olfactory stria, left	127	15.28

	entorhinal cortex		
#3	right piriform cortex, right periamygdaloid cortex, right entorhinal cortex	94	14.71
#4	parietal cortex	36	11.26

Table 3.4 Cluster-level statistics of activations for awake dogs for odorant with no nanoparticles.

Number of activated clusters: 2, total number of activated voxels: 205			
Cluster	Anatomical areas included	Number of activated voxels	Peak F value
#1	mid cingulate cortex, superior frontal cortex, left caudate	171	14.84
#2	olfactory bulb	34	8.42

Table 3.5 Cluster-level statistics of activations for awake dogs for odorant with zinc nanoparticles.

Number of activated clusters: 12, total number of activated voxels: 433			
Cluster	Anatomical areas included	Number of activated voxels	Peak F value
#1	left entorhinal cortex	20	14.88
#2	right entorhinal cortex, right hippocampus	64	14.03
#3	left occipital cortex, cerebellum, posterior cingulate	132	12.78
#4	mid occipital cortex	24	12.44
#5	olfactory bulb, orbitofrontal cortex	36	12.39
#6	right entorhinal cortex	31	12.38
#7	right periamygdaloid cortex	16	11.93
#8	medial and posterior frontal cortex	37	10.72
#9	cerebellum	22	10.66
#10	left periamygdaloid cortex	21	8.96
#11	left superior frontal cortex	15	8.67
#12	thalamus	15	6.43

Table 3.6 Cluster-level statistics of activations for awake dogs for odorant with gold nanoparticles.

Number of activated clusters: 11, total number of activated voxels: 331			
Cluster	Anatomical areas included	Number of activated voxels	Peak F value
#1	posterior cingulate, mid occipital cortex, cerebellum	154	13.57
#2	anterior cingulate cortex	38	12.90
#3	right superior frontal cortex	18	10.99

#4	left cerebellum	26	9.33
#5	left caudate	19	8.52
#6	left superior frontal cortex	29	7.91
#7	right entorhinal cortex, right periamygdaloid cortex	31	7.50
#8	thalamus	16	7.15

While Fig.3.4 and Fig.3.5 show the spatial localization of areas activated, Figs.3.6 and 3.7 show the temporal profile of activation in selected ROIs for anesthetized and awake dogs, respectively. The fitted time series, representing temporal profiles of activations [43], were obtained from the GLM for selected ROIs that of most interest in our study: olfactory bulb and medial frontal cortex. Olfactory bulb, as is well known, is a very major and crucial part in olfactory perception, and it is activated for most of our scenarios. On the other hand, medial frontal cortex participates in the cognition of olfaction, and is hypothesized to be activated to a different extent in conscious and anesthetized states. The medial frontal cortex is selected because it has strong activations by zinc nanoparticles for conscious dogs, while the superior frontal cortex has activations in all experimental conditions for conscious dogs and these activations are not at the same spot. In each ROI, a sphere of 2 mm radius was defined with the strongest activated voxel as the center. Then the average fitted time series from this sphere was extracted and plotted. Fig.3.6 gives a comparison of the fitted time series obtained in response to odorant stimulation with no/zinc/gold nanoparticles in anesthetized dogs. Likewise, Fig.3.7 gives a comparison of the fitted time series obtained in response to odorant stimulation with no/zinc/gold nanoparticles in conscious dogs.

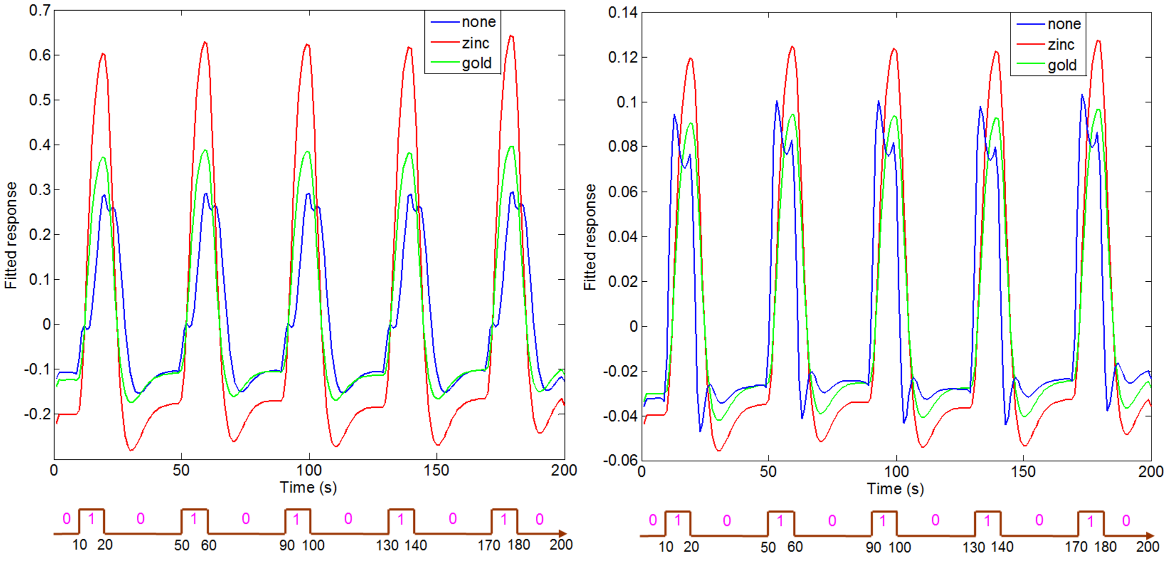

(A) Olfactory bulb (B) Medial frontal cortex

Figure 3.6 Comparisons of fitted time series obtained from the GLM for ROIs in anesthetized dogs. The fitted time series were obtained for two selected ROIs that are closely related with olfaction and of most interest to our study: olfactory bulb and medial frontal cortex. The average fitted time series are shown for olfactory bulb (A) and medial frontal cortex (B). Fitted time series for odorant stimulus without nanoparticles are shown in blue, for odorant stimulus with zinc nanoparticles in red and for odorant stimulus with gold nanoparticles in green. There is no unit for fitted time series and the experimental block design is shown below for each subfigure as a reference.

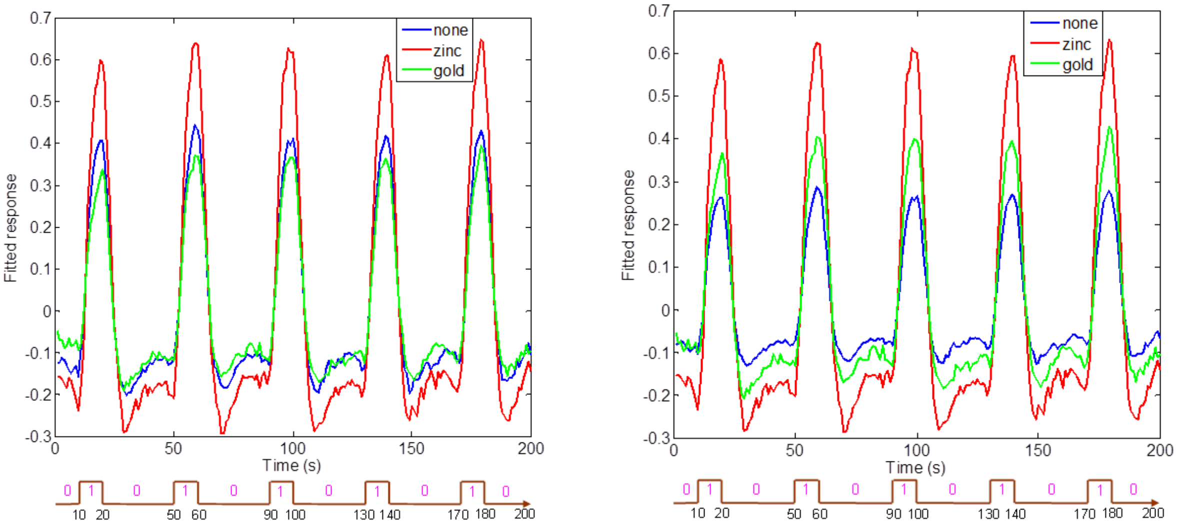

(A) Olfactory bulb (B) Medial frontal cortex

Figure 3.7 Comparisons of fitted time series obtained from the GLM for ROIs in awake dogs. The fitted time series were obtained for two selected ROIs that are closely related with olfaction and of most interest to our study: olfactory bulb and medial frontal cortex. The average fitted time series are shown for olfactory bulb (A) and medial frontal cortex (B). Fitted time series for odorant stimulus without nanoparticles are shown in blue, for odorant stimulus with zinc nanoparticles in red and for odorant stimulus with gold nanoparticles in green. There is no unit for fitted time series and the experimental block design is shown below for each subfigure as a reference.

Based on the activation maps resulted, two hypotheses can be tested as follows. First, according to many authors, specifically [102] [103], it is specified that in humans, the intensity of odor is presented by piriform cortex, amygdala complex (including periamygaloid cortex), entorhinal cortex, and inferior frontal gyrus, while the valence of odor is shown in the orbitofrontal cortex. Zinc nanoparticles enhance odor intensity without change of odor valence, according to previous works [33] [94]. Therefore, it is desirable to test this hypothesis in this work on dogs. Table 3.7 shows statistics including number of activated voxels and mean F values for bilateral piriform lobes and orbitofrontal cortex for each condition (pure odor/zinc nanoparticles/gold nanoparticles) in conscious dogs, separately. To more in depth examine this hypothesis, both statistics with and without multiple comparison correction are given in Table 3.7. It can be seen that activation increases in the piriform lobes when odorant is mixed with metal nanoparticles (more so for zinc than gold) while no such effect is apparent in the orbitofrontal cortex. So, these results support the hypothesis that zinc nanoparticles enhance odor intensity without change of odor valence. Given that anesthetized dogs cannot infer the valence of odorant, this analysis was carried out only in awake dogs.

The second hypothesis is pertaining to sniffing. It has been shown that in humans, whether odorant is present or absent, sniffing induces activation primarily in the piriform cortex of the temporal lobe and in the medial and posterior orbitofrontal gyri of the frontal lobe. In contrast, a smell, regardless of sniffing, induces activation mainly in the lateral and anterior orbitofrontal gyri of the frontal lobe [104] [82]. Since only awake dogs can sniff, sniff-related regions should be exclusively activated in them. To test this hypothesis in canines, we calculated the mean activation map of 3 conditions for anesthetized dogs and that for awake dogs, and put them into manually created mask including bilateral piriform lobes and ventral frontal cortex (including anterior olfactory cortex, olfactory stria and tubercle), and medial and posterior frontal cortex mask to only preserve activations within the masks. The masks were created with reference to existing dog atlas [71]. The result is shown in Fig.3.8. Mean activations for awake dogs are rendered using cool colormap, while those for anesthetized dogs are rendered using hot colormap (the overlapped area is purple, if any). It is quite clear that the medial and posterior frontal area, together with piriform in right temporal lobe are only activated for awake dogs, while anterior part of piriform lobes and ventral frontal area are only activated for anesthetized dogs. Thus, our results support this hypothesis about sniffing.

Table 3.7 Comparison of spatial extent and strength of activations in bilateral piriform lobes and orbitofrontal cortex for awake dogs.

Condition	Awake, bilateral piriform lobes (no multiple comparison correction)		
	Pure odorant	Odorant + zinc	Odorant + gold
Number of activated voxels	28	118	76
Mean F value	5.08	6.31	5.47
Condition	Awake, bilateral piriform lobes (multiple comparison corrected)		
	Pure odorant	Odorant + zinc	Odorant + gold
Number of activated voxels	0	103	26
Mean F value	0	6.41	5.26
Condition	Awake, orbito-frontal cortex (no multiple comparison correction)		
	Pure odorant	Odorant + zinc	Odorant + gold
Number of activated voxels	4	2	5
Mean F value	4.92	4.65	5.55
Condition	Awake, orbito-frontal cortex (multiple comparison corrected)		

	Pure odorant	Odorant + zinc	Odorant + gold
Number of activated voxels	4	2	0
Mean F value	4.92	4.65	0

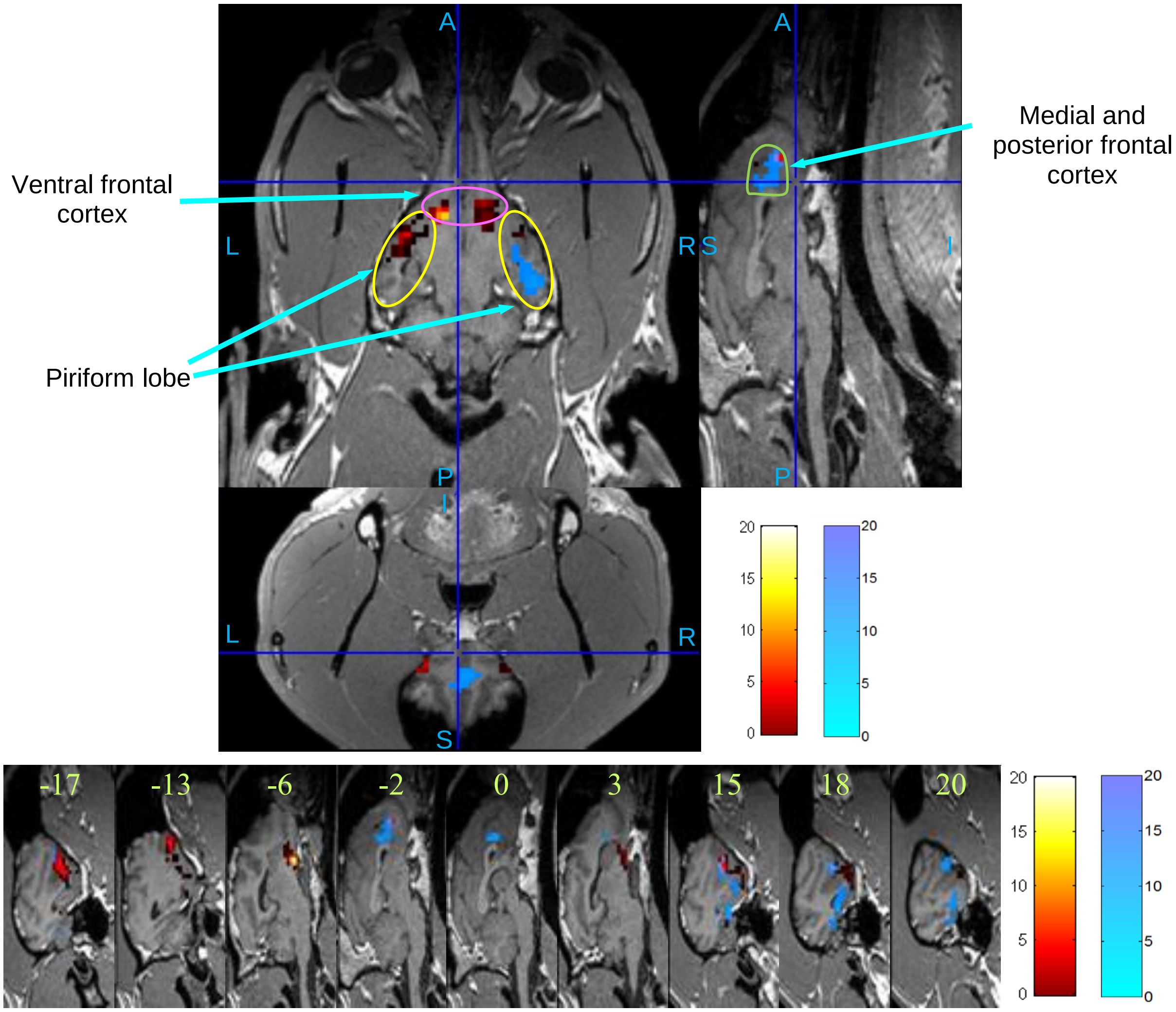

Figure 3.8 Mean activation maps for anesthetized and awake dogs within piriform lobes, ventral frontal cortex, medial and posterior frontal cortex (F test, p-value threshold (FDR corrected) =0.05, cluster threshold =15 voxels using AlphaSim). Two mean activation maps are calculated by averaging activation maps (Fig.3.4 and 3.5) of 3 conditions for anesthetized (hot colormap for activation intensity) and awake dogs (cool colormap for activation intensity), respectively. The green outline defines the medial and posterior frontal cortex, the pink outline defines ventral frontal cortex, and the yellow outline defines piriform lobes (including piriform cortex, periamygdaloid cortex, entorhinal cortex). Three orthogonal views are shown above and key sagittal slices are shown below. The image order in sagittal slices is from left to right hemisphere, with coordinate labels shown atop. Important areas are indicated by arrows with labels. (A: Anterior, P: posterior, S: superior, I: inferior, L: left, R: right)

3.4 Discussion

Canines have much more olfactory sensitivity than many other animals, including humans. This makes them a powerful tool in odor detection, which has been utilized by humans for a wide range of tasks including locating and identifying explosives and other illicit substances. Consequently, investigations leading to a mechanistic understanding of the canine olfactory system and enhancement of its olfactory capabilities are required. Such efforts have mostly concentrated on either *in vitro* cellular approaches or behavioral approaches. For example, at the cellular level, distribution of putative neurotransmitter amino acids in the dog olfactory bulb [28] and anisole binding protein in dog olfactory epithelium [29] have been studied. Electrophysiological responses from the olfactory epithelium to odorant mixtures have been investigated to characterize the relationship between odorant stimulation and olfactory response [31] [32] [33]. At the behavioral level, psychophysical studies regarding the dog's olfactory sensitivity [73] [74], discrimination [75] [76], as well as behavioral assessments of trained detector dog performance characteristics have been explored [34] [35]. However, *in vivo* exploration of the cognitive basis of canine olfaction which links cellular level findings with behavior has been largely missing. In order to address this gap, our previous work in Chapter 2 described, for the first time, a framework to investigate the cognitive basis of canine olfaction using non-invasive imaging techniques such as fMRI. This study is a continuation of the work in Chapter 2 with the same canine olfactory fMRI system, but for investigating previously reported *in vitro* cellular results regarding the enhancement of the canine olfactory response by zinc nanoparticles.

Specifically, we test the hypothesis that enhancement of cellular response in olfactory receptor neurons by zinc nanoparticles will lead to corresponding increase in activity in olfaction-related and higher order brain areas of the canine brain. This hypothesis is motivated by previous works which have shown *in vitro* enhancement of olfactory response in olfactory sensory neurons (as measured by EOG) in the presence of zinc nanoparticles [33] [94]. Additionally, it was reported that zinc nanoparticles alone without odorants, or Zn^{2+} ions did not produce any enhancement of the cellular response. Gold, silver, and copper nanoparticles produced mildly stronger response than pure odorants which faded away rapidly. Our hypothesis is that similar *in vivo* effects can be observed in higher order brain regions by non-invasive imaging using fMRI. The results presented in the previous section clearly provide support for this hypothesis, both in terms of higher activation intensity and larger spatial extent of activation for odorant stimulation in the presence of zinc nanoparticles as compared to odorant stimulation in the presence of gold/no nanoparticles.

An additional factor which we investigate is the dependence of the results on the state of consciousness of the dog, i.e. whether the dog is anesthetized or is fully conscious. As indicated in Chapter 2, anesthetized dogs cannot sniff but conscious dog can, and activities in higher cognitive areas such as the frontal cortex would be greatly influenced by anesthesia. Therefore, we hypothesize that brain regions recruited in response to olfactory stimulation will be different between anesthetized and awake dogs. Accordingly, our results show that for anesthetized dogs, most olfaction related regions including olfactory bulb, anterior olfactory cortex, piriform cortex, periamygdala, entorhinal cortex, hippocampus, superior frontal cortex (we predict activations in these regions as shown in Fig.3.1), are activated strongly (both intensity and spatial extent) for odorant stimulation with zinc nanoparticles as compared to activation from odorants with no nanoparticles. The brain regions with the enhanced activations for zinc nanoparticles' experiments are consistent with known anatomical projections from the olfactory cortex [79]

[80]. Activations obtained from odorants with gold nanoparticles show enhancement of activations in olfactory bulb and olfactory cortex as compared to no nanoparticles situation, but the enhancement is not as strong as that obtained by odorant with zinc nanoparticles, which is in agreement with *in vitro* cellular results [33] [94]. It is noteworthy that odorant with zinc nanoparticles induces enhanced response in the hippocampus while that is not the case for odorant stimulation with gold nanoparticles.

Some activations in anesthetized dogs are found outside of the conventional olfactory pathway laid out in Fig.3.1. Below, we discuss the implications of such findings. First, mid cingulate cortex is activated by odorant stimulation with zinc nanoparticles. The role of cingulate cortex in odorant perception has been shown in some human studies [101]. However, the activation in this area is very small and it is also activated in awake dogs, pure odorant. So we cannot conclude the enhancement effect of zinc nanoparticles exists in this area. Second, we observe activations in caudate and brainstem due to odorant stimulation in the presence of zinc nanoparticle. Previous human studies have shown that during discrimination of odor quality, activations can be found in caudate and brainstem [101], whereas discrimination of odor intensity mainly recruits core olfactory regions. Besides, anatomical evidence shows that the neurons in olfactory cortex and amygdala reach targets including brainstem and caudate [101]. Third, the anterior cingulate which is a posterior part of medial frontal cortex is activated for pure odorant (also in awake dogs, gold nanoparticles). Previous works have shown its link to odor perception [98] [99] [105]. A direct anterior cingulate pathway to the primate primary olfactory cortex is also found in shaping olfaction [106].

For conscious dogs, we observe activations in the olfactory bulb and superior frontal cortex with pure odorant. Other activated areas include caudate and mid cingulate. Zinc nanoparticles enhance the activations in many regions of the olfactory pathway listed in Fig.3.1 such as piriform cortex, periamygdalda, entorhinal cortex, hippocampus, thalamus and medial frontal cortex. Also, regions outside the traditional olfactory pathway such as the posterior cingulate, visual cortex, and cerebellum are also activated by odorant with zinc nanoparticles. Though activation in the olfactory bulb does not survive multiple comparisons correction for odorant stimulation with gold nanoparticles, activations in the thalamus, anterior cingulate cortex, posterior cingulate, visual cortex, and cerebellum are observed.

The modulatory effect of metal nanoparticles (zinc & gold>none) is observed by visual comparison over thalamus, visual cortex, cerebellum, and posterior cingulate. Also, through visual inspection, for olfactory cortex, medial frontal cortex and hippocampus, zinc nanoparticles enhancement effect is quite conspicuous, larger than gold nanoparticles. Visual comparison of activation maps (and accompanying statistics in the Tables) obtained by odorant with zinc nanoparticles with those obtained by pure odorant and odorant with gold nanoparticles reveals that enhancement of activation, both in terms of intensity and spatial extent, in the latter case is evident in olfactory bulb, medial frontal cortex, hippocampus, thalamus, visual cortex, cerebellum, and posterior cingulate. Figs.3.6 and 3.7 illustrate the fitted response for two chosen ROIs: the olfactory bulb and the medial frontal cortex, in anesthetized and awake dogs, respectively. The following inferences can be drawn about the enhancement effect of zinc nanoparticles from these results. First, the fitted time series demonstrate higher amplitude of the BOLD response for odorant stimulation with zinc nanoparticles, as compared to odorant stimulation with gold nanoparticles and odorant with no nanoparticles. This demonstrates the enhancement of odor-induced activity by zinc nanoparticles in these ROIs. Second, the amplitude of the fitted time series for odorant with gold nanoparticles is comparable with no nanoparticles in both anesthetized and conscious dogs for selected ROIs.

Next, we discuss the comparison of activation maps obtained from anesthetized dogs and conscious dogs. For both anesthetized and conscious dogs, visual inspection reveals that there exists bilateral asymmetry of activations appearing in olfactory cortex for gold nanoparticles, and this becomes more symmetric for zinc nanoparticles. This phenomenon is in agreement with previous reports of bilateral symmetry of activation in the olfactory cortex in human data [81]. Second, in general, we find that the medial frontal cortex, visual cortex, cerebellum, thalamus and posterior cingulate are much more activated for conscious dogs than anesthetized dogs, while olfactory bulb and olfactory cortex are less activated for conscious dogs than anesthetized dogs. This can be explained as follows. Medial frontal cortex, visual cortex, cerebellum, thalamus and posterior cingulate [107] are involved in higher order cognitive processing of olfaction. The visual cortex is reported to have an influence on high-level olfactory perception for humans [108]. Also, it has been shown in humans that the medial part of the frontal cortex is involved in cognitive integration of all sensory stimuli in relation to prior experiences [25] and the cerebellum is implicated in sniffing and odorant threshold detection [82]. This indicates that the olfactory stimulus is not being processed in higher cognitive structures in anesthetized dogs to the extent that it is in conscious dogs.

In addition, two hypotheses which have been proven validate on human olfactory perception are tested on canines in this work and justified. First, the zinc nanoparticles dramatically enhance the response in piriform cortex, periamygaloid cortex, and entorhinal cortex which is associated with intensity of odor, and gold nanoparticles have a moderate enhancement in these areas. And we find zinc and gold nanoparticles have no apparent enhancement effect in orbitofrontal cortex as compared to pure odorant for awake dogs. Previous works have shown the valence of odor is presented in the orbitofrontal cortex for humans and zinc nanoparticles do not enhance the perception of odor valence. Therefore, our results generally support the hypothesis that the above conclusion on humans can be transplanted to canines. Noteworthy, for anesthetized dogs, the ratio of number of activated voxels between zinc + odorant and pure odorant is roughly 2-3.5, and the ratio between zinc + odorant and gold + odorant is roughly 1.5. After examining Table 2.1 and Table 2.2 in Chapter 2, we find the number of activated voxels related to odor intensity for high concentration is 280, and that for low concentration is 84, the ratio is 280/84 ≈3.3. This ratio is approximate to the first ratio above mentioned, which solidifies the conclusion about zinc nanoparticles' enhancement effect on odor intensity perception.

Second, we have shown that the sniffing related areas, including medial and posterior frontal area, as well as piriform cortex in close approximation to temporal lobe are only activated for awake dogs, while anterior part of piriform lobes and ventral frontal area are only activated for anesthetized dogs. Although the sniffing related areas are derived from studies on humans, the activation patterns in perfect agreement with the fact that dogs can sniff only in conscious state inform us that the sniffing related areas for canines are the same as for humans.

The results described in this work imply that if the odorant is mixed with zinc nanoparticles, it will enhance the neural response to olfaction in the dog brain's olfactory and higher order cognitive areas, possibly leading to better olfactory sensitivity and better detection of target substances. Future behavioral studies must perform verification of enhanced olfactory sensitivity of canines in the presence of zinc nanoparticles. Further, the conclusions of this study may be applicable to other animals and further research is needed in the future to test this. Also in this work, we used a standard odorant mixture at a concentration of 0.016mM and zinc/gold nanoparticles at concentrations of 5nM. Future studies must explore the enhancement effect induced by combinations of odorant and zinc/gold nanoparticles at different concentrations and with different combinatorial ratios, and find the optimal one which can maximally enhance the olfactory sensitivity of canines.

Chapter 4 Dynamic Multivariate Analysis: Behavioral Relevance of the Dynamics of Functional Brain Connectome

In fMRI the concept of multivariate analysis is based on the assumption that the information in each voxel/region is not independent of other voxels/regions. The time series for each voxel/region affects and is affected by time series from other voxels/regions. There exists information exchange between them. A prevailing concept, called connectivity, is to describe this interaction. Generally, there are two kinds of connectivities. One is instantaneous correlation between two voxels/regions, which we call functional connectivity (FC) which is usually calculated via correlation technique. The other one is the causal influence between two voxels/regions, called effective connectivity (EC). It is usually mathematically formulated via multivariate general linear regression model, such as Granger causality. Also, connectivities can be classified through another categorization: static connectivity and dynamic connectivity. The static one is measured over the entire time series from two voxels/regions, while the dynamic one is calculated in a time-varying way, implying the correlation/causality between two voxels/regions is dynamically changing over time. A comprehensive elaboration on multivariate analysis can be found in Ref. [18] and its application in fMRI can be found in Ref. [19]. Our main contribution for the work in this chapter is that we proposed an adaptive windowing strategy for calculating dynamic FC, applied adaptive evolutionary clustering algorithm for clustering brain FC network states, and showed FC dynamics had better predictive capability of behaviors than FC statics.

4.1 Introduction

The view that human brain works as a structurally connected and functionally integrated entity has been widely appreciated for more than a decade [109] [110] [111] [112] [113] [114] [115] [116] [117] [118] [119] [120]. With the advent of fMRI, different methods for characterizing brain connectivity and integration from a functional view point has received a lot of attention [113] [114] [115] [116] [117]. FC measures the instantaneous (zero-lag) temporal correlation of fMRI signals obtained from different brain regions. FC in different brain networks have been characterized both during resting state and task performance [114] [121]. The resting state studies assume importance given the sensitivity of resting state networks to brain pathology [122] [123] [124] and the ease of performing resting state studies in patient populations.

Previous resting state FC studies suffered from a few limitations. First, previous studies mainly investigated FC by obtaining one connectivity value for the entire duration of the experiment based on the assumption that connectivity did not change significantly over time [125] [126]. Given that the brain is a dynamic and adaptive system whose state is likely to change over time, the stationarity assumption has been relaxed by some recent works which explored the dynamics of connectivity in time and frequency domains [127, 128, 129, 130, 131, 132, 133, 134, 135, 136] [137, 138, 139, 140, 141, 142, 143, 144, 145]. For a comprehensive review, please see Hutchison's work [135]. Further, recent works have also reported diagnostic implications of dynamic connectivity for mental disorders such as PTSD (post-traumatic stress disorder) [146], and schizophrenia [144]. As pointed out in Hutchison's work [147], resting-state FC can exhibit non-stationary and spontaneous relationships which can be smeared when using single, averaged connectivity for the entire length of the experiment. For exploring dynamics of FC, previous studies have used sliding windows of fixed length [130] [131]. However, it cannot be assumed that non-stationary dynamics implies fixed stationary windows. In order to address this issue, we propose an approach capable of capturing temporal variations in FC by employing dynamic windows of changing length such that FC dynamics is statistically guaranteed to be stationary within a given window. In order to demonstrate the feasibility of this approach, we performed simulations followed by application to human resting state fMRI data obtained from the Human Connectome Project (HCP) (Q3 release, 40 subjects; (http://humanconnectome.org).

The amount of information obtained from the assessment of dynamic FC can be quite large. Hence, it has been often difficult to interpret the underlying neuroscientific meaning [127]. Some previous studies showed snapshots of FC at various points during the experiment obtained by using different window lengths [131, 132] or template pattern matching [134]. Some other studies, such as a study by Kiviniemi et al. [148], did not use any criterion for the determination of sliding window length and the window length was assumed to be constant over time. Though these are very good exploratory technique, the results and interpretation from such approaches can become subjective, depending on the window length and frames chosen. One principled approach adopted by some recent reports is to find connectivity configurations which are quasi-stable for a certain period of time [146]. This follows from similar quasi-stable scalp voltage configurations, called microstates, obtained from agglomerative clustering of electroencephalographic (EEG) data [138] [149]. Such approaches assume that a single functional configuration exists across the whole brain at any given time instant. Additionally, they also assume that the dynamics of connectivity is essentially due to the brain changing from one across-the-brain connectivity configuration to another. The assumptions behind agglomerative clustering and PCA [130] to some extent lose generality. For example, each of the two networks shown in Fig.4.1 (A) does not change over time (having same nodes), but the connections change with time. Though previous studies have attempted to capture this type of dynamics, the example showed in Fig.4.1 (B), wherein both connections between nodes and the networks themselves change with time (having different nodes at different time instants), represents a more general scenario of dynamic changes in FC. In order to capture the latter type of dynamics without losing generality, we propose an approach based on adaptive evolutionary clustering (AEC) [150] for finding brain network FC configurations at each time instant. The network configurations at different time instants differ in terms of connectivity strength between regions/nodes, as well as the nodal configuration itself. Then, by performing second-level clustering over these time-varying configurations, we found several patterns (2nd level clusters) which could represent different brain states alternating over time.

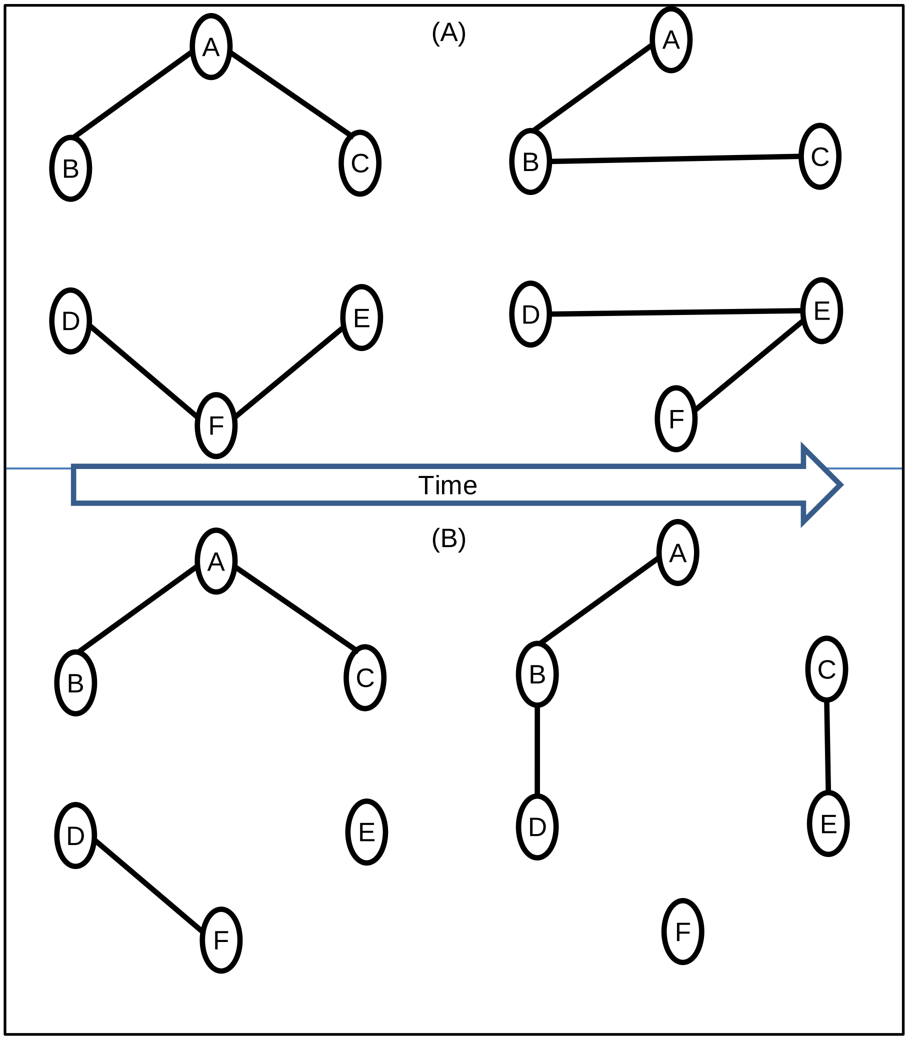

Figure 4.1 Schematic of two types of temporally dynamic FC network configurations. (A) The first type illustrating a dynamic network configuration wherein all nodes are part of the same FC network, only the connections between them change with time. (B) The second type illustrating a dynamic FC network configuration wherein both connections between nodes and the networks themselves are changing with time.

Second, there is an abundance of resting state connectivity studies examining specific networks, usually involving less than ten anatomically identified regions, rather than the entire brain. These studies are motivated by specific hypotheses regarding the functionality of specific networks. The methods used for this purpose include seed-based correlation [151] [152] [115], as well as PCA (principle component analysis) and ICA (independent component analysis) based multivariate analysis [153] [154] [155]. For example, Greicius et al. specially investigated the default mode network (DMN) [118] [151], Deshpande et al. investigated the connectivity within DMN, hippocampal cortical memory network (HCMN), dorsal attention network (DAN) and fronto-parietal control network (FPCN) [114], and Roy et al. considered amygdala-based network to analyze adolescent anxiety disorder [156]. Even though convenient for testing targeted hypotheses, the effect of other regions in the brain cannot be ignored and it is difficult to obtain the complete picture when investigating brain networks consisting of a few regions in isolation. Accordingly, many studies have explored whole-brain static FC [157] [158]. Even a few recent studies employed a method based on principal component analysis for investigating whole-brain dynamic FC patterns [130] [159]. However, they suffered from the following limitations. First, some works, such as Leonardi et al. [130], employed a partitioning of the whole brain according to AAL (automated anatomical labeling) atlas whose segmentation is solely based on anatomy, thus making the ROIs functionally heterogeneous. Second, some other works, like Allen et al. [159], employed ICA based functional definition of ROI such that anatomically distant regions were combined into a single ROI which is really not an appropriate parcellation scheme. We recognize that some sort of dimensionality reduction is essential given that dynamic evaluation of connectivity from all voxels in the brain can be quite expensive in terms of time and computational resources. Therefore, unlike previous studies, we have adopted a dimensionality reduction strategy which parcellated voxel time series into 190 functionally homogeneous gray matter regions using spectral clustering [160]. This 190-region atlas was derived using a large resting state dataset [160]. We extracted mean time series from each of the 190 regions and fed it into the dynamic FC model.

One of the imports of conducting connectivity analysis lies in its diagnostic implications as well as its link to human behavior. Previous works have shown that FCs between brain regions is more informative in predicting behavior than activity of functional regions in isolation. For example, Cole et al. found global connectivity of prefrontal cortex predicted control and intelligence [161] and He et al. investigated the influence of FC on episodic memory for old people [162]. Further, aberrant behavior in subjects with mental and neurological disorders has been linked to alterations in FC of specific brain networks [163] [164]. Notably, recent works have linked both inter-individual and intra-individual variability in FC to corresponding variability in behavior [165] [166]. Given these reports, we hypothesize that the variance of the dynamics of the whole brain resting state functional connectome will predict human behavior in various domains such as alertness, cognition, emotion and personality traits. Further, we surmise that greater temporal variability of FC increases the adaptability and efficiency of brain networks. Accordingly, we hypothesize that variance of FC dynamics will be a better predictor of human behavior than conventional static measures of FC obtained from the entire length of the time series. In order to test these hypotheses, we obtained whole brain FC dynamics using the proposed model involving adaptive windowing and evolutionary clustering and then correlated its temporal variance with behavioral data from the HCP database (for details, please go to http://humanconnectome.org/documentation/Q3 /Q3_Release_Reference_Manual.pdf). For comparison, a similar analysis was carried out using conventional static FC measures.

4.2 Materials and Methods

4.2.1 Data Acquisition and Pre-processing

All HCP subjects were scanned on a customized Siemens 3T "Connectome Skyra" housed at Washington University in St. Louis. The resting-state fMRI (rfMRI) session1 minimally preprocessed data were downloaded and used in this work. This data set included 40 unrelated subjects (age range: 22~35 years, 21 females), each having 2 runs. During the scan, subjects were instructed to lie at rest with eyes open and fixated on bright cross-hair on a dark background. For each subject, oblique axial acquisitions alternated between phase encoding in a right-to-left direction in one run and phase encoding in a left-to-right direction in the other run. The rfMRI raw images were collected with a multiplexed gradient echo planar imaging sequence and the following parameters: 1200 volumes, field of view (FOV) =208×180 mm^2; flip angle (FA) =52°; TR (repetition time)/TE (echo time) =720ms/33.1ms, in-plane matrix: 104×90; 72 slices per volume with slice thickness =2mm; multiband factor=8; echo spacing=0.58 ms. For details about scanner hardware, data acquisition and preprocessing, please see HCP Q3 release manual (http://humanconnectome.org/documentation/Q3/Q3_Release_Reference_Manual.pdf).

The HCP's minimal preprocessing of rfMRI images involved a functional pipeline named fMRIVolume. It removed spatial distortions (gradient distortion correction, field map based correction), realigned volumes to compensate for subject motion, registered the fMRI data to the structural image, nonlinear registration from structural to MNI, reduced the bias field, normalized the 4D image to a global mean, and masked the data with the final brain mask based on FreeSurfer [167] segmentation. For details regarding HCP minimal preprocessing, please refer to HCP Q3 release reference manual. We performed additional preprocessing using Data Processing Assistant for Resting-State fMRI software (DPARSF) [168] including mean and linear trend removal for each voxel time series, temporal filtering with passing band: 0.01~0.1Hz, and regressing out the white matter and CSF signals. Subsequently, the 190-region version of the CC200 brain atlas [160], which contains a parcellation of all gray matter voxels in the brain to 190 homogeneous functional regions based on spectral clustering, was employed for ROI definition. We extracted the mean time series from all 190 regions for subsequent use. Please refer to Appendix A, Table A1 for anatomical labels and MNI coordinates of the 190 regions.

4.2.2 Behavioural and Individual Difference Measures

Apart from rfMRI data, we also used HCP's behavioral data from the same subjects to investigate the relevance of the dynamics of FC to human behavior as compared to conventional static FC. The HCP collected behavioral measures developed for the NIH (National Institutes of Health) Toolbox Assessment of Neurological and Behavioral function (http://www.nihtoolbox.org) and several additional measures to assess domains not covered by the NIH Toolbox. The behavioral measures were categorized into several domains and the domains that were employed in this work were: alertness, cognition, personality, and emotion. We did not incorporate categories of motor and sensory functions into our analysis since they were relatively less relevant to resting state data. Details about all behavioral measures can be found at http://humanconnectome.org/documentation/Q3/Q3_Release_Reference_Manual.pdf. For detailed description about behavioral measures employed in this work, please refer to Appendix A, Table A2.

4.2.3 Dynamic Functional Connectivity Model

Functional connectivity is a measure of instantaneous (zero-lag) temporal association between time series from different brain regions. Pearson’s correlation, by measuring the normalized statistical covariance between time series, is a widely employed direct measure of FC in the brain. Pearson’s correlation calculated over entire time series reflects the average FC over the entire length of the experiment, or in other words, static FC. For capturing the dynamic variations in FC, we used sliding windowed Pearson’s correlation along the time axis. Previous reports used fixed window length with rectangular [127] [130], or Hamming windows [131]. But there was no evidence supporting the superiority of any given window shape over others. Therefore, we have employed a rectangular window shape for simplicity. However, for fixed window length, the length adopted mattered very much and different lengths produced different results [130] [127] (for an overview, please see Hutchison’s work [135]). This is because previous studies made arbitrary choices for the length of the fixed window. On the contrary, we employed an approach wherein the stationarity of the time series under consideration dictated the length of the window. To guarantee that the time series within the length of the window was locally stationary, we employed the Dickey-Fuller test (DF test) [169] to determine the window length. The DF test is a hypothesis test for the existence of unit root in a given time series with zero mean. A given time series $y(t)$ can be modeled as.

$$y(t) = \alpha y(t-1) + \varepsilon(t) \tag{4.1}$$

Where t is the time index, α is a coefficient, and $\varepsilon(t)$ is the error term. A unit root is present when $\alpha = 1$, in which case, the mean and variance of $y(t)$ are a function of time t, implying that $y(t)$ is non-stationary. The DF test has a null hypothesis that a unit root exists and the time series is non-stationary. The test procedure in our work was as follows. At a given time point t_1, we chose the initial window length to be m_{-} (m_{-}=14 TRs in this work. The deduction of this initial window length is described in Appendix A, Section A.1), and did the DF test on time series within [t_1-m_-+1, t_1] from all 190 regions. If no unit root existed for all 190 time series, we assumed they were consistently stationary and used these windowed time series to calculate Pearson's correlation for time point t_1. Otherwise, the window length was increased by 1 time point (or 1 TR) such that the windowed time series started from t_1-m_- to t_1, and then we redid the DF test. We iterated this procedure until consistent stationarity was achieved or the maximum window length was reached. The maximum window length m_+ was chosen as 140 TRs. (see Appendix A, Section A.1 for mathematical deduction). The windowed Pearson's correlation calculated was the "valid" section of it, i.e. only those parts that were calculated without the zero-padded edges. The sliding window was moved forward one TR each time, i.e. from t_1 to t_1+1, and we repeated the above procedure to calculate the window length at that time point. The first 140 data points of the time series were utilized for the DF test of the first sliding window. Thus, t_1 started from 141st time point and dynamic FC had a length of 1060 time points (1200 is the total number of time points for human resting state data).

4.2.4 Clustering

The output from the dynamic connectivity model was a matrix of size A×A×B×C where A =190, the number of brain regions covering all gray matter, B=1060, the number of time points of dynamic FC and C=80, the number of runs over all subjects. Note that at each time point of each run, A×A represented a functional connectivity matrix of all possible paths between the 190 regions. Then, we employed adaptive evolutionary clustering method [150] to adaptively cluster all regions according to their FC matrix at each time point such that the smoothness of the transition of the whole brain clustering from one time point to the next is controlled by a forgetting factor. This first-level clustering allowed us to capture dynamic FC network configurations wherein both connections between regions and the networks themselves were changing with time (Fig.4.1 (B)). In second-level clustering, we investigated which of the first-level clustering configurations consistently occurred over time, i.e. it was a clustering of the first-level results over time. This informed us of brain network configurations which were similar to each other at different time instants, thus shaped into a pattern for a given subject. Then the second-level brain network patterns which occurred consistently across runs and subjects were identified using a third-level clustering across runs and subjects. A schematic illustrating all three levels of clustering is illustrated in Fig.4.2. Below, we elaborate on each of these clustering approaches.

First level clustering

The input to the first-level clustering algorithm was a distance matrix constructed from the dynamic FC matrix. We assumed that higher the absolute value of FC, the closer the two regions were in feature space. Note that we did not differentiate between "correlated" and "anti-correlated" interregional relationships in this work, whereas we plan to add this additional layer of complexity in future work. However, we cannot directly use interregional FC as the "distance measure" for the following reasons. First, the closer the two regions in feature space, the smaller their distance should be, but their connectivity's absolute value was bigger. This implies a monotonically decreasing transformation be required to convert FC to distance measure. Second, distances should be nonnegative, with the value being zero if and only if the distance is between one region to itself. But the FCs have negative values and the FC from one region to itself is one. In order to meet these requirements, we used a distance measure D, defined by $D=1-|P|$, where Pearson's correlation P ranges between -1 and 1. This transform is monotonically decreasing, the result is nonnegative, and the distance from one region to itself is zero. Other requirements of distance measures including reciprocity (the distance from one region to another should be same as the other way around) and triangular inequality are also met by *D*.

After the distance matrix ***D*** was obtained for each time instant, it was fed to the adaptive evolutionary clustering algorithm [150]. This clustering was based on the distances between regions at each time point and the smoothness of the transition of the whole brain clustering of FC patterns from one time point to the next was controlled by a forgetting factor. The forgetting factor was actually a weighting of previous clustering results on the calculation of clustering at current time instant, which was determined by Bayesian information criterion (BIC) [170]. The hierarchical method [171]was chosen as the clustering method.

The choice of the number of clusters in any clustering algorithm can be based on mathematical criteria such as the silhouette index [172] or based on heuristics and prior information regarding the underlying variables. The latter case is preferable when information is available to make that decision, otherwise mathematical criteria are preferred. Specifically with respect to the number of FC networks in the brain, many previous works used methods including fuzzy clustering [173], ICA based methods, especially PICA (probabilistic ICA) [174] and tensor PICA [175], graph theory-based network analysis [176], and fully exploratory network ICA (FENICA) [177] [178] [179] to find the number of consistent resting state networks (RSNs). The current understanding of human resting state networks comprises a set of 10 confirmed networks that are specialized in functionality: visual network, working memory network, executive network, dorsal attention network, ventral attention network, auditory network, sensorimotor network, basal ganglia network, language network, as well as the well-known default mode network. Further, the RSNs are hierarchically organized [179] [173]. This implies that when the number of networks (clusters) increase, some networks will split into sub-networks, usually into left and right lateral parts or peripheral and foveal parts, rather than reshape into a new network which seemingly has no relation with the previous ones. Previous studies have demonstrated that if the number of networks is 2, the brain can be functionally divided into task-positive and task-negative networks [173]. However, if the number of clusters/networks increases to a number between 5 and10, aforementioned 10 networks emerge gradually one by one [175] [173]. Specifically, Damoiseaux et al. [175] used tensor PICA in which a three-dimensional tensor represented spatial, temporal and subject-specific loadings to find group representatives of these 10 networks. Futher, Kalcher et al. [179] regressed a linear relationship between scan time and number of networks. According to this work, it can be inferred that when scan time reduce to smaller than 100s, the number of networks that can be consistently found across groups was approximately 10. The first level clustering was conducted at each time instant, which can be seen as having a very short scan time. In this regard, 10 was an appropriate choice for the number of clusters at the first level. Also, when the number of networks is specified to be more than 10, these RSNs will split into its subparts, but it is noteworthy that structured artifacts (such as head motion and field inhomogeneity) may also appear as individual networks [179]. Given these factors, we specified 10 as the number of clusters during first-level clustering.

Second level clustering

We investigated which of the first-level clustering configurations consistently occurred over time using second level clustering. Technically speaking, second-level clustering was the clustering of first-level results over time. Unlike first-level clustering which was dynamic in nature, i.e. clustering configurations at each time instant impacted those at later time instants, second level clustering was static in nature. Hierarchical approach to clustering was employed and the number of clusters was determined by silhouette index (with a search range between 2 and 20) given that *a priori* heuristics for determining the number of clusters in this situation are yet to be established. The search range was determined according to current understanding of the number of quasi-stable FC configurations which recur over time during the course of an experiment. The number of temporal FC patterns found by previous works is normally less than 20. For example, Li et al. [146] found 16 reproducible temporal FC patterns across healthy people via effective dictionary learning and sparse coding algorithms. Zhang et al. [180] found 12 representative functional states using a dynamic Bayesian variable partition model. Besides, the number of temporally quasi-stable patterns of EEG topography, called microstates, found by previous literatures is also generally less than 20. Britz et al. [138] found the optimal number to be 4, Musso et al. [149] found 10 recurrent microstates. Thus, we set the search range to be 2-20 to accommodate all possibilities.

The distance measure between two first level clustering configurations was calculated using a procedure illustrated in Fig.A5 of Appendix A, Section A.7. Suppose at time point t_m, the first level clustering result is called M and at a different time point t_n, the first level clustering result is called N. M has 10 clusters represented by m_i, i=1, 2…10, and N has 10 clusters represented by n_j, j=1, 2…10. Firstly, we compare the number of common regions (common members) between each possible pair m_i, n_j, and then among them we select the pair m_{i*}, n_{j*} that has the maximal number of common regions, and we assign the same label to all regions in m_{i*} and all regions in n_{j*}. Then we remove this pair and find the next pair which has the maximal number of common regions in remaining possible pairs, and assign regions belonging to this pair the same label (this label is different from previous label). Then we remove this pair and continue this procedure for remaining clusters. If the maximal number of common regions becomes zero for remaining possible pairs, then we assign all regions in all remaining clusters in M some label (different from all previous labels) and all regions in all remaining clusters in N a different label (different from all previous labels). Consequently, no pairs are left in M and N and all regions are labeled in both M and N. Finally, the distance measure is devised to be the number of regions having different labels in M and N. It is evident that this distance measure meets requirements of reciprocity, non-negativeness, triangular inequality, and self-distance being zero.

The outcome of second-level clustering was a number of clusters with first level configurations as their members. Theoretically, each second-level cluster centroid was a weighted sum of first level configurations such that each region in theoretical centroid had fuzzy belongingness to each first level cluster. This was awkward to maneuver, display, and used for next level clustering. So, for each second level cluster, we calculated the mean matrix $\bar{\boldsymbol{D}}$ from first level distance matrices $\boldsymbol{D_i}$ of all its members, wherein *i* indexes all members in the given second level cluster. The member whose distance matrix was closest to $\bar{\boldsymbol{D}}$ in the Euclidean sense was chosen to represent the theoretical centroid of the second level cluster. The Euclidean distance *E* between $\bar{\boldsymbol{D}}$ and $\boldsymbol{D_i}$ was calculated using Eq.4.2 below.

$$E^2 = \sum_{n=1}^{r}\sum_{m=1}^{r}(\boldsymbol{D}_i(m,n) - \bar{\boldsymbol{D}}(m,n))^2 \tag{4.2}$$

Where *r* represents the number of columns (and rows), which is equal to the number of regions, in the corresponding matrix.

Third level clustering

Each second level cluster represented a brain network pattern in one run. Not all second-level patterns were of interest to us, only those patterns with a lot of members (first level configurations) were dominating and important patterns. The dominating second-level patterns which occurred consistently across runs/subjects were identified using the third-level clustering across all runs. For the third-level clustering, the centroids representing dominating second-level patterns as mentioned above were used as members for clustering. Dominating second-level patterns were predicated based on the histogram of second level clusters' occurrence times (the number of first level members included in one second level cluster, one member took up 1 TR) obtained from all runs/subjects (Fig.4.3). It is evident that the majority of second-level clusters had occurrence times less than 100 TRs. Therefore, we used occurrence times of 100 as the threshold to determine dominating second level clusters, which were then input to third level clustering. Transient second level patterns with occurrence times less than 100 were inconsistent and hence were not input to third level clustering since the objective of performing third level clustering was to find dominant and consistent brain network patterns across subjects/runs.

To calculate the distance measure between dominating second level centroids, the strategy adopted in second level clustering was not feasible since each centroid had a weight, i.e. the occurrence times of the second level cluster it represented. Therefore, we performed weighted clustering at the third level. For any dominating second level centroid i, we had its FC distance matrix $\boldsymbol{D}_i$. We picked out all the lower (or upper) triangular elements of $\boldsymbol{D}_i$ and vectorized it to represent its corresponding point in feature space. The diagonal elements were all zeros and hence not considered. Then weighted K-means algorithm was employed to cluster these points in feature space. The number of clusters was determined by silhouette criterion and each cluster's centroid was calculated by weighted mean. Similar to the second level clustering, each region in theoretical third level centroid had fuzzy memberships to each second level cluster centroid, hindering display and subsequent analysis. So, the member whose distance matrix was nearest to the theoretical third level centroid was selected as third level centroid agent. The procedure for all three levels of clustering is schematically illustrated in Fig.4.2.

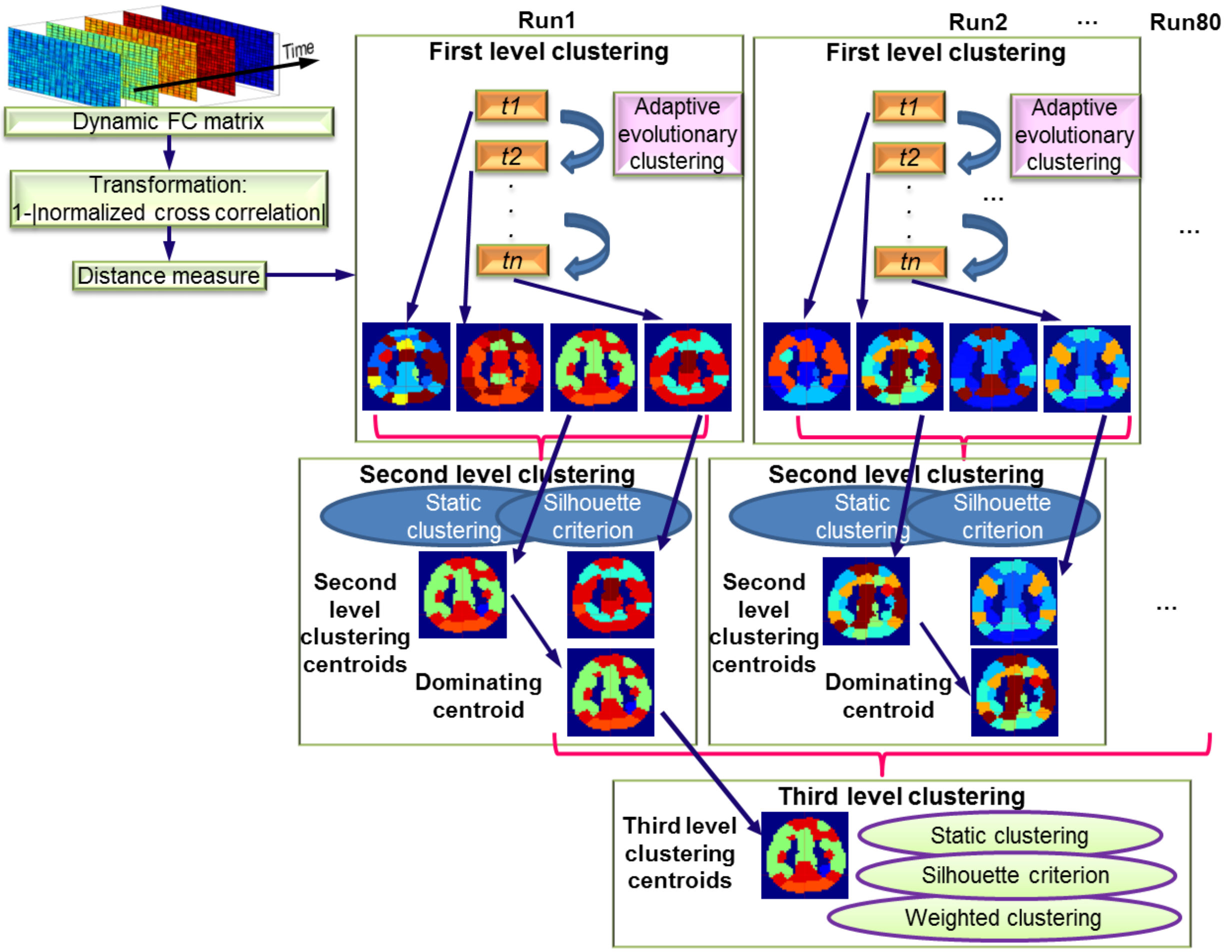

Figure 4.2 Schematic of the procedure for all three levels of clustering. The top left part illustrates the transformation of dynamic FC to a distance measure; top right part is the first level clustering; below is the second level clustering and at the bottom is the third level clustering.

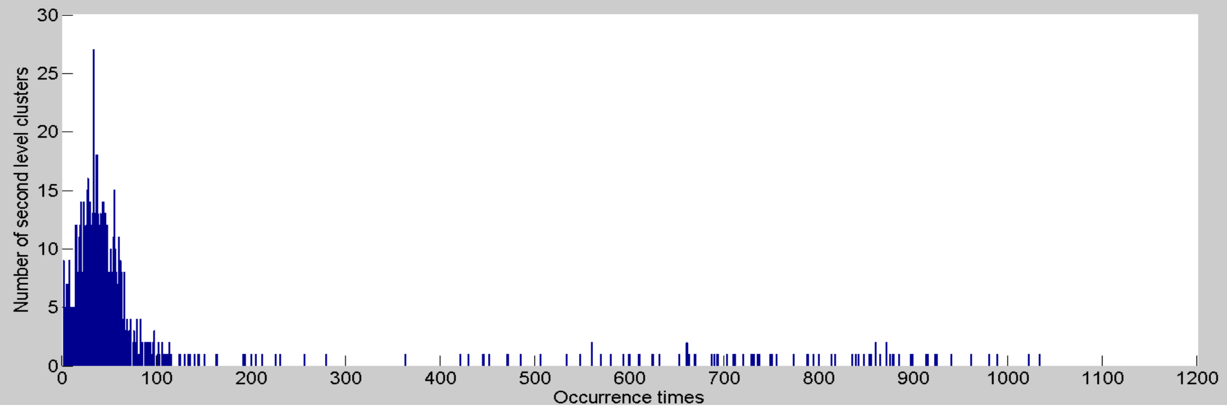

Figure 4.3 Histogram of occurrence times (in TRs) of second level clusters from all runs

4.2.5 Behavioral Relevance of Dynamic FC

We defined three metrics to represent dynamic FC based on the first level clustering result. The first was the mean time that two regions were in connected (or disconnected) state before transitioning into a disconnected (or connected) state, called mean time before state transition (MTST). The second was standard deviation of the time before state transition (SDTST). The third was called CFP (clustering frequency percentage), which measured the percentage of total time that two regions were clustered relative to total scanning time. In addition, the conventional static FC (SFC) obtained from the entire time series was adopted as the fourth metric. An illustrative example demonstrating state transitions and the procedure to calculate MTST, SDTST and CFP is shown in Fig.A6 in Appendix A, Section A.8.

The behavioral scores obtained from a variety of behavioral tests capturing alertness, cognition, emotion, and personality were input into a GLM as the dependent variables with dynamic and static FC metrics as explanatory variables as given below:

$$B_{i,j} = \alpha_{i,j} \cdot \mathrm{MTST}_{i,j} + \beta_{i,j} \cdot \mathrm{SDTST}_{i,j} + \gamma_{i,j} \cdot \mathrm{CFP}_{i,j} + \delta_{i,j} \cdot \mathrm{SFC}_{i,j} + \varepsilon_{i,j} \tag{4.3}$$

Where i indexes different behavioral tests, j indexes the FCs between different pairs of regions, $B_{i,j}$ is a vector of behavioral scores for all subjects, $\mathrm{MTST}_{i,j}$, $\mathrm{SDTST}_{i,j}$, $\mathrm{CFP}_{i,j}$ and $\mathrm{SFC}_{i,j}$ are vectors of corresponding metrics for all subjects. $\alpha_{i,j}$, $\beta_{i,j}$, $\gamma_{i,j}$, and $\delta_{i,j}$ are their coefficients, respectively, and $\varepsilon_{i,j}$ is residual. It should be noted that we had the 4 metrics from 80 runs (2 runs for each of the 40 subjects), but behavioral scores only from 40 subjects. So each subject's behavioral score was used twice corresponding to its two runs. The coefficients from this GLM were estimated using a standard least squares procedure and were tested for statistical significance using a z test. A Bonferroni corrected p-value threshold of p=0.05/75=0.00067 (75 is the number of behavioral tests) was used to infer significant relationships between dynamic and static FC metrics and behavior. Then, the variance explained in this GLM model by each metric was calculated. For example, $\overline{\left(\alpha_{i,j}\,\mathrm{MTST}_{i,j}\right)^2}$ is the variance explained by MTST. The overline denotes mean operation over all *i*s and *j*s. And $\overline{\left(\alpha_{i,j}\,\mathrm{MTST}_{i,j}\right)^2} \Big/ \left(\overline{\left(\alpha_{i,j}\cdot\mathrm{MTST}_{i,j}\right)^2} + \overline{\left(\beta_{i,j}\,\mathrm{SDTST}_{i,j}\right)^2} + \overline{\left(\gamma_{i,j}\,\mathrm{CFP}_{i,j}\right)^2} + \overline{\left(\delta_{i,j}\,\mathrm{SFC}_{i,j}\right)^2}\right)$ represents the relative percentage of variance explained by MTST.

4.3 Results

4.3.1 Simulations

To validate our proposed method for dynamic FC calculation and clustering, simulations were performed on artificial data. We simulated time series from 12 regions, each with 1000 time points, using a multivariate vector autoregressive model (MVAR) given as:

$$\boldsymbol{V}(t)=\sum_{i=1}^{p} A_i \cdot \boldsymbol{V}(t-i)+\boldsymbol{\varepsilon} \tag{4.4}$$

Where $\boldsymbol{V}(t)$ denotes the vector of signals from 12 regions, $\boldsymbol{A}_i$ is the regression coefficient matrix, and $\boldsymbol{\varepsilon}$ represents noise vector with covariance matrix $\boldsymbol{C}$, which has autocorrelation coefficients normalized to 1. To exclusively test time-varying FC, 3 scenarios were used:

(i) $\boldsymbol{A}_i$s were all zero matrices (thus time-lagged connectivity was excluded, and there was no need to specify *p*), $\boldsymbol{C}$ was constant over time, 12 regions' time series were divided into 4 clusters each having 3 members connected to each other (regions 1, 2, 3 were in one cluster, regions 4, 5, 6 were in one cluster, regions 7, 8, 9 were in one cluster, and regions 10, 11, 12 were in one cluster). In this case, $\boldsymbol{C}$ was a blocked symmetric positive definite matrix with 3×3 blocks on the diagonal.

(ii) Same as first scenario except that every non-zero element in ***C*** was slowly varying over time in a sinusoidal manner with period equal to 200π and randomized phases. The belongingness of each region to each cluster was not changed as compared to scenario (i).

(iii) Same as first scenario except after every 200 time points, ***C*** was circularly shifted by one column and one row such that the membership of each time series changed with respect to its cluster.

It should be noted that the lower and upper limits of sliding window length for DF test were set to 10 and 100 time points as derived in Appendix A, Section A.1. And the windowed Pearson's correlation calculated was the "valid" section of it, i.e. only those parts that were calculated without the zero-padded edges. The sliding window moved forward one time point each time, and the [1, 100] section of simulated time series were preserved for DF test of the first sliding window. Thus the resultant time series of dynamic FC had 900 time points, corresponding to [100, 1000] section of simulated MVAR time series. Above rule was applied to experimental fMRI data analysis also.

The simulation was conducted 100 times for each scenario and the results are shown in Figure 4.4. The mean and standard deviation (over all 100 iterations) of the resulting time-varying FC time series from several representative regions are illustrated. In Fig.4.4, subfigure (A) corresponds to scenario (i) specifically showing the connections from region 1. As shown on the left, the ground truth FCs between regions are constant and the auto-correlation is one. The estimated time-varying FCs (right) approach the ground truth very well and the auto-correlation is constantly one. Subfigures (B) and (C) show the results corresponding to scenarios (ii) and (iii) wherein the estimated time-varying FCs track the ground truth sufficiently well, and the regions belonging to different clusters (regions 4 & 11 in Fig.4.4 (B) and regions 1 & 8 in Fig.4.4 (C)) have nearly zero correlation, indicating no false positives. In particular, when the simulated cluster belongingness changes in Fig.4.4 (C), the estimated time-varying FCs respond to it swiftly and converge quickly. Subfigure (D) demonstrates one representative realization of AEC algorithm over time (first level clustering) for simulated time-varying FCs of scenario (iii). Along the time axis, regions rendered the same color belong to the same cluster. After 200 time points, the cluster belongingness (and hence the nodal configuration for the networks) is simulated to be circularly shifted once. For example, from time points 1 to 200, regions 1, 2, 3 are clustered together, region 4, 5, 6 are clustered together, and so on. Then from time points 201 to 400, regions 2, 3, 4 belong to the same network, regions 5, 6, 7 belong to the same network, …, regions 11, 12, 1 belong to the same network. This switching pattern is tracked correctly using estimated dynamic FCs, with only short transitional time. (Fig.4.4 (D), right). Note that since the time-varying FC time series corresponds to [100, 1000] section of MVAR time series, the cluster belongingness switches occur at time point 100, 300, 500, and 700. In summary, the simulations demonstrate the feasibility of the proposed approach for tracking dynamic FC and ascertaining the clustering of regions based on dynamic FC over time through the AEC algorithm.

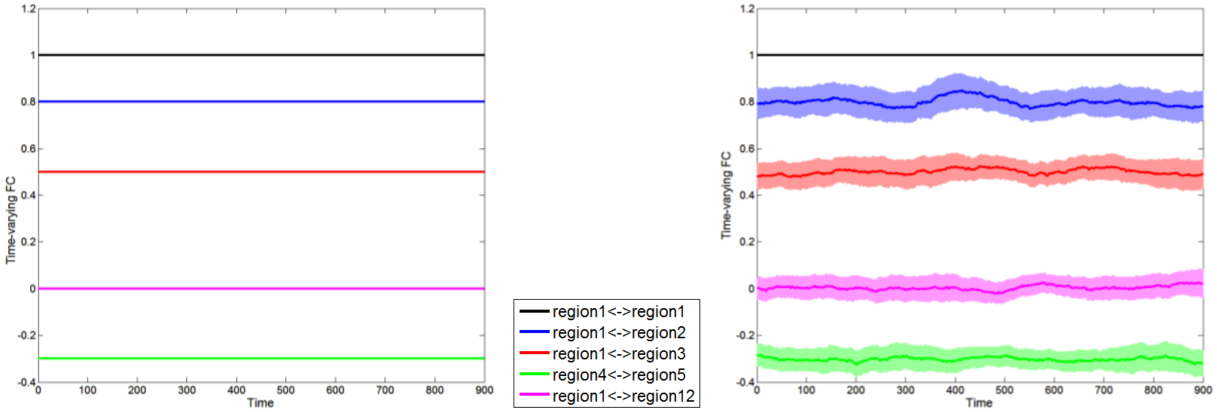

(A)

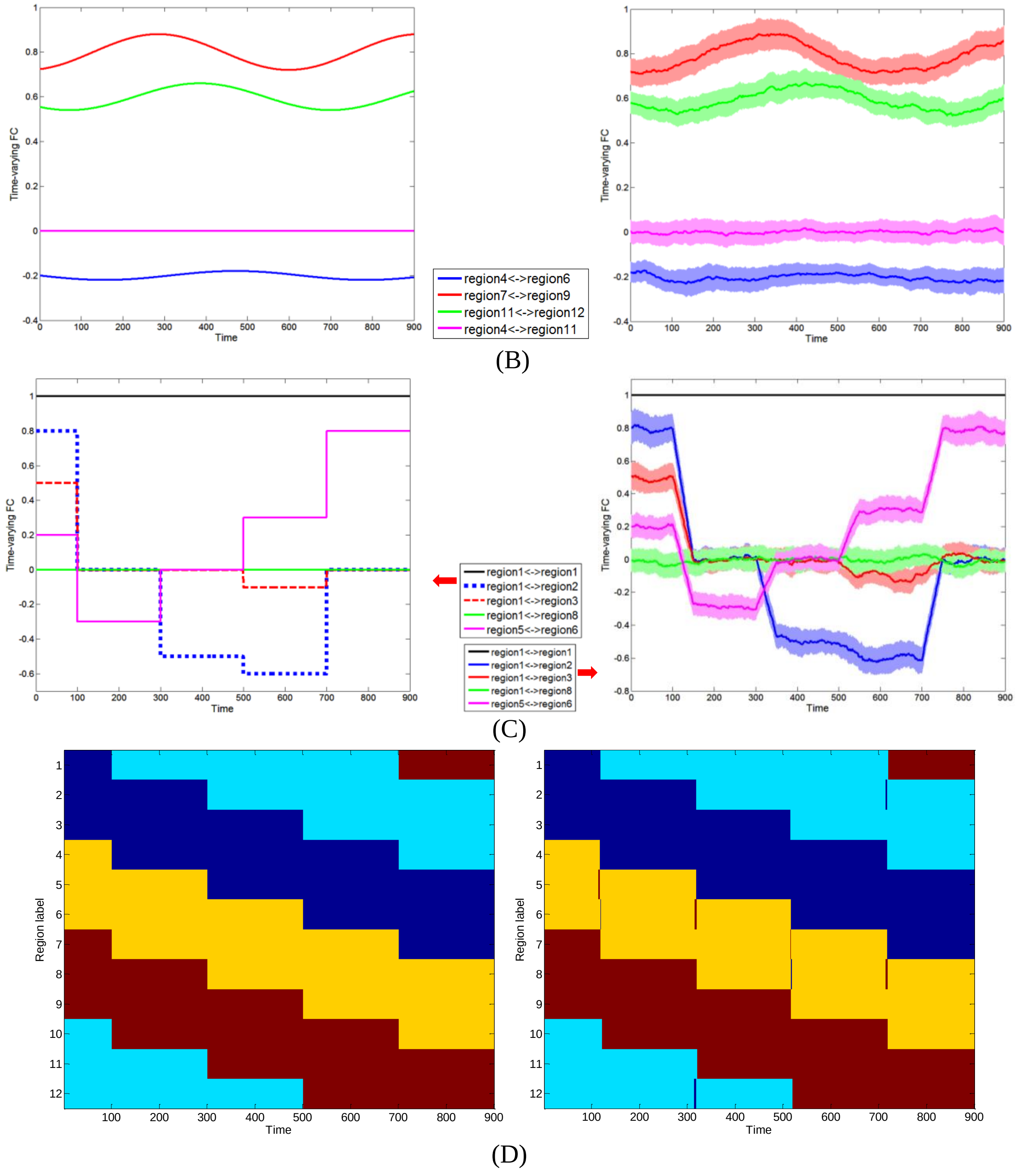

Figure 4.4 Simulation results for time-varying FC and first level clustering. The simulated MVAR processes consisted of 12 regional time series, each with 1000 time points. (A) left: example showing simulated ground truth for time-varying FCs of scenario (i); right: estimated mean and standard deviation (std) of simulated time-varying FCs. Color bands span [mean-std, mean+std] with mean in the middle. (B) left: example showing simulated ground truth for time-varying FCs of scenario (ii); right: estimated mean and standard deviation of simulated time-

varying FCs. (C) left: example showing simulated ground truth for time-varying FCs of scenario (iii); right: estimated mean and standard deviation of simulated time-varying FCs. (D) left: ground truth clustering pattern for one representative example of simulated time-varying FCs corresponding to scenario (iii); right: corresponding estimated clustering pattern calculated using AEC algorithm. Regions rendered with the same color are connected to each other and hence belong to the same cluster.

4.3.2 Application to Experimental Resting State FMRI Data from HCP

Resting state fMRI data obtained from HCP were minimally preprocessed and underwent additional pre-processing by us as elaborated in Material and Methods section. We applied our framework for calculating dynamic FC and three levels of clustering to this fully pre-processed dataset. Figure 4.5 shows the centroids obtained from third level clustering, which represent whole brain connectivity patterns which appear consistently across time and subjects. In this figure, brain regions with the same color are functionally connected to each other and the strength of those connections are stronger than those between them and brain regions with a different color. Note that clustering is a vector quantization scheme which assigns each region in the brain to a cluster such that the distance between the given region and other regions inside the cluster is minimized and the distance between the given region and other regions outside the cluster is maximized. A statistical summary is listed in Table 4.1, which presents each third level cluster's statistics including number of members (dominating second level centroids), and the sum of occurrence times of members in TRs. Together, these two metrics determine the relative dominance of each third level cluster. We obtained 8 third level clusters according to the silhouette criterion [172]. It is clear that cluster #1, 2, 6 and 7 are more dominant than others, and cluster #8 is the least dominant. Note that the numbers assigned to clusters are incidental and carry no particular meaning. Also, the cluster centroids in Fig.4.5 are in the same order as in Table 4.1. The DMN can be observed in the centroids of cluster #3, #4, #6 and #8. These four clusters account for approximately 32% of the total occurrence times of dominating second level clusters (OTDSLC). Also, it is to be noted that the regions of the DMN are connected to regions outside the DMN in addition to being connected to each other in clusters #2, #5, and #7. Taken together, this implies that the regions of the DMN are connected to each other and appear as part of the same cluster for approximately 78% of OTDSLC. The visual network, comprising of regions in the primary and secondary visual cortices, appears in centroids #1, #3, #4, #5 and #6, with #6 having only occipital area, #3 having occipital-parietal-frontal interaction (merged with dorsal attention network) and others having frontal-occipital interaction. They account for 57% of OTDSLC. The language network, comprising of Broca’s and Wernicke’s areas, appears in centroid #6 and clusters with cerebellar regions. This network accounts for 15% of OTDSLC. The sensorimotor network appears in centroid #1 and splits into bilateral parts in centroid #4, accounting for 33% of OTDSLC. The dorsal attention network merges with the visual network in centroid #3 and appears as an individual network in centroid #6. So, in total it accounts for 19% of OTDSLC. The executive network can be seen only in centroid #4 which accounts for 11% of OTDSLC. The ventral attention network appears as a clear network (dark red) only in centroid #8 which accounts for 11% of OTDSLC. The limbic network can be seen in its entirety in centroid #1 which accounts for 22% of OTDSLC, and splits into several parts (thalamus, caudate, basal ganglia, etc.) with each part having connections with cortical regions in centroids #3, #5, and #7. Brainstem appears as an individual cluster in centroid #2, and in centroid #2 we can observe that the ventral frontal areas also shapes into individual clusters, such as rectus, indicating that they have weak FC with other areas. It should be noted that since many networks co-occur in certain centroids, percentages of the total occurrence times of dominating second level clusters for all RSNs do not sum to 100%.

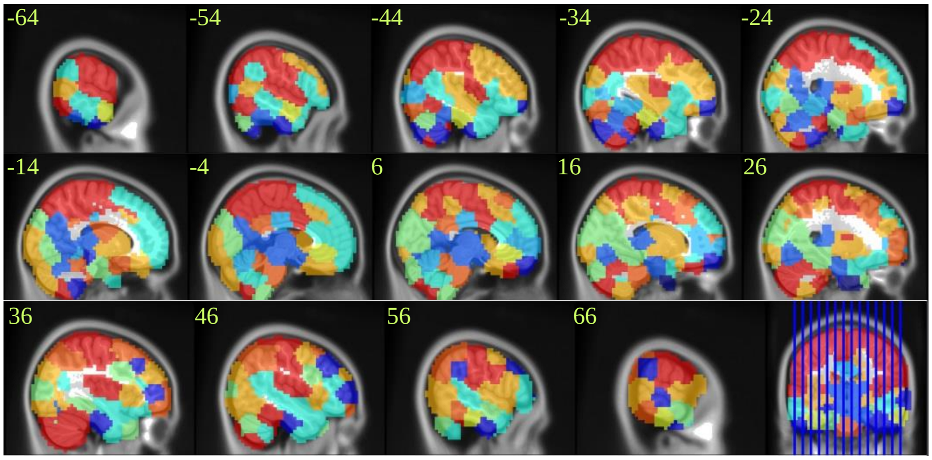

(A) Third level clustering centroid #1

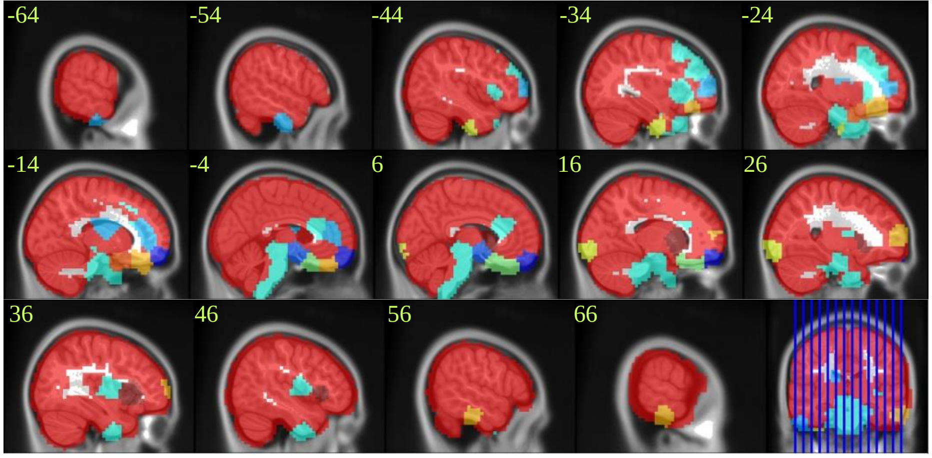

(B) Third level clustering centroid #2

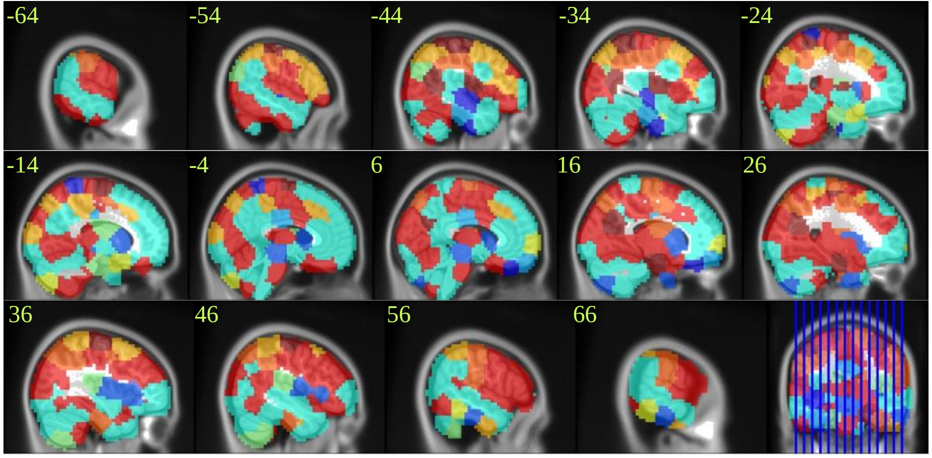

(C) Third level clustering centroid #3

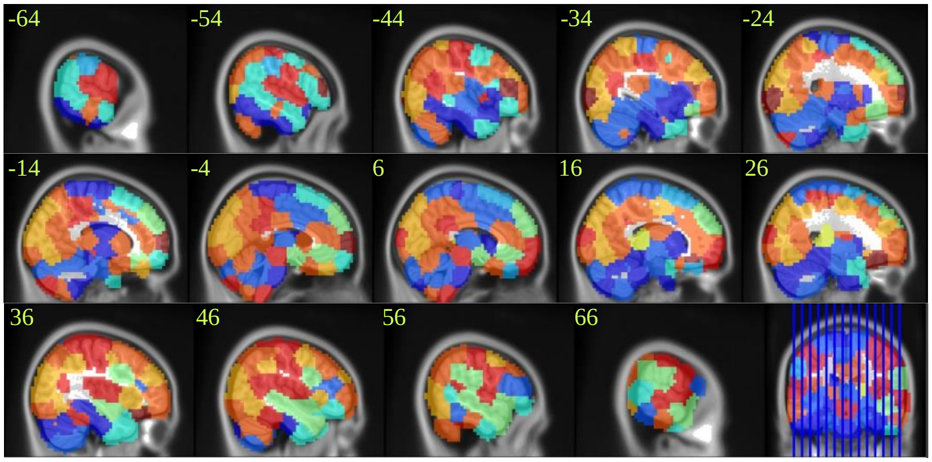

(D) Third level clustering centroid #4

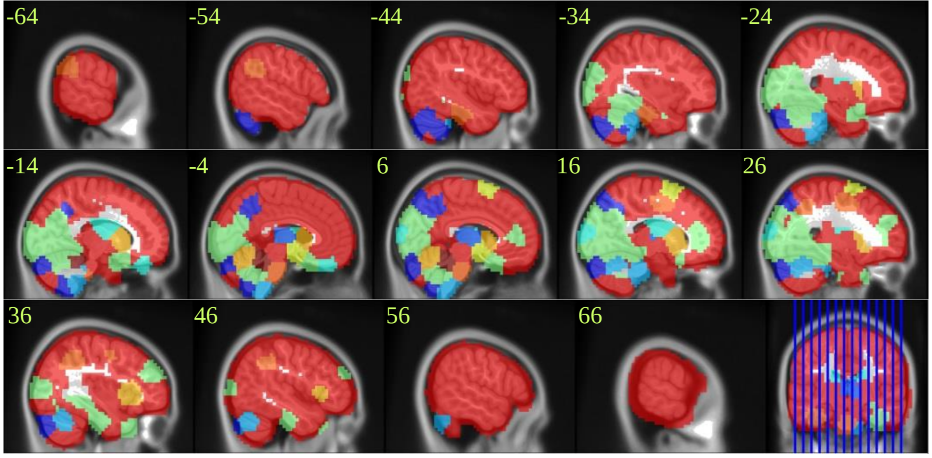

(E) Third level clustering centroid #5

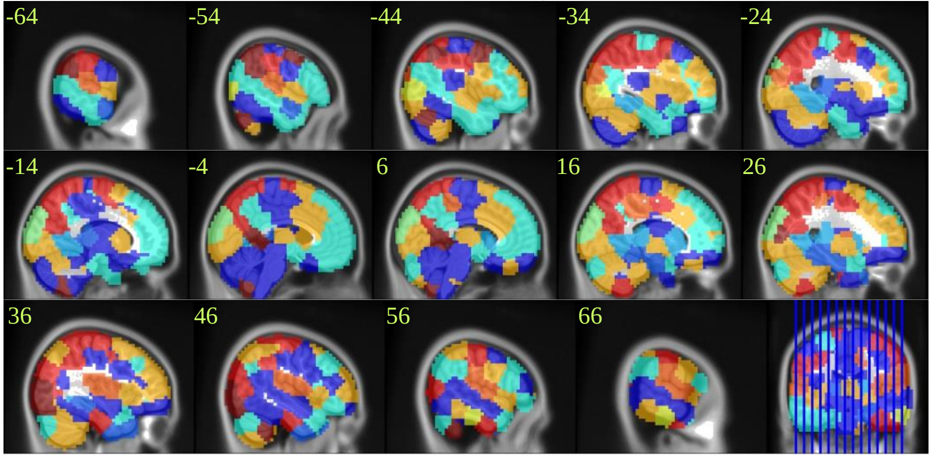

(F) Third level clustering centroid #6

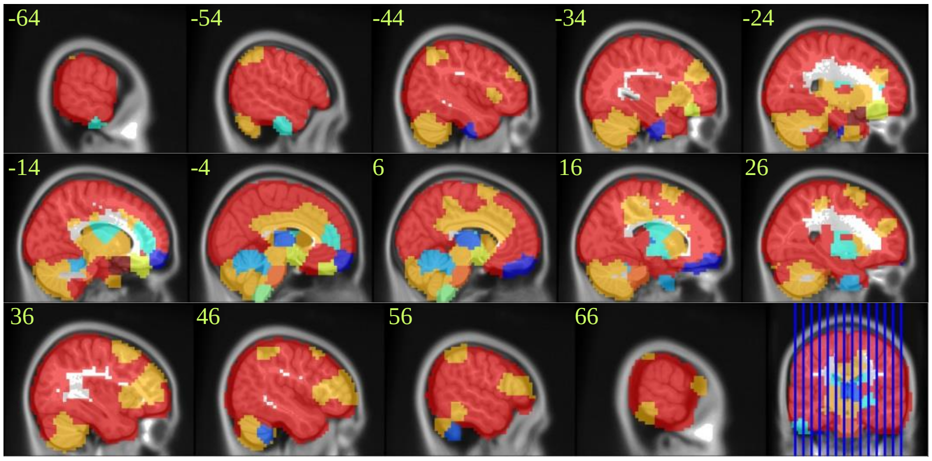

(G) Third level clustering centroid #7

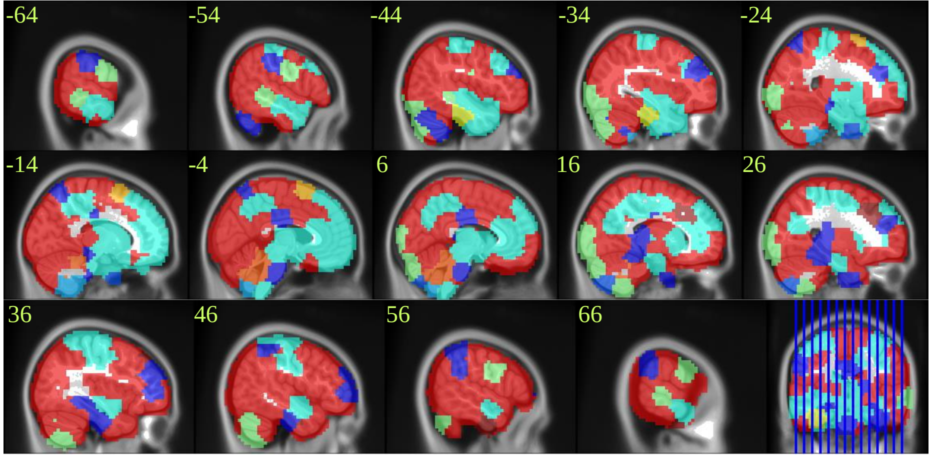

(H) Third level clustering centroid #8

Figure 4.5 Third level clustering centroids. Each subfigure shows one third level centroid. The order of third level centroids is the same as in Table 4.1. There are a total of 8 clusters with each centroid chosen as the cluster member (which is one of second level dominating centroids) that is nearest to the theoretically calculated centroid. Each color in each subfigure represents regions connected to each other. The number shown at the top left of each sagittal slice is the x coordinate (left to right), in mm.

Table 4.1 Statistical summary of third level clustering

Third level cluster	**Cluster #1**	**Cluster #2**	**Cluster #3**	**Cluster #4**	**Cluster #5**	**Cluster #6**	**Cluster #7**	**Cluster #8**	**Sum**
No. of cluster members	33	19	7	19	4	15	15	1	113
Sum of all members' occurrence times (TR)	13776	14702	2787	6838	2744	9140	11209	813	62009

Characterization and quantification of dynamic and static FC

We used three metrics: MTST, SDTST, and CFP to characterize dynamic FC based on the first level clustering result. In addition, the SFC obtained from the entire time series was adopted as the fourth metric.

Fig.4.6 shows interregional MTST, SDTST, CFP and SFC matrices averaged over all runs. Generally a higher value of MTST indicates lesser dynamic variations of FC between regions. We can observe that several regions have much less dynamics of FC in relation to other regions, such as regions 35, 36 and region 168, corresponding to brainstem and right rectus gyrus (for corresponding AAL anatomical area of each region, please see Appendix A, Section A.2). Also noteworthy is that many regions having higher MTSTs generally have lower CFPs and SFCs. This indicates that regions such as brainstem and rectus gyrus with high MTSTs are barely connected with other regions during the course of the experiment.

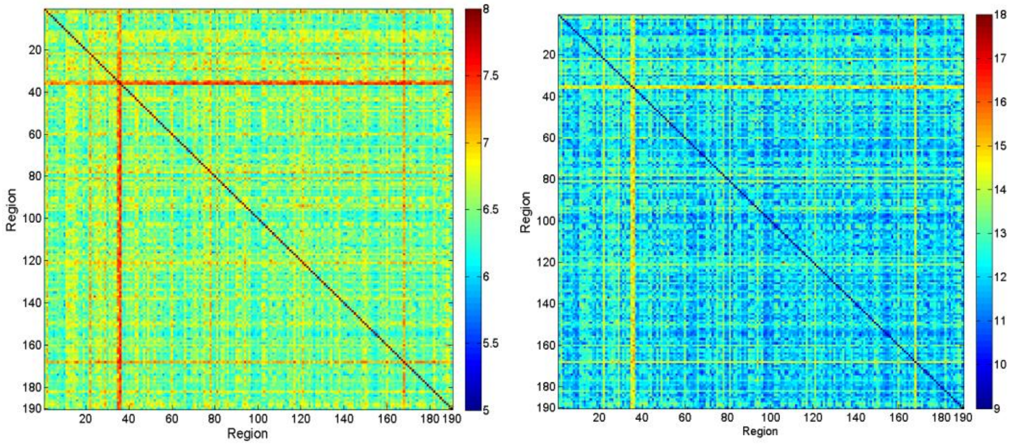

(A)		(B)

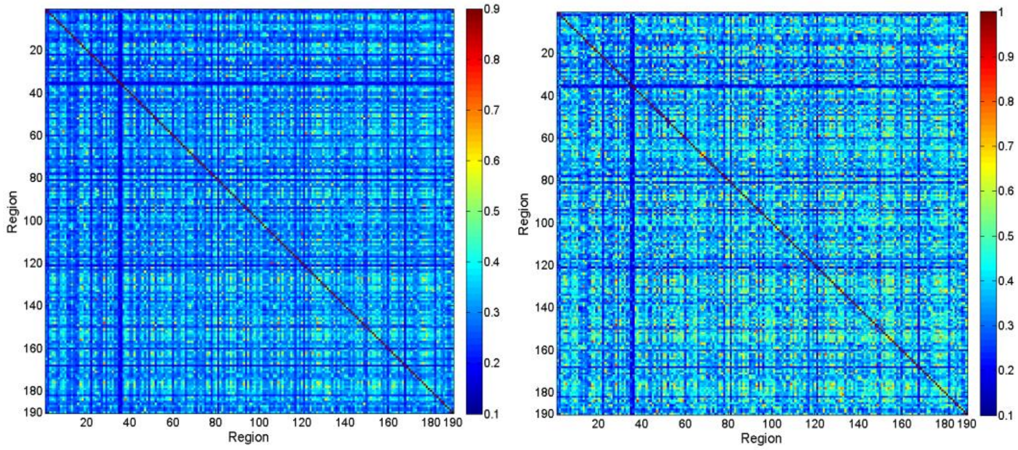

(C) (D)

Figure 4.6 Interregional MTST, SDTST, CFP, SFC matrices averaged over all runs. Numbers along horizontal and vertical axis are region labels. For the AAL nomenclature corresponding to these numeric labels, please see Appendix A, Section A.2. (A) MTST; (B) SDTST; (C) CFP; (D) SFC. (Note: for each matrix, diagonal elements represent the dynamic or static FC metric between a given region and itself. Therefore, the colors of diagonal elements have no meaning and not comparable to off-diagonal elements)

Fig.4.7 shows the paths (connections between regions) with MTSTs within the top and bottom 0.1% of MTSTs of all paths. The MTSTs here are averaged over all runs. The red paths represent interregional MTSTs whose values are among the top 0.1% of all MTSTs, and blue paths represent interregional MTSTs whose values are among the bottom 0.1% of all MTSTs. We choose top and bottom 0.1% here in order to improve visualization such that paths with most significance could be emphasized. Figures showing top and bottom 0.5% and 1% MTSTs are in Appendix A, Section A.4 (Fig.A1 and A2, respectively). If the threshold is set beyond 1%, the number of paths is too big such that it prevents any meaningful visualization. These results reinforce the point we made about large MTSTs for the rectal gyrus, that it is seldom clustered with other regions and for most of the time it appears as a sole cluster at the first level, implying that it has very weak dynamic FC with other regions. On the other hand, right superior occipital cortex and left cuneus had a large MTST due to the fact that they are always connected, indicating a very strong FC in between. This can be verified by inspecting interregional CFP matrix (Fig.4.6 (C)). The blue paths with low MTSTs represent connections with highly dynamic FC. One network involving the mid-frontal cortex, anterior and mid cingulate, insula and supplemental motor area, as well as another intra-cerebellar network stands out.

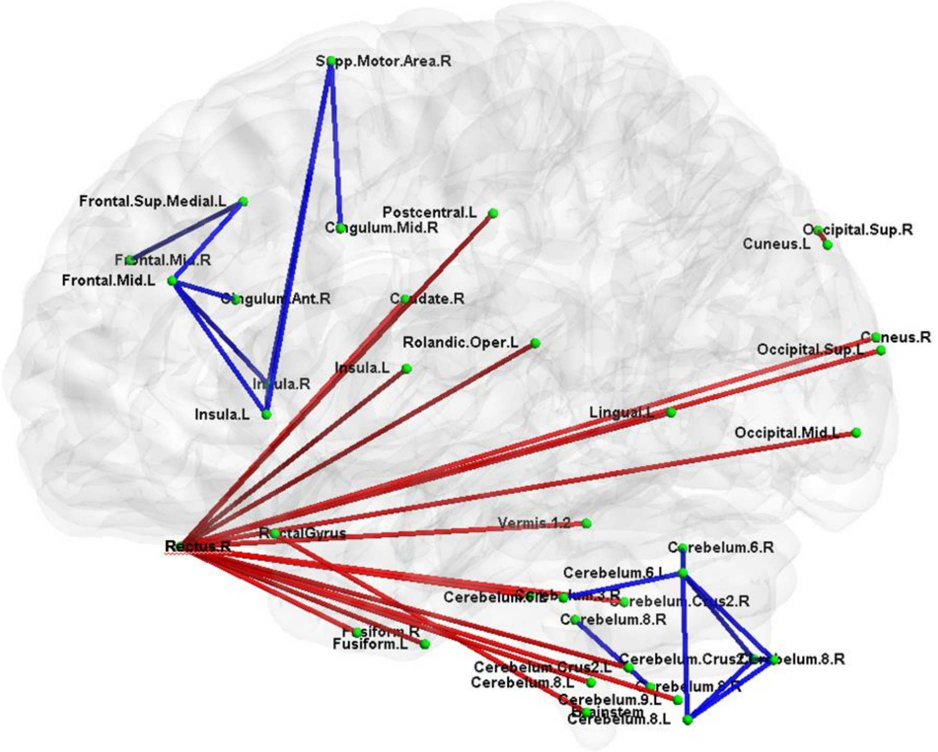

Figure 4.7 Paths with most and least interregional MTSTs. The red paths represent interregional MTSTs whose values are among the top 0.1% of all MTSTs, and blue paths represent interregional MTSTs whose values are among the bottom 0.1% of all MTSTs. All MTSTs have been averaged over all runs.

Each brain region has 189 paths associated with it and hence the same number of MTSTs. We define a metric, regional MTST (rMTST), by finding the mean MTST of all paths associated with a given region. Brain regions with rMTST in the top 30% and bottom 30% are shown in Fig.4.8 (A) and (B), respectively. Similarly, regional CFP (rCFP) is defined as the mean CFP of all paths associated with a given region and regions with rCFP in the top 30% and bottom 30% are shown in Fig.4.8 (C) and (D), respectively. We choose top and bottom 30%, because at this proportion, known RSNs are revealed. For comparison, a figure showing regions with top and bottom 20% rMTST and rCFP is shown in Appendix A, Section A.5 (Fig.A3). It is noted that fewer number of regions, which do not constitute known RSNs are revealed in this figure. It can be seen from Fig.4.8 that the brainstem and rectus have highest rMTST and lowest rCFP, which is in agreement with the results presented above, i.e. low dynamics and unconnected to other regions for a major portion of the experiment. Superior occipital cortex has high rMTST as well as high rCFP for the reason that it is frequently connected with nearby occipital regions. Besides, DMN, DAN, and FPCN have low rMTST, indicating high dynamics of FC. Especially noteworthy is DMN, which has the lowest rMTST, i.e. highest dynamics of FC. Most occipital, temporal, superior frontal and parietal areas have high CFP, indicating they generally have strong FC to other regions.

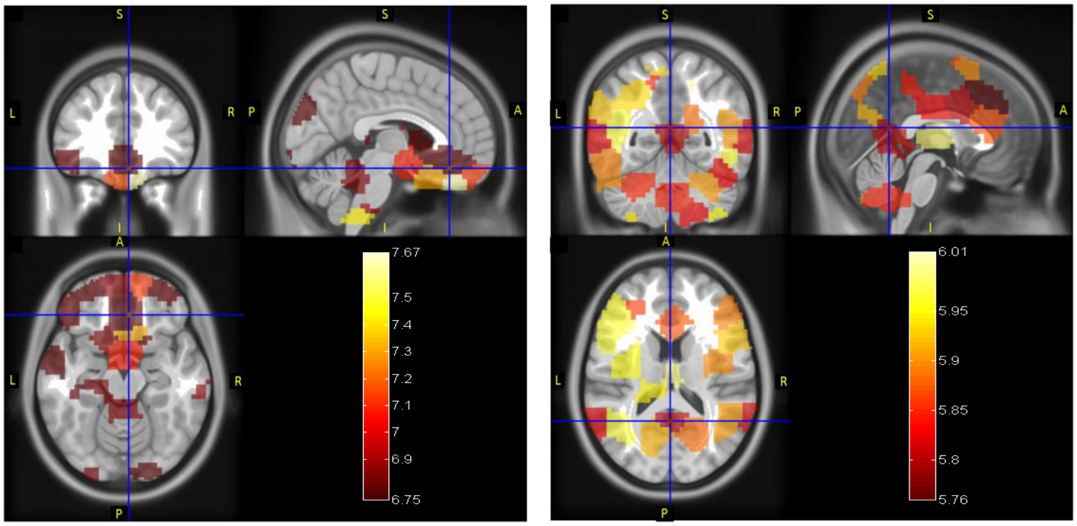

(A) (B)

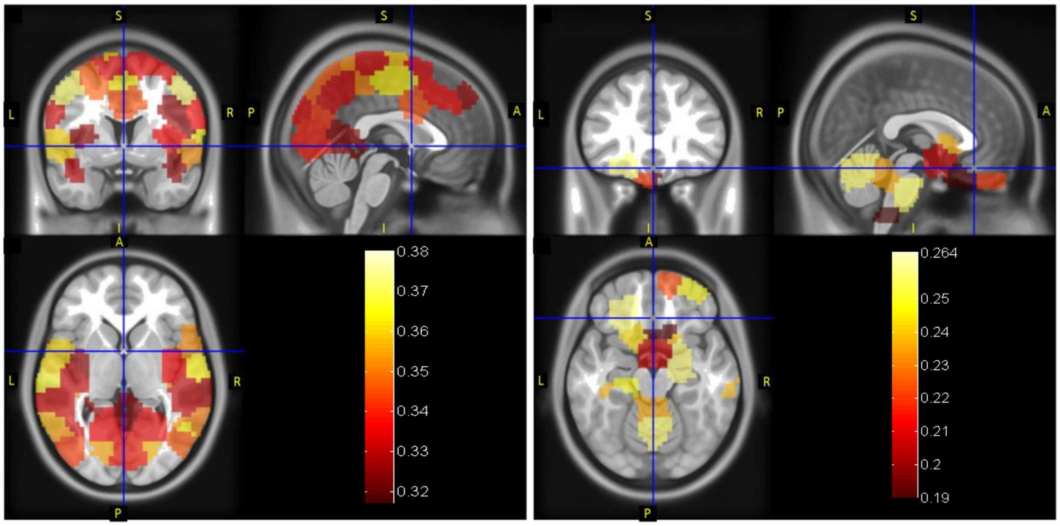

(C) (D)

Figure 4.8 Regions with top and bottom 30% rMTST and rCFP. Each brain region has 189 paths associated with it and hence the same number of MTSTs. We define a metric, regional MTST (rMTST) and regional CFP (rCFP), by finding the mean MTST/CFP of all paths associated with a given region. Regions with top 30% of all rMTST are shown in (A) and with bottom 30% of all rMTST are shown in (B).Corresponding maps for top and bottom 30% rCFP are shown in (C) rand (D), respectively. Hot colormap is used to represent the numeric value of corresponding metric for each region shown. (A: anterior, P: posterior, S: superior, I: inferior, L: left, R: right)

Behavioral relevance of dynamic and static FC

Dynamic and static FC metrics were together input into a general linear model with HCP behavioral measures as dependent variables for investigating their behavioral relevance. Fig.4.9 presents the relative percentage of variance explained by each metric for 75 behavioral scores pertaining to alertness, cognition, emotion, and personality, obtained using a general linear model with each behavioral score as the dependent variable and dynamic and static FC metrics as independent variables. Each relative percentage of variance explained is shown as an error bar with mean and standard deviation derived across all paths between 190 regions in the brain. It is remarkable that the variances explained by dynamic FC metrics MTST and SDTST are clearly higher than those by CFP and SFC for every behavioral measure. MTST in particular, has much more power in explaining behavioral variability than the other three. This is significant because it implies the dynamics of FC can be a better predictor of human behavior than conventional static FC.

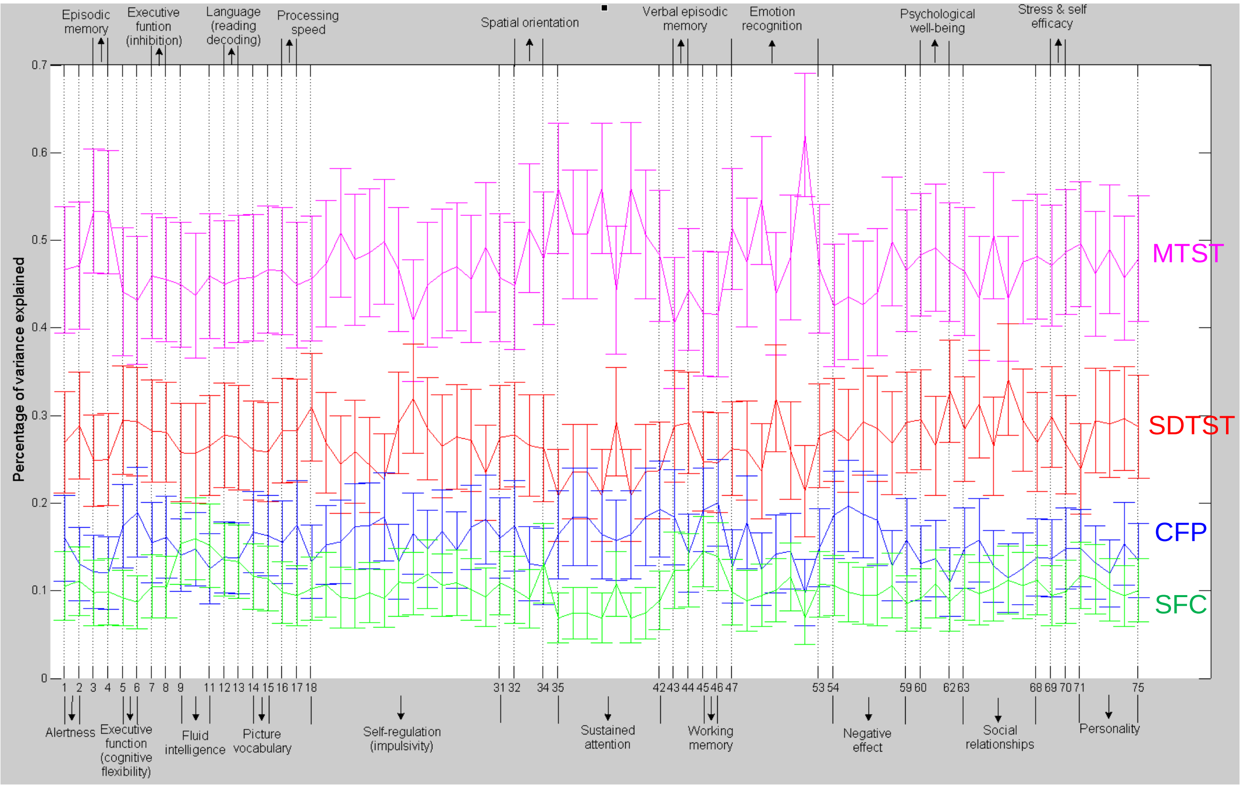

Figure 4.9 Percentage of variances in behavioral measures explained by dynamic and static FC metrics. Percentages of variances are shown as error bars with mean and standard deviation derived across all paths between the 190 regions in the brain. Three metrics were derived from dynamic FC: MTST (mean time before state transition), SDTST (standard deviation of the time before state transition) and CFP (clustering frequency percentage. SFC (static FC) is the conventional Pearson's correlation between time series. Along the horizontal axis are labels for various behavioral tests (a total of 75 tests, for details of each test, please refer to Appendix A, Section A.3). The broad behavioral domains of groups of behavioral tests are indicated above and below the figure.

Fig.4.10 shows the paths whose MTSTs significantly predicted several selected behavioral measures (for some other selected behavioral measures, please see Appendix A, Section A.6; for details of behavioral measures, please go to http://humanconnectome.org/documentation/Q3/Q3_Release_ Reference_Manual.pdf.), wherein the predictive ability was quantified by regression coefficient α for each MTST in the GLM shown in Eq.4.3 of the Materials and Methods section. The coefficient α was passed through a z-test and Bonferroni corrected for multiple comparisons (corrected p=0.05/75=0.00067, where 0.05 is uncorrected p value, and 75 is number of behavioral tests). In each subfigure, cobalt blue paths have negative α values, and red paths have positive α values. Note that subfigure (C) and (F) underwent further processing. Since there were a lot of paths whose MTSTs significantly correlated with true positives and false negatives of SCPT (Short Penn Continuous Performance Test) task, we obtained a distribution of the number of paths emanating from each region and found that only 10% of regions had more than 4 paths emanating from them. Based on this, we retained only those paths which connected at least one of the regions with a nodal degree of 5 or more. In this way, we were able to identify only the prominent hubs for proper visualization. However, the original figures without any processing are shown in Appendix A, Section A.6 and all of our conclusions would still be valid with the original result. In Fig.4.10 (A), all paths are cobalt blue, implying that higher the episodic memory score, lower the MTST and greater the dynamics of FC (please refer to Appendix A, Section A.3 for description of the picture sequence memory task corresponding to episodic memory). Many of these paths involve the cerebellum which makes sense given previous reports of its role in episodic memory retrieval [181] [182]. Other important areas include frontal cortex, occipital cortex, temporal cortex, parahippocampal area, precentral and parietal areas. Previous works have shown that these areas are activated in an episodic memory retrieval task [182] [183]. As stated by Miyashita [184], the temporal cortex is involved in memory encoding and retrieval, and acts as the integrator of memory and perception of objects. In Fig.4.10 (B), all paths' MTSTs are significantly negatively correlated with self-regulation and impulsivity (please refer to Appendix A, Section A.3 for description of the delay discounting task corresponding to self-regulation). The regions seen in this figure, i.e.

prefrontal cortex [185], interior parietal cortex [186], thalamus and caudate [187] [188], have been previously implicated in self-regulation. Fig.4.10 (C), (D), (E), and (F) belong to the behavior test of the same category: sustained attention, also termed vigilance (please refer to Appendix A, Section A.3 for description of the behavioral tests and associated scores corresponding to sustained attention). It is conspicuous that Fig.4.10 (C) and (F) are exactly the same except for the color (cobalt blue and red); and so are Fig.4.10 (D) and (E). This is due to the fact that (C) corresponds to true positives of SCPT as behavioral scores in the GLM and (F) corresponds to false negatives of SCPT. Similarly, (D) corresponds to true negative and (E) corresponds to false positives of SCPT. Also noteworthy is that paths in (C) and (D) are almost all cobalt blue and in (E) and (F) are almost all red. Taken together, these imply that lower MTST and hence greater dynamics of FC are associated with better performance on SCPT (i.e. true positives and true negatives in Fig.4.10 (C) and (D)). On the other hand, higher MTST and hence lower dynamics of FC are associated with poorer performance on SCPT (i.e. false positives and false negatives in Fig.4.10 (E) and (F)). The specific paths whose MTSTs predict behavioral variability involve brain regions including frontal cortex, precentral cortex, insula, occipital cortex, temporal cortex, inferior parietal cortex, and cingulate gyrus, which have been previously implicated in sustained attention and vigilance [189] [190] [191].

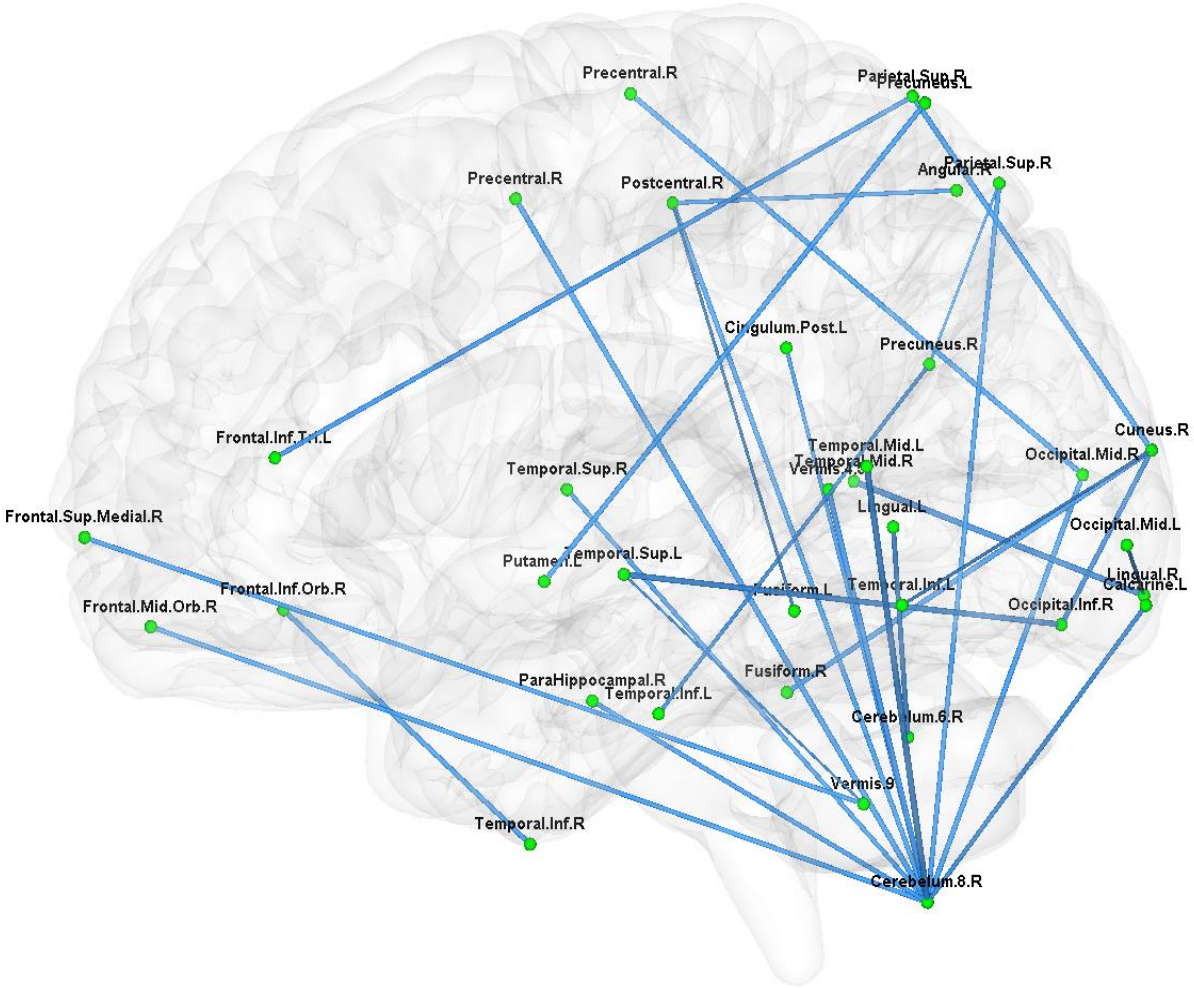

(A) Episodic memory (picture sequence adjusted)

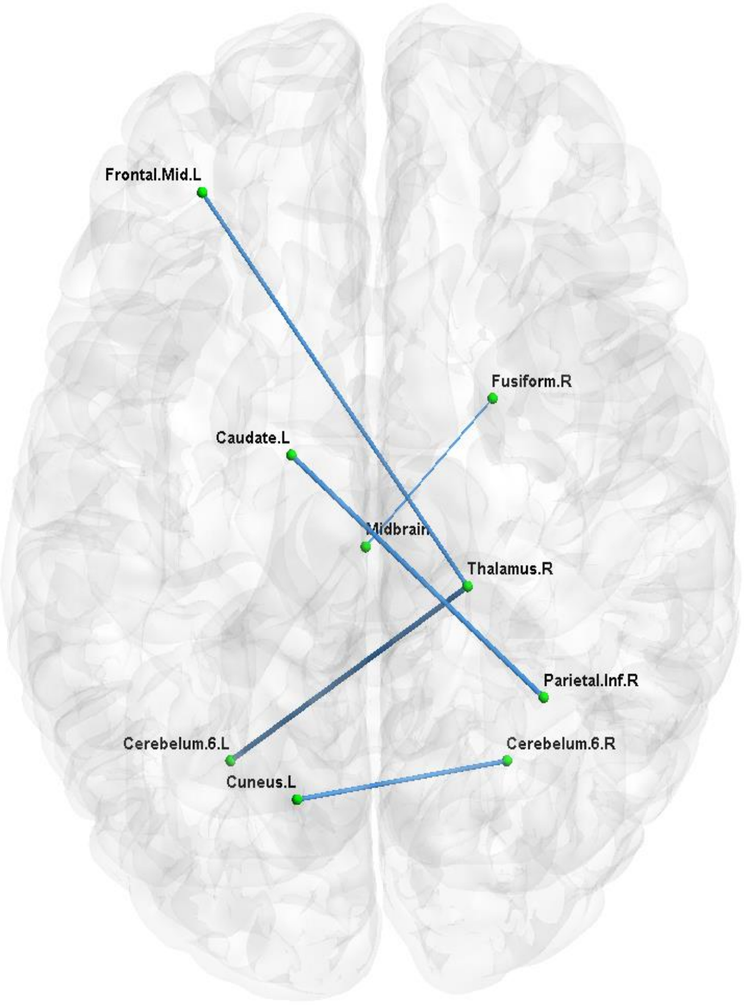

(B) Self-regulation/impulsivity (AUC_40k)

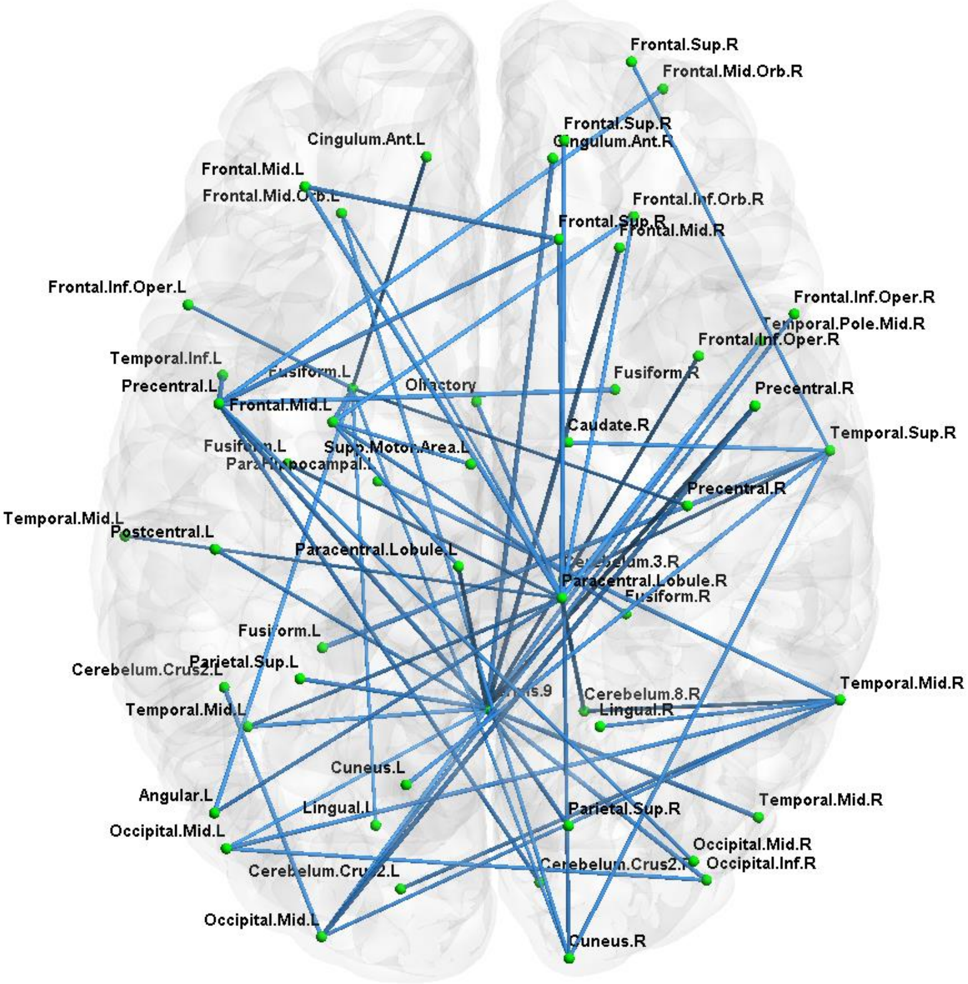

(C) Sustained attention (SCPT_TP)*

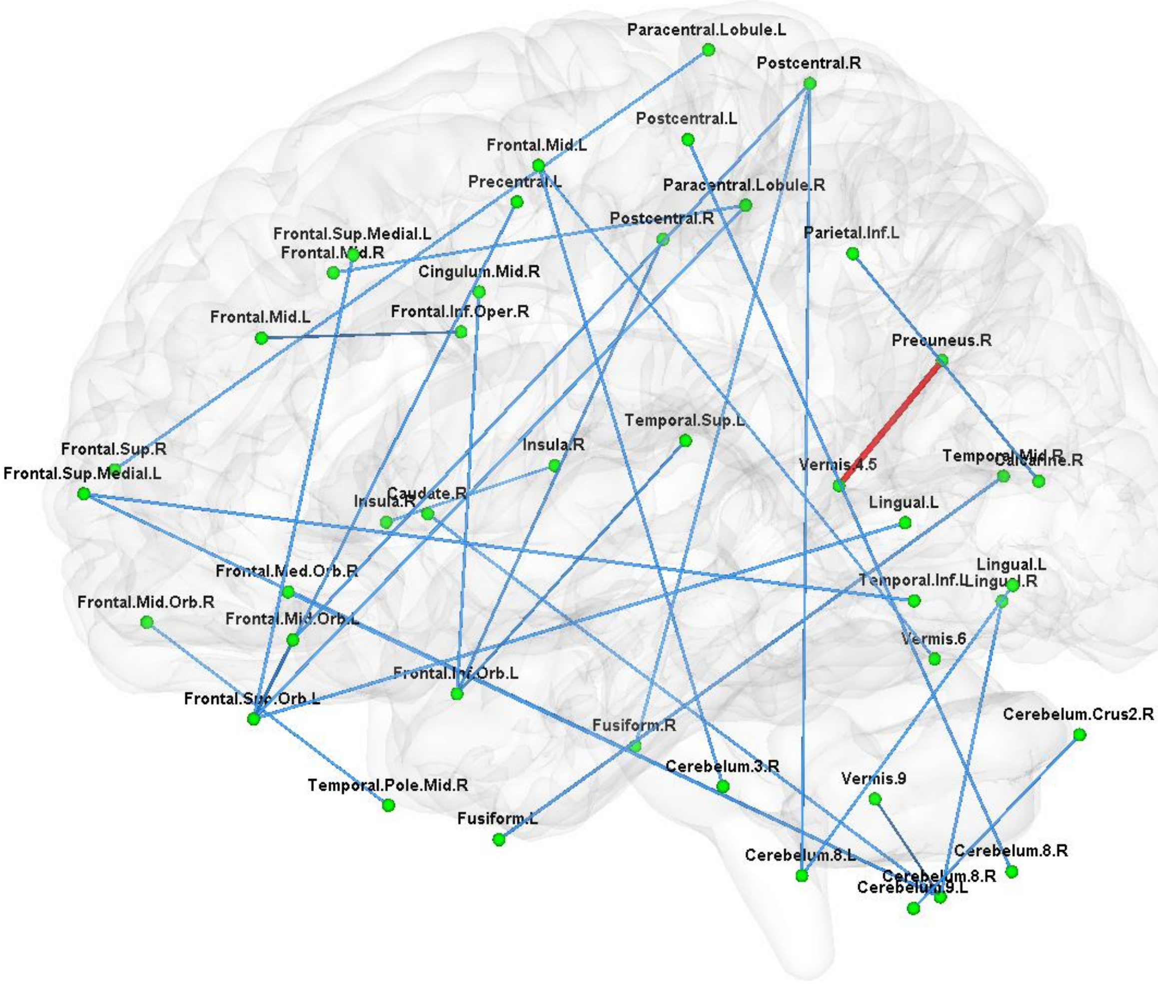

(D) Sustained attention (SCPT_TN)

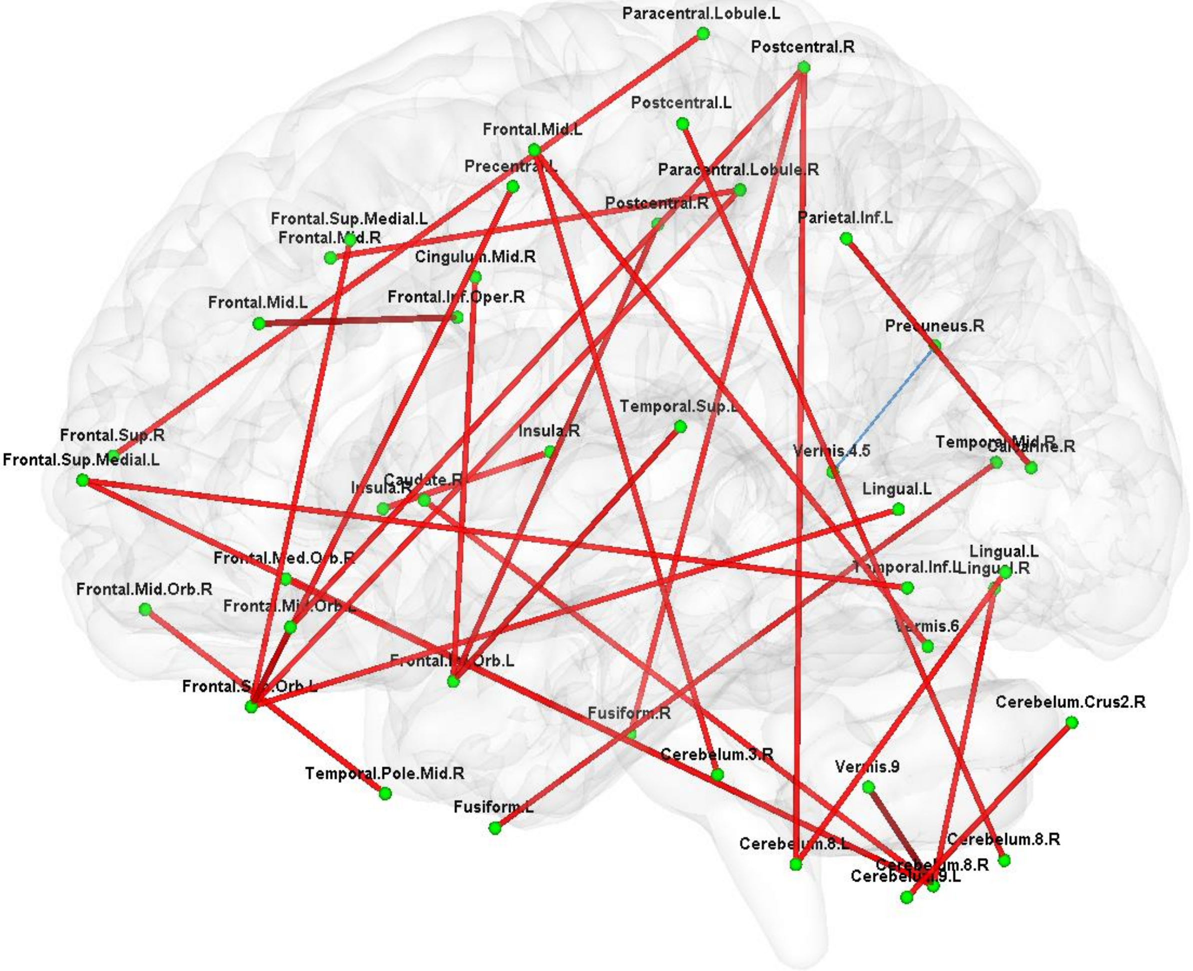

(E) Sustained attention (SCPT_FP)

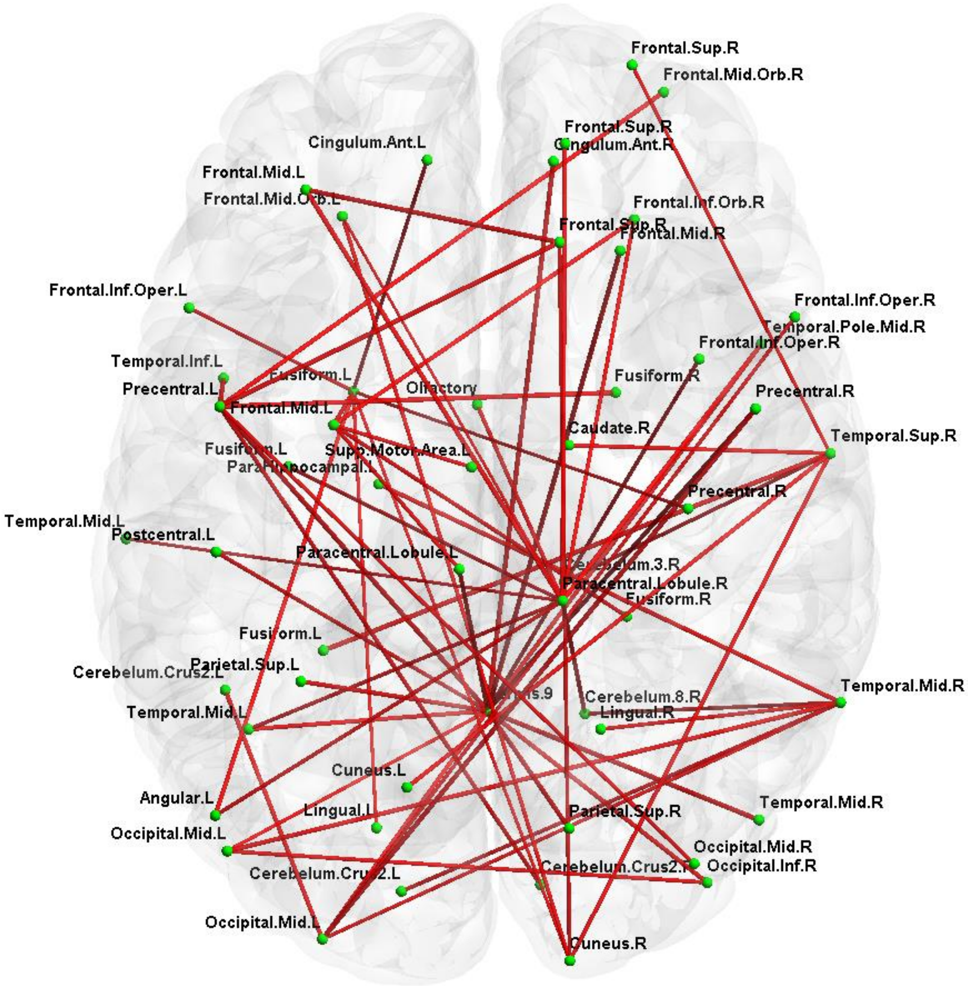

(F) Sustained attention (SCPT_FN)*

Figure 4.10 Paths whose MTSTs significantly predict variability in selected behavioral measures. The predictive ability is quantified by regression coefficient α for each MTST in the GLM shown in Eq.4.3 of the Materials and Methods section. The coefficient α is passed through a z-test and Bonferroni corrected for multiple comparisons (corrected p=0.05/75=0.00067, where 0.05 is uncorrected p value, and 75 is number of behavioral tests). In each subfigure, cobalt blue paths have negative α values, and red paths have positive α values. The behavior tests for subfigure are: (A) episodic memory (picture sequence test, adjusted). (B) Self-regulation/impulsivity (AUC_40k). (C) Sustained attention (SCPT_TP) processed. (D) Sustained attention (SCPT_TN). (E) Sustained attention (SCPT_FP). (F) Sustained attention (SCPT_FN) processed. Please refer to Appendix A, Section A.3 for description of behavioral tests and corresponding scores (*: subfigure (C) and (F) have been further processed. Original subfigures have too many paths that hamper visualization. Therefore, we only show paths that connect to nodes with 5 or more paths in subfigure (C) and (F). Please see Appendix A, Section A.6 for original subfigures.)

4.4 Discussion

In this work, we have proposed a framework for estimating dynamic FC between functionally homogeneous regions across the entire brain using adaptive windowing based on time series stationarity. This framework was first validated using simulations and subsequently applied to resting state fMRI data obtained from healthy individuals recruited through the HCP. The multi-dimensional connectivity pattern obtained from each subject was subjected to three levels of clustering across space, time and subjects in order to find brain FC network patterns and derive metrics for capturing connectivity dynamics. Both dynamic and conventional static FC metrics were correlated with behavioral variables in order to test the hypothesis that information derived from dynamic variations in FC better predicts behavior as compared to conventional static measures and that greater dynamic variability supports superior behavioral performance in healthy individuals. This section is organized as follows. We first discuss the third-level clustering results which show the most consistent whole-brain connectivity patterns across time and subjects. Second, we discuss the implications of paths as well as regions which exhibit highest and lowest dynamics. Third, we discuss the behavioral relevance of the dynamics of FC and support for the above stated hypothesis based on our results. Finally, we list certain future directions that may be worth pursuing.

First, among the RSNs revealed by third-level clustering results shown in Fig.4.5, DMN and visual network occupy more than 50% of the total occurrence times of dominating second level clusters, apparently higher than other RSNs. This is easy to apprehend since DMN has been shown to be a commonly observed network in the resting human brain by many previous reports [118] [151] and visual information processing is expected to be an ongoing phenomenon during resting with eyes open.

Second, results shown in Fig.4.6, 4.7, and 4.8 consistently indicate that gyrus rectus has very weak static FC and low dynamics of FC with other regions reflected as high MTST, low CFP, and low SFC. This indicates that it seldom clusters with other regions, i.e. appears as an individual cluster. The function of gyrus rectus is currently yet unclear, but anterior parts of the orbito-frontal cortex in general have been implicated in the processing of motivational information [192, 193]. Given that there is little motivational information to process during a resting state scan inside a scanner with eyes open and fixed on a target, it is understandable that there is very little static connectivity as well as its dynamics associated with paths between this region and other parts of the brain. The brainstem also has low FC and high MTST with other regions. Brainstem does not show up in Fig.4.7 which only displays top and bottom 0.1% of MTSTs. But in Fig.A1 and A2 (shown in Appendix A, Section A.4) showing top and bottom 0.5% and 1%, respectively, of MTSTs it does appear as the second hub with a lot of red paths associated with high MTSTs. The brainstem plays an important role in regulating cardiac, respiratory function, maintaining consciousness and regulating sleep. Brain stem's resting state connectivity with the neocortex is tightly coupled with corresponding variations in physiological fluctuations [140]. Therefore, removal of physiological fluctuations during pre-processing might have decreased the variance of the brain stem's signal to an extent that it appears disconnected with large parts of the brain for most of the time.

On the other hand, a network consisting of the mid frontal cortex, anterior and mid cingulate, insula, supplemental motor area, as well as an intra-cerebellum network stand out as having highly dynamic FC (Fig.4.7). Results with a higher threshold of 0.5% indicate that these two networks are connected by paths converging to the parietal cortex (Fig. A1 in Appendix A, Section A.4). In other words, the fontal-parietal-cerebellar circuit displays high FC dynamics.

When the threshold is further heightened to 1% (Fig. A2 in Appendix A, Section A.4), direct fronto-cerebellar paths emerge. These regions are involved in a range of functions which are too exhaustive to be listed here. Briefly, the mid frontal cortex is implicated in planning complicated cognitive processes [194], while the anterior cingulate plays a role in many cognitive functions such as initiation, motivation, and goal-directed behaviors [195]. Insula plays a role in various functions including perception, motor control, self-awareness, cognitive functioning, and interpersonal experience [196]. Stoodley et al. [197] suggested that different regions of the cerebellum containing sensorimotor, cognitive and limbic representations interacted with the parietal cortex. Taken together, fronto-parietal, intra-cerebellar and cortico-cerebellar networks which support a large range of brain functions appear to display highest dynamics of FC.

A closer look at regions having high dynamics of FC to all other brain regions in Fig.4.8 (B) reveals that nodes of common RSNs such as DMN, DAN and FPCN have similar dynamics. As pointed out by Vincent et al. [198], DAN and DMN are two opposing brain networks that are implicated in attention to the external world versus internally directed mentation, and the fronto-parietal control network (which includes regions implicated in cognitive control and are structurally located in between DMN and DAN regions) controls the switching between DAN and DMN. This controlling mechanism and the competing roles of DAN and DMN may underlie their high dynamics of FC. The PCC (posterior cingulate cortex) and precuneus have high dynamic FC and high CFP, probably as a result of strong FC paths with high dynamics linking it to frontal and cerebellar regions as discussed above.

Third, emerging evidence suggests that important individual differences can be associated with patterns of resting state brain connectivity, and the variability of static FC patterns across individuals can be reflected in corresponding variability of important cognitive and behavioral variables that affect real world function [163] [165] [166] [161] [162]. Recent reports indicate that dynamic FC is also predictive of behavioral performance in healthy individuals [165] [166]. However, it is yet unclear whether dynamic FC can provide additional predictive value over and above that provided by static FC. In order to answer this question, we obtained the predictive power of both dynamic and static FC on behavioral performance using a single general linear model. Our results clearly demonstrate that dynamic FC metrics, especially MTST, have much more power in explaining variance in behavioral performance tasks than static FC metric for each of the 75 behavioral tests considered, which include tests of alertness, cognition, emotion and personality. Further, results from Fig.4.10 demonstrate that higher dynamics of FC is predictive of superior behavioral performance. For example, higher episodic memory score, better sustained attention, higher self-regulation and lower impulsivity are all predicted by lower MTST and hence greater dynamics of FC. This supports our hypothesis that information derived from dynamic variations in FC better predicts behavior as compared to conventional static measures and that greater dynamic variability supports superior behavioral performance in healthy individuals.

The results presented here have profound implications for our understanding of what constitutes a healthy and desirable brain. Conventional wisdom dictates that deviations of static FC from what one would typically observe in a matched control population represent altered neural circuitry underlying various disorders. For example, hyper-connectivity has been observed in psychiatric disorders such as psychosis [199], schizophrenia [200] and post-traumatic stress disorder [201] [202] and hypo-connectivity has been observed in disorders such as autism [203]. In addition to the static FC value, the amount of variability of FC values over time may provide additional dimensions on which brain alterations may be assessed. For example, the inability to disengage from a state of altered connectivity may explain why one observes altered static connectivity in the first place. The fact that higher dynamics predicts better behavioral performance in healthy individuals indicates that the ease with which brain regions engage or disengage with other regions may be potential biomarkers for disorders involving altered neural circuitry.

We suggest that future work should be oriented in three directions. First, for dynamic FC calculation, we did not differentiate between “correlated” and “anti-correlated” interregional relationships in this work, and we plan to add this additional layer of complexity in future study. This is important because in addition to characterizing functional associations between regions, the nature of such associations can be characterized by including the sign. Second, fluctuations of brain states represented by RSNs measured by fMRI should coordinate with EEG microstates [204]. Thus, it is necessary to conduct a similar analysis using simultaneously acquired EEG data. Third, FC does not provide information on the directionality of connections. Previous reports have shown that directional connections provide a complimentary mode of communication between brain regions in resting state and that regions which seem to be dissociated at zero-lag might as well have time-lagged relationships [114]. Therefore, a similar analysis must be carried out using EC. Further, the predictive ability of dynamic EC on human behavior must be deduced and compared with that of dynamic FC and static EC.

Chapter 5 Dynamic Multivariate Analysis:

Finite Number of Directional Brain Network Configurations Revealed from Time-Varying Connectivity Assessment of Resting State FMRI

The work in this chapter is a continuation of that in Chapter 4. Chapter 4 deals with FC statics and dynamics with clustering strategy and correlation with behavioral measures, while in this chapter, we investigate the EC dynamics of the issue with similar clustering strategy, and we survey its relationship to cognitive behaviors in a somewhat different way. Our main contribution is that we proposed a dynamic EC model, applied AEC algorithm for dynamic EC pattern clustering, showed dynamics of EC network pattern had fractal-like quasi-stable character, and related them to real world functionalities.

5.1 Introduction

Previous Chapter 4 focuses on the exploration of functional connectivity (FC) and its correlates with behavioral measures. In this chapter, we focus on the study of effective connectivity (EC) and its relationship with real world functionalities. EC is a term used to describe measures of directional relationships between brain activity in different brain regions [110] [111] [114] [116]. Not only did most previous studies investigating FC assume the connectivity is stationary in time, but also most studies on EC assumed so. These static studies on connectivities have been linked to behavior and brain disorders for FC [125] [126] and EC [205] [206]. Further, some studies have reported that static EC relationships at rest represent a mode of communication between brain regions whose activities are not synchronized [114], and hence, both FC and EC taken together, provide complementary characterizations of brain connectivity at rest. As discussed in Chapter 4, evidences have pointed out that resting state FC is not stationary in time and an array of methods have been proposed to capture dynamic variations in FC. This raises the possibility that dynamic alterations in resting state EC cannot be ignored and needs to be investigated. This raises the possibility that dynamic alterations in resting state EC cannot be ignored and needs to be investigated. However, to the best of our knowledge, there has been no literature on dynamic EC of resting state fMRI, and most focus is drawn on task-based fMRI dynamic EC [207] [129].

As discussed in Chapter 4, to characterize the whole picture of resting state brain networks, it is necessary to employ the whole brain regions to conduct connectivity analysis. In this regard, FC runs ahead of EC. There exists a bulk of works exploring whole-brain static FC [157] [158], and several others exploring whole-brain dynamic FC [130] [159] using PCA or ICA based method. However, literatures on whole-brain EC are far less. This may due to the reason that the computational complexity is prohibitively high and very time-consuming if whole-brain regions are employed. And methods such as dynamic causal modeling [208] and structural equation modeling [209] impose restrictions on the number of regions that can be included in the model. In addition, it becomes difficult to formulate *a priori* hypotheses regarding connections between all brain regions which are required by these methods. Therefore, data driven approaches have become more popular while investigating EC between large numbers of brain regions. One such model is the multivariate autoregressive (MVAR) model which is used to capture time-lagged Granger causal influences between brain regions [210, 211] [114]. It has been previously demonstrated that the precision of the MVAR model increases when more variables containing information regarding the underlying system are included in the model [212]. Yet, to estimate the parameters of an MVAR model fit using all voxel time series in the brain would have a very high time cost which makes it practically impossible. Besides, an MVAR model with too many voxel time series as regressors is ill-conditioned and highly sensitive to noise. To address this issue, dimensionality reduction strategy is devised and an exemplary work employing whole-brain regions/voxels for static EC can be found in [213]. But, to the best of our knowledge, no work has been done on whole-brain dynamic EC analysis. In this work, we adopted dynamic Granger causality to represent dynamic EC, and the same dimensionality reduction strategy as in Chapter 4 which spectrally clusters voxel time series into functionally homogeneous brain regions. The CC200 atlas was designed for this purpose, partitioning the whole brain (gray matter) into functionally homogeneous regions [160]. The 190-region version within CC200 atlas was adopted in this work and this version took into account the balance between functional homogeneity and anatomic homology using a large resting state dataset [160]. But, our data did not have coverage of the cerebellum, thus we considered the leftover 164 cerebral regions from the 190-region version of CC200 atlas and fed mean time series from these regions into the dynamic MVAR model. This can be thought of as a pilot study to employ all cerebrum brain regions to assess dynamic EC.

As suggested in Chapter 4, evidences from dynamic FC analysis with fMRI and EEG data show the synchronized BOLD signal fluctuations over the brain organize into a finite number of ordered and patterned configurations alternating with each other in time [127] [146] [138] [149]. In this work, we hypothesized that dynamics of EC can also organize into a finite number of ordered and patterned configurations alternating with each other in time. To examine this hypothesis, we employed a similar clustering strategy to that in Chapter 4. Specifically, we performed simulations in order to demonstrate the efficacy of the dynamic EC model and then applied it to resting state fMRI data, and the resulting dynamic EC metric was transformed to distance measure for clustering. The adaptive evolutionary clustering (AEC) algorithm was adopted at this stage to find time-varying configurations of EC networks, a second level and a third level clustering were conducted to find dominant patterns across all runs and subjects. As shown in the case of static connectivity [114], absence of significant zero-lag connectivity does not imply the absence of brain connectivity. Rather, such regions could be connected via time-lagged relationships. This work is supposed to complement our FC work as introduced in Chapter 4, since both synchronization and causality are established mechanisms of brain connectivity and one needs to assess both measures in order to gain a complete understanding [110].

As discussed in Chapter 4, the amount of information obtained from assessment of dynamic connectivities over the whole brain is enormous, hindering the interpretation of underlying neuroscientific meaning [127]. To evade this issue, a lot of works such as those based on agglomerative clustering [138] [149] and principal component analysis [130] assume that the connectivity networks may have different weights in spatial or temporal domain, but the connectivity networks themselves do not change. This assumption suffers from loss of generality. The AEC approach proposed in Chapter 4 can evade the drawbacks brought by this assumption and we will continue to base our analysis on this approach for dynamic EC. A schematic illustrating both directional connections between nodes and the networks themselves change with time is in Fig.5.1.

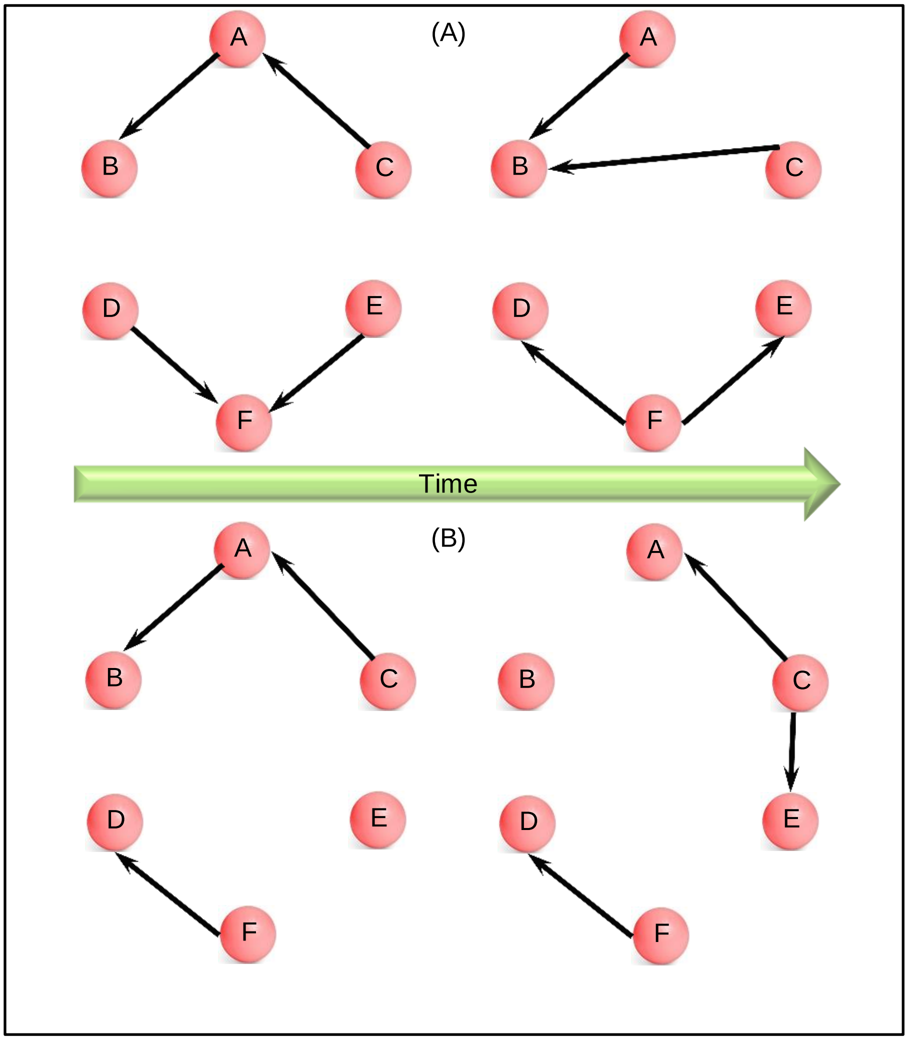

Figure 5.1 Schematic of two types of dynamic EC network configurations. (A) Schematic illustrating network configuration over time wherein all nodes are part of the same network, only the directional connections between them change with time. (B) Schematic illustrating network configuration over time wherein both directional connections between nodes and the networks themselves are changing with time.

5.2 Material and Methods

5.2.1 Data Acquisition and Pre-processing

Resting state fMRI data were acquired from a 3T Siemens Verio scanner in Auburn University MRI Research Centre from 21 healthy adults (aged 29.68±11.06 years, 6 females). Informed consent was obtained from all subjects after explaining and reviewing detailed written information about the study protocol, which was approved by the IRB of Auburn University. In all experiments, subjects were lying at rest during the scan with eyes open, and they were instructed to relax without falling asleep or thinking about anything in particular. After the scan, all subjects confirmed adherence to these guidelines. T2*-weighted echo planar imaging with the following parameters were used for fMRI data acquisition: 1000 volumes (TRs (repetition time)) per run, in-plane matrix of 64×64, 16 axial slices covering the entire cerebral cortex, field of view (FOV) =225×225 mm^2, flip angle (FA) =90°, TR/TE (echo time) =1000ms/29ms, in plane voxel size =3.5156×3.5156 mm^2, slice thickness 5mm with 1.25 mm gap. Preprocessing was performed using Data Processing Assistant for Resting-State fMRI software (DPARSF) [168] and included slice timing, rigid body registration to first functional image, normalization to MNI template with resampling to 2×2×2 mm^3 resolution, spatial smoothing with 4×4×4 mm^3 FWHM (full width at half magnitude) Gaussian kernel, 0.01~0.1 Hz band pass filtering, detrending of mean and linear trend, and regressing out of white matter (WM) and cerebrospinal fluid (CSF) signals as well as six motion parameters. Then, the 190-region version of the CC200 brain atlas [160] was used as the reference brain segmentation template. We extracted the mean time series from 164 cerebral regions for subsequent use (26 regions of the CC200 template belonging to the cerebellum were not considered because our field of view covered only the cerebrum; this was done in order to reduce the TR which would be beneficial for EC analysis).

5.2.2 Dynamic Effective Connectivity Model

Various techniques have been invented for eliciting static measure of effective connectivity, prevailing among which are dynamic causal modeling (DCM) [208], structural equation modeling (SEM) [214] and Granger causality [215, 216]. But, when it changes to dynamic situation, many methods fail to adapt themselves for dynamic version such as DCM and SEM. First this is because of the high computational demanding [217], and secondly, methods like

DCM and SEM are model based methods which require much *a priori* information, but this high volume of *a priori* information is impracticable to be estimated in a time-varying manner timely. By contrast, Granger causality is totally data driven, and does not impose such high computational complexity as for DCM and SEM, therefore it can be dynamically computed. On the other hand, we have segmentations of 164 regions over the whole brain, and it is impracticable to make *a priori* assumptions about underlying causal connections once for all regions. Thus, we adopted dynamic version of Granger causality to calculate whole brain EC dynamics.

To facilitate the derivation of formulae for dynamic Granger causality, we first illustrate the traditional static formulation of Granger causality. The Granger causality can be modeled on multivariate vector autoregressive (MVAR) process as shown below.

$$\boldsymbol{X}(t) = \boldsymbol{V} + \sum_{n=1}^{p} \boldsymbol{A}(n) \cdot \boldsymbol{X}(t-n) + \boldsymbol{E}(t) \tag{5.1}$$

Where $\boldsymbol{X}(t) = [x_1(t)\ x_2(t)\ \ldots\ x_k(t)]$, a vector autoregressive process including k individual univariate processes (in our scenario, k is 164), $\boldsymbol{V}$ is the intercept vector representing nonzero mean component, n denotes time lag and $\boldsymbol{A}(n)$ is corresponding model coefficient matrix, p is regressive order, and $\boldsymbol{E}(t)$ is the vector noise process. During preprocessing, the data was detrended such that $\boldsymbol{V}$ vanished. Then, the Granger causality (static version) representing direct causal influences from region i to region j is formulated as below.

$$D_{ij} = \sum_{n=1}^{p} [a_{ij}(n)]^2 \tag{5.2}$$

Where each a_{ij}, i, j=1: k, is one entry of matrix $\boldsymbol{A}$ which is determined in the least square sense. The order p of this MVAR model is determined by Bayesian Information Criterion (BIC) [170]. For estimation of EC in a time-varying manner, we adopted dynamic Granger causality (DGC).

In this, the coefficient matrix ***A*** is allowed to vary over time. Such a temporally adaptive MVAR model with ***X***(*t*) as input time series is shown below.

$$\boldsymbol{X}(t) = \boldsymbol{V}(t) + \sum_{n=1}^{p} \boldsymbol{A}(n,t) \cdot \boldsymbol{X}(t-n) + \boldsymbol{E}(t) \tag{5.3}$$

It is noteworthy that coefficient matrix ***A***(*n*,*t*) is now a function of both lag *n* and time *t*, and can be updated with Kalman filter [218]. The DGC metric is then given by

$$DGC_{ij}(t) = \sum_{n=1}^{p} [a_{ij}(n,t)]^2 \tag{5.4}$$

The model order is determined by BIC. A forgetting factor (*FF*) is introduced in order to take recent past Kalman filter estimate into account of current estimation to enhance stability. The determination of forgetting factor is accomplished by minimizing the variance of estimated error energy [207] [219].

$$FF = \arg\{\min(\text{var}(\,\hat{\boldsymbol{E}}(t)^2)\} \tag{5.5}$$

Where $\hat{\boldsymbol{E}}(t)$ is the estimate of ***E***(*t*) and “var” is the variance operation over time.

In order to estimate a reasonable initial condition for the Kalman filter we used the following procedure. The Kalman filter coefficients were randomly initialized and updated coefficients were obtained from the first run of the first subject which were in turn used as initial conditions for the following run/subject. Using this procedure iteratively, Kalman coefficients which were updated using the entire subject group were obtained. This represented Kalman coefficients of the entire group as a whole. This group value was used as the initial condition for all runs/subjects and DGC values were re-estimated at the individual subject level. This procedure ensured that for each subject, the Kalman filter coefficients were initialized to the same value which was representative of the group average, to help achieving a quick convergence. However, the DGCs obtained from the first 50 time points were discarded before being input into the clustering algorithm for the following reasons. First, initial time points in fMRI time series are routinely discarded to allow the MR signal to achieve T1 equilibration. Second, even with group-averaged Kalman coefficients as the starting condition, the Kalman filter needed time to converge to ground truth connectivity.

5.2.3 Clustering

The DGC matrix calculated via above procedures was of size A×A×B×C where A=164, counting of cerebral regions, B=950, the number of TRs in dynamic Granger causality calculation (each run had a total of 1000 TRs, first 50 TRs discarded), and C=21, the number of runs over all subjects. So, for each run, at each time instant, the EC between all pairs of regions had a dimension of A×A. This DGC matrix was then fed into AEC algorithm [150]. This algorithm dynamically adaptively clustered all 164 regions according to their distances (the distances were transformed from the EC metric, see next section: First level clustering) at every time instant. Likewise, a forgetting factor was introduced to control the impact of recent past of clustering result on current calculation, with the purpose of enhancing stability of clustering operation. This clustering is termed first level clustering in the following. The first level clustering result was time-varying brain network configurations which were then fed to second level clustering as members. Through second level clustering, similar configurations at the first level were clustered forming a “pattern”. So through second level clustering, several patterns were resulted reflecting the distribution and consistency of the integrity of first level configurations for a given run. Last but not the least, the dominating second level patterns from all runs were identified and used as members for the third level clustering. Resultantly, by the third level clustering the dominant and consistent brain EC network patterns across all runs and subjects were identified.

First level clustering

The first level clustering was implemented using the AEC algorithm employing a distance measure computed from the DGC matrix. A reasonable assumption is that the higher the absolute value of DGC, the closer the two regions are in feature space. Note that we did not differentiate between positive and negative DGC influences since the neuronal underpinnings of their sign are yet unclear. Also noteworthy is that the DGC values between regions cannot be utilized directly as distances between regions for clustering. We know that the distance is inversely proportional to the closeness between regions, but the DGC metric (magnitude) is proportional to the closeness. Next, distance measure is greater or equal to zero, being zero only when it is measured from one region to itself. However, DGC metrics have both positive and negative values, and the diagonal entries of DGC matrix measuring auto-DGC are not zeros. Moreover, DGC matrices are not symmetric, i.e. the distance from one region to another is not equal to the other way around, violating the condition of reciprocity required of any distance measure.

In order to convert DGC values into distance measure, we devised a transformation algorithm as described below. We represent the DGC from region i to region j by DGC_{ij}, and the other way around is DGC_{ji}. DGC is transformed as shown below to meet the nonnegative and reciprocity requirements.

$$C = (|DGC_{ij}|^m + |DGC_{ji}|^m)^{1/n} \tag{5.6}$$

Where m and n determine the characteristics of this transformation. According to Eq.5.6, C will increase along with the increase of either DGC_{ij} or DGC_{ji}. We chose m=2 and n=1 in this work, as such is usually employed for second order matrix norm. If n is relatively big compared to m, then C would not be sensitive to the change of DGC, thus cannot distinguish significant connectivity from trivial one. If m is relatively big compared to n, the result will be sensitive to noise. Next, we used a reversed “S” shaped function applied to C to meet the requirement of a monotonically decreasing transformation:

$$D = \frac{1}{a + b \cdot f^{C}} \tag{5.7}$$

Where a, b, f are control parameters determining the behavior of this function. After this transformation, the significant connectivity between two regions is highlighted while non-significant ones are not. In order to find the boundary between significant and insignificant connectivities, we employed the method of surrogate data [210] [220]. Specifically, we transformed the time series to their frequency domain representation, randomized the phase of time series from all 164 regions in the frequency domain with magnitude unchanged, reconverted the phase-randomized data into time domain signals, and then the DGC was recalculated. Since the temporal structure of time series relative to each other was destructed, the DGCs obtained belonged to a null distribution of no influence between regions. After this procedure was repeated in a Monte Carlo manner (1000 times) a statistical null distribution of insignificant DGCs was obtained. Then we applied Eq.5.6 to get the null distribution of C and found the threshold at 95th percentile, denoted by th_0. It is obvious that parameter a just controls the scaling of D, thus is trivial, and hence we set it to 1 for normalization. In this way, D can attain its maximum at $1/(1+b)$ and minimum at around 0. Assume b is sufficiently small such that the maximal value that D can reach is nearly 1. Then it is reasonable to let D be 0.5 when C is equal to th_0, and when C approaches 0, D is approximate 1 adequately with low steepness. With surrogate data, we found th_0 to be equal to 0.01. To find b, we restricted D to be no less than 0.8 and steepness to be less than 0.02 when C is 0. So, when D=0.8, steepness is 0.02 when C is 0, we calculated b to be 0.2, and f as 5^{100} which were used subsequently. Above sigmoid curve design aims to balance the separation of null and significant connectivities, and sensitivity to noise. The sigmoid curve design and parameters determination have been widely applied in many fields [221] [222]. After the transformation of Eq.5.7, we let the Ds which were from one region to itself be zero, resulting in the final distance measure D_{final}. Then matrix D_{final} at each time point was fed into the AEC algorithm [150]. In AEC, the clustering method was chosen to be hierarchical [171].

The number of clusters can be chosen either based on prior information about the neurophysiological system being investigated (which is preferable when that information is available) or based on mathematical criteria such as the silhouette index [172] (which is preferable when no *a priori* heuristics are available). Many previous studies have reported on the appropriate number of clusters, or in other words, the number of resting state networks (RSNs). To derive an eloquent result, various methods have been tried. The most representative ones are ICA based methods. In particular, PICA (probabilistic ICA) [174] and tensor PICA [175] are variants of ICA which attract a lot of attention recently. Operating at a grand scale, fully exploratory network ICA (FENICA) [177] [178] [179] [223] is best to find consistent networks among a group which may include thousands of subjects. Besides, fuzzy clustering [173] and graph theory [176] are also two prevailing methods to find the number of RSNs with their own merits. Except a few studies which employ task-related data [223], most studies focus on resting state fMRI data. However, these findings are in terms of FC, and corresponding EC results are very sparse. A data-driven pilot study conducted by Wu *et al* [213], reported 6 communities from resting state EC networks. Therefore, we used 6 as the number of clusters at first level clustering. Also, we assume that EC networks are hierarchically organized, similar to FC networks [179] [173]. Accordingly, if the specified number of networks or clusters increases, some networks will split into sub-networks, such as into left and right lateral parts, rather than reshape into a new set of networks which has no relation with the previous one. Based on this assumption, if the number of networks/clusters is heuristically specified to be 6, it will not lead to loss of generality.

Second level clustering

We performed second level clustering for characterizing the consistently recurring first-level configurations over time. This aided us to answer the question about whether there exists finite number of directional brain network patterns which consistently recur in time at an individual subject level. The difference from first level clustering is that this is a static clustering along the time axis. Hierarchical method was employed as the clustering method, and the number of clusters was determined by silhouette criterion in the absence of prior heuristics.

The calculation for the distance measure, between first level clustering configurations at two different time instants is the same as in Chapter 4. Please refer to Section 4.2.4 in Chapter 4 for details.

The result from second level clustering is a number of clusters with first level clustering configurations as their members. Each second level cluster can be represented by its centroid but the theoretical centroid would be a weighted sum of first level clustering configurations such that each region in this sum has fuzzy belongingness to each first level cluster. To address this issue, Chapter 4 uses second level centroid agent to represent the theoretical centroid (Eq.4.2 in Chapter 4). In this work, the same strategy was adopted.

Third level clustering

The second level clustering gave clustered patterns over time for each run. The dominating second level patterns/clusters were predicated based on the histogram of second level clusters' occurrence times. Here the occurrence times is formulated as follows. For each run, each second level cluster covered a number of first level clustering configurations, the number of which was the times this second level cluster “occurred”, so was defined as occurrence times for this second level cluster. The histogram mentioned above was calculated over second level clusters from all runs. The threshold separating dominating and non-dominating clusters was determined as follows. The point where the histogram value first hit zero and the first order derivative was also zero was set as the threshold. Then this threshold was found to be at 95 (occurrence times). There was clearly a gap encompassing 95, and the majority of second level clusters had occurrence times less than 95, while beyond 95, second level clusters were relatively scarce and mainly distributed over the range: 100-200, 270-360, and 450-850, clearly indicating they were dominant clusters. In order to assess the consistency of these dominating patterns across subjects, we performed the third level clustering.

The strategy used to calculate the distance measure between dominating second level centroid agents was the same as for FC in Chapter 4. Also, the weighted K-means was employed for clustering at the third level. Same as second level, the number of clusters were optimized using silhouette criterion, and each third level cluster theoretical centroid was represented by its agent since the regions in theoretical centroid had fuzzy memberships to dominating second level clusters. The agent had smallest Euclidean distance to the theoretical centroid in terms of distance matrix. Above three-level clustering procedure for dynamic EC is illustrated in Fig.5.2.

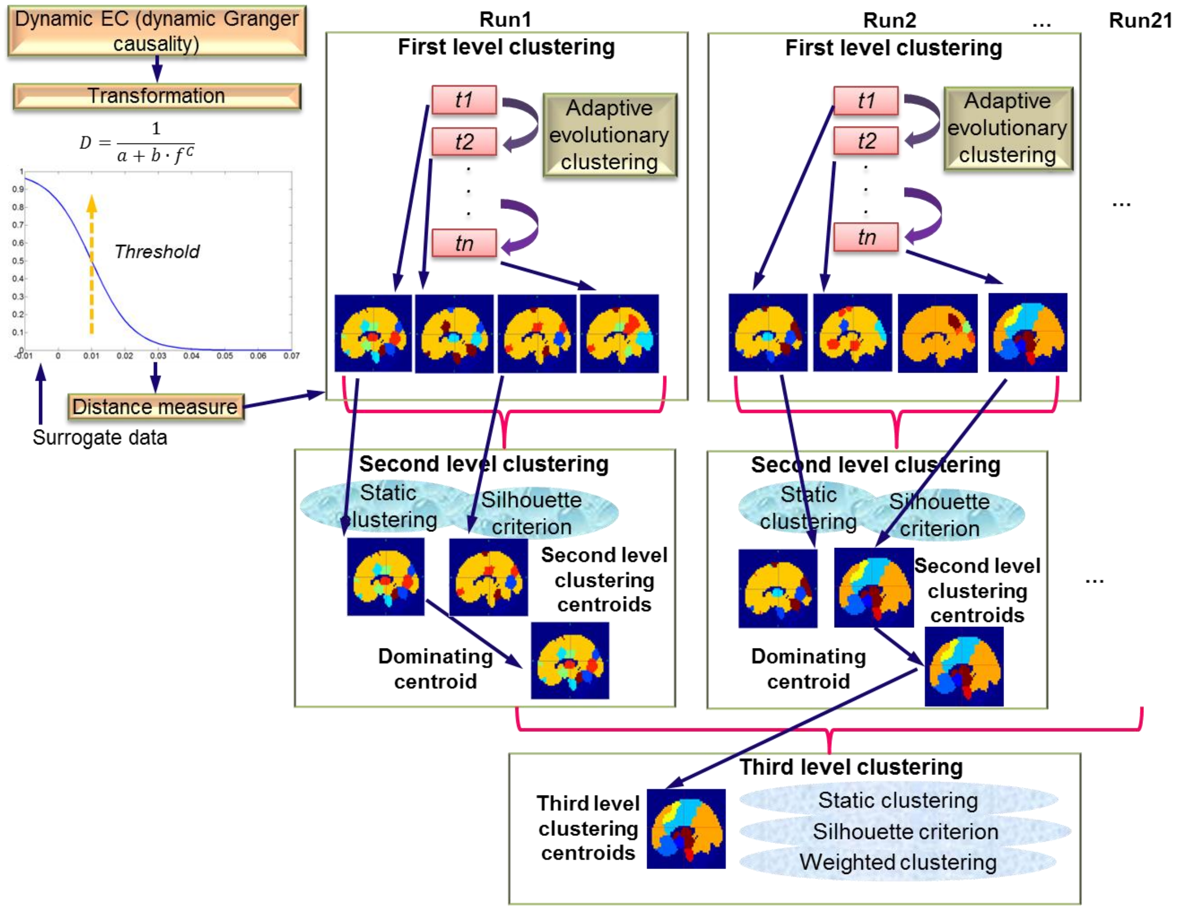

Figure 5.2 Schematic of the three-level clustering procedure for EC. The top left part shows the transformation of dynamic EC measure (DGC) to a distance measure. The top right part shows first level clustering, below which, second and third level clustering are illustrated.

5.2.4 Potential Correlates with Real World Functionalities

Through the third level clustering, the brain EC network patterns which were dominant and consistent across all subjects were obtained. To interpret the connotation of these patterns, we related them to real world cognitive functionalities using Brainmap Sleuth search engine [224]. Specifically, for a given third level centroid agent, the 164 regions inside the cerebrum were divided into 6 clusters as mentioned before. It should be noted that one of the 6 clusters (networks) was trivial because it included all other brain regions which were not present in the 5 other clusters. This is because clustering algorithm partitions all members exhaustively. If the 5 networks are definitive networks, the 6th one will include every other member not inside the 5 networks. The trivial cluster can be separated from 5 other networks by visual inspection since it embodies the most regions. As such, for each of the 5 definitive networks, we used the set of regions it included as input to Brainmap Sleuth search engine to find literatures that found involvement of these regions in certain kinds of cognitive functionalities. In this way, the correlates between these networks and real world cognitive functionalities were established.

5.2.5 Simulation Setup

Simulations were performed in order to validate the proposed method for calculating DGC and the efficacy of subsequent clustering using the AEC algorithm. We simulated time series with a total length of 1000 time points from 12 regions using an autoregressive model as given below:

$$\boldsymbol{V}(t) = \sum_{i=1}^{p} A_i \cdot \boldsymbol{V}(t-i) + \boldsymbol{\varepsilon} \tag{5.8}$$

Where $\boldsymbol{V}(t)$ denotes the vector of signals from multiple regions, $\boldsymbol{A}_i$ is the regression coefficient matrix, and $\boldsymbol{\varepsilon}$ represents noise term with covariance matrix $\boldsymbol{C}$, which has autocorrelation coefficients set to 1 for normalization. The order p was chosen to be 1. Three scenarios were used:

(i) $\boldsymbol{C}$ was identity matrix and did not change over time so as to remove the effect of instantaneous correlation, i.e. FC part. 12 time series were divided into 4 clusters each having 3 members (region1, 2, 3 were in one cluster, region4, 5, 6 were in one cluster, region 7, 8, 9 were in one cluster, and region 10, 11, 12 were in one cluster). Thus, $\boldsymbol{A}_1$ had block structure with 3×3 blocks on the diagonal, but constant over time. Each non-zero element in $\boldsymbol{A}_1$ was selected such that $\boldsymbol{A}_1$ had all eigenvalues within unit circle and all diagonal terms being negative, so that the simulated time series were stable and power spectral energy was concentrated in the low frequency band, in accordance with the fact that the signal of interest in fMRI lies in the low frequency band.

(ii) Same as first scenario, but each non-zero element in $\boldsymbol{A}_1$ was slowly varying over time sinusoidally with period equal to 200π and randomized phases. The scope of this variation was limited to guarantee the stability of each time series. The belongingness of each region was the same as (i).

(iii) Same as first scenario but after every 200 time points, $\boldsymbol{A}_1$ was circularly shifted by one column and one row to change the cluster belongingness of each region. Specifically, from time point 1 to 200, regions 1, 2, 3 belonged to the same cluster (i.e. they were connected to each other), regions 4, 5, 6 belonged to the same cluster, and so on. Then from time point 201 to 400, regions 2, 3, 4 belonged to the same cluster, regions 5, 6, 7 belonged to the same cluster… and regions 11, 12, 1 belonged to the same cluster. Then from time point 401-600, region 3, 4, 5 belonged to the same cluster, and so on.

It should be noted that in the simulation, the DGCs calculated for all time points were used in AEC algorithm, as illustrated in Fig.5.3. However for real fMRI data, initial 50 time points were discarded for calculation of DGCs and the Kalman filter initial condition was calculated by running over all runs, rather than released condition as in the simulation. Both of these concerns were for a better tracking performance of DGC.

For each scenario listed above, the simulation was conducted 1000 times to get a group of simulated MVAR processes, and then the statistics of the DGCs were obtained.

5.3 Results

5.3.1 Simulation Result

The simulation results are shown in Fig.5.3. In each subfigure of Fig.5.3, the simulated ground truth of DGCs are shown on the left and the estimated DGCs using the dynamic MVAR model employed in this work are shown on the right. The estimated DGCs converge to the ground truth quickly, and suitably respond to dynamic variations in ground truth DGC as shown in subfigure (B) and (C). Also, the regions belonging to different clusters have nearly zero causality, such as region1→region12 in subfigure (A) and region4→region8 in subfigure (B), indicating no false positives. The standard deviations of estimated DGCs over all instantiations of the MVAR process are modest, indicating good fidelity. Subfigure (D) presents a representative realization of first level clustering using AEC algorithm for simulated DGCs in scenario (iii). Along the time axis, regions rendered the same color belong to the same cluster. It can be seen that in subfigure (D), the AEC first level clustering clearly separates the 12 regions into clusters with correct memberships in a time-varying manner (maybe with very short transitions). In summary, the simulations demonstrate that the proposed DGC model qualifies for tracking true dynamic ECs, and the true time-varying clustering patterns can be reliably reproduced by the AEC algorithm.

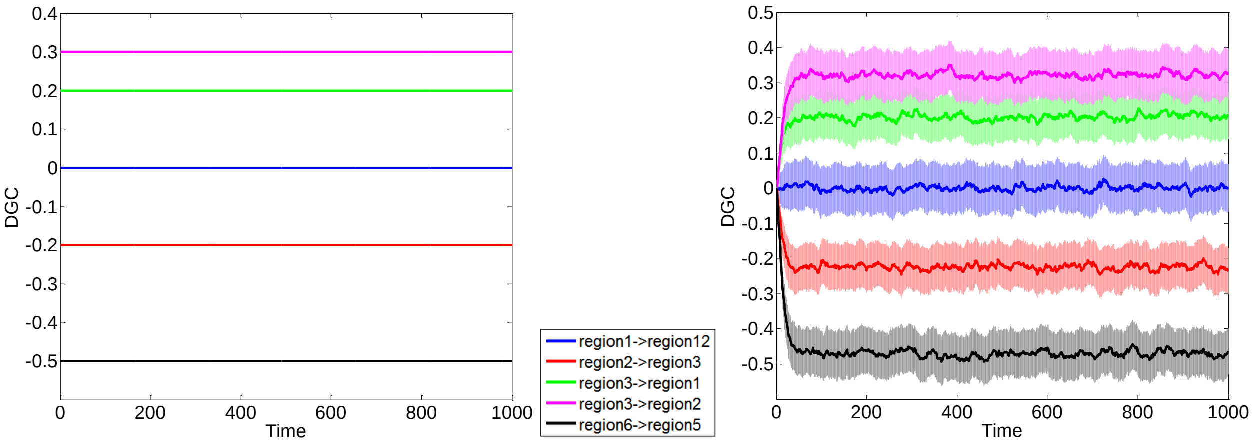

(A)

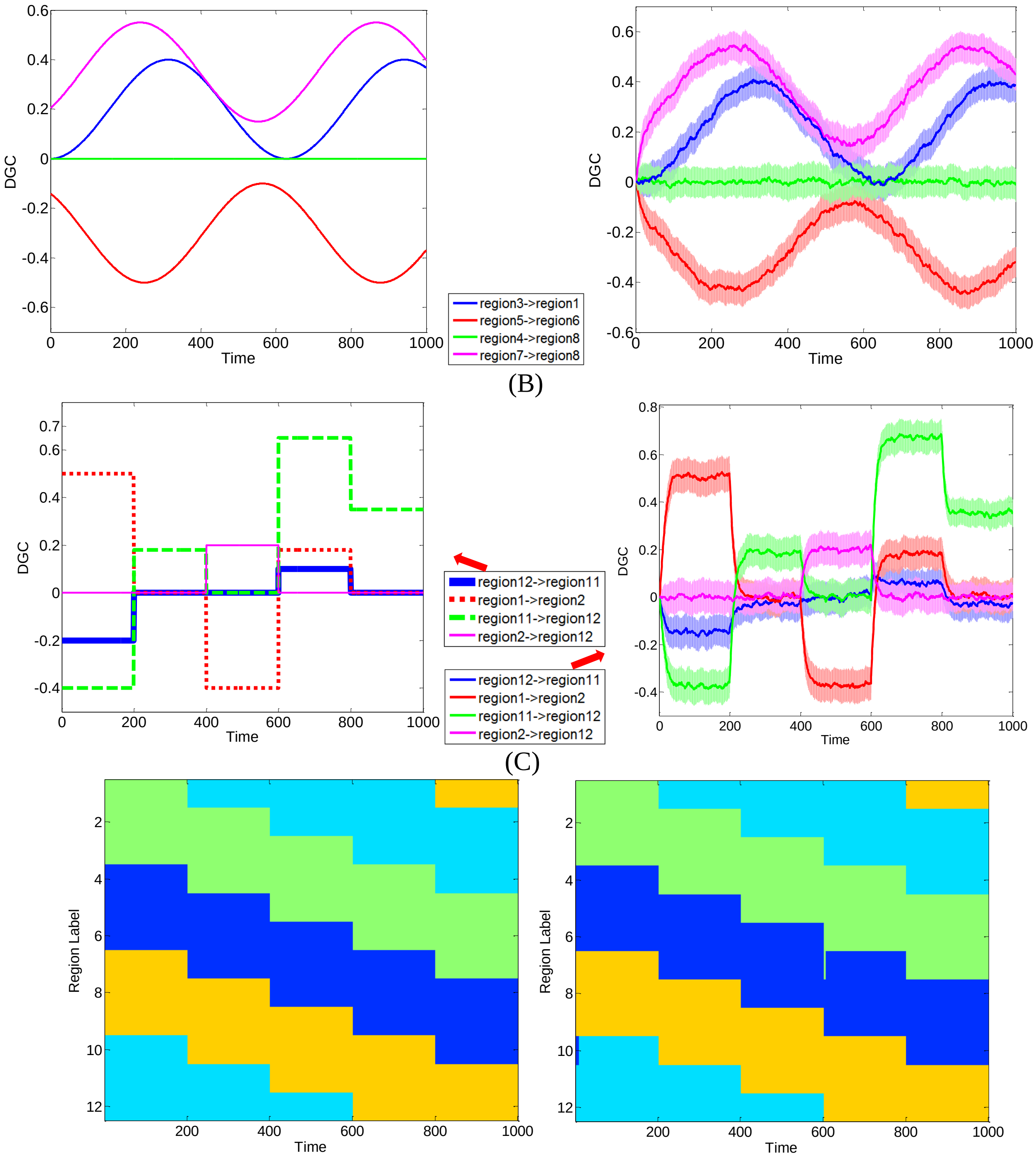

(B)

(C)

(D)

Figure 5.3 Exemplary simulation result for dynamic Granger causality and first level AEC clustering. MVAR processes of 12 regions were simulated, with a length of 1000 time points. Three scenarios were used to corroborate the validity of formulated DGC. Exemplary ground truth causality of scenario (i) is shown in subfigure (A) left, and corresponding mean ± standard deviation (std) of calculated DGCs is shown at right. Color bands extend from mean-std to mean+std with mean values at the center. Below is same. Exemplary ground truth causality of scenario (ii) is shown in subfigure (B) left, and corresponding mean ± standard deviation (std) of calculated DGCs is shown at right. Exemplary ground truth causality of scenario (iii) is shown in subfigure (C) left, and corresponding mean ± standard deviation (std) of calculated DGCs is shown at right. Exemplary ground truth clustering pattern corresponding to scenario (iii) is shown in subfigure (D) left and corresponding clustering result estimated using AEC algorithm is shown at right. Regions rendered the same color belong to the same cluster.

5.3.2 Experimental Data Result

We estimated the DGC metric for each run of pre-processed resting state fMRI data and fed it into the three-level clustering algorithm. The results are shown in Figs.5.4, 5.5, 5.6 and relevant statistics are summarized in Tables 5.1 and 5.2. Fig.5.4 presents exemplary second level clustering patterns along the time axis. Different colors represent different clusters. The numbers of second level clusters from the top bar to the bottom bar in Fig.5.4 are 10, 6, 6, 10, 11 and 11. These numbers are representative numbers of second level clusters, as reflected in Table 5.1. Please note the same colors in different runs do not mean they are of the same pattern. Table 5.1 presents corresponding second level clustering statistics for all fMRI runs. By visual inspection, it is clear that there exist 1-3 dominant clusters at the second level. Critically, we can observe features similar to quasi-stability in Fig.5.4, i.e. each dominant pattern lasts for a period of time, during which it may swiftly switch to a few non-dominant patterns and switch back, and then switches to another dominant pattern. Certainly, dominant patterns last longer than non-dominant patterns, as expected.

Table 1 also conveys information about the number of second level clusters for each subject and the time spent before state (pattern) transition. Normally, the larger the number of clusters, the smaller the mean time (and its standard deviation) spent before a state transition. Their relationship is illustrated in Fig.5.5 using linear regression. The regression of mean time spent before state transition with respect to number of clusters is shown in Fig.5.5 (A), and corresponding results for standard deviation of time spent before state transition is shown in Fig.5.5 (B).

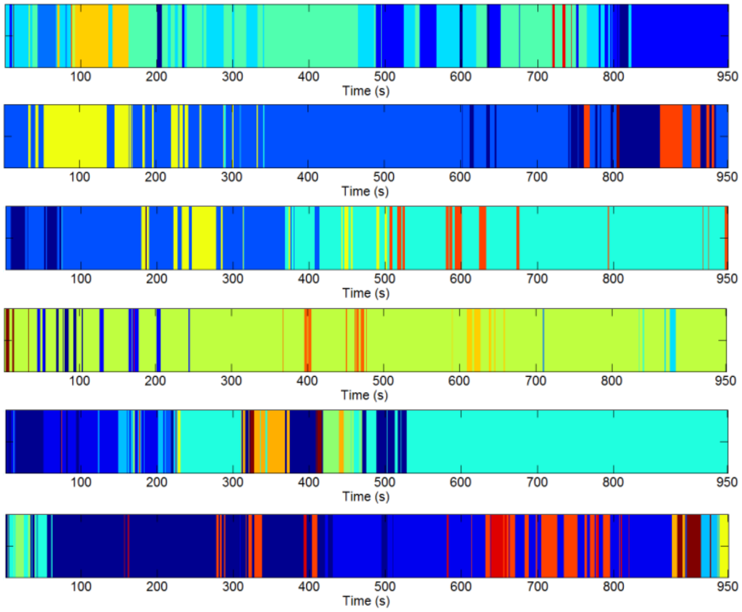

Figure 5.4 Exemplary second level clustering patterns over time axis from six runs. Along each bar, each color represents one second level cluster and the time instants it occupies indicate the first-level configurations at these time instants belong to it. Different colors represent different second-level clusters. The number of second level clusters for each bar is 10, 6, 6, 10, 11 and 11 (from top to bottom). Please note the same colors in different runs do not mean they are of the same pattern.

Table 5.1 Summary of statistical characteristics of second level clusters

Subject	No. of clusters	Time spent (s) before any state transition (mean ±standard deviation)	Time spent (s) in each cluster (descending)
#1	11	9.79 ±18.65	350, 329, 116, 33, 31, 28, 22, 17, 13, 10, 1
#2	7	35.19 ±67.08	777, 69, 60, 26, 13, 4, 1
#3	16	16.18 ±21.62	456, 172, 79, 69, 62, 27, 22, 19, 11, 10, 6, 4, 4, 3, 3, 3
#4	4	30.65 ±105.84	732, 179, 24, 15
#5	12	11.59 ±18.61	348, 307, 112, 70, 68, 16, 8, 8, 5, 4, 2, 2
#6	7	15.57 ±36.98	775, 135, 24, 9, 3, 2, 2
#7	6	13.97 ±34.38	636, 143, 105, 57, 5, 4

#8	15	13.19±30.04	662, 78, 59, 56, 23, 19, 18, 11, 9, 7, 4, 1, 1, 1, 1
#9	14	10.92±14.45	294, 149, 132, 85, 81, 65, 53, 49, 14, 12, 9, 5, 1, 1
#10	10	12.18±20.94	369, 226, 220, 68, 26, 25, 8, 6, 1, 1
#11	7	24.36±43.06	591, 196, 112, 26, 20, 4, 1
#12	6	13.57±24.68	506, 277, 77, 51, 38, 1
#13	15	7.98±11.36	574, 147, 47, 39, 36, 34, 15, 15, 15, 12, 5, 5, 3, 2, 1
#14	11	12.18±48.36	534, 140, 123, 53, 38, 36, 12, 7, 4, 2, 1
#15	16	10.78±19.03	346, 296, 147, 65, 42, 11, 11, 5, 5, 5, 4, 3, 3, 3, 2, 2
#16	10	13.19±25.68	839, 29, 23, 21, 16, 9, 8, 3, 1, 1
#17	5	45.24±101.86	851, 74, 15, 9, 1
#18	14	10.88±12.97	476, 116, 108, 96, 52, 34, 26, 11, 7, 6, 5, 5, 4, 4
#19	12	11.88±22.20	659, 169, 25, 22, 15, 13, 13, 12, 8, 7, 6, 1
#20	9	27.14±70.18	813, 84, 20, 17, 7, 4, 2, 2, 1
#21	10	25.00±44.62	582, 326, 13, 11, 6, 4, 3, 2, 2, 1
Summary (Mean±standard deviation)	10.52±4.05	13.47±35.95	90.27±177.96

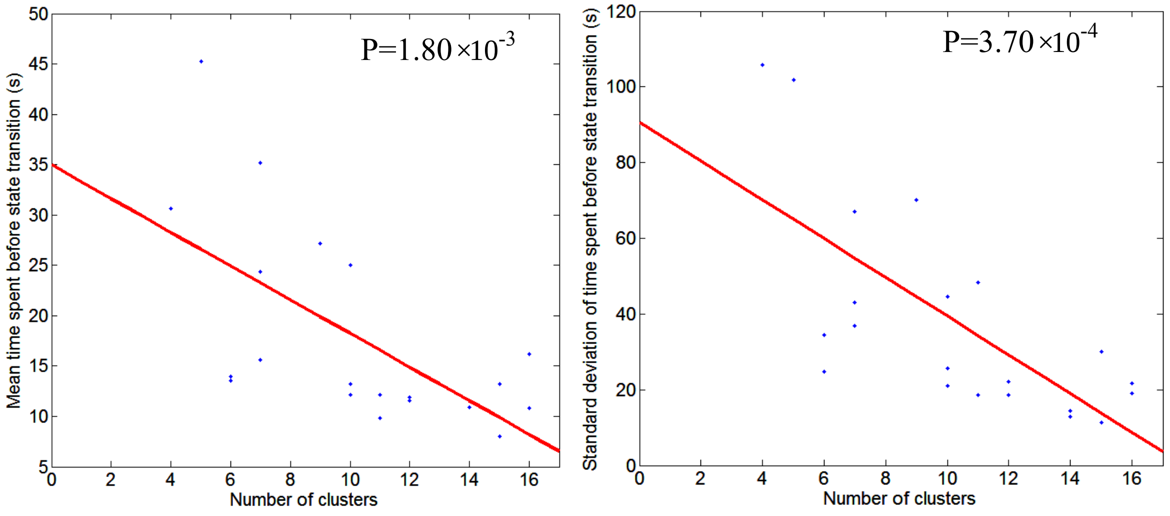

(A) (B)

Figure 5.5 Illustration of regression of mean/std of time spent before state transition with regard to number of second level clusters. (A) is for mean time spent before state transition and (B) is for standard deviation of time spent before state transition. Regression line is shown in red, and scattered dots represent data points from 21 resting state runs.

The result for third level clustering is illustrated in Fig.5.6 and Table 5.2, and potential neural correlates of those connectivity patterns to real world functionalities is depicted in Fig.5.7. At the third level, 7 clusters were found from all dominating second level clusters obtained from all subjects, but only the 4th cluster was dominant and consistent across all subjects (see Table 5.2). Fig.5.6 visualizes the 5 first level clusters which make up the centroid of the 4th third level cluster. It is noted that at the first level, the number of clusters was set to 6, and one of those clusters (networks) was trivial because it included all other brain regions which were not present in the 5 other clusters. This happened because clustering partitioned the input space, and if there were 5 definitive clusters, the 6th cluster would include everything that was excluded from the 5 clusters. In Fig.5.6, green dots represent the centers of the functionally homogeneous CC200 regions under consideration, and arrowed paths represent directional connectivities between regions with thickness and color indicating the absolute connectivity value. Network #1 in Fig.5.6 (A) illustrates directional causal influences among right mid temporal area, left calcarine, left postcentral and left inferior temporal area, as well as pons and left superior orbital frontal area. According to activation likelihood estimation (ALE) based meta-analyses using the BrainMap database these regions are co-activated by emotional stimuli [225], language processing [226], working memory [227], spatial information processing [228]. Network #2 in Fig.5.6 (B) involves supplementary motor area (SMA), postcentral area, supramarginal area, mid temporal area, and thalamus in the right hemisphere, and insula, mid and inferior temporal area, precentral area in the left hemisphere. These regions are mostly distributed in parietal lobe, temporal lobe, as well as limbic lobe. According to ALE based meta-analyses using BrainMap, the co-activation of most of these regions is due to interoception [229] [196], working memory

[230], language [231], observation [229], execution [231], as well as emotion regulation [232] [233]. Besides the functionalities for areas above mentioned in network #1, the supplementary motor area and precentral area involve in movement control and execution [234]; insula involves in emotion, perception, motor control, self-awareness and interoception; postcentral area involves in tactile sense. Network #3 shown in Fig.5.6 (C) involves frontal middle area, inferior and mid temporal in the right hemisphere, and mid temporal area, caudate, inferior orbital frontal area in the left hemisphere. We can clearly see the temporal to caudate causal pass way and frontal to caudate causal pass way. Caudate nucleus has been demonstrated to highly involve in learning and memory [235], particularly regarding feedback processing (rewarding and motivation) [187], as well as emotion [236] [237]. Together with temporal area and frontal area, these two pass ways indicate several functionalities using Brainmap Sleuth: memory [238]; execution, emotion [239]; social cognition [240]. Network #4 as in subfigure (D) includes inferior parietal area, caudate, rectus, superior frontal area in the right hemisphere, as well as left inferior temporal area. Rectal gyrus has been linked to attention and memory processing [241]. Inferior parietal lobule involves in interpretation of sensory input and perception of emotions. By using Brainmap Sleuth, the co-activation of most these areas involves in functionalities of execution [242], memory [243], visual and somesthesis perception [244] and language processing [226] [245]. Lastly, Network #5 in subfigure (E) involves left SMA, left postcentral area, left supramarginal area, bilateral lingual gyrus, bilateral cuneus, superior bilateral occipital area, right fusiform, right inferior orbital & opercular frontal area, left parahippocampus gyrus, part of vermis and left thalamus. Using Brainmap Sleuth, most of these areas are co-activated by emotion & social cognition [240], interoception & observation [229]. Fusiform, superior occipital area, cuneus relate to visual perception and processing, lingual gyrus participates in

visual processing and visual memory encoding, supramaginal relates to language processing, and postcentral area and parahippocampal gyrus relate to memory encoding and retrieval.

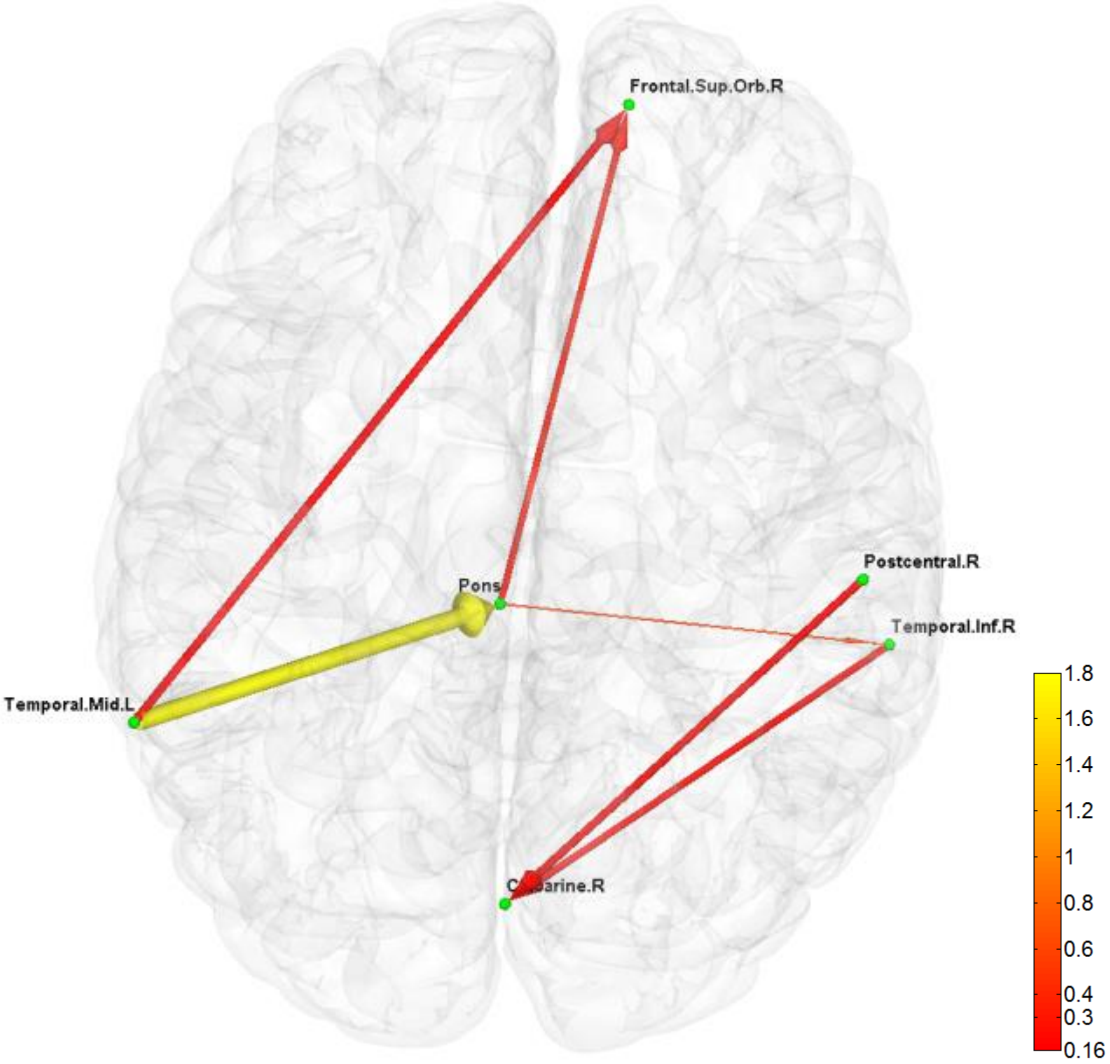

(A)

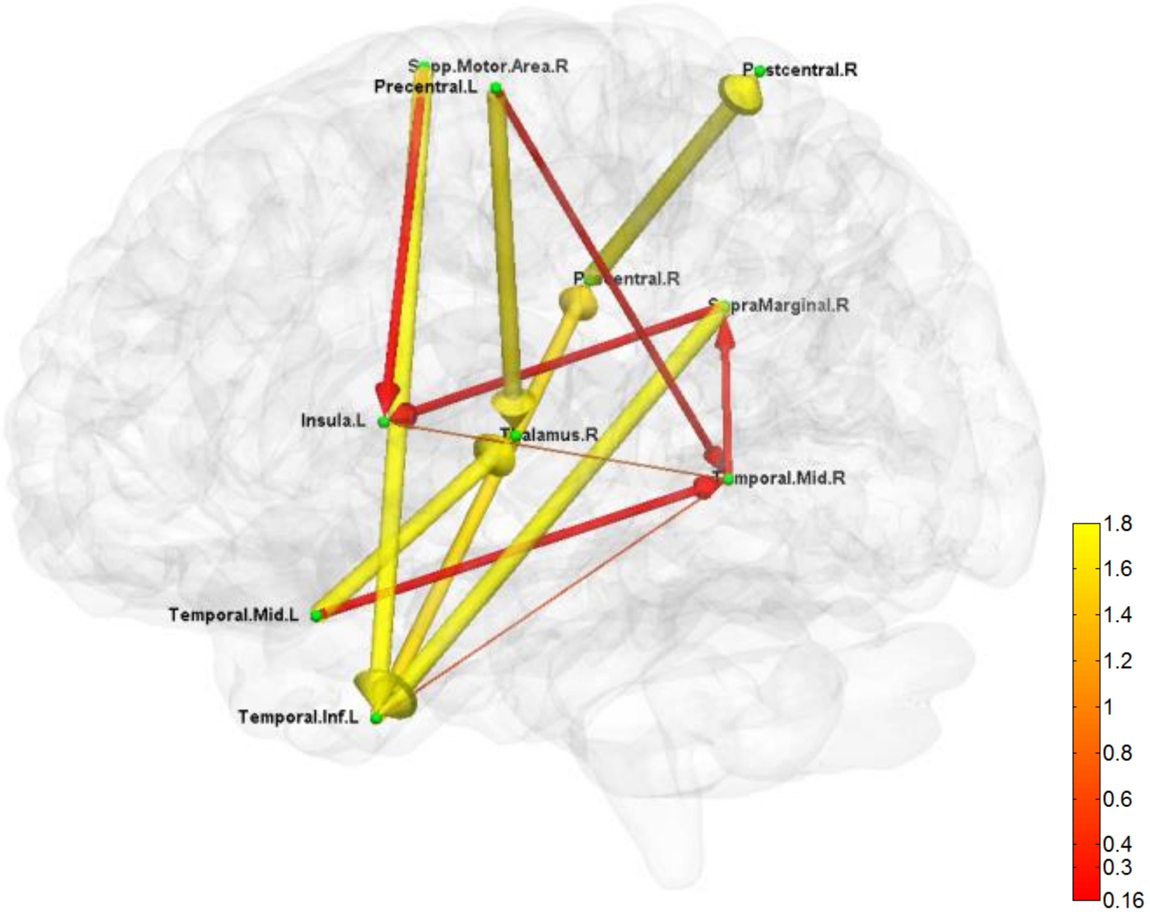
Supp.Motor.Area.R
Precentral.L
Postcentral.R
Precentral.R
SupraMarginal.R
Insula.L
Thalamus.R
Temporal.Mid.R
Temporal.Mid.L
Temporal.Inf.L
1.8
1.6
1.4
1.2
1
0.8
0.6
0.4
0.3
0.16

(B)

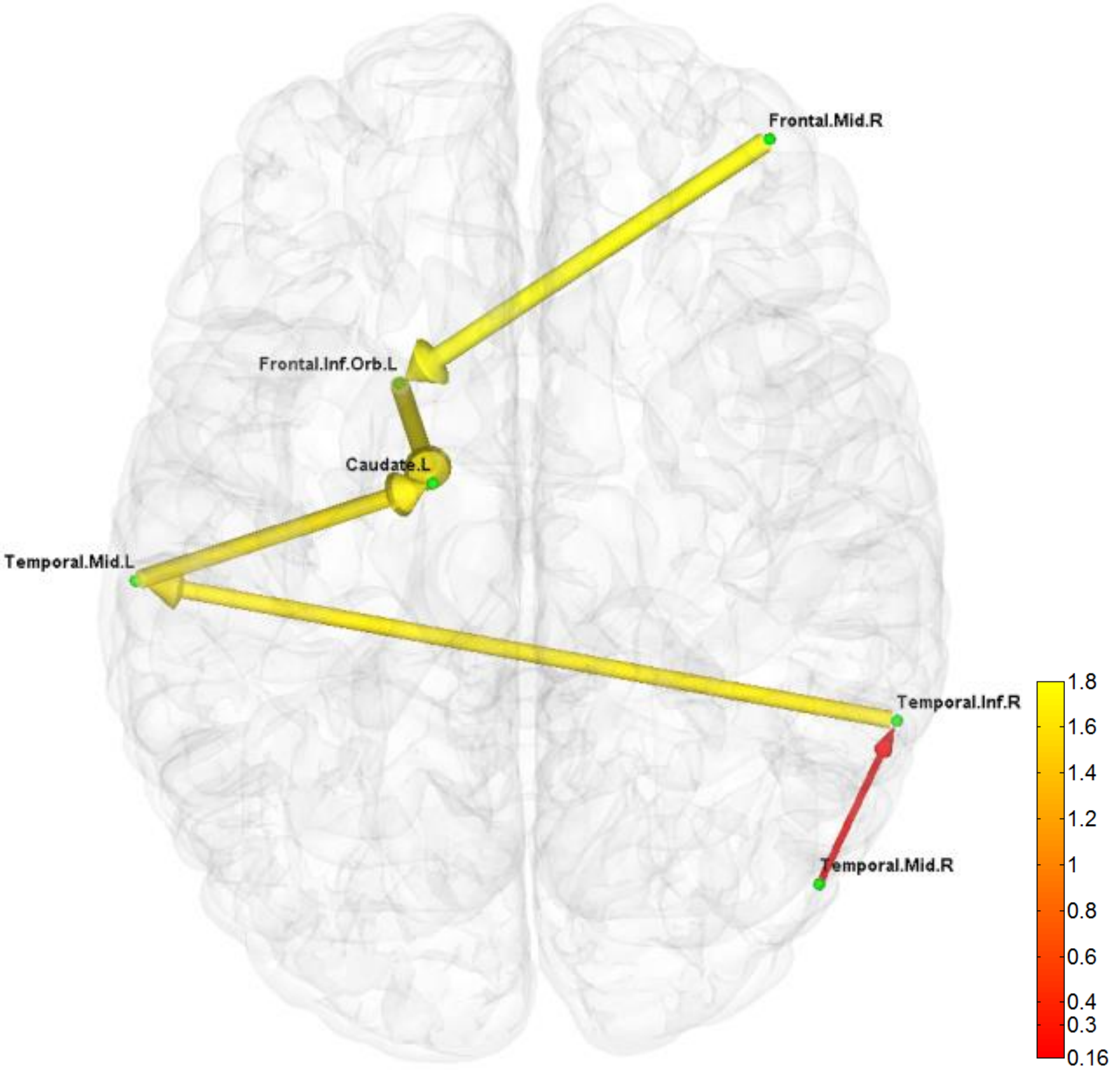
Frontal.Mid.R
Frontal.Inf.Orb.L
Caudate.L
Temporal.Mid.L
Temporal.Inf.R
Temporal.Mid.R
1.8
1.6
1.4
1.2
1
0.8
0.6
0.4
0.3
0.16

(C)

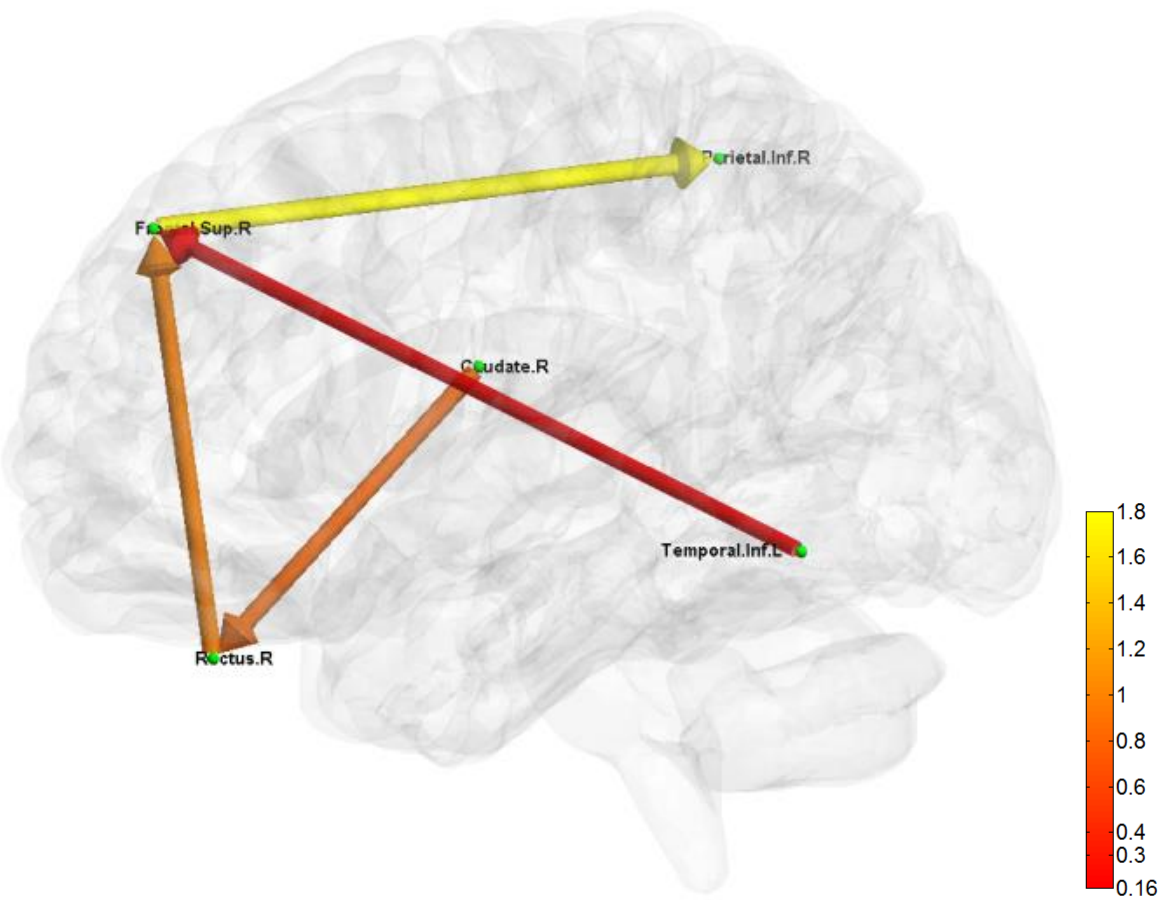
Parietal.Inf.R
Frontal.Sup.R
Caudate.R
Temporal.Inf.L
Rectus.R
1.8
1.6
1.4
1.2
1
0.8
0.6
0.4
0.3
0.16

(D)

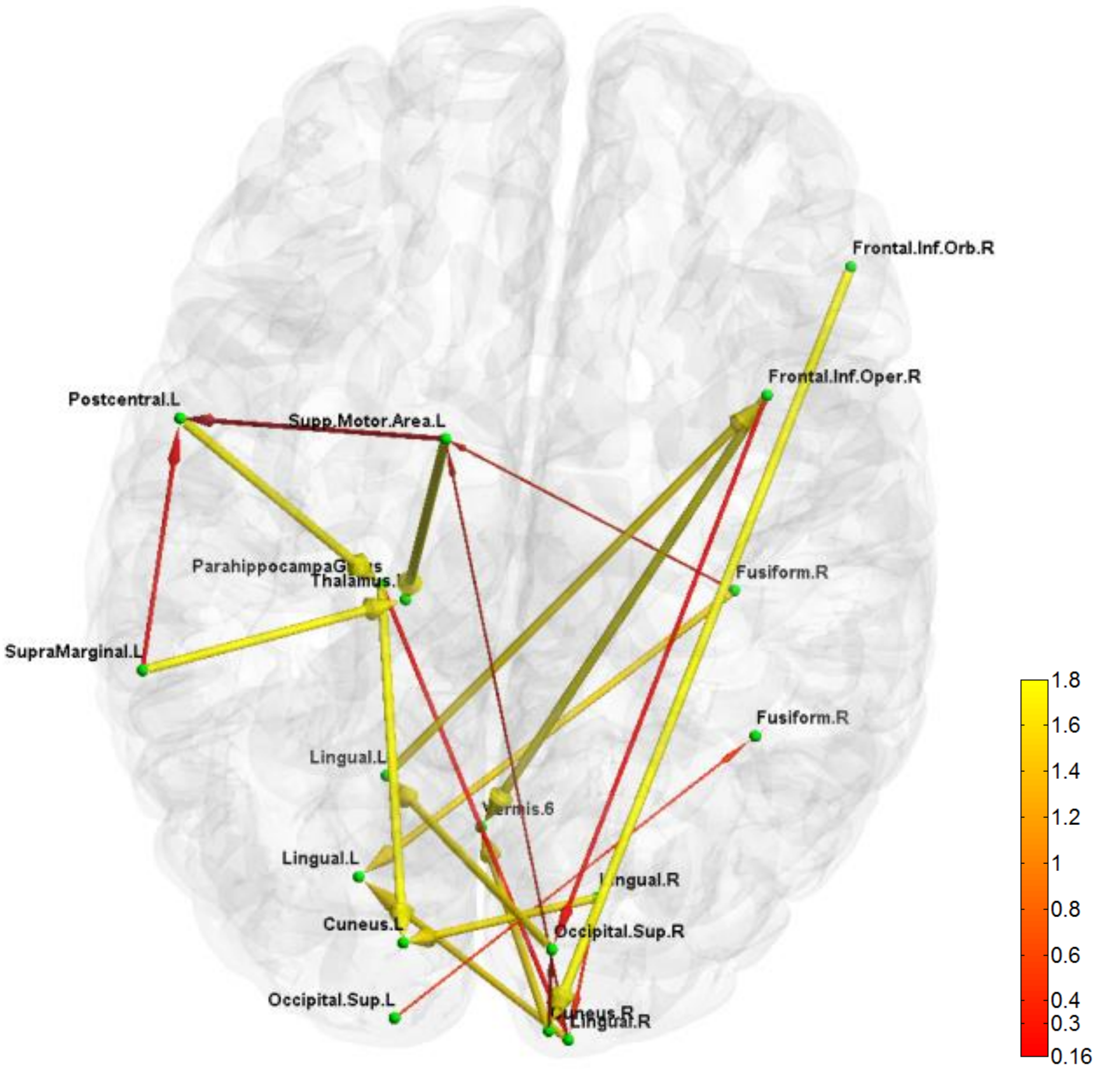

(E)

Figure 5.6 Five directional connectivity networks of the most reproducible third level clustering centroid. In each subfigure, green dots represent the centers of corresponding functionally homogeneous CC200 regions and arrowed paths represent directional connectivity between regions with thickness and color representing the absolute connectivity value. Autumn colormap is used with red indicating small value and yellow indicating big value.

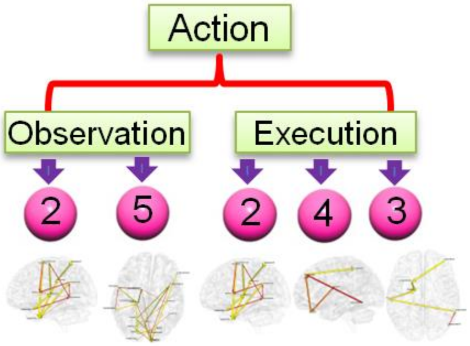
Action
Observation
Execution
2
5
2
4
3

(A)

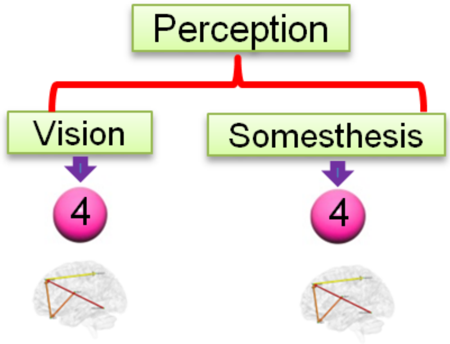
Perception
Vision
Somesthesis
4
4

(B)

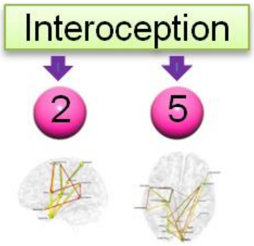
Interoception
2
5

(C)

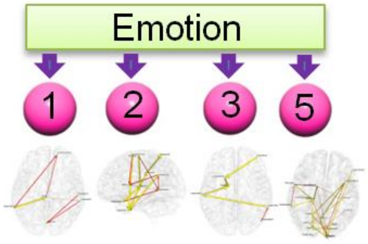
Emotion
1
2
3
5

(D)

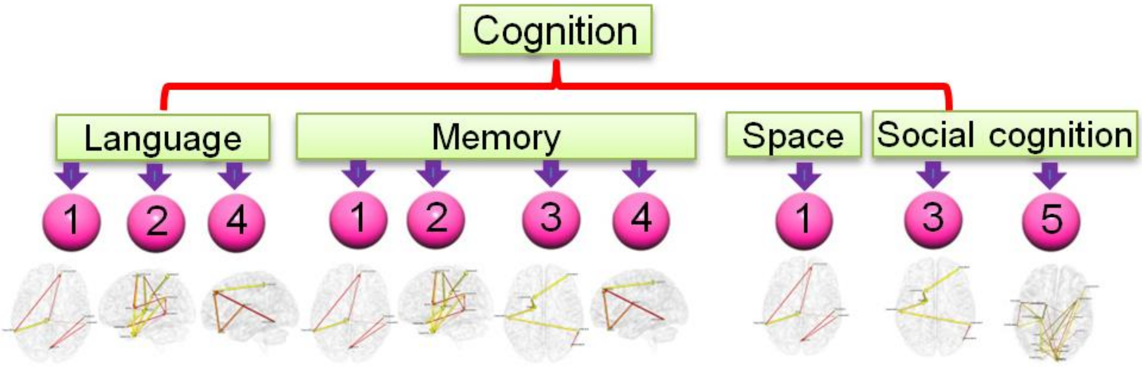

(E)

Figure 5.7 Functional relevance of the five networks obtained from the most consistent third level clustering centroid. The digits in pink balls mark the corresponding directional networks in Fig.5.6. The head nodes of networks indicate the functionality that co-activates the regions of corresponding networks as ascertained through activation likelihood estimation (ALE) based meta-analyses using the BrainMap database.(A) is for functionality of action; (B) is for perception; (C) is for interoception; (D) is for emotion; (E) is for cognition.

Table 5.2 Summary of number of members and total occurrence times for third level clusters

Cluster	Number of members (dominant 2nd level clustering patterns)	Total occurrence times (TRs)
#1	3	789
#2	3	899
#3	2	910
#4	31	11850
#5	4	796
#6	2	783
#7	2	721
Sum	47	16748

5.4 Discussion

We devised a method of three levels of clustering based on dynamic EC measure calculated through dynamic Granger causality as to find time-varying EC configurations, dominating and consistent EC patterns across all subjects, and the relation to real word functionalities. The major contributions of this work can be concluded into three aspects as below. First, to the best of our knowledge, this is the first time the dynamics, EC measure, clustering, and whole brain gray matter regions are put together to analyze human brain EC networks. We believe that the work reported here will serve as a seminal exploration of whole brain EC dynamics.

Second, the second level results showing the alternating brain EC network patterns feature one to three dominating patterns, and assume quasi-stable fractal-like property. This phenomenon means the second level clustering result over time has a hierarchical organization. A dominating pattern will dominate for a period of time and during this period, no other dominating patterns exist. After this period, another dominating pattern takes over. Within the period it dominates, there may appear several sub-patterns, and each sub-pattern will appear and alternate with the dominating one for only an episode of time, and after this time episode, another sub-pattern takes over. Then, under the sub-patterns, there may appear even smaller sub-patterns which behave similarly to the former sub-patterns, but at a finer scale. Previous reports have found this fractal-like quasi-stable phenomenon on EEG/fMRI analysis [138] [149] [204]. Both functional connectivity networks and the topography of the spontaneous EEG show stable global brain states remaining quasi-stationary for a period of time, called microstates. But to our knowledge, no such work has been reported on EC networks. This is the first time the EC microstates are found. It suggests that not only the simultaneous correlation over distant brain regions can assume quasi-stable microstates, but the time lagged causal influence between distant brain regions also can. Further study is necessary to inspect this phenomenon and verify this conclusion, which is one of our future research directions.

Third, at the third level, we obtained 7 clusters and among them, we found one dominating and consistent EC network pattern across all subjects. Detailed analysis of all networks in this pattern demonstrates that there are 5 EC networks in this pattern, and these networks centralize on nodes of several regions: mid and inferior temporal cortex, frontal cortex, supplementary motor area, pre and postcentral area, parietal cortex and occipital cortex. These areas are frequently recruited when the brain is engaged in visual and motor processing, memory retrieval, and emotion regulation. These cognitive functions are most frequently encountered for resting state human brain when lying in scanner. Other regions like caudate, hippocampus, fusiform, lingual cortex are also implicated in above functions [246] [247] [248]. The language and execution functions each involve 3 networks which is less than that of memory and emotion. This may be due to the reason that language and execution processes are not as frequently recruited as memory and emotion. Functionalities such as observation, interoception, space cognition, and social cognition involve even less networks maybe due to the reason these functions are less frequently employed when lying rest during fMRI scan.

Admittedly, this work suffers from several drawbacks. First, the data did not cover cerebellum such that this part was not considered into analysis. For future work, using resting state data covering the whole brain for analysis of this kind is necessitated. It is expected that whether the cerebellum will appear as an individual network or cluster with other brain areas. On the other hand, the switching pattern of brain network configurations in this work is similar to that of EEG microstates which have been shown to have fractal property [204]. In the future, it is advised to conduct a simultaneous EEG-fMRI study, and compare the patterns obtained from EEG and fMRI. A cross validation from both EEG and fMRI sides will further deepen and fortify our knowledge about connectivity dynamics, and thus its clinical indications.

Chapter 6 Dynamic Multivariate Analysis:

Dynamic Brain Connectivity Is a Better Predictor of PTSD than Static Connectivity

The work in this chapter continues the works in Chapter 4 and 5. Chapter 4 deals with FC statics and dynamics and Chapter 5 deals with EC dynamics, while this chapter frames together all of above plus EC statics and systematically compares their efficacies in clinical diagnostics. Our main contribution is that we compared EC and FC statics and dynamics in terms of their capabilities of discriminating patients with mental disorders and healthy individuals using support vector machine classification, and concluded that the dynamics of connectivities was more sensitive to the changes brought by mental disorders.

6.1 Introduction

Previous Chapter 4 and 5 demonstrate the significance and use of dynamics of FC and EC in neuro-scientific research, by exploring dynamic brain network patterns and relation to various behavioral measures and cognitive functions. In this chapter, both FC and EC metrics, and both static and dynamic measures are framed together in an effort to systematically compare their values in diagnostic implications. As mentioned in Chapter 4 and 5, dynamics of connectivity received a lot of attention in recent years and many works have explored them using resting state fMRI. The studies investigating dynamic FC used the strategy of sliding windows to account for the dynamics [128] [130] [134] [140] [141] [143]. In particular, Handwerker *et al*. conducted a sliding window analysis on dynamic FC mainly in frequency domain [131], Lee *et al*. explored sliding windowed dynamic FC at different frequency bands using high sampling rate achieved through MR-encephalography [132], and Chang & Glover explored dynamic FC by using wavelet based time-frequency analysis [127]. In addition, observations from electrophysiological studies using EEG [137] and simultaneous EEG/fMRI [133] [145] [138] have demonstrated the existence of temporal variations in FC derived from resting state fMRI and their electrophysiological correlates. On the other hand, there have been few studies exploring dynamic EC brain networks. For example, Havlicek *et al*. proposed an approach to estimate dynamic Granger causality in in the frequency domain [207], while Sato *et al*. [129], Lacey *et al*. [249], and Kapogiannis *et al* [250] used wavelet extension of Granger causality to investigate dynamic EC in the time domain. These studies were illustrated with applications to task-based fMRI.

While there is evidence to believe that non-stationary dynamics exists in brain networks obtained from resting state fMRI, it is yet unclear whether such dynamics provide any additional sensitivity to underlying neuronal processes, especially in clinical diagnostic applications. A recent report showed that dynamic FC is related to real-world cognitive behaviors [166]. Further, recent works have shown that dynamic connectivity signatures in healthy subjects are different from that in subjects diagnosed with mental diseases such as PTSD (post-traumatic stress disorder) [146] and schizophrenia [144]. However, the above studies do not answer the key question of whether dynamic connectivity provides any additional sensitivity to underlying neuronal processes than what is provided by conventional static connectivity.

In this study, we propose that the ability of brain regions to engage and disengage from other brain regions provides a characterization which is fundamentally different from that obtained from conventional static connectivity. Consequently, we hypothesize that the healthy brain is characterized by greater temporal variability of corresponding brain connections as compared to unhealthy brains in general. We specifically test this hypothesis in case of PTSD, wherein we postulate that brains with PTSD symptoms can be characterized by elevated static connectivities (as shown by previous reports [251] [201]), coupled with decreased temporal variability of those connections, leading to a situation wherein hyper-connected brain regions do not disengage frequently enough. Further, we hypothesize that dynamic FC and EC will provide additional sensitivity to the discrimination of PTSD from healthy controls than that provided by static counterparts.

In this work, we tested the above hypotheses by estimating both dynamic FC (DFC) and dynamic EC (DEC) in addition to conventional static measures, static FC (SFC) and static EC (SEC) from resting state fMRI data. For obtaining DFC, we adopted the same strategy as in Chapter 4, i.e., employing moving windowed Pearson's correlation with window length being determined by Dickey-fuller unit root test (DF test). SFC was estimated using Pearson's correlation between the entire time series. For obtaining DEC, we employed dynamic Granger causality (DGC) while correlation-purged Granger causality (CPGC) [211] was used as the SEC measure. Similar to Chapter 4 and 5, these measures were estimated from mean resting state time series extracted from 190 functionally homogeneous regions from CC200 atlas [160]. In order to test whether dynamic connectivity measures provide additional sensitivity to underlying neuronal processes which are altered in PTSD, we used each of the measures: SFC, SEC, variance of DFC and variance of DEC, as features for four separate recursive cluster elimination support vector machine (RCE-SVM) classifiers in order to estimate the accuracy with which they were able to predict the diagnosis of a novel subject.

6.2 Material and Methods

6.2.1 Data Acquisition and Preprocessing

PTSD patients and healthy controls (all right handed) were recruited after the 2008 Wenchuan earthquake, Sichuan, China. Data analysed in this work came from 99 runs from 76 trauma-exposed healthy subjects and 146 runs from 73 PTSD patients. Informed consent was obtained from all subjects after they understood detailed information about the study protocol, which was approved by the IRB of the Second Xiangya Hospital and the Central South University, Changsha, China. Controls were matched in terms of gender and age (within 2 years), as well as education (within 5 years).

T2*-weighted echo planar functional images were acquired from participants. The acquisition parameters were: 200 volumes per scan, In-plane matrix of 64×64 (voxels), 30 axial slices, field of view (FOV) $=220 \times 220$ mm^2, flip angle (FA) $=90^{\circ}$, TR (repetition time)/TE (echo time) =2000ms/30ms, slice thickness 4mm with 1 mm gap. Preprocessing of data was accomplished using Data Processing Assistant for Resting-State fMRI software (DPARSF) [168] and included slice timing correction, rigid body registration, normalization to MNI template with $2 \times 2 \times 2$ mm^3 resolution, spatial smoothing with $4 \times 4 \times 4$ mm^3 Gaussian kernel, 0.01~0.1 Hz band pass filtering, detrending, and regressing out of white matter (WM) and cerebrospinal fluid (CSF) signals as well as 6 motion parameters. 190 functionally homogeneous brain regions derived from spectral clustering of resting state fMRI data were identified from the CC200 brain atlas [160]. Finally, mean time series from each of the 190 regions was extracted from each subject for subsequent use.

6.2.2 Static and Dynamic Effective Connectivity

As discussed in Chapter 5, we used 190 regions covering the entire brain, no assumptions could be made about the underlying connectional architecture, thus the totally data driven measure, Granger causality was recruited for representing EC. Further, model-based methods become computationally intractable when the number of ROIs becomes very large [217].

The Granger causality is based on the principle that if the past of one time series helps predict the present and future of another time series, then there must be a causal influence from the former time series to the latter. We used CPGC to represent SEC and DGC to represent DEC. To elicit the concept of CPGC, we restate the multivariate vector autoregressive (MVAR) model below. Given k time series $\boldsymbol{X}(t)$ =[$x_1(t)$ $x_2(t)$ … $x_k(t)$], with k being 190 in this study, the MVAR model with parameters $\boldsymbol{A}(n)$ of order p is given by:

$$\boldsymbol{X}(t) = \boldsymbol{V} + \sum_{n=1}^{p} \boldsymbol{A}(n) \cdot \boldsymbol{X}(t-n) + \boldsymbol{E}(t) \tag{6.1}$$

Where $\boldsymbol{V}$ is the intercept vector representing nonzero mean component, n is the time lag, and $\boldsymbol{E}(t)$ is the vector corresponding to the residuals. In our scenario, time series were detrended so that $\boldsymbol{V}$=0. Direct causal influences among k time series can be inferred from the MVAR coefficients as follows.

$$D_{ij} = \sum_{n=1}^{p} [a_{ij}(n)]^2 \tag{6.2}$$

Where each a_{ij}, i, j=1:k, is one element of matrix $\boldsymbol{A}$. The effects of instantaneous correlation is modeled as the zero-lag terms and introduced into the modified MVAR model as below [211].

$$\boldsymbol{X}(t) = \boldsymbol{V} + \sum_{n=0}^{p} \boldsymbol{A}'(n) \cdot \boldsymbol{X}(t-n) + \boldsymbol{E}'(t) \tag{6.3}$$

Where the diagonal elements of $\boldsymbol{A}'(0)$ are zeros such that only instantaneous cross-correlation, rather than zero-lag auto-correlation, are modeled. Accordingly, correlation-purged Granger causality (CPGC) [211] is defined as:

$$CPGC_{ij} = \sum_{n=1}^{p} [a'_{ij}(n)]^2 \tag{6.4}$$

Where each a'_{ij} is one element of the matrix $\boldsymbol{A}'$. Note that $\boldsymbol{A}'(1)$ … $\boldsymbol{A}'(p) \neq \boldsymbol{A}(1)$ … $\boldsymbol{A}(p)$ and the $\boldsymbol{A}'(1)$ … $\boldsymbol{A}'(p)$ represent the causal influence which is purged of zero-lag correlation "leakage" effects as shown before [211]. The order *p* of this modified MVAR is determined by Bayesian Information Criterion (BIC) [252]. For methodological details and applications of Granger causality based SEC to task-based and resting state fMRI data, please refer to the following previous publications [253, 254, 255, 256, 257, 258, 259, 260] [261, 262, 170, 263, 264] [114] [210].

For formulation of DGC, please refer to Section 5.2.2 in Chapter 5. Note that it was empirically observed that the Kalman filter estimated needed 10-15 time points to converge. Also considering the fact that initial time points in fMRI time series are routinely discarded to allow the MR signal to achieve equilibration, the DGC values obtained from the first 20 time points were discarded in this work.

6.2.3 Static and Dynamic Functional Connectivity

In this work, we used Pearson correlation between entire time series from different ROIs as SFC measure, and sliding windowed Pearson correlation as DFC measure. Both were the same as those in Chapter 4. The sliding window length was determined by DF test. For details regarding this, please see Section 4.2.3 in Chapter 4.

Being worthy of mentioning, previous studies have used fixed sliding windows of lengths varying from 15 to 120 TRs and similar step size [130] [265] [131] [127] [147]. The data used in this work had a relatively longer TR of 2 seconds, and hence we set the minimum window length to be 10 TRs (20 seconds) and maximum window length to be 40 TRs (80 seconds). The choice of minimum window length was motivated by the consideration that it must have sufficient sampling points to capture temporal dynamics of FC. Two factors influenced the choice of maximum window length. First, it had to be long enough to capture the slowest variations, but short enough so that it does not encompass a large portion of the relatively short time series of

200 TRs we had at our disposal. In order to balance these requirements, a maximum window length of 40 TRs was chosen. We empirically observed that in a vast majority of cases, the window lengths calculated by the DF test were between 10 and 40 TRs. However, it is noteworthy that if the time series were longer, it is possible to choose a bigger maximum window length while performing the DF test. The first 40 data points of time series were preserved for performing the DF test of the first sliding window and the sliding window moved forward by one TR each time. Thus, the dynamic FC had a length of 160 time points (200 is the total number of time points).

6.2.4 RCE-SVM Classification

Here we describe the method used to classify PTSD subjects and healthy controls data using dynamic and static connectivity metrics. Four separate classifiers were employed, with each one receiving one of the following metrics as features from all subjects as inputs: CPGC for SEC, Pearson's correlation for SFC, variance of DGC for variance of DEC and variance of windowed Pearson's correlation for variance of DFC. The variances of dynamic connectivity metrics were employed in order to capture information regarding the temporal variability of brain connectivities. For each of the four classes of features (SEC, SFC, DEC, DFC), there were 190 (number of regions) × 190 (number of regions) =36,100 features for every subject. To effectively reduce the number of features, we conducted a two sample t-test in order to determine those features which were significantly ($p<0.05$) different between the two groups (PTSD and healthy controls). After this t-test filtering, the number of features dramatically reduced to around 2000 (the precise number of features which were significantly different between the groups were different for different metrics). In order to make the classifier performances comparable, we selected the top 1000 features with the lowest p-values and input those into the RCE-SVM [266] [267] classifier.

The statistical separation of features obtained from a t-test does not guarantee the predictive power or generalizability of those features for inferring the diagnostic label of a novel subject, which can be provided by classifiers. Wide applicability of support vector machine (SVM) as a machine learning approach [268] with successful applications in many different fields [269] motivated our choice of SVM for classification. More so, SVM has been the most popular classifier in neuroimaging applications [270]. The recursive cluster elimination (RCE) algorithm is a "wrapper" method for feature selection within SVM wherein uninformative feature clusters are eliminated based on their contribution to classification accuracy, and is considered to be more powerful than "filtering" methods such as t-test which pick the discriminative features *a priori* based on statistical separation [271] [272]. However, we used t-test "filtering" to reduce the number of input features and then used the RCE "wrapper" approach on the remaining significant features in an effort to utilize the merits of both "filtering" and "wrapper" approaches. A schematic illustrating the roles of t-test and RCE algorithm within the overall analysis pipeline is shown in Fig.6.1. The classification accuracy was obtained at each iteration. Also, the contribution of each feature towards obtaining highest classification accuracy was estimated and an SVM "score" was assigned to each feature. As shown in previous works, the RCE-SVM algorithm maintained full separation of training and testing data [273] and hence avoided any bias in classification.

Specifically in this work, the 1000 significant features for all 146 PTSD and 99 healthy subjects were evenly partitioned into 10 subsets in terms of subjects, i.e., the first subset had all 1000 significant features for 15 PTSD subjects and 10 healthy subjects, …, the 10th subset had all 1000 significant features for last 11PTSD subjects and 9 healthy subjects. We did this because with less number of subjects, the classification result was relatively reliable and converged quickly. Then for each subset, the following procedure of RCE-SVM was realized. At the start, all input features were allocated into two parts, each containing half of PTSD subjects and half of healthy controls. The first part was aimed for training and the second part for testing. Next was the clustering step. Input features were clustered into *n* clusters using clustering method (k-means was used and *n*=40 for our scenario). Then SVM scoring step followed. The SVM score of one cluster was a measure of its ability to correctly classify the two groups of subjects, as reflected in the hit rate of classification. Linear SVM scheme was employed because of its computational efficiency and sufficient quality [274]. Specifically, to calculate the score of each cluster, the training features were first randomly divided into 6 subsets of equal size (6 folds) without overlap. Then 5 subsets were trained using linear SVM and the last one was used to test classification performance. After that, the training features were randomly re-divided into 6 subsets, and the SVM training and cross-validation were conducted again. This procedure repeated 100 times in order to account for all possible groupings of features. The score for one cluster was determined as its average accuracy of SVM over all folds and repetitions. Next followed the cluster elimination step, in which 50% of the clusters with lowest scores were eliminated. The surviving features were merged and re-clustered using k-means, with *n* being halved. Then the above three steps were iterated until there was only one cluster left. For each iteration, the testing data was used to evaluate the performance of the classifier with half number of features in previous iteration. Nevertheless, the useful information for subsequent analysis was only the classifier performance and feature scores when maximum accuracy was reached. The features corresponding to that iteration were tabulated and rank ordered based on their scores, and then summed over all 10 subsets, resulting in their global performance index. A flowchart of RCE-SVM algorithm is shown in Fig. 6.2. Please refer to previous publications for more details about the RCE-SVM algorithm [267, 266, 264].

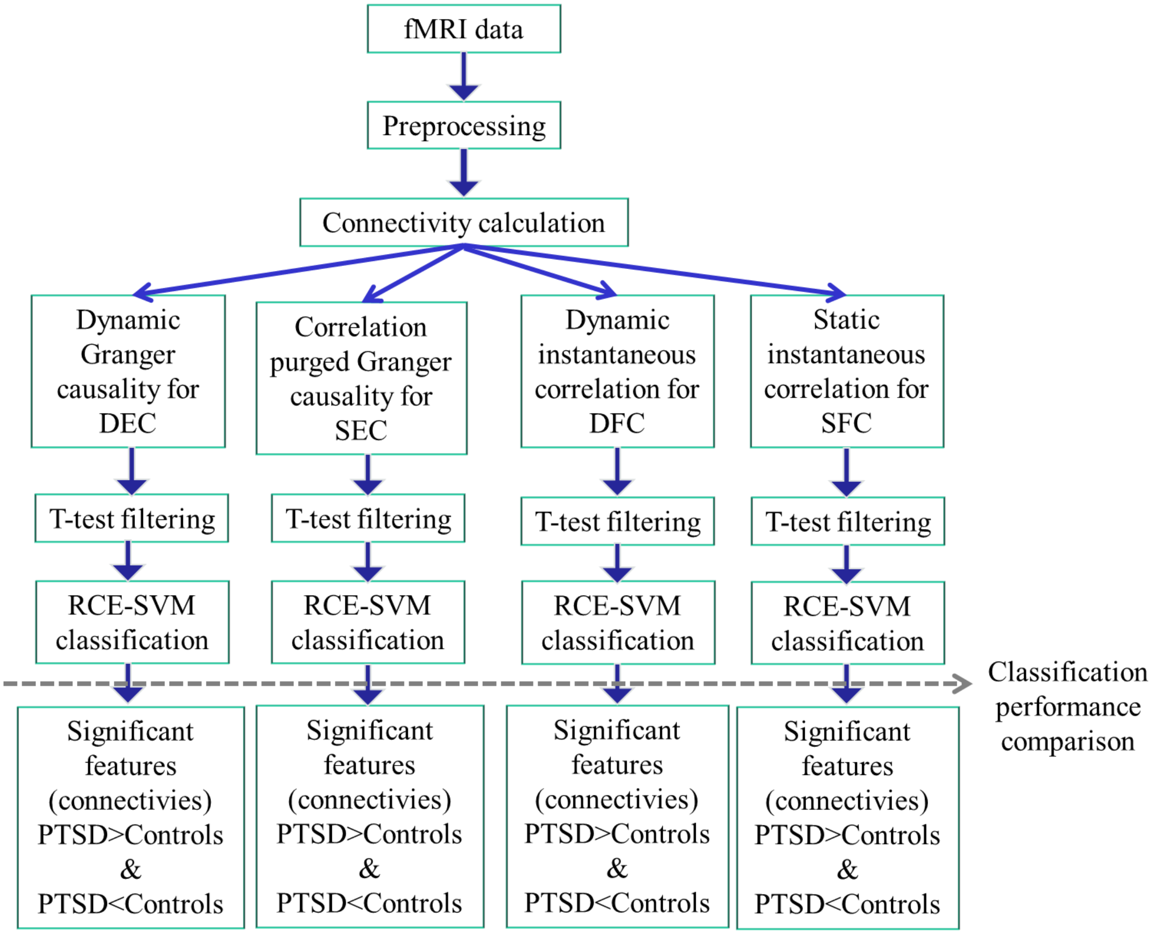

Figure 6.1 Schematic illustrating the roles of t-test and RCE-SVM algorithm within the overall analysis pipeline

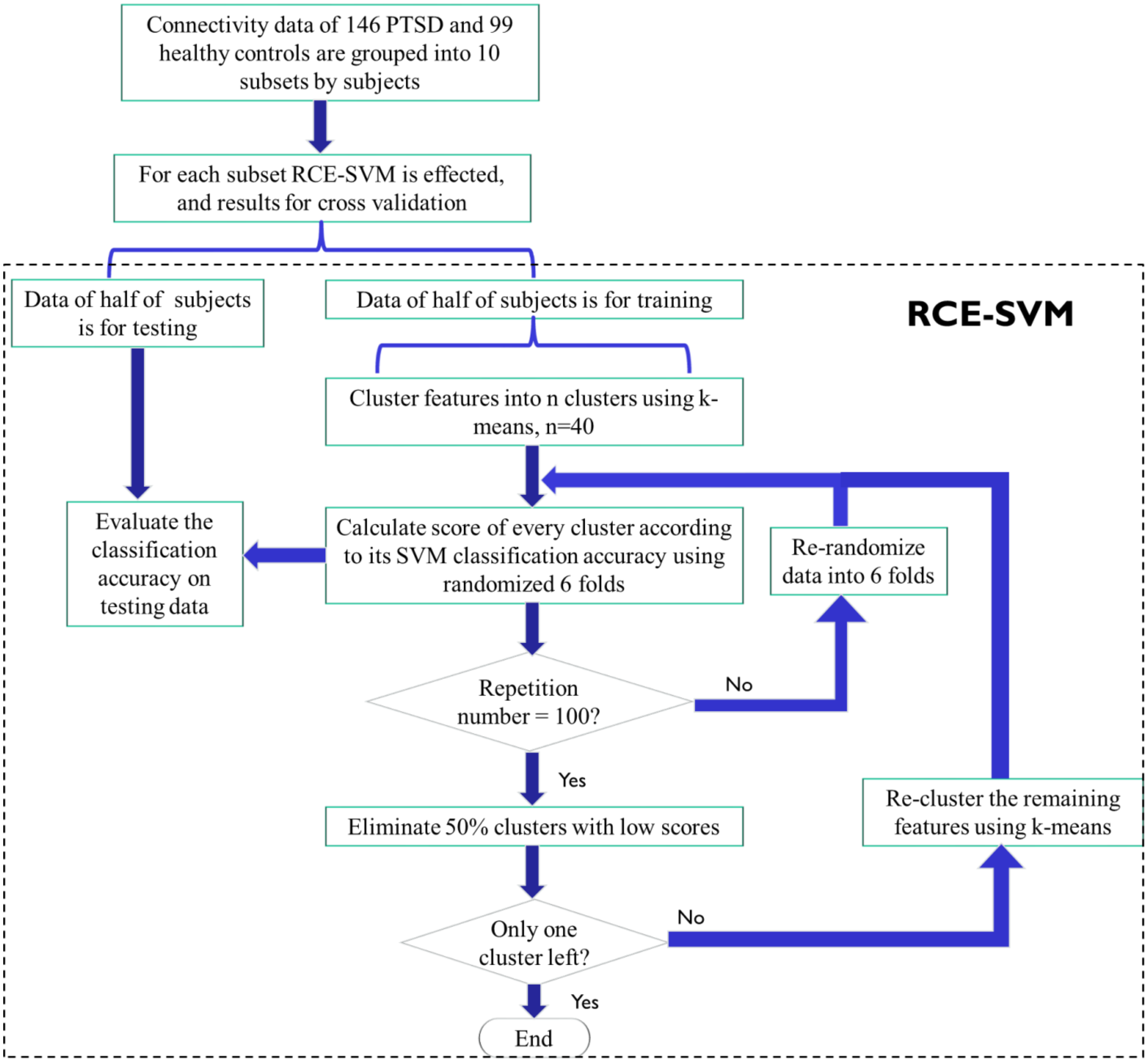

Figure 6.2 Flowchart of RCE-SVM algorithm for scenario in this work

6.3 Results

Fig.6.3 shows the mean classification accuracies obtained by SFC and DFC while Fig.6.4 shows the mean classification accuracies obtained by SEC and DEC. It can be seen that with each RCE step, uninformative features are eliminated and the remaining features are re-classified until we are left with only two feature clusters. The classification accuracy tends to increase with the removal of redundant features at each RCE step. However, there exists a point of inflection for variance of DFC and DEC, which is at the fourth RCE step with only 5 feature-clusters remaining, at which the accuracy peaks at 94.5% and 91.3% for variance of DFC and DEC, respectively.

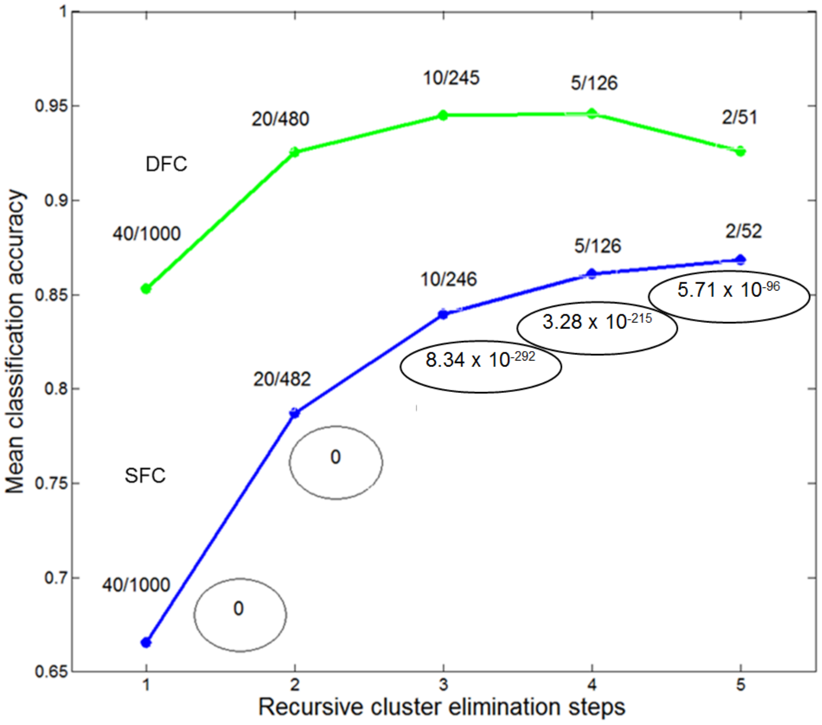

Figure 6.3 Mean classification accuracy obtained from SFC and variance of DFC. X-axis represents recursive cluster elimination steps in RCE-SVM algorithm. Green line: mean classification accuracy obtained using variance of DFC. Blue line: mean classification accuracy obtained using SFC. The number pairs above each knot denote the number of feature-clusters remaining (first number) and the number of features remaining (second number) at every cluster elimination step. Numbers in circles represent the p-value obtained by doing a one-sided t-test comparing classification accuracy obtained by SFC with variance of DFC (alternative hypothesis: accuracy using variance of DFC > accuracy using SFC) at every cluster elimination step.

Removal of any more DFC and DEC features resulted in decreased accuracy indicating that those features were essential for peak accuracy. This was not the case for SFC and SEC, wherein the accuracy kept increasing until the final RCE step with peak accuracies of 86.8% and 88% for SFC and SEC, respectively.

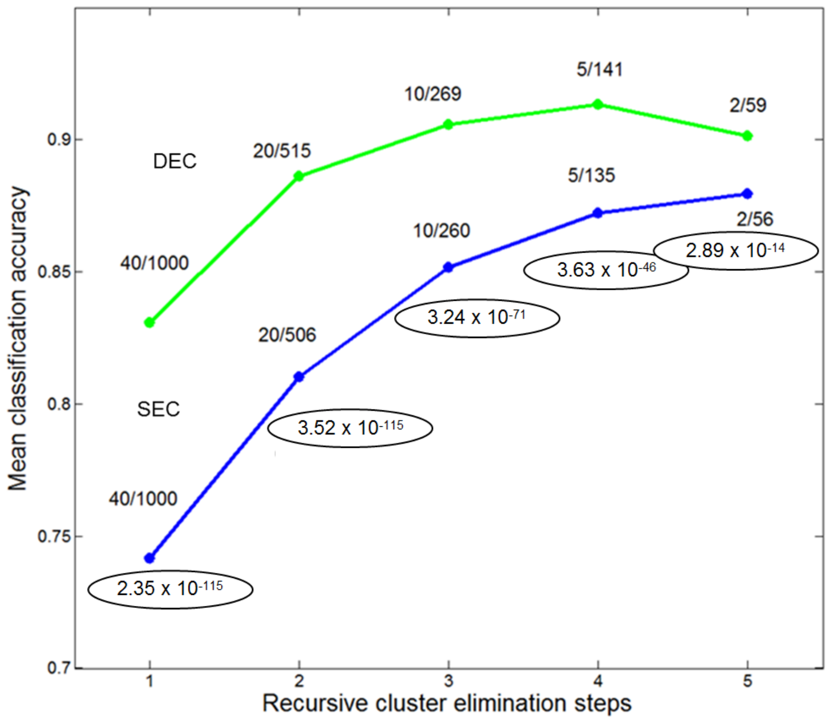

Figure 6.4 Mean classification accuracy obtained from SEC and variance of DEC. X-axis represents recursive cluster elimination steps in RCE-SVM algorithm. Green line: mean classification accuracy obtained using variance of DEC. Blue line: mean classification accuracy obtained using SEC. The number pairs above each knot denote the number of feature-clusters remaining (first number) and the number of features remaining (second number) at every cluster elimination step. Numbers in circles represent the p-value obtained by doing a one-sided t-test comparing classification accuracy obtained by SEC with variance of DEC (alternative hypothesis: accuracy using variance of DEC > accuracy using SEC) at every cluster elimination step.

It is noteworthy here that for both functional and effective connectivity measures, the variances of their dynamics have higher discriminatory power between the groups as compared to their conventional static counterparts. Digits in circles at every feature-cluster elimination step represent the p-value obtained by performing a one-sided t-test comparing classification accuracy of DFC to SFC, and DEC to SEC. The alternative hypothesis for this t-test is that the accuracy by the variance of DFC/DEC is greater than that obtained by SFC/SEC. Fig.6.3 and 6.4 demonstrate that at each RCE step, the accuracies obtained by dynamic connectivity metrics are significantly greater than that obtained by static connectivity metrics.

The features responsible for obtaining maximum accuracy were ascertained and displayed as a network of interconnected nodes using BrainNet Viewer visualization toolbox [275] as shown in Fig.6.5. The nodes represent centroids of brain regions, and each path represents each individual feature. The labels for the nodes in Fig.6.5 correspond to the names of corresponding ROIs derived from the AAL atlas (please refer to Table A1 in Appendix A, Section A.2 for MNI co-ordinates and AAL labels of all regions in the CC200 atlas). Paths with arrows denote EC, while paths without arrows denote FC. Further, the width and color of the paths correspond to their weights, which are calculated based on their SVM scores. Specifically, the SVM scores denote the importance of the corresponding feature for classification between the two groups [270].

From Fig.6.5, a pattern emerges wherein PTSD subjects have stronger overall connectivity, but reduced temporal variability as compared to healthy controls. Specifically, we observe substantially less number of DEC and DFC paths whose variances are larger in PTSD subjects as compared to healthy controls than the other way around (Fig.6.5 (A), (B) and (E)). Conversely, we observe substantially more number of SEC and SFC paths whose connectivity strength are larger in PTSD subjects as compared to healthy controls than the other way around (Fig.6.5 (C), (D) and (F)). Note that no significant DFC paths are observed whose variances are larger in PTSD subjects as compared to healthy controls and at the same time have the discriminatory power to classify subjects with highest accuracy. Also, no significant SFC paths are observed whose connectivities are stronger in healthy controls as compared to PTSD and simultaneously have the discriminatory power to classify subjects with highest accuracy.

Apart from the general pattern mentioned above, there are specific patterns in each subfigure of Fig.6.5 which are noteworthy. First, it can be seen that both static and dynamic connectivity in cortico-cerebellar pathways are implicated in almost all subfigures of Fig.6.5 with predominantly increased static connectivity and decreased temporal variability in PTSD. Mid prefrontal cortex, pre- and post-central cortices, caudate and insula also show increased static connectivity with decreased variability in PTSD. Inferior and medial temporal lobes emerge as important hubs with highly ranked paths associated in Fig.6.5 (B), (C) and (D), indicating their important roles in altered causal brain networks underlying PTSD. On the other hand, the brainstem has predominantly stronger SFC in the PTSD. The numbers of incoming and outgoing paths for each region in each subfigure of Fig.6.5 (or just the number of paths associated with a given region for FC measures) along with their summed connectivity weight are shown in Tables B1 and Table B2 in Appendix B.

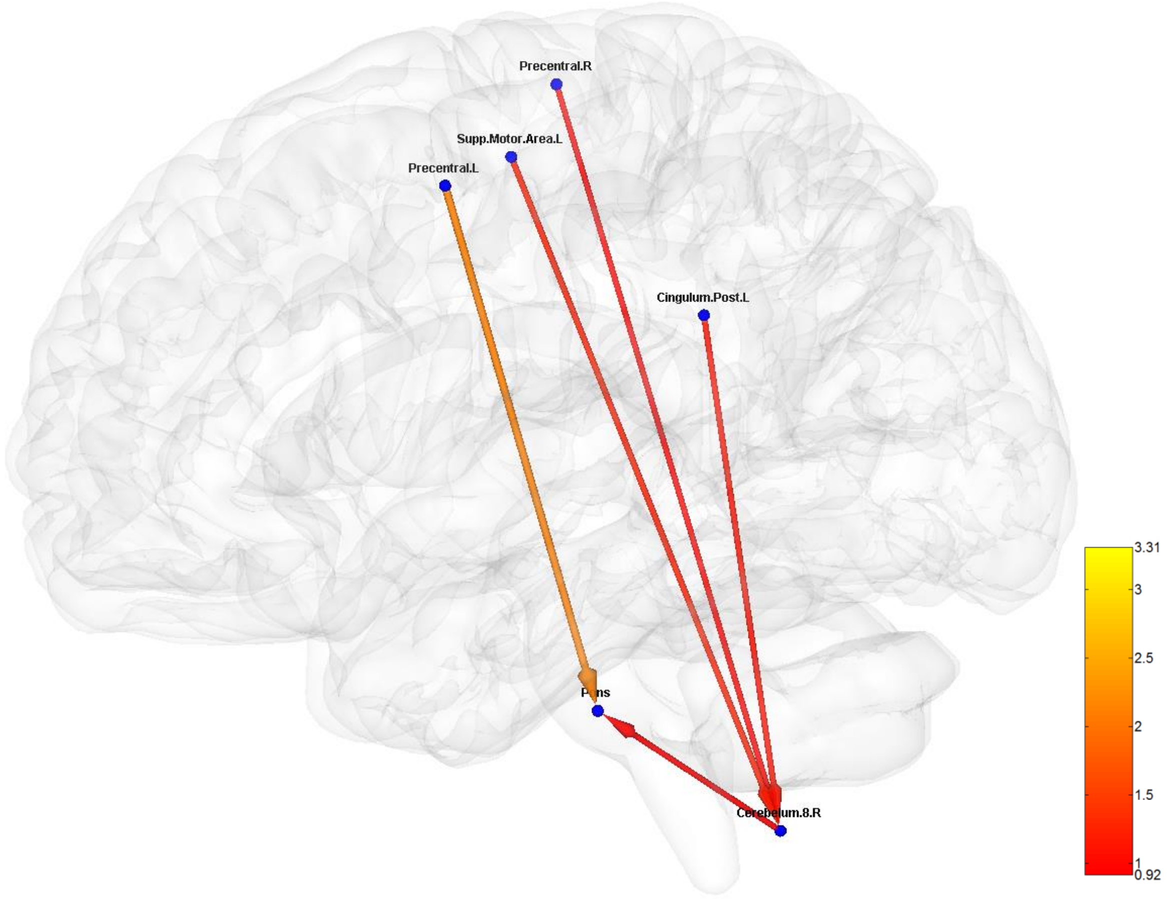

(A) Variance of DEC: PTSD>Control

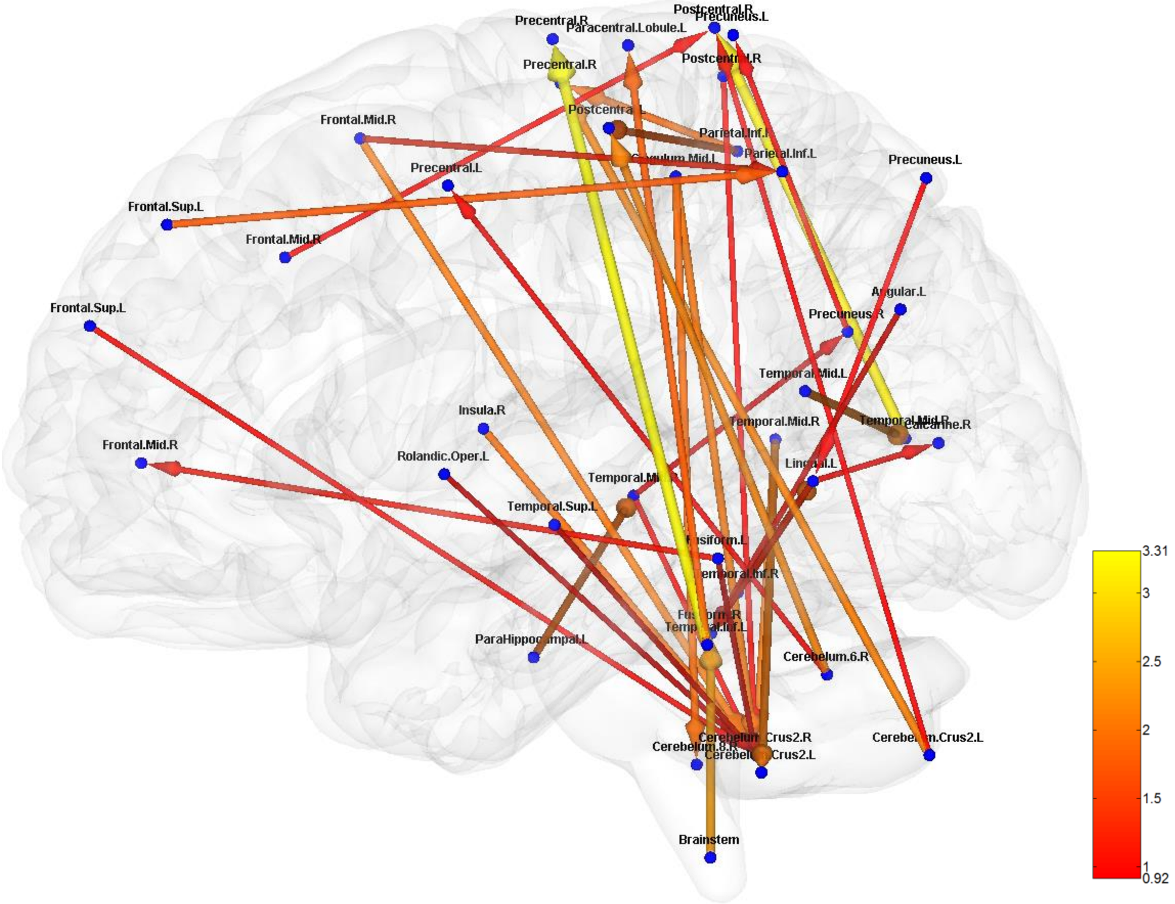

(B) Variance of DEC: Control> PTSD

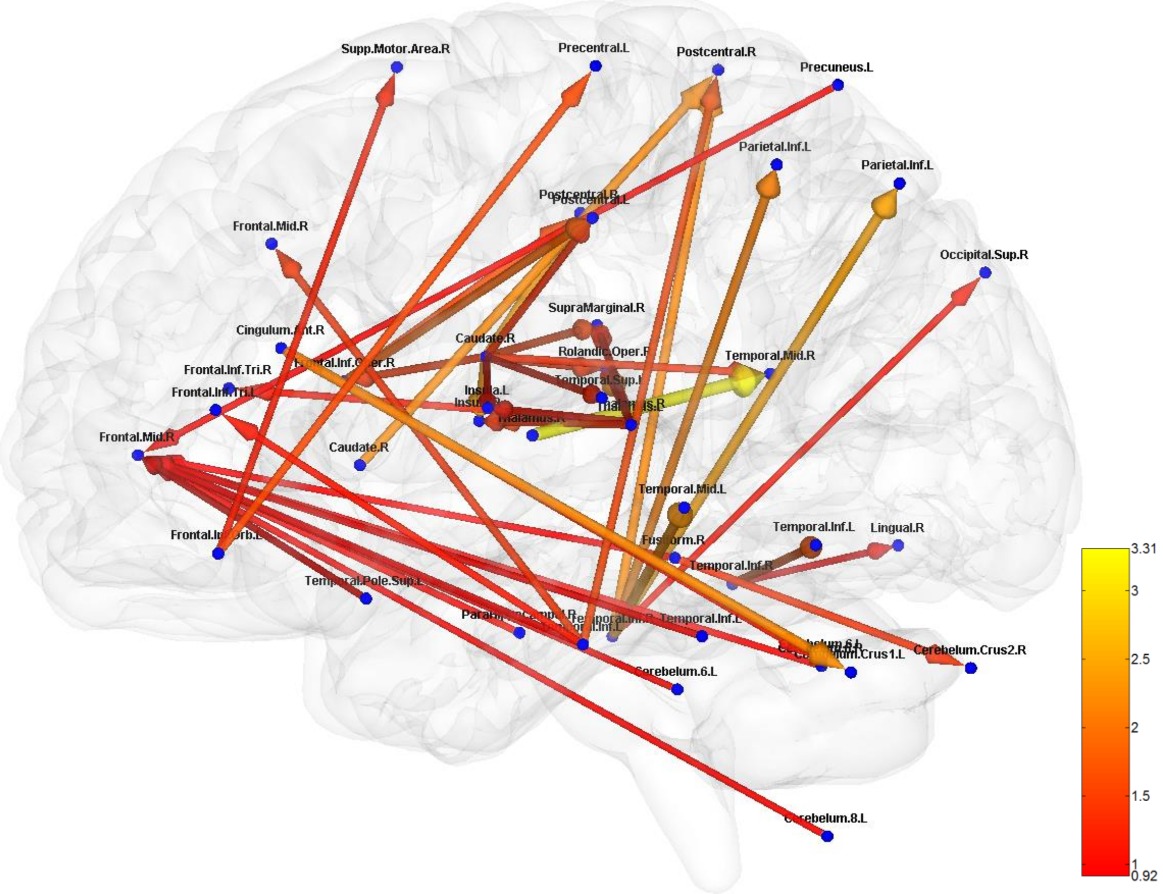

(C) SEC: PTSD>Control

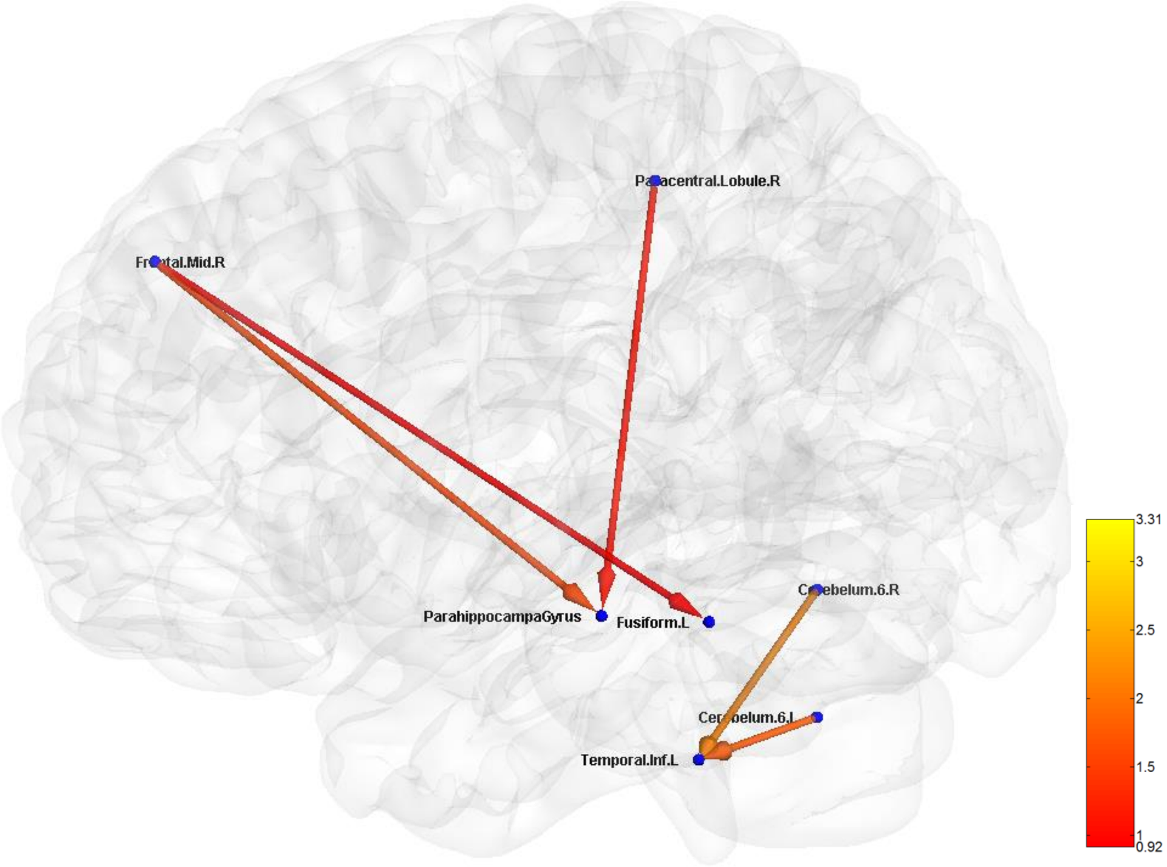

(D) SEC: Control> PTSD

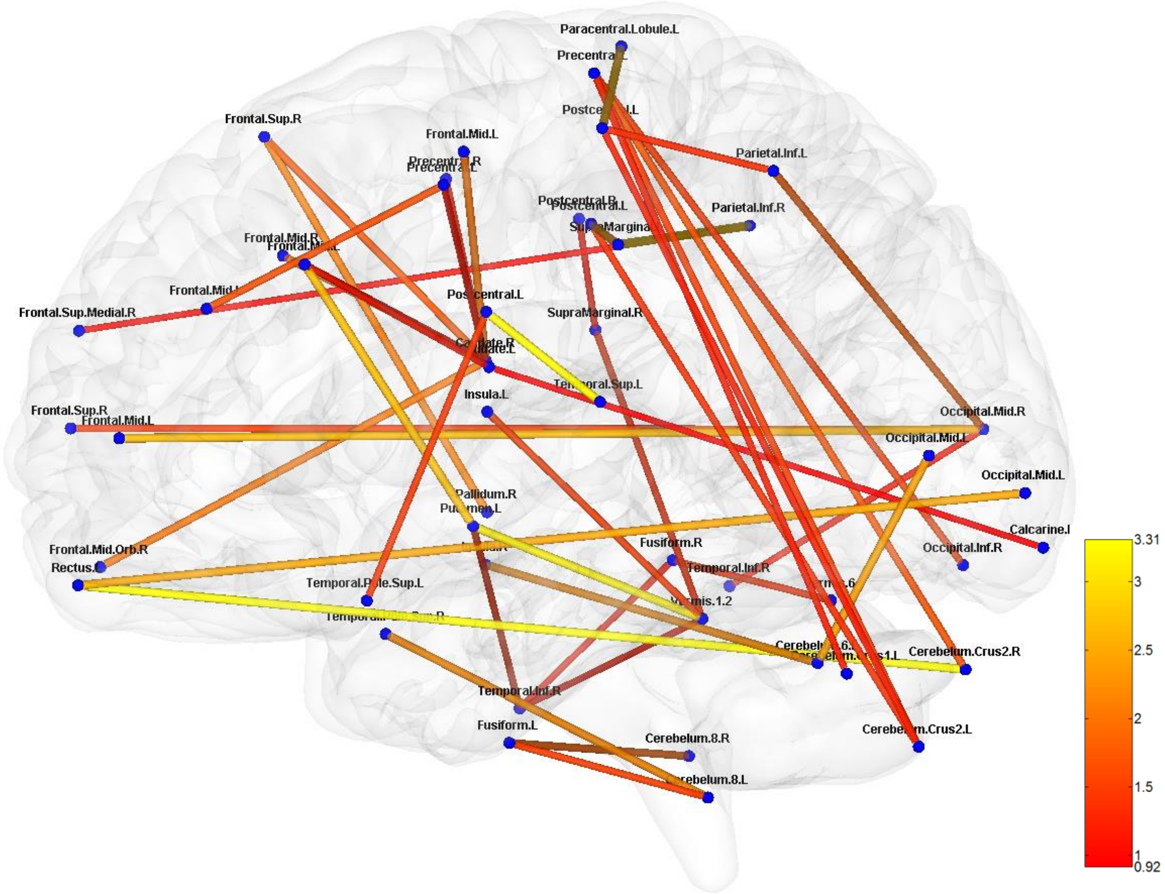

(E) Variance of DFC: Control>PTSD

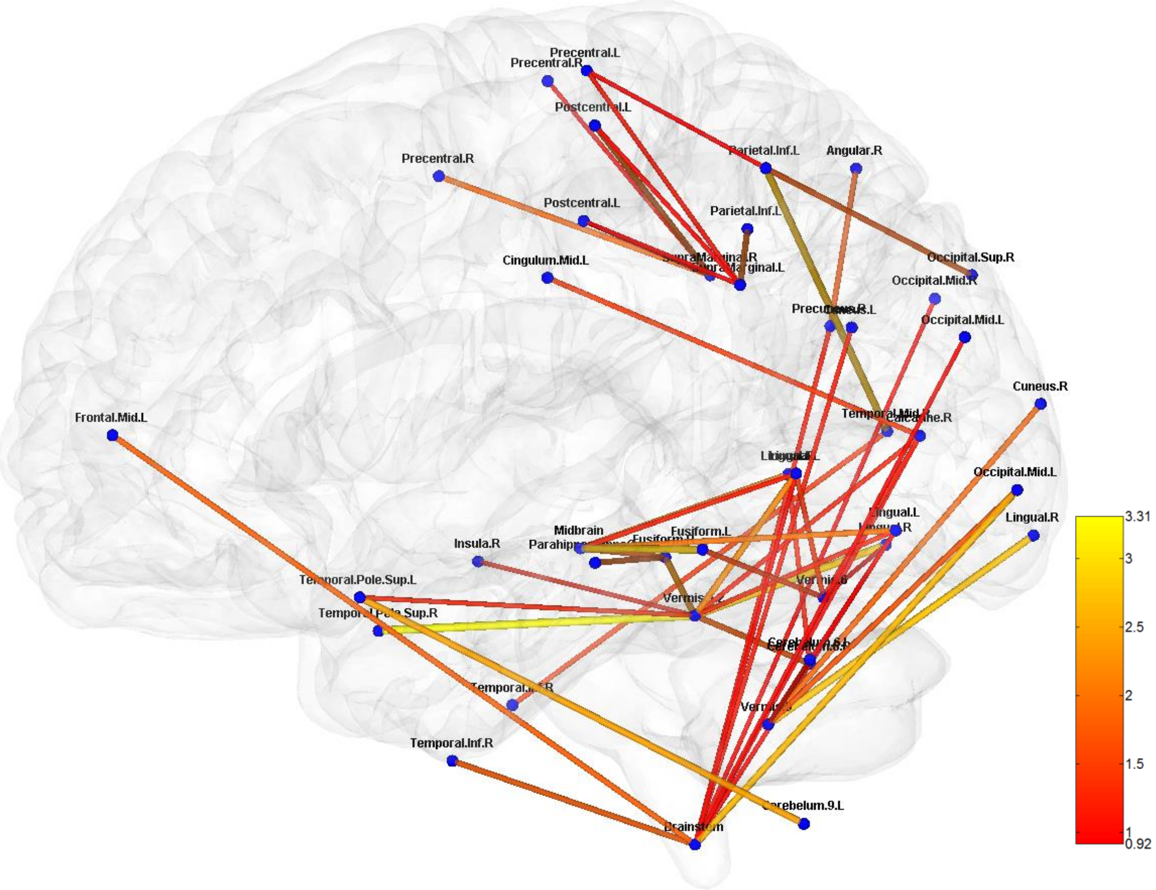

(F) SFC: PTSD>Control

Figure 6.5 Static and Dynamic connectivity features responsible for providing maximum classification accuracy between PTSD and healthy control groups. (A) Top ranked paths whose variances of DEC over time for PTSD subjects are significantly greater than those for healthy controls ($p<0.05$). (B) Top ranked paths whose variances of DEC over time for healthy controls are significantly greater than those for PTSD subjects ($p<0.05$). (C) Top ranked SEC paths which are significantly ($p<0.05$) stronger in PTSD subjects as compared to healthy controls. (D) Top ranked SEC paths which are significantly ($p<0.05$) stronger in healthy controls as compared to PTSD subjects. (E) Top ranked paths whose variances of DFC over time for healthy controls are significantly greater than those for PTSD subjects ($p<0.05$). (F) Top ranked SFC paths which are significantly ($p<0.05$) stronger in PTSD subjects as compared to healthy controls. DFC and SFC Paths have no arrows since correlation has no directionality. Note that no significant DFC paths are observed whose variances are larger in PTSD subjects as compared to healthy controls and at the same time have the discriminatory power to classify subjects with highest accuracy. Also, no significant SFC paths are observed whose connectivities are stronger in healthy controls as compared to PTSD and at the same time have the discriminatory power to classify subjects with highest accuracy. Therefore no subfigures are displayed for them. In all sub-figures, blue nodes represent centroids of functionally homogeneous CC200 brain regions, and paths with arrows connecting nodes represent EC metrics, whereas those without arrows represent FC metrics. The thickness and color of paths correspond to their weights (SVM scores) calculated from RCE-SVM. Autumn color map is used with red representing low SVM score and yellow representing high SVM score.

6.4 Discussion

In this work, we tested the hypothesis that brains with mental disorders are characterized by reduced temporal variability of their brain connections compared to healthy brains, as inferred through resting state fMRI. The motivation for this general hypothesis stems from evidence in biological systems pointing to dynamic adaptability of function as a hallmark of health [276]. We specifically tested this hypothesis in subjects diagnosed with PTSD, and predicted that their brains will be characterized by elevated static connectivity (as shown in previous reports [251] [201]), coupled with decreased temporal variability of those connections. Further, we investigated whether temporal variability of brain connectivity will provide additional sensitivity for predicting the diagnostic label of a novel subject, over and above the discriminatory power provided by conventional static connectivity.

The results presented in this paper support the hypotheses stated above. Specifically, large number of DEC and DFC paths have variances which are significantly larger in healthy controls as compare to PTSD. In comparison, substantially less number of DEC paths, and no DFC paths, whose variances are larger in PTSD subjects as compared to healthy controls are observed. On the other hand, large number of SEC and SFC paths whose connectivity strengths are higher in PTSD subjects as compared to healthy controls are observed. In comparison, substantially less number of SEC paths, and no SFC paths, whose connectivities are significantly stronger in healthy controls as compared to PTSD are observed. Taken together, these results support the notion that PTSD subjects have stronger overall connectivity, but reduced temporal variability as compared to healthy controls. Consequently, they serve as an example for our general hypothesis that unhealthy brains are characterized by reduced temporal variability of their brain connections compared to healthy brains. Future studies must examine whether this hypothesis holds true for other mental disorders.

Even though previous studies have demonstrated that dynamic connectivity signatures in healthy subjects are different from that in subjects diagnosed with mental diseases such as PTSD [146] and schizophrenia [144], a key question has remained unanswered: whether dynamics of connectivity inferred from resting state fMRI provides additional sensitivity to underlying causes of pathology or is it just a detailed characterization of conventional static connectivity with no additional predictive value. Our results support the hypotheses that dynamic connectivity indeed provides novel information as compared to static connectivity which has additional predictive value in clinical diagnosis. The classification results demonstrate that, at every iteration including the one providing maximum accuracy, variance of DFC and DEC provide significantly higher classification accuracy than that provided by SFC and SEC. The fact that the maximum accuracies provided by variances of DFC and DEC exceed 90% shows that it holds promise as a potential neuroimaging biomarker of PTSD.

PTSD is a psychiatric disorder which is associated with exposure to traumatic events that have a profound impact such that three symptom clusters ensue: re-experiencing of the event and flashback, avoidance/numbing/depression, hyper-arousal, along with a high rate of dissociative symptoms [277] [278]. The pathogenesis of PTSD is not yet clear. FMRI studies have provided invaluable information about PTSD, although many of them are task-related and hence difficult for subjects to perform with same accuracy as healthy controls [279] [280]. Recent studies have increasingly explored the use of resting state data [281] [201] [202] given the ease of acquiring such data from patient populations and lack of requirements such as matching task performance with a control group. Below we discuss some specific dynamic and static connectivity patterns (as in Fig.6.5) that emerge from a statistical comparison between the groups in the context of the three symptom clusters mentioned above. Note that these paths as shown in Fig.6.5 are significantly different between the groups, as well as possess the most predictive power (as ascertained through SVM score) for determining the diagnostic label of a novel subject. First, both dynamic and static EC/FC paths associated with cerebellum emerge as having significant differences between the two groups in Fig.6.5. As pointed out by Schmahmann *et al*. [282], the cerebellum is engaged in the experience and regulation of emotions, especially fear perception, anxiety, anticipation, and recollection, and has afferent and efferent connections to the limbic system and brainstem [283]. Thus, cerebellar function is known to be associated with PTSD symptom clusters [284] [285]. In addition, paths associated with the vermis region of the cerebellum are mainly implicated in FC differences between the groups. This region is believed to be functionally implicated with bodily posture and locomotion [286], and has been shown to be associated with early traumatic life experiences [284]. Many EC paths associated with inferior and medial temporal lobes are significantly different between the two groups. Previous studies have shown that inferior and medial temporal lobes are crucial in relaying information among frontal lobe, limbic areas, cerebellum, and visual cortex. For example, as discussed by Miyashita [184], the inferior temporal cortex is referred to as the link from visual cortices to limbic system and frontal lobe, acting to bind object perception with memory [287]. Medial temporal lobe is known to be involved in memory encoding and retrieval [288]. Since PTSD symptoms such as flashback and event re-experiencing are associated with memory systems, connectivity alterations in these regions are in line with previous research implicating them in PTSD [202]. The precentral and postcentral cortices, which contain the primary motor cortex and primary somatosensory cortex, respectively, have many associated EC and FC (both static and dynamic) paths which are different between PTSD and controls. In association with mid and inferior temporal cortices (these regions are connected to postcentral gyrus in Fig.6.5 (B) and (C)), postcentral gyrus has been previously implicated in emotion recognition, especially in social anxiety disorder [289] [290], which relates to PTSD symptoms of numbing and depression. The precentral gyrus has been shown to be activated with the contrast of flashbacks versus ordinary episodic trauma memories in PTSD, as shown by Whalley *et al* [279]. Additional activated areas for this contrast are sensory and motor areas including the insula, supplementary motor area (SMA), and mid-occipital cortex, as well as decreased activation in the midbrain, parahippocampal gyrus, and precuneus/posterior cingulate cortex. These regions are indeed involved in the significant differentiation between the two groups as in Fig.6.5: mid brain in Fig.6.5 (F); mid-occipital cortex reflected in FC subfigures; precuneus in Fig.6.5 (B), (C) and (F); parahippocampal gyrus in Fig.6.5 (B), (C), (D) and (F); SMA in Fig.6.5 (A) and (C); insula in Fig.6.5 (B), (C), (E) and (F). The brain stem has many SFC connections to occipital and precuneus regions, as well as a path to the mid frontal cortex and a path to inferior temporal cortex, which are stronger in PTSD as compared to controls. The brain stem has been previously implicated in various PTSD symptom clusters [291] [292]. However, this feature is not as discriminative as DFC differences between the groups. Other regions with multiple paths showing group differences, and which have been previously shown to be important regions underlying the pathophysiology of PTSD, are the caudate and insula [293], parietal and occipital cortex [279], fusiform [294] and thalamus [201]. Among them, the insular cortex deserves to be highlighted since it is closely associated with pain and emotion, and an increasing number of neuroimaging studies show that both physical pain and depression involve the insular cortex [295] [296] [297]. The activation of fusiform has been shown by Shaw *et al*. [294] to be linked to hyper-arousal and abnormal reactivity in PTSD. Besides, the parietal cortex is involved in the dorsal visual stream which appears to be altered in PTSD as compared to healthy controls [279].

This paper presents some methodological advances which are noteworthy. First, few studies in the past have simultaneously examined both SFC and SEC from resting state fMRI [114]. None has done so using both DFC and DEC in addition to conventional static metrics. Second, most previous studies limit the number of ROIs either because they are using a seed-based approach [201] or because including more ROIs in EC models make them computationally intractable [217]. Exceptions to this include whole brain FC studies employing PCA [298], ICA [125] and graph-theoretic approaches [299] [300] and a limited number of whole brain EC studies employing conditional Granger causality [213]. None so far has simultaneously examined both FC and EC at the whole brain level and our approach demonstrates a framework for doing so. Third, since truly multivariate EC models (which do not make sparcity assumptions) cannot be estimated in a voxel-wise fashion across the whole brain for typical lengths of time series obtained in fMRI studies, prior studies have used anatomically defined ROIs (for example, from the AAL atlas [130], which makes ROIs functionally heterogeneous) or have considered ROIs from pre-defined networks such as the default mode network [202]. Contrary to previous approaches, we have used functionally homogeneous ROIs obtained from spectral clustering of resting state fMRI data [160]. This allowed us to perform whole brain analysis without adopting a voxel-wise approach (and hence avoiding computational intractability issues), and at the same time respect functional boundaries in the brain in ROI definition. Fourth, previous dynamic FC studies have used fixed-length sliding windows of arbitrary length. However, different window lengths would produce different smoothing effects [130] [127] and there is no data to suggest that the minimum length of the window within which resting state fMRI data is stationary, is constant over time. Therefore, we relaxed the restriction of fixed window length and used time-varying window lengths instead. The principle we adopted is that the window length used must be the minimum length at which the time series becomes stationary, so that FC can be calculated over a period when the signals are stationary. The minimum window length condition allows us to capture maximum available dynamics. Similarly for dynamic EC calculation, adapting the Kalman filter based approach [301] and calculating the forgetting factor (which controls the smoothness) from the data make parameter choices objective and hence the results reproducible. These proposed windowing strategies provide a principled approach for controlling the smoothness of estimated dynamic connectivity while respecting non-stationarity in the data. Finally, we propose a framework using machine learning based approach called RCE-SVM to determine the predictive values of connectivity metrics for diagnosis.

Chapter 7 Conclusion

In this dissertation, five projects are put forward with analysis on functional MRI data. Basically, the five projects can be divided into two categories. One is treating fMRI data in view of univariate process, in which time series from each voxel is assumed to be independent from others. We investigated the olfactory system in canines using fMRI from this view point. The other one is treating fMRI data as an integrated entity of dynamic multivariate processes, in which the signal from each voxel/region is interacting with others. With this view point, we investigated resting state human fMRI data to find its connectivity metrics, correlated them to behavior and real world functionalities, and compared the capabilities of connectivity metrics to predict the diagnostic label of a patient with mental disorders or a healthy control.

Through univariate analysis, we located the olfaction related canine brain areas, examined how their activations were modulated with the change of odorant concentration and dog's consciousness state: lightly anesthetized or fully conscious. We also inspected zinc nanoparticles' enhancement effect on canines' olfactory processing occurring in the anesthetized and conscious brain, compared to pure odorant and gold nanoparticles + odorant as controls. In addition, we framed the canine fMRI olfactory system and utilized the single camera optical motion tracking system to minimize motion effect. The result shows that olfactory bulb and piriform lobes were commonly activated in both awake and anesthetized dogs, while the frontal cortex and cerebellum were activated mainly in conscious dogs. Responses to high odorant concentration showed enhancement in either the intensity or spatial extent of activation in the olfactory bulb, piriform lobes, cerebellum, and frontal cortex as compared to low odorant concentration. Zinc nanoparticles immensely enhanced activations of olfactory bulb, olfactory cortex, and olfactory related sub-cortical areas for anesthetized dogs and apparent enhancement for conscious dogs in areas of olfactory bulb, olfactory cortex, medial and posterior frontal areas, compared to pure odorant condition. Gold nanoparticles showed moderate enhancement for activations in olfaction related areas as compared to pure odorant condition. The optical motion tracking system was proven effective in eliminating jerky movements.

Through multivariate analysis, human resting state fMRI data were studied and four connectivity metrics: static FC, dynamic FC, static EC, and dynamic EC were thoroughly researched and compared. With dynamic FC and EC, we conducted a three-leveled clustering over time, space, and subjects to find the major brain network patterns. We correlated dynamic FC metrics with behavioral measures and compared dynamic FC’s ability to predict behavior with static FC. We also linked dynamic EC patterns to real world functionalities. The major findings are briefed as follows. First, we observed several major patterns of brains states alternating with each other in a quasi-stable way, featuring default mode network (DMN) in FC patterns and temporal-parietal-frontal interactions in EC patterns. Second, the dynamics of FC had much more power in explaining and predicting a wide variety of behaviors than its static counterpart. Third, the major dynamic EC patterns mainly engaged in the functionalities of execution, emotion, and memory, in agreement with our knowledge. The last project was in an effort to use fMRI technique to find its diagnostic value. It compared above four connectivity metrics with regard to their ability to distinguish between patients with mental disorders and healthy controls. We used support vector machine technique as a classifier to classify PTSD patients and healthy controls. Our result favorably indicates that the temporal variability of connectivities had more sensitivity in predicting the diagnostic label of a novel subject than static connectivities, based on their classification performances.

Chapter 8 Information on Published and Submitted Papers

The work described in Chapter 2 (see Chapter2) has been published in PLoS One and a snapshot of relevant information is shown in Fig.8.1. Author contributions: conceived and designed experiments: PW, CW, JB, EM, NS, TD, VV, GD. Performed experiments: HJ, OP, PW, RB, JS. Analyzed data: HJ. Contributed reagents/materials/analysis tools: HJ, OP, PW, CW, VV, GD. Wrote the paper: HJ, PW, VV, GD.

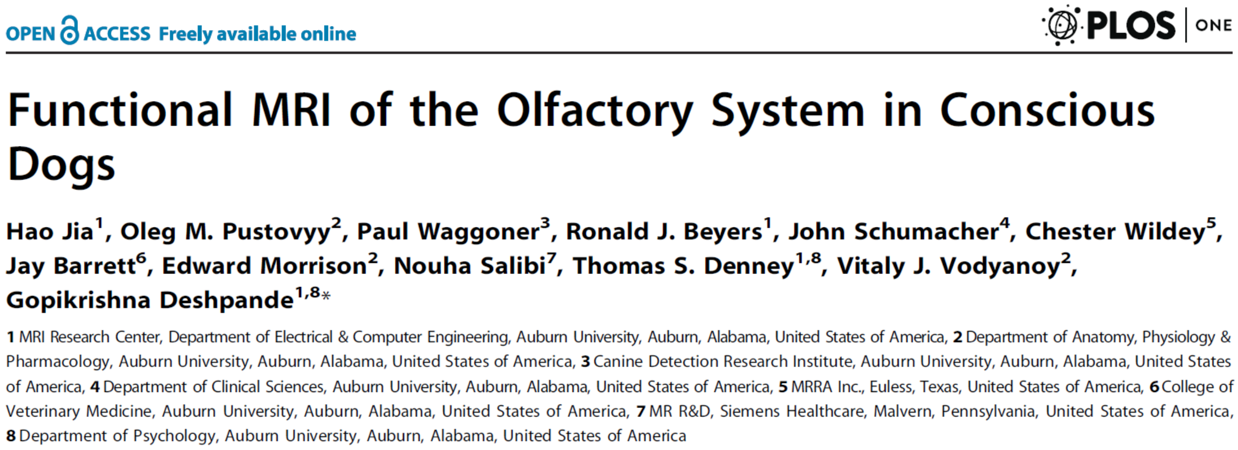

OPEN ACCESS Freely available online

PLOS ONE

Functional MRI of the Olfactory System in Conscious Dogs

Hao Jia[1], Oleg M. Pustovyy[2], Paul Waggoner[3], Ronald J. Beyers[1], John Schumacher[4], Chester Wildey[5], Jay Barrett[6], Edward Morrison[2], Nouha Salibi[7], Thomas S. Denney[1,8], Vitaly J. Vodyanoy[2], Gopikrishna Deshpande[1,8]*

1 MRI Research Center, Department of Electrical & Computer Engineering, Auburn University, Auburn, Alabama, United States of America, **2** Department of Anatomy, Physiology & Pharmacology, Auburn University, Auburn, Alabama, United States of America, **3** Canine Detection Research Institute, Auburn University, Auburn, Alabama, United States of America, **4** Department of Clinical Sciences, Auburn University, Auburn, Alabama, United States of America, **5** MRRA Inc., Euless, Texas, United States of America, **6** College of Veterinary Medicine, Auburn University, Auburn, Alabama, United States of America, **7** MR R&D, Siemens Healthcare, Malvern, Pennsylvania, United States of America, **8** Department of Psychology, Auburn University, Auburn, Alabama, United States of America

Figure 8.1 A snapshot of the publication information of the work in Chapter 2.

The paper for the work in Chapter 3 (see Chapter3) is currently under review, with title "Enhancement of Odor-induced Activity in the Canine Brain by Zinc Nanoparticles: A Functional MRI Study in Conscious Dogs" and authors: Hao Jia, Oleg M Pustovyy, Paul Waggoner, Ronald J Beyers, John Schumacher, Chester Wildey, Jay Barrett, Edward Morrison, Nouha Salibi, Thomas S Denney, Vitaly J Vodyanoy, and Gopikrishna Deshpande. Author contributions: conceived and designed experiments: PW, CW, JB, EM, NS, TD, VV, GD. Performed experiments: HJ, OP, PW, RB, JS. Analyzed data: HJ. Contributed reagents/materials/analysis tools: HJ, OP, PW, CW, VV, GD. Wrote the paper: HJ, PW, VV, GD.

The paper for the work in Chapter 4 (see Chapter4) is currently under review, with title "Behavioral Relevance of the Dynamics of Functional Brain Connectome" and authors: Hao Jia, Xiaoping Hu, and Gopikrishna Deshpande. Author contributions: conceived the idea: XH, GD. Performed simulations and analyzed data: HJ. Contributed reagents/materials/analysis tools: HJ, GD. Wrote the paper: HJ, XH, GD.

The paper for the work in Chapter 5 (see Chapter5) is currently under review, with title "Finite Number of Directional Brain Network Configurations Revealed from Time-Varying Connectivity Assessment of Resting State fMRI" and authors: Hao Jia, Xiaoping Hu and Gopikrishna Deshpande. Author contributions: conceived and designed experiments: GD. Performed experiments: HJ, GD. Performed simulations and analyzed data: HJ. Contributed reagents/materials/analysis tools: HJ, GD. Wrote the paper: HJ, XH, GD.

The paper for the work in Chapter 6 (see Chapter6) is currently under review, with title "Dynamic Brain Connectivity Is a Better Predictor of PTSD than Static Connectivity" and authors: Hao Jia, Changfeng Jin, Lingjiang Li, Tianming Liu, Xiaoping Hu and Gopikrishna Deshpande. Author contributions: conceived and designed experiments: CJ, LL, TL, GD (only conceived and designed the analysis part presented in Chapter 6). Performed experiments: CJ. Analyzed data: HJ. Contributed reagents/materials/analysis tools: HJ, GD. Wrote the paper: HJ, XH, GD.

BIBLIOGRAPHY

[1] A. G. Filler, "The history, development and impact of computed imaging in neurological diagnosis and neurosurgery: CT, MRI, and DTI." *The Internet Journal of Neurosurgery,* vol. 7, no. 1, pp. 1-76, 2010.

[2] H. Carr, Free precession techniques in nuclear magnetic resonance, PhD thesis (Cambridge, MA: Harvard University), 1952.

[3] E. M. Haacke, R. F. Brown, M. Thompson and R. Venkatesan, Magnetic resonance imaging: physical principles and sequence design. New York: J. Wiley & Sons., 1999.

[4] D. B. Twieg, "The k-trajectory formulation of the NMR imaging process with applications in analysis and synthesis of imaging methods." *Medical Physics,* vol. 5, pp. 610–621, 1983.

[5] W. Golder, "Magnetic resonance spectroscopy in clinical oncology." *Onkologie,* vol. 3, pp. 304–309, 2007.

[6] M. Deck, C. Henschke, B. Lee, R. Zimmerman, R. Hyman, J. Edwards, L. Saint Louis, P. Cahill, H. Stein and J. Whalen, "Computed tomography versus magnetic resonance imaging of the brain. A collaborative interinstitutional study." *Clinical Imaging,* vol. 1, pp. 2-15, 1989.

[7] S. Ogawa, D. Tank, R. Menon, J. Ellermann, S. Kim, H. Merkle and K. Ugurbil, "Intrinsic signal changes accompanying sensory stimulation: functional brain mapping with magnetic resonance imaging." *Proceedings of National Academy of Sciences of U.S.A.,* vol. 89, no. 13, pp. 5951–5955, 1992.

[8] S. Kim and K. Ugurbil, "Functional magnetic resonance imaging of the human brain." *Journal of Neuroscience Methods,* vol. 74, no. 2, pp. 229-243, 1997.

[9] R. B. Buxton, Introduction to Functional Magnetic Resonance Imaging. Principles and Techniques. 2nd Edition, University of California, San Diego, 2009.

[10] S. A. Huettel, A. W. Song and G. McCarthy, Functional Magnetic Resonance Imaging, Sinauer Associates, Incorporated, 2009.

[11] S. Ogawa, T. Lee, A. Kay and D. Tank, "Brain magnetic resonance imaging with contrast dependent on blood oxygenation." *Proceedings of National Academy of Sciences of U.S.A.,* vol. 87, no. 24, pp. 9868-9872, 1990.

[12] P. Fox and M. Raichle, "Focal physiological uncoupling of cerebral blood flow and oxidative metabolism during somatosensory stimulation in human subjects." *Proceedings of National Academy of Sciences of U.S.A.,* vol. 4, pp. 1140-1144, 1986.

[13] K. Bush and J. Cisler, "Decoding neural events from fMRI BOLD signal: a comparison of existing approaches and development of a new algorithm." *Magnetic Resonance Imaging,* vol. 6, pp. 976-989, 2013.

[14] D. D. Langleben and J. C. Moriarty, "Using brain imaging for lie detection: where science, law, and policy collide." *Psychology, Public policy & Law,* vol. 19, no. 2, pp. 222-234., 2013.

[15] S. A. Rombouts, F. Barkhof and P. Scheltens, Clinical applications of functional brain MRI, UK: Oxford University Press, 2007.

[16] J. Ashburner and K. Friston, "Nonlinear spatial normalization using basis functions." *Human Brain Mapping,* vol. 7, no. 4, pp. 254-266, 1999.

[17] J. Lancaster, D. Tordesillas-Gutiérrez, M. Martinez, F. Salinas, A. Evans, K. Zilles, J. Mazziotta and P. Fox, "Bias between MNI and Talairach coordinates analyzed using the ICBM-152 brain template." *Human Brain Mapping,* vol. 11, pp. 1194-1205, 2007.

[18] T. Wragg, Univariate and Multivariate Methods for the Analysis of Repeated Measures Data, GRIN Verlag, 2011.

[19] M. Murray and M. Wallace, "Chapter 13: Characterization of multisensory integration with fMRI." in *The Neural Bases of Multisensory Processes*, Boca Raton (FL), CRC Press, 2012.

[20] P. Jensen, The Behavioral Biology of Dogs, Cambridge, MA: CAB International, 2007.

[21] D. Harel, L. Carmel and D. Lancet, "Towards an odor communication system." *Computational Biology and Chemistry,* vol. 27, pp. 121-133, 2003.

[22] L. Haberly, "Parallel-distributed processing in olfactory cortex: new insights from morphological and physiological analysis of neuronal circuitry." *Chemical Senses,* vol. 26, no. 5, pp. 551-576, 2001.

[23] D. Zald and J. Pardo, "Emotion, olfaction, and the human amygdala: amygdala activation during aversive olfactory stimulation." *Proceedings of National Academy of Sciences of U.S.A.,* vol. 94, no. 8, pp. 4119-4124, 1997.

[24] G. Shepherd, "Discrimination of molecular signals by the olfactory receptor neuron." *Neuron,* vol. 13, pp. 771-790, 1994.

[25] N. Ramnani and A. Owen, "Anterior prefrontal cortex: insights into function from anatomy and neuroimaging." *Nature Reviews. Neuroscience,* vol. 5, no. 3, pp. 184-194, 2004.

[26] S. Zobel, T. Hummel, J. Ilgner, A. Finkelmeyer, U. Habel, D. Timmann, J. Schulz and M. Kronenbuerger, "Involvement of the human ventrolateral thalamus in olfaction." *Journal of Neurology,* vol. 257, no. 12, pp. 2037-2043, 2010.

[27] M. Bear, B. Connors and M. Paradiso, Neuroscience: Exploring the Brain, Baltimore: Lippincott Williams & Wilkins, 2007, pp. 265–275.

[28] N. S. Nadi, J. D. Hirsch and F. L. Margolis, "Laminar distribution of putative neurotransmitter amino acids and ligand binding sites in the dog olfactory bulb." *Journal of Neurochemistry,* vol. 34, no. 1, pp. 138–146, 1980.

[29] S. Price, "Anisole binding protein from dog olfactory epithelium." *Chemical Senses,* vol. 3, no. 1, pp. 51-55, 1978.

[30] T. Hirai, S. Kojima, A. Shimada, T. Umemura, M. Sakai and C. Itakurat, "Age-related changes in the olfactory system of dogs." *Neuropathology and Applied Neurobiology,* vol. 22, no. 6, pp. 531–539, 1996.

[31] R. Doty, D. Kreiss and R. Frye, "Human odor intensity perception: correlation with frog epithelial adenylate cyclase activity and transepithelial voltage response." *Brain Research,* vol. 527, no. 1, pp. 130-134, 1990.

[32] G. Lowe, T. Nakamura and G. Gold, "Eog amplitude is correlated with odor-stimulated adenylate-cyclase activity in the bullfrog olfactory epithelium." *Chemical Senses,* vol. 13, no. 4, pp. 710, 1988.

[33] N. Viswaprakash, J. Dennis, L. Globa, O. Pustovyy, E. Josephson, P. Kanju, E. Morrison and V. Vodyanoy, "Enhancement of odorant-induced response in olfactory recptor neurons by zinc nanoparticles." *Chemical Senses,* vol. 34, pp. 547-557, 2009.

[34] V. Szetei, Á. Miklósi, J. Topál and V. Csányi, "When dogs seem to lose their nose: an investigation on the use of visual and olfactory cues in communicative context between dog and owner." *Applied Animal Behaviour Science,* vol. 83, pp. 141–152, 2003.

[35] M. Williams and J. Johnston, "Training and maintaining the performance of dogs (Canis familiaris) on an increasing number of odor discriminations in a controlled setting." *Applied Animal Behaviour Science,* vol. 78, pp. 55-65, 2002.

[36] H. Ross and D. Murray, (Ed. and Transl.) E.H.Weber on the tactile senses, 2nd ed., Hove: Erlbaum (UK) Taylor & Francis, 1996.

[37] P. Bandettini, E. Wong, R. Hinks, R. Tifosky and J. Hyde, "Time course EPI of human brain function during task activation." *Magnetic Resonance in Medicine,* vol. 25, pp. 390-398, 1992.

[38] K. Sicard, Q. Shen, M. Brevard, R. Sullivan, C. Ferris, J. King and T. Duong, "Regional cerebral blood flow and BOLD responses in conscious and anesthetized rats under basal and hypercapnic conditions: implications for functional MRI studies." *Journal of Cerebral Blood Flow & Metabolism,* vol. 23, no. 4, pp. 472-481, 2003.

[39] R. Peeters, I. Tindemans, E. De Schutter and A. Van Der Linden, "Comparing BOLD fMRI signal changes in the awake and anesthetized rat during electrical forepaw stimulation." *Magnetic Resonance Imaging,* vol. 19, pp. 821-826, 2001.

[40] G. De Groof, E. Jonckers, O. Güntürkün, P. Denolf, J. V. Auderkerke and A. V. Der Linden, "Functional MRI and functional connectivity of the visual system of awake pigeons." *Behavioural Brain Research,* vol. 239, pp. 43-50, 2013.

[41] C. Wildey, D. MacFarlane, A. Goyal, K. Gopinath, S. Cheshkov and R. Briggs, "Single-camera motion measurement and monitoring for magnetic resonance applications." *Applied Optics,* vol. 50, no. 14, pp. 2088-2097, 2011.

[42] I. Savic, "Brain imaging studies of the functional organization of human olfaction." *Chemical Senses,* vol. 30, Suppl. 1, pp. i222-i223, 2005.

[43] D. Zald and J. Pardo, "Functional neuroimaging of the olfactory system in humans." *International Journal of Psychophysiology*, vol. 36, no. 2, pp. 165-181, 2000.

[44] J. Boyett-Anderson, D. Lyons, A. Reiss, A. Schatzberg and V. Menon, "Functional brain imaging of olfactory processing in monkeys." *Neuroimage*, vol. 20, pp. 257-264, 2003.

[45] K. Mori, Y. Takahashi, K. Igarashi and S. Nagayama, "Odor maps in the dorsal and lateral surfaces of the rat olfactory bulb." *Chemical Senses*, vol. Suppl.1, pp. i103-i104, 2005.

[46] Functional Imaging Lab (FIL), The Welcome Trust Centre for NeuroImaging, in the Institute of Neurology at University College London (UCL), UK., [Online]. Available: http://www.fil.ion.ucl.ac.uk/spm/software/spm8/.

[47] Warner Instruments, [Online]. Available: http://vt-8-valve-timer.software.informer.com/.

[48] G. Berns, A. Brooks and M. Spivak, "Functional MRI in awake unrestrained dogs." *PLoS One*, vol. 7, no. 5, pp. e38027, 2012.

[49] T. Lorig, D. Elmes, D. Zald and J. Pardo, "A computer-controlled olfactometer for fMRI and electrophysiological studies of olfaction." *Behavior Research Methods, Instruments & Computers*, vol. 31, pp. 370-375, 1999.

[50] J. Sommer, W. Maboshe, M. Griebe, C. Heiser, K. Hörmann, B. Stuck and T. Hummel, "A mobile olfactometer for fMRI-studies," *Journal of Neuroscience Methods*, vol. 209, no. 1, pp. 189-194, 2012.

[51] S. Lowen and S. Lukas, "A low-cost, MR-compatible olfactometer." *Behavior Research Methods*, vol. 38, no. 2, pp. 307-313, 2006.

[52] R. Popp, M. Sommer, J. Müller and G. Hajak, "Olfactometry in fMRI studies: odor presentation using nasal continuous positive airway pressure." *Acta Neurobiologiae Experimentalis*, vol. 64, no. 2, pp. 171-176, 2004.

[53] B. Slotnick and D. Restrepo, "Olfactometry with mice." unit 8.20., Hoboken (NJ), Wiley InterScience, 2005.

[54] Smiths Medical, [Online]. Available: http://www.surgivet.com/pet-oxygen-masks/index.html.

[55] S. Pathirana, W. Neely, L. Myers and V. Vodyanoy, "Chiral recognition of odorants (+)-carvone and (-)-carvone by phospholipid monolayers." *Journal of the American Chemical Society*, vol. 114, pp. 1404-1405, 1992.

[56] R. Bednarski, K. Grimm, R. Harvey, V. Lucasik, W. Penn, B. Sargent, K. Spelts and American Animal Hospital Association, "AAHA anesthesia guidelines for dogs and cats." *Journal of American Animal Hospital Association*, vol. 47, no. 6, pp. 377-385, 2011.

[57] C. Ferris, B. Smerkers, P. Kulkarni, M. Caffrey, O. Afacan, S. Toddes, T. Stolberg and M. Febo, "Functional magnetic resonance imaging in awake animals." *Reviews in Neurosciences*, vol. 22, no. 6, pp. 665-674, 2011.

[58] D. Macfarlane and C. Wildey, "fMRI headtracking using a single camera and a lightweight fiducial." *Conference Proceedings: IEEE Engineering in Medicine & Biology Society*, pp. 5673-5676, 2010.

[59] C. Martin, D. Grenier, M. Thévenet, M. Vigouroux, B. Bertrand, M. Janier, N. Ravel and P. Litaudon, "fMRI visualization of transient activations in the rat olfactory bulb using short odor stimulations." *Neuroimage*, vol. 36, no. 4, pp. 1288-1293, 2007.

[60] D. Ottoson, "Analysis of the electrical activity of the olfactory epithelium." *Acta physiologica Scandinavica*, vol. Supplementum 35, no. 122, pp. 1-83, 1955.

[61] A. Poellinger, R. Thomas, P. Lio, A. Lee, N. Makris, B. Rosen and K. Kwong, "Activation and habituation in olfaction--an fMRI study." *Neuroimage*, vol. 13, no. 4, pp. 547-560, 2001.

[62] X. Yang, R. Renken, F. Hyder, M. Siddeek, C. Greer, G. Shepherd and R. Shulman, "Dynamic mapping at the laminar level of odor-elicited responses in rat olfactory bulb by functional MRI." *Proceedings of Natioal Academy of Sciences of U.S.A.*, vol. 95, no. 13, pp. 7715-7720, 1998.

[63] D. Wilson, "Habituation of odor responses in the rat anterior piriform cortex." *Journal of Neurophysiology*, vol. 79, no. 3, pp. 1425-1440, 1998.

[64] K. Butts, S. J. Riederer, R. L. Ehman, R. M. Thompson and C. R. Jack, "Interleaved echo planar imaging on a standard MRI system." *Magnetic Resonance in Medicine*, vol. 31, no. 1, pp. 67–72, 1994.

[65] M. Brant-Zawadzki, G. Gillan and W. Nitz, "MP RAGE: a three-dimensional,T1-weighted, gradient-echo sequence–initial experience in the brain." *Radiology*, vol. 182, pp. 769–775, 1992.

[66] S. Frey, D. Pandya, M. Chakravarty, L. Bailey, M. Petrides and D. Collins, "An MRI based average macaque

monkey stereotaxic atlas and space (MNI monkey space)." *Neuroimage,* vol. 55, no. 4, pp. 1435-1442, 2011.

[67] R. Datta, J. Lee, J. Duda, B. Avants, C. Vite, B. Tseng, J. Gee, G. Aguirre and G. Aguirre, "A digital atlas of the dog brain." *PLoS One,* vol. 7, no. 12, pp. e52140, 2012.

[68] S. Forman, J. Cohen, M. Fitzgerald, W. Eddy, M. Mintun and D. Noll, "Improved assessment of significant activation in functional magnetic resonance imaging (fMRI): use of a cluster-size threshold." *Magnetic Resonance in Medicine,* vol. 33, no. 5, pp. 636-647, 1995.

[69] J. Xiong, J. Gao, J. L. Lancaster and P. T. Fox, "Clustered pixels analysis for functional MRI activation studies of the human brain." *Human Brain Mapping,* vol. 3, no. 4, pp. 287-301, 1995.

[70] B. Ward. [Online]. Available: http://afni.nimh.nih.gov/pub../pub/dist/doc/manual/AlphaSim.pdf.

[71] T. Fletcher and T. Saveraid, "Canine Brain MRI Atlas," [Online]. Available: http://vanat.cvm.umn.edu/mriBrainAtlas/index.html.

[72] T. Kondoh, S. Yamada, S. Shioda and K. Torii, "Central olfactory pathway in response to olfactory stimulation in rats detected by magnetic resonance imaging." vol. 30, no. Suppl. 1, pp. i172-i173, 2005.

[73] D. Krestel, D. Passe, J. Smith and L. Jonsson, "Behavioral determination of olfactory thresholds to amyl acetate in dogs." *Neuroscience and Biobehavioral Reviews,* vol. 8, pp. 169-174, 1984.

[74] D. Walker, J. Walker, P. Cavnar, J. Talyor, D. Pickel, S. Hall and J. Suarez, "Naturalistic quantification of canine olfactory sensitivity." *Applied Animal Behaviour Scinece,* vol. 97, pp. 241-254, 2006.

[75] B. R. Frederick, K. J. Edward and J. Markee, "Studies on olfactory discrimination in dogs: II. discriminatory behavior in a free environment." *Journal of Comparative and Physiological Psychology,* vol. 55, no. 5, pp. 773-780, 1962.

[76] M. Williams, J. Johnston, M. Cicoria, E. Paletz, P. Waggoner, C. Edge and S. Hallowell, "Canine detection odor signatures for explosives." *SPIE Proceedings,* vol. 3575, pp. 291-301, 1998.

[77] E. Kandel, J. Schwartz and T. Jessell, Priciples of neural science, 4th ed., New York: McGraw-Hill, 2000.

[78] G. Orban, "Imaging image processing in the human brain." *Current Opinion in Neurology,* vol. 14, no. 1, pp. 47-54, 2001.

[79] [Online]. Available: http://emedicine.medscape.com/article/835585-overview.

[80] J. Gottfried and D. Zald, "On the scent of human olfactory orbitofrontal cortex: meta-analysis and comparison to non-human primates." *Brain Research Reviews,* vol. 50, no. 2, pp. 287-304, 2005.

[81] M. Bensafi, E. Iannilli, J. Gerber and T. Hummel, "Neural coding of stimulus concentration in the human olfactory and intranasal trigeminal systems." *Neuroscience,* vol. 154, no. 2, pp. 832-838, 2008.

[82] N. Sobel, V. Prabhakaran, J. Desmond, G. Glover, R. Goode, E. Sullivan and J. Gabrieli, "Sniffing and smelling: separate subsystems in the human olfactory cortex." *Nature,* vol. 392, no. 6673, pp. 282-286, 1998.

[83] K. Friston, A. Mechelli, R. Turner and C. Price, "Nonlinear responses in fMRI: the Ballon model, Volterra kernels, and other hemodynamics." *Neuroimage,* vol. 12, pp. 466-477, 2000.

[84] C. Studzinski, J. Araujo and N. Milgram, "The canine model of human cognitive aging and demintia: pharmacological validity of the model for assessment of human cognitive-enhancing drugs." *Progress in Neuro-Psychopharmacology & Biological Psychiatry,* vol. 29, pp. 489-498, 2005.

[85] J. Oxley and P. Waggoner, "Detection of explosives by dogs." in Marshall, M., and Oxley, J. eds., *Aspects of Explosives Detection,* Elsevier: Amsterdam, 2009, pp. 27-40.

[86] S. Youngentob, B. Johnson and M. Leon, "Predicting odorant quality from multidimensional scaling of olfactory bulb glomerular activity patterns." *Behavioral Neuroscience,* vol. 120, no. 6, pp. 1337-1345, 2006.

[87] A. Kruse, "Defense Sciences Research and Technology Special Focus Area: RealNose." 2007. [Online]. Available: https://www.fbo.gov/index?s=opportunity&mode=form&tab=core&id=32bb6977f45cc0b870f0837f32ad7fcf&_cview=0.

[88] T. Howell, R. Conduit, S. Toukhsati and P. Bennett, "Auditory stimulus discrimination recorded in dogs, as indicated by mismatch negativity (MMN)." *Behavioural Processes,* vol. 89, no. 1, pp. 8-13, 2012.

[89] M. Kujala, H. Törnqvist, S. Somppi, L. Hänninen, C. Krause, O. Vainio and J. Kujala, "Reactivity of dogs' brain oscillations to visual stimuli measured with non-invasive electroencephalography." *PLoS One,* vol. 8, no. 5, pp. e61818, 2013.

[90] H. Törnqvist, M. Kujala, S. Somppi, L. Hänninen, M. Pastell, C. Krause, J. Kujala and O. Vainio, "Visual event-related potentials of dogs: a non-invasive electroencephalography study." *Animal Cognition,* vol. 16, no. 6, pp. 973-982, 2013.

[91] V. Vodyanoy and E. Morrison, "Apparatus and method for the measurement of the aerodynamics of olfaction in animals and man." US Patent 6,979,298, 27 12 2005.

[92] L. Qin, P. van Gelderen, J. Derbyshire, F. Jin, J. Lee, J. de Zwart, Y. Tao and J. Duyn, "Prospective head movement correction for high resolution MRI using an in-bore optical tracking system." *Magnetic Resonance in Medicine,* vol. 62, pp. 924-934, 2009.

[93] M. Tremblay, F. Tam and S. Graham, "Retrospective coregistration of functional magnetic resonance imaging data using external monitoring." *Magnetic Resonance in Medicine,* vol. 53, pp. 141-149, 2005.

[94] C. Moore, O. Pustovyy, J. Dennis, T. Moore, E. Morrison and V. Vodyanoy, "Olfactory responses to explosives associated odorants are enhanced by zinc nanoparticles." *Talanta,* vol. 88, pp. 730-733, 2012.

[95] V. Vodyanoy, "Zinc nanoparticles interact with olfactory receptor neurons." *Biometals,* vol. 23, pp. 1097-1103, 2010.

[96] P. Lledo, G. Gheusi and J. Vincent, "Information processing in the mammalian olfactory system." *Physiological Reviews,* vol. 85, no. 1, pp. 281-317, 2005.

[97] A. Samoylov, T. Samoylova, O. Pustovyy, A. Samoylov, M. Toivio-Kinnucan, N. Morrison, L. Globa, W. Gale and V. Vodyanoy, "Novel metal clusters isolated from blood are lethal to cancer cells." *Cells,Tissues,Organs,* vol. 179, no. 3, pp. 115-124, 2005.

[98] K. Azuma, I. Uchiyama, H. Takano, M. Tanigawa, M. Azuma, I. Bamba and T. Yoshikawa, "Changes in cerebral blood flow during olfactory stimulation in patients with multiple chemical sensitivity: a multi-channel near-infrared spectroscopic study." *PLoS One,* vol. 8, no. 11, pp. e80567, 2013.

[99] R. Fulbright, P. Skudlarski, C. Lacadie, S. Warrenburg, A. Bowers, J. Gore and B. Wexler, "Functional MR imaging of regional brain responses to pleasant and unpleasant odors." *American Journal of Neuroradiology,* vol. 19, no. 9, pp. 1721-1726, 1998.

[100] K. Hadland, M. Rushworth, D. Gaffan and R. Passingham, "The effect of cingulate lesions on social behaviour and emotion." *Neuropsychologia,* vol. 41, no. 8, pp. 919-931, 2003.

[101] I. Savic, B. Gulyas, M. Larsson and P. Roland, "Olfactory functions are mediated by parallel and hierarchical processing." *Neuron,* vol. 26, no. 3, pp. 735-745, 2000.

[102] A. Anderson, K. Christoff, I. Stappen, D. Panitz, D. Ghahremani, G. Glover, J. Gabrieli and N. Sobel, "Dissociated neural representations of intensity and valence in human olfaction." *Nature Neuroscience,* vol. 6, no. 2, pp. 196-202, 2003.

[103] Y. Yeshurun and N. Sobel, "An odor is not worth a thousand words: from multidimensional odors to unidimensional odor objects." *Annual Review of Psychology,* vol. 61, pp. 219-241, C211-215, 2010.

[104] J. Mainland and N. Sobel, "The sniff is part of the olfactory percept." *Chemical Senses,* vol. 31, no. 2, pp. 181-196, 2006.

[105] L. Levy, R. Henkin, A. Hutter, C. Lin, D. Martins and D. Schellinger, "Functional MRI of human olfaction." *Journal of Computer Assisted Tomography,* vol. 21, no. 6, pp. 849-856, 1997.

[106] M. García-Cabezas and H. Barbas, "A direct anterior cingulate pathway to the primate primary olfactory cortex may control attention to olfaction." *Brain, Structures & Function,* (DOI 10.1007/s00429-013-0598-3), 2013.

[107] G. Wintermann, M. Donix, P. Joraschky, J. Gerber and K. Petrowski, "Altered olfactory processing of stress-related body odors and artificial odors in patients with panic disorder." *PLoS One,* vol. 8, no. 9, pp. e74655, 2013.

[108] J. Jadauji, J. Djordjevic, J. Lundström and C. Pack, "Modulation of olfactory perception by visual cortex stimulation." *Journal of Neuroscience,* vol. 32, no. 9, pp. 3095-3100, 2012.

[109] B. P. Rogers, S. B. Katwald, V. L. Morgana, C. L. Asplunde and J. C. Gore, "Functional MRI and multivariate autoregressive models." *Magnetic Resonance Imaging,* vol. 28, no. 8, pp. 1058-1065, 2010.

[110] G. Deshpande and X. Hu, "Investigating effective brain connectivity from fMRI data: past findings and current issues with reference to Granger causality analysis." *Brain Connectivity,* vol. 2, no. 5, pp. 235-245,

2012.

[111] P. Valdes-Sosa, A. Roebroeck and J. F. K. Daunizeau, "Effective connectivity: influence, causality and biophysical modeling." *Neuroimage,* vol. 58, no. 2, pp. 339-361, 2011.

[112] K. Stephan and A. Roebroeck, "A short history of causal modeling of fMRI data." *Neuroimage,* vol. 62, no. 2, pp. 856-863, 2012.

[113] M. Kaminski, M. Ding, W. A. Truccolo and S. L. Bressler, "Evaluating causal relations in neural systems: Granger causality, directed transfer function and statistical assessment of significance." *Biological Cybernetics,* vol. 85, no. 2, pp. 145-157, 2001.

[114] G. Deshpande, P. Santhanam and X. Hu, "Instantaneous and causal connectivity in resting state brain networks derived from functional MRI data." *Neuroimage,* vol. 54, no. 2, pp. 1043-1052, 2011.

[115] R. S. Patel, F. D. Bowman and J. K. Rilling, "A Bayesian approach to determining connectivity of the human brain." *Human Brain Mapping,* vol. 27, no. 3, pp. 267-276, 2006.

[116] K. Friston, "Functional and effective connectivity in neuroimaging: a synthesis." *Human Brain Mapping,* vol. 2, no. 1-2, pp. 56-78, 1994.

[117] K. Friston, C. Frith, P. Liddle and R. Frackowiak, "Functional connectivity: the principal-component analysis of large (PET) data sets." *Journal of Cerebral Blood Flow & Metabolism,* vol. 13, no. 1, pp. 5-14, 1993.

[118] M. Greicius, K. Supekar, V. Menon and R. Dougherty, "Resting-state functional connectivity reflects structural connectivity in the default mode network." *Cerebral Cortex,* vol. 1, pp. 72-78, 2009.

[119] M. Kim, R. Loucks, A. Palmer, A. Brown, K. Solomon, A. Marchante and P. Whalen, "The structural and functional connectivity of the amygdala: from normal emotion to pathological anxiety." *Behavioral Brain Research,* vol. 2, pp. 403-410, 2011.

[120] M. Guye, G. Bettus, F. Bartolomei and P. Cozzone, "Graph theoretical analysis of structural and functional connectivity MRI in normal and pathological brain networks." *MAGMA,* vol. 5-6, pp. 409-421, 2010.

[121] T. Kellermann, S. Caspers, P. Fox, K. Zilles, C. Roski, A. Laird, B. Turetsky and S. Eickhoff, "Task- and resting-state functional connectivity of brain regions related to affection and susceptible to concurrent cognitive demand." *Neuroimage,* vol. 72, pp. 69-82, 2013.

[122] R. Buckner, J. Andrews-Hanna and D. Schacter, "The brain's default network: anatomy, function, and relevance to disease." *Annuals of the New York Academy of Sciences,* vol. 1124, pp. 1-38, 2008.

[123] E. Sanz-Arigita, M. Schoonheim, J. Damoiseaux, S. Rombouts, E. Maris, F. Barkhof, P. Scheltens and C. Stam, "Loss of 'small-world' networks in Alzheimer's disease: graph analysis of fMRI resting-state functional connectivity." *PLoS One,* vol. 5, no. 11, pp. e13788, 2010.

[124] S. Rombouts, F. Barkhof, R. Goekoop, C. Stam and P. Scheltens, "Altered resting state networks in mild cognitive impairment and mild Alzheimer's disease: an fMRI study." *Human Brain Mapping,* vol. 26, no. 4, pp. 231-239, 2005.

[125] V. van de Ven, E. Formisano, D. Prvulovic, C. Roeder and D. Linden, "Functional connectivity as revealed by spatial independent component analysis of fMRI measurements during rest." *Human Brain Mapping,* vol. 22, no. 3, pp. 165-178, 2004.

[126] M. Greicius, B. Flores, V. Menon, G. Glover, H. Solvason, H. Kenna, A. Reiss and A. Schatzberg, "Resting-state functional connectivity in major depression: abnormally increased contributions from subgenual cingulate cortex and thalamus." *Biological Psychiatry,* vol. 5, pp. 429-437, 2007.

[127] C. Chang and G. H. Glover, "Time–frequency dynamics of resting-state brain connectivity measured with fMRI." *Neuroimage,* vol. 50, no. 1, pp. 81-98, 2010.

[128] G. Deshpande, S. LaConte, S. Peltier and X. Hu, "Connectivity analysis of human functional MRI data: from linear to nonlinear and static to dynamic." *Lecture Notes in Computer Science,* vol. 4091, pp. 17-24, 2006.

[129] J. Sato, E. Junior, D. Takahashi, F. M. de Maria, M. Brammer and P. Morettin, "A method to produce evolving functional connectivity maps during the course of an fMRI experiment using wavelet-based time-varying Granger causality." *Neuroimage,* vol. 31, no. 1, pp. 187-196, 2006.

[130] N. Leonardi, J. Richiardi, M. Gschwind, S. Simioni, J. Annoni, M. Schluep, P. Vuilleumier and D. Van De Ville, "Principal components of functional connectivity: a new approach to study dynamic brain connectivity

during rest." *Neuroimage,* vol. 83, pp. 937-950, 2013.

[131] D. Handwerker, V. Roopchansingh, J. Gonzalez-Castillo and P. Bandettini, "Periodic changes in fMRI connectivity." *Neuroimage,* vol. 63, no. 3, pp. 1712-1719, 2012.

[132] H. Lee, B. Zahneisen, T. Hugger, P. LeVan and J. Hennig, "Tracking dynamic resting-state networks at higher frequencies using MR-encephalography." *Neuroimage,* vol. 65, pp. 216-222, 2013.

[133] C. Chang, Z. Liu, M. Chen, X. Liu and J. Duyn, "EEG correlates of time-varying BOLD functional connectivity." *Neuroimage*, vol. 72, pp. 227-236, 2013.

[134] W. Majeed, M. Magnuson, W. Hasenkamp, H. Schwar, E. Schumacher, L. Barsalou and S. Keilholz, "Spatiotemporal dynamics of low frequency BOLD fluctuations in rats and humans." *Neuroimage,* vol. 54, pp. 1140-1150, 2011.

[135] R. Hutchison, T. Womelsdorf, E. Allen, P. Bandettini, V. Calhoun, M. Corbetta, P. S. Della, J. Duyn, G. Glover, J. Gonzalez-Castillo and et al., "Dynamic functional connectivity: promise, issues, and interpretations." *Neuroimage,* vol. 80, pp. 360-378, 2013.

[136] A. Rack-Gomer and T. Liu, "Caffeine increases the temporal variability of resting-state BOLD connectivity in the motor cortex." *Neuroimage,* vol. 59, pp. 2994-3002, 2012.

[137] S. Dimitriadis, N. Laskaris, V. Tsirka, M. Vourkas and S. Micheloyannis, "An EEG study of brain connectivity dynamics at the resting state." *Nonlinear dynamics, Psychology, and Life sciences,* vol. 16, no. 1, pp. 5-22, 2012.

[138] J. Britz, D. Van De Ville and C. Michel, "BOLD correlates of EEG topography reveal rapid resting-state network dynamics." *Neuroimage,* vol. 52, pp. 1162–1170, 2010.

[139] C. Chang, X. Shen and G. Glover, "Behavioral correlates of temporal variations in brain network connectivity." in *Proceedings of Human Brain Mapping*, 2011.

[140] C. Chang, C. Metzger, G. Glover, J. Duyn, H. Heinze and M. Walter, "Association between heart rate variability and fluctuations in resting-state functional connectivity." *Neuroimage,* vol. 68, pp. 93-104, 2013.

[141] I. Cribben, R. Haraldsdottir, L. Atlas, T. Wager and M. Lindquist, "Dynamic connectivity regression: determining state-related changes in brain connectivity." *Neuroimage,* vol. 61, pp. 907-920, 2012.

[142] A. Fornito, B. Harrison, A. Zalesky and J. Simons, "Competitive and cooperative dynamics of large-scale brain functional networks supporting recollection." *Proceedings of National Academy of Sciences of U.S.A.,* vol. 109, pp. 12788–12793, 2012.

[143] S. Keilholz, M. Magnuson, W. Pan, M. Willis and G. Thompson, "Dynamic properties of functional connectivity in the rodent." *Brain Connectivity,* vol. 3, no. 1, pp. 31-40, 2013.

[144] U. Sakoğlu, G. Pearlson, K. Kiehl, Y. Wang, A. Michael and V. Calhoun, "A method for evaluating dynamic functional network connectivity and task-modulation: application to schizophrenia." *MAGMA,* vol. 23, no. 5-6, pp. 351-366, 2010.

[145] E. Tagliazucchi, F. von Wegner, A. Morzelewski, V. Brodbeck and H. Laufs, "Dynamic BOLD functional connectivity in humans and its electrophysiological correlates." *Frontiers in Human Neuroscience,* vol. 6, pp. 339, 2012.

[146] X. Li, D. Zhu, X. Jiang, C. Jin, X. Zhang, L. Guo, J. Zhang, X. Hu, L. Li and T. Liu, "Dynamic functional connectomics signatures for characterization and differentiation of PTSD patients." *Human Brain Mapping,* (DOI: 10.1002/hbm.22290), 2013.

[147] R. Hutchison, T. Womelsdorf, J. Gati, S. Everling and R. Menon, "Resting-state networks show dynamic functional connectivity in awake humans and anesthetized macaques." *Human Brain Mapping,* vol. 34, no. 9, pp. 2154-2177, 2012.

[148] V. Kiviniemi, T. Vire, J. Remes, A. Elseoud, T. Starck, O. Tervonen and J. Nikkinen, "A sliding time-window ICA reveals spatial variability of the default mode network in time." *Brain Connectivity,* vol. 1, pp. 339-347, 2011.

[149] F. Musso, J. Brinkmeyer, A. Mobascher, T. Warbrick and G. Winterer, "Spontaneous brain activity and EEG microstates. A novel EEG/fMRI analysis approach to explore resting-state networks." *Neuroimage,* vol. 52, no. 4, pp. 1149-1161, 2010.

[150] K. S. Xu, M. Kliger and A. O. Hero III, "Adaptive evolutionary clustering." *Data Mining and Knowledge*

Discovery, vol. 28, pp. 304-336, 2014.

[151] M. Greicius, B. Krasnow, A. Reiss and V. Menon, "Functional connectivity in the resting brain: a network analysis of the default mode hypothesis." *Proceedings of National Academy of Sciences of U.S.A.,* vol. 100, no. 1, pp. 253-258, 2003.

[152] M. Lowe, B. Mock and J. Sorenson, "Functional connectivity in single and multislice echoplanar imaging using resting-state fluctuations." *Neuroimage,* vol. 7, no. 2, pp. 119-132, 1998.

[153] J. Radua, M. Phillips, T. Russell, N. Lawrence, N. Marshall, S. Kalidindi, W. El-Hage, C. McDonald, V. Giampietro, M. Brammer, A. David and S. Surguladze, "Neural response to specific components of fearful faces in healthy and schizophrenic adults." *Neuroimage,* vol. 49, no. 1, pp. 939-946, 2010.

[154] N. Soldati, V. Calhoun, L. Bruzzone and J. Jovicich, "The use of a priori information in ICA-based techniques for real-time fMRI: an evaluation of static/dynamic and spatial/temporal characteristics." *Frontiers in Human Neuroscience,* vol. 7, pp. 64, 2013.

[155] F. Esposito, E. Seifritz, E. Formisano, R. Morrone, T. Scarabino, G. Tedeschi, S. Cirillo, R. Goebel and F. Di Salle, "Real-time independent component analysis of fMRI time-series." *Neuroimage,* vol. 20, no. 4, pp. 2209-2224, 2003.

[156] A. K. Roy, J. L. Fudge, C. Kelly, J. S. Perry, T. Daniele, C. Carlisi, B. Benson, F. Castellanos, M. P. Milham, D. S. Pine and M. Ernst, "Intrinsic functional connectivity of amygdala-based networks in adolescent generalized anxiety disorder." *Journal of American Academy of Child & Adolescent Psychiatry,* vol. 52, no. 3, pp. 290-299. e2, 2013.

[157] W. Shirer, S. Ryali, E. Rykhlevskaia, V. Menon and M. Greicius, "Decoding subject-driven cognitive states with whole-brain connectivity patterns." *Cerebral Cortex,* vol. 22, no. 1, pp. 158-165, 2012.

[158] L. Zeng, H. Shen, L. Liu, L. Wang, B. Li, P. Fang, Z. Zhou, Y. Li and D. Hu, "Identifying major depression using whole-brain functional connectivity: a multivariate pattern analysis." *Brain,* vol. 135, no. 5, pp. 1498-1507, 2012.

[159] E. Allen, E. Damaraju, S. Plis, E. Erhardt, T. Eichele and V. Calhoun, "Tracking whole-brain connectivity dynamics in the resting state." *Cerebral Cortex,* vol. 24, no. 3, pp. 663-676, 2014.

[160] R. Craddock, G. James, P. Holtzheimer, X. Hu and H. Mayberg, "A whole brain fMRI atlas generated via spatially constrained spectral clustering." *Human Brain Mapping,* vol. 33, no. 8, pp. 1914-1928, 2012.

[161] M. Cole, T. Yarkoni, G. Repovs, A. Anticevic and T. Braver, "Global connectivity of prefrontal cortex predicts cognitive control and intelligence." *Journal of Neuroscience,* vol. 32, no. 26, pp. 8988-8999, 2012.

[162] J. He, O. Carmichael, E. Fletcher, B. Singh, A. Iosif, O. Martinez, B. Reed, A. Yonelinas and C. Decarli, "Influence of functional connectivity and structural MRI measures on episodic memory." *Neurobiology of Aging,* vol. 33, no. 11, pp. 2612–2620, 2012.

[163] M. Filippi, F. Agosta, E. Scola, E. Canu, G. Magnani, A. Marcone, P. Valsasina, F. Caso, M. Copetti, G. Comi, S. Cappa and A. Falini, "Functional network connectivity in the behavioral variant of frontotemporal dementia." *Cortex,* vol. 49, no. 9, pp. 2389-2401, 2012.

[164] C. Han, S. Yoo, S. Seo, D. Na and J. Seong, "Cluster-based statistics for brain connectivity in correlation with behavioral measures." *PLoS One,* vol. 8, no. 8, pp. e72332, 2013.

[165] A. Kelly, L. Uddin, B. Biswal, F. Castellanos and M. Milham, "Competition between functional brain networks mediates behavioral variability." *Neuroimage,* vol. 39, pp. 527-537, 2008.

[166] G. Thompson, M. Magnuson, M. Merritt, H. Schwarb, W. Pan, A. McKinley, L. Tripp, E. Schumacher and S. Keilholz, "Short-time windows of correlation between large-scale functional brain networks predict vigilance intraindividually and interindividually." *Human Brain Mapping,* vol. 34, no. 12, pp. 3280-3298, 2013.

[167] "FreeSurfer," [Online]. Available: http://surfer.nmr.mgh.harvard.edu/.

[168] C. Yan and Y. Zang, 2010. [Online]. Available: http://www.restfmri.net.

[169] S. E. Said and D. A. Dickey, "Testing for unit roots in autoregressive moving average models of unknown order." *Biometrika,* vol. 71, no. 3, pp. 599-607, 1984.

[170] A. Roebroeck, E. Formisano and R. Goebel, "Mapping directed influence over the brain using Granger causality and fMRI." *Neuroimage,* vol. 25, pp. 230–242, 2005.

[171] H. Joe and J. Ward, "Hierarchical grouping to optimize an objective function." *Journal of the American Statistical Association,* vol. 58, no. 301, pp. 236–244, 1963.

[172] P. J. Rousseeuw, "Silhouettes: a graphical aid to the interpretation and validation of cluster analysis." *Journal of Computational and Applied Mathematics,* vol. 20, pp. 53-65, 1987.

[173] M. Lee, C. Hacker, A. Snyder, M. Corbetta, D. Zhang, E. Leuthardt and J. Shimony, "Clustering of resting state networks." *PLoS One,* vol. 7, no. 7, pp. e40370, 2012.

[174] M. De Luca, C. Beckmann, N. De Stefano, P. Matthews and S. Smith, "fMRI resting state networks define distinct modes of long-distance interactions in the human brain." *Neuroimage,* vol. 29, no. 4, pp. 1359-1367, 2006.

[175] J. Damoiseaux, S. Rombouts, F. Barkhof, P. Scheltens, C. Stam, S. Smith and C. Beckmann, "Consistent resting-state networks across healthy subjects." *Proceedings of National Academy of Sciences of U.S.A.,* vol. 103, no. 37, pp. 13848-13853, 2006.

[176] M. Moussa, M. Steen, P. Laurienti and S. Hayasaka, "Consistency of network modules in resting-state fMRI connectome data." *PLoS One,* vol. 7, no. 8, pp. e44428, 2012.

[177] V. Schöpf, C. Kasess, R. Lanzenberger, F. Fischmeister, C. Windischberger and E. Moser, "Fully exploratory network ICA (FENICA) on resting-state fMRI data." *Jounal of Neuroscience Methods,* vol. 192, no. 2, pp. 207-213, 2010.

[178] N. Wang, W. Zeng and L. Chen, "A fast-FENICA method on resting state fMRI data." *Journal of Neuroscience Methods,* vol. 209, no. 1, pp. 1-12, 2012.

[179] K. Kalcher, W. Huf, R. Boubela, P. Filzmoser, L. Pezawas, B. Biswal, S. Kasper, E. Moser and C. Windischberger, "Fully exploratory network independent component analysis of the 1000 functional connectomes database." *Frontiers in Human Neuroscience,* vol. 6, no. 301, pp. 1-11, 2012.

[180] J. Zhang, X. Li, C. Li, Z. Lian, X. Huang, G. Zhong, D. Zhu, K. Li, C. Jin, X. Hu, J. Han, L. Guo, X. Hu, L. Li and T. Liu, "Inferring functional interaction and transition patterns via dynamic bayesian variable partition models." *Human Brain Mapping,* (DOI: 10.1002/hbm.22404), 2013.

[181] N. Andreasen, D. O'Leary, S. Paradiso, T. Cizadlo, S. Arndt, G. Watkins, L. Ponto and R. Hichwa, "The cerebellum plays a role in conscious episodic memory retrieval." *Human Brain Mapping,* vol. 8, no. 4, pp. 226-234, 1999.

[182] C. Wiggs, J. Weisberg and A. Martin, "Neural correlates of semantic and episodic memory retrieval." *Neuropsychologia,* vol. 37, no. 1, pp. 103-118, 1999.

[183] T. Tsukiura, T. Fujii, T. Takahashi, R. Xiao, M. Sugiura, J. Okuda, T. Iijima and A. Yamadori, "Medial temporal lobe activation during context-dependent relational processes in episodic retrieval: an fMRI study. Functional magnetic resonance imaging." *Human Brain Mapping,* vol. 17, no. 4, pp. 203-213, 2002.

[184] Y. Miyashita, "Inferior temporal cortex: where visual perception meets memory." *Annual Review of Neuroscience,* vol. 16, no. 1, pp. 245-263, 1993.

[185] K. Jimura, M. Chushak and T. Braver, "Impulsivity and self-control during intertemporal decision making linked to the neural dynamics of reward value representation." *Journal of Neuroscience,* vol. 33, no. 1, pp. 344-357, 2013.

[186] K. Louie and P. Glimcher, "Separating value from choice: delay discounting activity in the lateral intraparietal area." *Journal of Neuroscience,* vol. 30, no. 16, pp. 5498-5507, 2010.

[187] J. Kinnison, S. Padmala, J. Choi and L. Pessoa, "Network analysis reveals increased integration during emotional and motivational processing." *Journal of Neuroscience,* vol. 32, no. 24, pp. 8361-8372, 2012.

[188] Y. Komura, R. Tamura, T. Uwano, H. Nishijo, K. Kaga and T. Ono, "Retrospective and prospective coding for predicted reward in the sensory thalamus." *Nature,* vol. 412, no. 6846, pp. 546-549, 2001.

[189] T. Breckel, C. Thiel, E. Bullmore, A. Zalesky, A. Patel and C. Giessing, "Long-term effects of attentional performance on functional brain network topology." *PLoS One,* vol. 8, no. 9, pp. e74125, 2013.

[190] S. Olbrich, C. Mulert, S. Karch, M. Trenner, G. Leicht, O. Pogarell and U. Hegerl, "EEG-vigilance and BOLD effect during simultaneous EEG/fMRI measurement." *Neuroimage,* vol. 45, no. 2, pp. 319-332, 2009.

[191] L. Seidman, H. Breiter, J. Goodman, J. Goldstein, P. Woodruff, K. O'Craven, R. Savoy, M. Tsuang and B. Rosen, "A functional magnetic resonance imaging study of auditory vigilance with low and high information

processing demands." *Neuropsychology,* vol. 12, no. 4, pp. 505-518, 1998.

[192] W. Orrison, Atlas of brain function, Thieme, 2008.

[193] M. Kringelbach and E. Rolls, "The functional neuroanatomy of the human orbitofrontal cortex: evidence from neuroimaging and neuropsychology." *Progress in Neurobiology,* vol. 72, no. 5, pp. 341-372, 2004.

[194] K. Ridderinkhof, M. Ullsperger, E. Crone and S. Nieuwenhuis, "The role of the medial frontal cortex in cognitive control." *Science,* vol. 306, no. 5695, pp. 443-447, 2004.

[195] O. Devinsky, M. Morrell and B. Vogt, "Contributions of anterior cingulate cortex to behaviour." *Brain,* vol. 118, no. 1, pp. 279-306, 1995.

[196] H. Karnath, B. Baier and T. Nägele, "Awareness of the functioning of one's own limbs mediated by the insular cortex?" *Jounal of Neuroscience,* vol. 25, no. 31, pp. 7134-7138, 2005.

[197] C. Stoodley and J. Schmahmann, "Evidence for topographic organization in the cerebellum of motor control versus cognitive and affective processing." *Cortex,* vol. 46, no. 7, pp. 831-844, 2010.

[198] J. Vincent, I. Kahn, A. Snyder, M. Raichle and R. Buckner, "Evidence for a frontoparietal control system revealed by intrinsic functional connectivity." *Jounal of Neurophysiology,* vol. 100, no. 6, pp. 3328-3342, 2008.

[199] D. Wotruba, L. Michels, R. Buechler, S. Metzler, A. Theodoridou, M. Gerstenberg, S. Walitza, S. Kollias, W. Rössler and K. Heekeren, "Aberrant coupling within and across the default mode, task-positive, and salience network in subjects at risk for psychosis." *Schizophrenia Bulletin,* (DOI: 10.1093/schbul/sbt161), 2013.

[200] A. Shinn, J. Baker, B. Cohen and D. Ongür, "Functional connectivity of left Heschl's gyrus in vulnerability to auditory hallucinations in schizophrenia." *Schizophrenia Research,* vol. 143, no. 2-3, pp. 260-268, 2013.

[201] Y. Yin, C. Jin, X. Hu, L. Duan, Z. Li, M. Song, H. Chen, B. Feng, T. Jiang, H. Jin, C. Wong, Q. Gong and L. Li, "Altered resting-state functional connectivity of thalamus in earthquake-induced posttraumatic stress disorder: a functional magnetic resonance imaging study." *Brain Research,* vol. 1411, pp. 98-107, 2011.

[202] L. Qin, Z. Wang, Y. Sun, J. Wan, S. Su, Y. Zhou and J. Xu, "A preliminary study of alterations in default network connectivity in post-traumatic stress disorder patients following recent trauma." *Brain Research,* vol. 1484, pp. 50-56, 2012.

[203] E. von dem Hagen, R. Stoyanova, S. Baron-Cohen and A. Calder, "Reduced functional connectivity within and between 'social' resting state networks in autism spectrum conditions." *Social Cognitive and Affective Neuroscience,* vol. 8, no. 6, pp. 694-701, 2013.

[204] D. Van de Ville, J. Britz and C. Michel, "EEG microstate sequences in healthy humans at rest reveal scale-free dynamics." *Proceedings of National Academy of Sciences of U.S.A.,* vol. 42, pp. 18179-18184, 2010.

[205] C. Inman, G. James, S. Hamann, J. Rajendra, G. Pagnoni and A. Butler, "Altered resting-state effective connectivity of fronto-parietal motor control systems on the primary motor network following stroke." *Neuroimage,* vol. 1, pp. 227-237, 2012.

[206] W. Liao, C. Qiu, C. Gentili, M. Walter, Z. Pan, J. Ding, W. Zhang, Q. Gong and H. Chen, "Altered effective connectivity network of the amygdala in social anxiety disorder: a resting-state fMRI study." *PLoS One,* vol. 12, pp. e15238, 2010.

[207] M. Havlicek, J. Jan, B. Milan and V. D. Calhoun, "Dynamic Granger causality based on Kalman filter for evaluation of functional network connectivity in fMRI data." *Neuroimage,* vol. 53, no. 1, pp. 65-77, 2010.

[208] K. Friston, L. Harrison and W. Penny, "Dynamic causal modeling." *Neuroimage,* vol. 19, no. 4, pp. 1273-1302, 2003.

[209] J. Zhuang, S. LaConte, S. Peltier, K. Zhang and X. Hu, "Connectivity exploration with structural equation modeling: an fMRI study of bimanual motor coordination." *Neuroimage,* vol. 25, no. 2, pp. 462-470, 2005.

[210] G. Deshpande, S. LaConte, G. James, S. Peltier and X. Hu, "Multivariate Granger causality analysis of fMRI data." *Human Brain Mapping,* vol. 30, no. 4, pp. 1361-1373, 2009.

[211] G. Deshpande, K. Sathian and X. Hu, "Assessing and compensating for zero-lag correlation effects in time-lagged Granger causality analysis of fMRI." *IEEE Transactions on Biomedical Engineering,* vol. 57, no. 6, pp. 1446-1456, 2010.

[212] R. Kus, M. Kaminski and K. Blinowska, "Determination of EEG activity propagation: pair-wise versus

multichannel estimate." *IEEE Transactions on Biomedical Engineering,* vol. 51, no. 9, pp. 1501-1510, 2004.

[213] G. Wu, S. Stramaglia, H. Chen, W. Liao and D. Marinazzo, "Mapping the voxel-wise effective connectome in resting state fMRI." *PLoS One,* vol. 8, no. 9, pp. e73670, 2013.

[214] A. McIntosh and F. Gozales-Lima, "Structural equation modelling and its application to network analysis in functional brain imaging." *Human Brain Mapping,* vol. 2, pp. 2-22, 1994.

[215] C. Granger, "Investigating causal relations by econometric models and cross-spectral methods." *Econometrica,* vol. 37, pp. 424–438, 1969.

[216] J. Geweke, "Measurement of linear dependence and feedback between multiple time series." *Journal of the American Statistical Association,* vol. 77, no. 378, pp. 304-313, 1982.

[217] G. Lohmann, K. Erfurth, K. Muller and R. Turner, "Critical comments on dynamic causal modelling." *Neuroimage,* vol. 59, no. 3, pp. 2322-2329, 2012.

[218] C. Büchel and K. Friston, "Dynamic changes in effective connectivity characterized by variable parameter regression and Kalman filtering." *Human Brain Mapping,* vol. 6, no. 5-6, pp. 403-408, 1998.

[219] A. Schlogl, S. Roberts and G. Pfurtscheller, "A criterion for adaptive autoregressive models." in *IEEE (Ed.), Proceedings of the 22nd IEEE International Conference on Engineering in Medicine and Biology*, 2000.

[220] J. Theiler, S. Eubank, A. Longtin, B. Galdrikian and D. Farmer, "Testing for nonlinearity in time series: the method of surrogate data." *Physica D: Nonlinear Phenomena,* vol. 58, no. 1-4, pp. 77-94, 1992.

[221] L. McDowall and R. Dampney, "Calculation of threshold and saturation points of sigmoidal baroreflex function curves." *American Journal of Physiology, Heart and Circulatory Physiology,* vol. 291, no. 4, pp. H2003-H2007, 2006.

[222] B. Kent, J. Drane, B. Blumenstein and J. Manning, "A mathematical model to assess changes in the baroreceptor reflex." *Cardiology,* vol. 57, no. 5, pp. 295-310, 1972.

[223] V. Schöpf, C. Windischberger, S. Robinson, C. Kasess, F. Fischmeister, R. Lanzenberger, J. Albrecht, A. Kleemann, R. Kopietz, M. Wiesmann and E. Moser, "Model-free fMRI group analysis using FENICA." *Neuroimage,* vol. 55, no. 1, pp. 185-193, 2011.

[224] Research Imaging Institute, UT Health Science Center San Antonio, [Online]. Available: http://www.brainmap.org/sleuth/.

[225] N. A. Shapira, Y. Liu, A. He, M. M. Bradley, M. C. Lessig, G. A. James, D. J. Stein, P. J. Lang and W. K. Goodman, "Brain activation by disgust-inducing pictures in obsessive-compulsive disorder." *Biological Psychiatry,* vol. 54, no. 7, pp. 751-756, 2003.

[226] S. Fu, Y. Chen, S. M. Smith, S. D. Iversen and P. M. Matthews, "Effects of word form on brain processing of written chinese." *Neuroimage,* vol. 17, no. 3, pp. 1538-1548, 2002.

[227] U. Sailer, S. Robinson, F. Fischmeister, E. Moser, I. Krypsin-Exner and H. Bauer, "Imaging the changing role of feedback during learning in decision-making." *Neuroimage,* vol. 37, no. 4, pp. 1474-1486, 2007.

[228] E. Ricciardi, D. Bonino, C. Gentili, L. Sani, P. Pietrini and T. Vecchi, "Neural correlates of spatial working memory in humans: a functional magnetic resonance imaging study comparing visual and tactile processes." *Neuroscience,* vol. 139, no. 1, pp. 339-349, 2006.

[229] S. Hu, N. Wei, Q. Wang, L. Yan, E. Wei, M. Zhang, J. Hu, M. Huang, W. Zhou and Y. Xu, "Patterns of brain activation during visually evoked sexual arousal differ between homosexual and heterosexual men." *American Journal of Neuroradiology,* vol. 29, no. 10, pp. 1890-1896, 2008.

[230] J. Medaglia, K. Chiou, J. Slocomb, N. Fitzpatrick, B. Wardecker, D. Ramanathan, J. Vesek, D. Good and F. Hillary, "The less BOLD, the wiser: support for the latent resource hypothesis after traumatic brain injury." *Human Brain Mapping,* vol. 33, no. 4, pp. 979-993, 2012.

[231] S. Bookheimer, T. Zeffiro, T. Blaxton, P. Gaillard and W. Theodore, "Activation of language cortex with automatic speech tasks." *Neurology,* vol. 8, pp. 1151-1157, 2000.

[232] A. Garrett and R. Maddock, "Separating subjective emotion from the perception of emotion-inducing stimuli: an fMRI study." *Neuroimage,* vol. 33, no. 1, pp. 263-274, 2006.

[233] A. L. Bokde, M. Karmann, S. J. Teipel, C. Born, M. Lieb, M. F. Reiser, H. J. Moller and H. Hampel, "Decreased activation along the dorsal visual pathway after a 3-month treatment with galantamine in mild Alzheimer disease: a functional magnetic resonance imaging study." *Journal of Clinical*

Psychopharmacology, vol. 29, no. 2, pp. 147-156, 2009.

[234] J. Ellermann, J. Siegal, J. Strupp, T. Ebner and K. Ugurbil, "Activation of visuomotor systems during visually guided movements: a functional MRI study." *Journal of Magnetic Resonance,* vol. 131, no. 2, pp. 272-285, 1998.

[235] A. Graybiel, "The basal ganglia: learning new tricks and loving it." *Current Opinion in Neurobiology,* vol. 15, no. 6, pp. 638-644, 2005.

[236] A. Aron, H. Fisher, D. Mashek, G. Strong, H. Li and L. Brown, "Reward, motivation, and emotion systems associated with early-stage intense romantic love." *Journal of Neurophysiology,* vol. 94, no. 1, pp. 327-337, 2005.

[237] T. Ishizu and S. Zeki, "Toward a brain-based theory of beauty." *PLoS One,* vol. 6, no. 7, pp. e21852, 2011.

[238] G. Malhi, J. Lagopoulos, A. Owen, B. Ivanovski, R. Shnier and P. Sachdev, "Reduced activation to implicit affect induction in euthymic bipolar patients: an fMRI study." *Journal of Affective Disorders,* vol. 97, no. 1-3, pp. 109-122, 2007.

[239] T. Lee, O. Josephs, R. Dolan and H. Critchley, "Imitating expressions: emotion-specific neural substrates in facial mimicry." *Social Cognitive and Affective Neuroscience,* vol. 1, no. 2, pp. 122-135, 2006.

[240] L. Strathearn, J. Li, P. Fonagy and P. Montague, "What's in a smile? maternal brain responses to infant facial cues." *Pediatrics,* vol. 122, no. 1, pp. 40-51, 2008.

[241] R. Morecraft, C. Geula and M. Mesulam, "Cytoarchitecture and neural afferents of orbitofrontal cortex in the brain of the monkey." *Journal of Comparative Neurology,* vol. 323, no. 3, pp. 341-358, 1992.

[242] S. Lissek, M. Hausmann, F. Knossalla, S. Peters, V. Nicolas, O. Güntürkün and M. Tegenthoff, "Sex differences in cortical and subcortical recruitment during simple and complex motor control: an fMRI study." *Neuroimage,* vol. 37, no. 3, pp. 912-926, 2007.

[243] A. Achim and M. Lepage, "Neural correlates of memory for items and for associations: an event-related functional magnetic resonance imaging study." *Journal of Cognitive Neuroscience,* vol. 17, no. 4, pp. 652-667, 2005.

[244] U. Bingel, J. Lorenz, E. Schoell, C. Weiller and C. Büchel, "Mechanisms of placebo analgesia: rACC recruitment of a subcortical antinociceptive network." *Pain,* vol. 120, no. 1-2, pp. 8-15, 2006.

[245] M. Liljeström, A. Tarkiainen, T. Parviainen, J. Kujala, J. Numminen, J. Hiltunen, M. Laine and R. Salmelin, "Perceiving and naming actions and objects." *Neuroimage,* vol. 41, no. 3, pp. 1132-1141, 2008.

[246] J. Grahn, J. Parkinson and A. Owen, "The cognitive functions of the caudate nucleus." *Progress in Neurobiology,* vol. 86, no. 3, pp. 141-155, 2008.

[247] T. Bliss and G. Collingridge, "A synaptic model of memory: long-term potentiation in the hippocampus." *Nature,* vol. 361, no. 6407, pp. 31-39, 1993.

[248] J. Bogousslavsky, J. Miklossy, J. Deruaz, G. Assal and F. Regli, "Lingual and fusiform gyri in visual processing: a clinico-pathologic study of superior altitudinal hemianopia." *Journal of Neurology, Neurosurgery, Psychiatry,* vol. 50, no. 5, pp. 607-614, 1987.

[249] S. Lacey, H. Hagtvedt, V. Patrick, A. Anderson, R. Stilla, G. Deshpande, X. Hu, J. Sato, S. Reddy and K. Sathian, "Art for reward's sake: visual art recruits the ventral striatum," *Neuroimage,* vol. 55, no. 1, pp. 420-433, 2011.

[250] D. Kapogiannis, G. Deshpande, F. Krueger, M. Thornburg and J. Grafman, "Brain networks shaping religious belief." *Brain Connectivity,* vol. 4, no. 1, pp. 70-79, 2014.

[251] J. Cisler, J. Steele, J. Lenow, S. Smitherman, B. Everett, E. Messias and C. Kilts, "Functional reorganization of neural networks during repeated exposure to the traumatic memory in posttraumatic stress disorder: an exploratory fMRI study." *Journal of Psychiatric Research,* vol. 48, no. 1, pp. 47-55, 2014.

[252] G. Schwartz, "Estimating the dimension of a model." *The Annals of Statistics,* vol. 5, no. 2, pp. 461-464, 1978.

[253] G. Deshpande, X. Hu, S. Lacey, R. Stilla and K. Sathian, "Object familiarity modulates effective connectivity during haptic shape perception." *Neuroimage,* vol. 49, no. 3, pp. 1991-2000, 2010.

[254] F. Krueger, S. Landgraf, E. van der Meer, G. Deshpande and X. Hu, "Effective connectivity of the multiplication network: a functional MRI and multivariate Granger causality mapping study." *Human Brain*

Mapping, vol. 32, no. 9, pp. 1419-1431, 2011.

[255] F. Pruesse, E. van der Meer, G. Deshpande, F. Krueger and I. Wartenburger, "Fluid intelligence allows flexible recruitment of the parieto-frontal network in analogical reasoning." *Frontiers in Human Neuroscience,* vol. 5, pp. 22, 2011.

[256] M. Strenziok, F. Krueger, G. Deshpande, R. Lenroot, E. van der Meer and J. Grafman, "Fronto-parietal regulation of media violence exposure in adolescents: a multi-method study." *Social Cognitive and Affective Neuroscience,* vol. 6, no. 5, pp. 537-547, 2011.

[257] G. Deshpande, X. Hu, R. Stilla and K. Sathian, "Effective connectivity during haptic perception: a study using Granger causality analysis of functional magnetic resonance imaging data." *Neuroimage,* vol. 40, no. 4, pp. 1807-1814, 2008.

[258] B. Hampstead, A. Stringer, R. Stilla, G. Deshpande, X. Hu, A. Moore and K. Sathian, "Activation and effective connectivity changes following explicit-memory training for face-name pairs in patients with mild cognitive impairment: a pilot study." *Neurorehabilitation and Neural Repair,* vol. 25, no. 3, pp. 210-222, 2011.

[259] R. Stilla, G. Deshpande, S. Laconte, X. Hu and K. Sathian, "Posteromedial parietal cortical activity and inputs predict tactile spatial acuity." *Journal of Neuroscience,* vol. 27, no. 41, pp. 11091-11102, 2007.

[260] K. Sathian, S. Lacey, R. Stilla, G. Gibson, G. Deshpande, X. Hu, S. LaConte and C. Glielmi, "Dual pathways for haptic and visual perception of spatial and texture information." *Neuroimage,* vol. 57, no. 2, pp. 462-475, 2011.

[261] R. Stilla, R. Hanna, E. Mariola, G. Deshpande, X. Hu and K. Sathian, "Neural processing underlying tactile microspatial discrimination in the blind: a functional magnetic resonance imaging study." *Journal of Vision,* vol. 8, no. 10, pp. 13.1-19, 2008.

[262] S. Bressler and A. Seth, "Wiener-Granger causality: a well established methodology." *Neuroimage,* vol. 58, no. 2, pp. 323-329, 2011.

[263] P. Liang, Z. Li, G. Deshpande, Z. Wang, X. Hu and K. Li, "Altered causal connectivity of resting state brain networks in amnesic MCI." *PLoS One,* 2014 (in press).

[264] G. Deshpande, L. Libero, K. Sreenivasan, H. Deshpande and R. Kana, "Identification of neural connectivity signatures of autism using machine learning." *Frontiers in Human Neuroscience,* vol. 7, pp. 670, 2013.

[265] D. Bassett, N. Wymbs, M. Porter, P. Mucha, J. Carlson and S. Grafton, "Dynamic reconfiguration of human brain networks during learning." *Proceedings of National Academy of Sciences of U.S.A.,* vol. 108, no. 18, pp. 7641-7646, 2011.

[266] M. Yousef, S. Jung, L. Showe and M. Showe, "Recursive cluster elimination (RCE) for classification and feature selection from gene expression data." *BMC Bioinformatics,* vol. 8, pp. 144, 2007.

[267] G. Deshpande, Z. Li, P. Santhanam, C. D. Coles, M. E. Lynch, S. Hamann and X. Hu, "Recursive cluster elimination based support vector machine for disease state prediction using resting state functional and effective brain connectivity." *PLoS One,* vol. 5, no. 12, pp. e14277, 2010.

[268] V. Vapnik, The Nature of Statistical Learning Theory, New York: Springer, 1995.

[269] L. Wang, Support Vector Machines: Theory and Applications, New York: Springer, 2005.

[270] R. Craddock, P. Holtzheimer III, X. Hu and H. Mayberg, "Disease state prediction from resting state functional connectivity." *Magnetic Resonance in Medicine,* vol. 62, no. 6, pp. 1619–1628, 2009.

[271] I. Inza, P. Larranaga, R. Blanco and A. J. Cerrolaza, "Filter versus wrapper gene selection approches in DNA microarray domains." *Artificial Intelligence in Medicine,* vol. 31, no. 2, pp. 91-103, 2004.

[272] W. Pan, "A comparative review of statistical methods for discovering differentially expressed genes in replicated microarray experiments." *Bioinformatics,* vol. 18, no. 4, pp. 546-554, 2002.

[273] N. Kriegeskorte, W. Simmons, P. Bellgowan and C. Baker, "Circular analysis in systems neuroscience: the dangers of double dipping." *Nature Neuroscience,* vol. 12, no. 5, pp. 535–540, 2009.

[274] D. Garrett, D. A. Peterson, C. W. Anderson and M. H. Thaut, "Comparison of linear, nonlinear, and feature selection methods for EEG signal classification." *IEEE Transactions on Neural Systems and Rehabilitation Engineering,* vol. 11, no. 2, pp. 141-144, 2003.

[275] [Online]. Available: http://www.nitrc.org/projects/bnv/.

[276] R. Kleiger, J. Miller, J. Bigger and A. Moss, "Decreased heart rate variability and its association with increased mortality after acute myocardial infarction." *American Journal of Cadiology,* vol. 59, no. 4, pp. 256–262, 1987.

[277] American Psychiatric Association, Diagnostic and statistical manual of mental disorders (DSM IV). 4th ed., Washington D.C.: American Psychiatric Association, 1994.

[278] R. Yehuda, "Post-traumatic stress disorder." *New England Journal of Medicine,* vol. 346, no. 2, pp. 108-114, 2002.

[279] M. Whalley, M. Kroes, Z. Huntley, M. Rugg, S. Davis and C. Brewin, "An fMRI investigation of posttraumatic flashbacks." *Brain and Cognition,* vol. 81, no. 1, pp. 151-159, 2013.

[280] A. Jatzko, A. Schmitt, T. Demirakca, E. Weimer and D. Braus, "Disturbance in the neural circuitry underlying positive emotional processing in post-traumatic stress disorder (PTSD). An fMRI study." *European Archives of Psychiatry & Clinical Neuroscience,* vol. 256, no. 2, pp. 112-114, 2006.

[281] Y. Yin, C. Jin, L. T. Eyler, H. Jin, X. Hu, L. Duan, H. Zheng, B. Feng, X. Huang, B. Shan, Q. Gong and L. Li, "Altered regional homogeneity in post-traumatic stress disorder: a resting-state functional magnetic resonance imaging study." *Neuroscience Bulletin,* vol. 28, no. 5, pp. 541-549, 2012.

[282] J. Schmahmann and D. Pandya, "The cerebrocerebellar system." in *The Cerebellum and Cognition*, San Diego, California, USA, Academic Press, 1997, pp. 31-60.

[283] U. Wolf, M. Rapoport and T. Schweizer, "Evaluating the affective component of the cerebellar cognitive affective syndrome." *Journal of Neuropsychiatry & Clinical Neuroscience,* vol. 21, no. 3, pp. 245-253, 2009.

[284] L. Baldacara, A. Jackowski, A. Schoedl, M. Pupo, S. Andreoli, M. Mello, A. Lacerda, J. Mari and R. Bressan, "Reduced cerebellar left hemisphere and vermal volume in adults with PTSD from a community sample." *Journal of Psychiatric Research,* vol. 45, no. 12, pp. 1627-1633, 2011.

[285] M. D. De Bellis and M. Kuchibhatla, "Cerebellar volumes in pediatric maltreatment-related posttraumatic stress disorder." *Biological Psychiatry,* vol. 60, no. 7, pp. 697-703, 2006.

[286] K. Coffman, R. Dum and P. Strick, "Cerebellar vermis is a target of projections from the motor areas in the cerebral cortex." *Proceedings of National Academy of Sciences of U.S.A.,* vol. 108, no. 38, pp. 16068-16073, 2011.

[287] G. Baylis and E. Rolls, "Responses of neurons in the inferior temporal cortex in short term and serial recognition memory tasks." *Experimental Brain Research,* vol. 65, no. 3, pp. 614-622, 1987.

[288] A. Dove, M. Brett, R. Cusack and A. Owen, "Dissociable contributions of the mid-ventrolateral frontal cortex and the medial temporal lobe system to human memory." *Neuroimage,* vol. 31, no. 4, pp. 1790-1801, 2006.

[289] C. Hattingh, J. Ipser, S. Tromp, S. Syal, C. Lochner, S. Brooks and D. Stein, "Functional magnetic resonance imaging during emotion recognition in social anxiety disorder: an activation likelihood meta-analysis." *Frontiers in Human Neuroscience,* vol. 6, pp. 347, 2013.

[290] E. Lindemer, D. Salat, E. Leritz, R. McGlinchey and W. Milberg, "Reduced cortical thickness with increased lifetime burden of PTSD in OEF/OIF veterans and the impact of comorbid TBI." *Neuroimage: Clinical,* vol. 2, pp. 601-611, 2013.

[291] K. Moores, C. Clark, A. McFarlane, G. Brown, A. Puce and D. Taylor, "Abnormal recruitment of working memory updating networks during maintenance of trauma-neutral information in post-traumatic stress disorder." *Psychiatry Research,* vol. 163, no. 2, pp. 156-170, 2008.

[292] A. Kemp, K. Felmingham, E. Falconer, B. Liddell, R. Bryant and L. Williams, "Heterogeneity of non-conscious fear perception in posttraumatic stress disorder as a function of physiological arousal: an fMRI study." *Psychiatry Research,* vol. 174, no. 2, pp. 158-161, 2009.

[293] R. Herringa, M. Phillips, J. Almeida, S. Insana and A. Germain, "Post-traumatic stress symptoms correlate with smaller subgenual cingulate, caudate, and insula volumes in unmedicated combat veterans." *Psychiatry Research,* vol. 203, no. 2-3, pp. 139-145, 2012.

[294] M. Shaw, K. Moores, R. Clark, A. McFarlane, S. Strother, R. Bryant, G. Brown and J. Taylor, "Functional connectivity reveals inefficient working memory systems in post-traumatic stress disorder." *Psychiatry Research,* vol. 172, no. 3, pp. 235-241, 2009.

[295] I. Mutschler, T. Ball, J. Wankerl and I. Strigo, "Pain and emotion in the insular cortex: evidence for

functional reorganization in major depression." *Neuroscience Letters,* vol. 520, no. 2, pp. 204-209, 2012.

[296] I. Strigo, S. Matthews and A. Simmons, "Decreased frontal regulation during pain anticipation in unmedicated subjects with major depressive disorder." *Translational Psychiatry,* vol. 3, pp. e239, 2013.

[297] P. Fusar-Poli, A. Placentino, F. Carletti, P. Landi, P. Allen, S. Surguladze, F. Benedetti, M. Abbamonte, R. Gasparotti, F. Barale, J. Perez, P. McGuire and P. Politi, "Functional atlas of emotional faces processing: a voxel-based meta-analysis of 105 functional magnetic resonance imaging studies." *Journal of Psychiatry Neuroscience,* vol. 34, no. 6, pp. 418-432, 2009.

[298] R. Viviani, G. Grön and M. Spitzer, "Functional principal component analysis of fMRI data." *Human Brain Mapping,* vol. 24, no. 2, pp. 109-129, 2005.

[299] M. van den Heuvel, C. Stam, M. Boersma and H. Hulshoff Pol, "Small-world and scale-free organization of voxel-based resting-state functional connectivity in the human brain." *Neuroimage,* vol. 43, no. 3, pp. 528-539, 2008.

[300] M. van den Heuvel, R. Mandl and H. Hulshoff Pol, "Normalized cut group clustering of resting-state fMRI data." *PLoS One,* vol. 3, no. 4, pp. e2001, 2008.

[301] M. Arnold, W. Miltner, H. Witte, R. Bauer and C. Braun, "Adaptive AR modeling of nonstationary time series by means of Kalman filtering." *IEEE Transactions on Biomedical Engineering,* vol. 45, no. 5, pp. 553-562, 1998.

Appendix A

A.1 Selection of Sliding Window Length Range

In this work, we use sliding windows to calculate dynamic FC at each time instant. The window length is determined by Dickey-Fuller (DF) test. However, this hypothesis test is just for testing stationarity for a given time series, i.e. to test the existence of unit root. It does not provide the window length that is most appropriate for correlation calculation. Consequently, there remain two issues to solve. First, at a given time point, for all window lengths that can successfully reject the null hypothesis (i.e. those window lengths within which the time series are stationary), which one should be chosen for appropriate calculation of dynamic FC? Second, within what range of window lengths should the DF test be conducted?

We adopt the following strategy in order to answer the first question. At a given time point, we start performing the DF test from the specified minimum window length and increase the window length by one time point (or one TR) if it could not reject the null hypothesis. Once stationarity is established at some window length for all 190 regions, we stop performing the test and use these windowed time series to calculate FC. In other words, the minimum length of the window which is stationary for all 190 regions is used. This strategy ensures that maximum available dynamics in FC is captured.

The second question pertains to the specification of the range of window length [m_-, m_+] within which the DF test should be conducted. The factors guiding the choice of the window length are elaborated below. Time series $y(t)$ can be modeled as an AR (1) process shown by the equation below

$$y(t) = \alpha y(t-1) + \varepsilon(t) \tag{A1}$$

Where t is the time index, α is a coefficient, and $\varepsilon(t)$ is the error term. A unit root is present when $\alpha = 1$, in which case, the mean and variance of $y(t)$ are a function of time (t). This implies that $y(t)$ is non-stationary.

$$\Delta y(t) = \gamma y(t-1) + \varepsilon(t) \tag{A2}$$

The DF test informs whether the process $y(t)$ is stationary or not within a given window. Given that our time series are restricted to the frequency band [0.01, 0.1] Hz, we provide a frequency domain explanation for the choice of minimum and maximum window lengths considered in this work. For a signal with highest and lowest frequencies of 0.1 Hz and 0.01 Hz, period T ranges from 10s to 100s. If we chose the maximum window length to be 100s, we can make sure that the window covers at least one period of the slowest varying signal component. Similarly, if we chose a minimum window length of 10s, we can guarantee that the window covers at least one period of the fastest varying signal component. It is imperative that the window encompasses at least one period of signal variation to capture all its dynamics. The above strategy ensures that the minimum window length can capture maximum available dynamics. Since fMRI data used in this work had a TR=0.72s, the minimum window length should be at least 10/0.72=14 (TRs), and maximum length should be 100/0.72=140 (TRs). This range was employed in this work.

As for simulations, we assumed the sampling rate was 1 sample/s (TR=1s), so to be consistent, the minimum window length should be 10/1=10 (TRs), and maximum length should be 100/1=100 (TRs), as stated in the main text.

A.2 190 ROI Version of CC200 Atlas: Anatomical Labels and MNI Co-ordinates

Table A1. MNI co-ordinates of the centroids of 190 regions of CC200 atlas with corresponding AAL anatomical labels

Region No.	AAL label of region centroid	Coordinate x (mm)	Coordinate y (mm)	Coordinate z (mm)
1	Pons	-3	-25	-38
2	Frontal_Sup_Orb_R	12	59	-22

3	Frontal_Inf_Tri_R	49	35	14
4	Lingual_R	22	-58	0
5	Insula_R	38	-6	9
6	Putamen_L	-25	-5	-8
7	Cerebelum_6_L	-29	-38	-35
8	Temporal_Mid_R	71	-30	-2
9	Precuneus_R	18	-65	25
10	Frontal_Sup_Medial_L	-1	25	41
11	ParahippocampaGyrus	-21	-26	-14
12	Temporal_Pole_Mid_L	-31	19	-40
13	Frontal_Sup_L	-13	46	42
14	Frontal_Inf_Orb_L	-20	9	-25
15	Temporal_Inf_R	63	-28	-26
16	Cerebelum_Crus1_L	-48	-67	-32
17	Postcentral_R	15	-43	75
18	Precuneus_L	-13	-64	64
19	Temporal_Mid_R	63	-7	-18
20	Frontal_Mid_R	35	14	57
21	Paracentral_Lobule_R	15	-35	48
22	Fusiform_L	-23	3	-47
23	Frontal_Inf_Tri_L	-45	37	11
24	Cuneus_L	-9	-90	33
25	Lingual_R	19	-99	-10
26	Cerebelum_Crus1_R	50	-68	-34
27	Caudate_R	15	14	2
28	Temporal_Sup_L	-62	-26	13
29	Caudate_L	-14	-8	19
30	Supp_Motor_Area_R	15	8	67
31	Temporal_Mid_L	-58	-5	-20
32	Calcarine_R	3	-80	7
33	Frontal_Mid_Orb_L	-31	57	-13
34	Frontal_Inf_Orb_R	50	36	-12
35	Brainstem	2	-43	-61
36	Rectus_R	12	37	-29
37	SupraMarginal_R	63	-45	33
38	Precuneus_L	-10	-78	50
39	Precentral_R	38	-18	66
40	Pallidum_R	24	-7	-5
41	Thalamus_R	20	-31	9
42	Postcentral_R	35	-45	67
43	Frontal_Inf_Orb_L	-46	37	-13
44	Temporal_Pole_Mid_R	34	20	-42
45	Cerebelum_8_R	39	-65	-56
46	SupraMarginal_L	-59	-29	39
47	Cingulum_Ant_L	-10	45	10

48	Parietal_Inf_R	34	-51	42
49	Caudate_Head_L	-11	12	4
50	Lingual_L	-19	-76	-9
51	Supp_Motor_Area_L	-12	-10	73
52	Cerebelum_Crus2_L	-34	-78	-44
53	Precentral_R	24	-4	50
54	Insula_R	36	20	1
55	Postcentral_R	40	-22	43
56	Cerebelum_8_L	-31	-63	-59
57	Temporal_Inf_R	63	-47	-18
58	Cuneus_L	-13	-69	25
59	Occipital_Mid_R	39	-82	30
60	Temporal_Inf_L	-55	-15	-37
61	Insula_L	-35	-7	11
62	Thalamus_R	3	-14	7
63	Cerebelum_6_R	27	-62	-31
64	Temporal_Mid_R	51	-32	-3
65	Cingulum_Mid_L	-12	-37	50
66	Temporal_Inf_R	56	-13	-38
67	Frontal_Mid_L	-45	23	36
68	Frontal_Mid_R	47	27	37
69	Frontal_Mid_L	-28	21	48
70	Cuneus_R	16	-100	12
71	Temporal_Inf_L	-39	-23	-27
72	Frontal_Sup_R	15	47	43
73	Cerebelum_Crus2_L	-13	-80	-49
74	Cingulum_Post_L	0	-43	27
75	Fusiform_L	-34	-11	-43
76	Postcentral_L	-38	-24	42
77	Occipital_Mid_R	35	-89	8
78	Frontal_Sup_Orb_L	-8	40	-29
79	Frontal_Mid_L	-31	39	28
80	Precentral_L	-47	0	49
81	Fusiform_R	24	3	-47
82	Cingulum_Mid_R	2	6	35
83	Frontal_Sup_Medial_R	10	60	25
84	Temporal_Inf_R	42	-3	-47
85	Lingual_L	-16	-59	1
86	Occipital_Mid_L	-28	-96	-2
87	Precentral_R	50	0	50
88	Calcarine_L	-8	-99	-11
89	Frontal_Mid_L	-26	-3	54
90	Frontal_Mid_Orb_R	33	57	-14
91	Frontal_Sup_L	-16	58	26
92	Angular_R	55	-66	32

93	Precentral_R	16	-17	73
94	Cerebelum_Crus2_L	-46	-51	-47
95	Parietal_Sup_L	-32	-50	65
96	Cerebelum_Crus2_R	33	-84	-37
97	Cerebelum_8_R	17	-76	-52
98	Temporal_Mid_R	65	-53	7
99	Cingulum_Mid_L	0	-18	33
100	Cerebelum_8_L	-21	-44	-52
101	Temporal_Mid_L	-61	-55	10
102	Temporal_Pole_Mid_R	51	11	-32
103	Temporal_Inf_L	-46	5	-39
104	Frontal_Sup_R	14	30	57
105	Thalamus_L	-16	-31	9
106	Postcentral_L	-57	-7	28
107	Frontal_Mid_R	42	50	4
108	Frontal_Mid_L	-33	54	7
109	Temporal_Sup_R	63	-8	6
110	ParaHippocampal_R	19	-12	-26
111	Lingual_R	21	-74	-11
112	Cingulum_Ant_R	2	27	21
113	Vermis_9	1	-55	-41
114	Temporal_Mid_L	-64	-24	-16
115	Postcentral_R	58	-25	49
116	Insula_L	-33	20	2
117	Caudate_R	16	-7	20
118	Angular_L	-48	-74	29
119	Frontal_Mid_Orb_L	-25	34	-17
120	Postcentral_R	60	-2	29
121	Olfactory	0	0	-13
122	Occipital_Mid_L	-30	-87	23
123	Fusiform_R	37	-18	-33
124	Frontal_Sup_Medial_L	-11	66	5
125	Temporal_Mid_R	50	-75	8
126	Vermis_4_5	2	-49	6
127	SupraMarginal_R	65	-25	25
128	Precentral_L	-29	-25	67
129	Insula_R	42	-7	-14
130	Frontal_Sup_Medial_L	-10	31	56
131	Parietal_Sup_R	18	-63	65
132	Temporal_Inf_L	-53	-61	-11
133	Occipital_Inf_R	41	-86	-14
134	Frontal_Sup_Medial_R	10	67	-1
135	Temporal_Sup_L	-42	-17	-7
136	Vermis_6	0	-64	-20
137	Occipital_Sup_R	15	-89	33

138	Frontal_Med_Orb_R	0	35	-10
139	Supp_Motor_Area_L	-11	11	65
140	Parietal_Inf_R	53	-47	54
141	Frontal_Mid_R	33	47	26
142	Cerebelum_8_R	32	-41	-46
143	Fusiform_L	-28	-44	-12
144	Cerebelum_9_L	-7	-61	-57
145	Precuneus_L	0	-57	45
146	Temporal_Pole_Sup_R	55	11	-6
147	SupraMarginal_L	-58	-50	32
148	Rolandic_Oper_L	-56	1	2
149	Cerebelum_Crus2_L	-14	-87	-30
150	Vermis_1_2	-2	-43	-23
151	Supp_Motor_Area_L	-2	-11	54
152	Angular_R	40	-69	51
153	Temporal_Mid_R	46	-53	17
154	Fusiform_R	44	-43	-24
155	Cerebelum_8_R	19	-55	-58
156	Precuneus_L	-12	-46	73
157	Parietal_Inf_L	-49	-54	51
158	ParaHippocampal_L	-18	-14	-28
159	Temporal_Pole_Sup_L	-42	13	-20
160	Cerebelum_3_R	15	-32	-39
161	Frontal_Mid_R	25	28	38
162	Occipital_Mid_L	-46	-80	4
163	Postcentral_L	-48	-26	58
164	Frontal_Inf_Oper_R	40	9	29
165	Midbrain	0	-24	-12
166	Precentral_L	-37	6	29
167	Rolandic_Oper_L	-40	-33	17
168	RectalGyrus	3	19	-26
169	Parietal_Inf_L	-32	-51	41
170	Frontal_Inf_Oper_L	-52	18	13
171	Occipital_Sup_L	-10	-101	12
172	Frontal_Inf_Orb_R	28	34	-17
173	Frontal_Sup_R	27	62	9
174	Cerebelum_6_L	-26	-62	-30
175	Fusiform_R	26	-38	-13
176	Rolandic_Oper_R	43	-27	17
177	Paracentral_Lobule_L	-4	-29	72
178	Temporal_Inf_R	51	-64	-11
179	Temporal_Mid_L	-42	-58	15
180	Temporal_Inf_L	-52	-42	-26
181	Fusiform_L	-38	-83	-18
182	Cerebelum_Crus2_R	51	-50	-44

183	Parietal_Inf_L	-33	-75	48
184	Parietal_Sup_R	16	-76	52
185	Temporal_Pole_Sup_R	28	10	-25
186	Cerebelum_Crus2_R	11	-86	-31
187	Temporal_Mid_L	-58	-39	-5
188	Rectus_L	-9	60	-17
189	Cingulum_Ant_R	13	44	6
190	Frontal_Inf_Oper_R	57	16	16

A.3 Description of Behavioral Measures Employed in This Work

Table A2. Description of categorized behavioral measures employed in this work (For more details, please refer to HCP Q3 release manual (http://humanconnectome.org/documentation/Q3/Q3_Release_Reference_Manual.pdf).)

Category: Alertness		
Variable Name	Description	Values
Instrument: Cognitive Status (Mini Mental Status Exam/MMSE)		
1. MMSE Score	Mini Mental Status Exam Total Score	
Instrument: Sleep (Pittsburgh Sleep Questionnaire/PSQI)		
2. PSQI Score	Sleep (Pittsburgh Sleep Questionnaire) Total Score	
Category: Cognition		
Variable Name	Description	Values
Instrument: Episodic Memory (Picture Sequence Memory)		
3. Picture Sequence Unadjusted	NIH Toolbox Picture Sequence Memory Test Unadjusted Scale Score	
4. Picture Sequence Adjusted	NIH Toolbox Picture Sequence Memory Test Age-Adjusted Scale Score	
Instrument: Executive Function/Cognitive Flexibility (Dimensional Change Card Sort)		
5. Card Sort Unadjusted	NIH Toolbox Dimensional Change Card Sort Test Unadjusted Scale Score	
6. Card Sort Adjusted	NIH Toolbox Dimensional Change Card Sort Test Age-Adjusted Scale Score	
Instrument: Executive Function/Inhibition (Flanker Task)		
7. Flanker Task Unadjusted	NIH Toolbox Flanker Inhibitory Control and Attention Test Unadjusted Scale Score	
8. Flanker Task Adjusted	NIH Toolbox Flanker Inhibitory Control and Attention Test Adjusted Scale Score	
Instrument: Fluid Intelligence (Penn Progressive Matrices)		
9. PMAT24_A_CR	Penn Matrix Test: Number of Correct Responses	0-24
10. PMAT24_A_SI	Penn Matrix Test: Total Skipped Items (items not presented because maximum errors allowed reached)	0-19
11. PMAT24_A_RTCR	Penn Matrix Test: Median Reaction Time for Correct Responses	Typical range: 2730…51730

Instrument: Language/Reading Decoding (Oral Reading Recognition)		
12. Reading Test Unadjusted	NIH Toolbox Oral Reading Recognition Test Unadjusted Scale Score	
13. Reading Test Adjusted	NIH Toolbox Oral Reading Recognition Test Adjusted Scale Score	
Instrument: Language/Receptive vocabulary		
14. Picture Vocabulary Test Unadjusted	NIH Toolbox Picture Vocabulary Test Unadjusted Scale Score	
15. Picture Vocabulary Test Adjusted	NIH Toolbox Picture Vocabulary Test Adjusted Scale Score	
Instrument: Processing Speed (Pattern Completion Processing Speed)		
16. Processing Speed Unadjusted	NIH Toolbox Pattern Comparison Processing Speed Test Unadjusted Scale Score	
17. Processing Speed Adjusted	NIH Toolbox Pattern Comparison Processing Speed Test Adjusted Scale Score	
Instrument: Self-regulation/Impulsivity (Delay Discounting)		
18. SV_1mo_200	Subjective Value for $200 at 1 month	0-200
19. SV_6mo_200	Subjective Value for $200 at 6 months	0-200
20. SV_3yr_200	Subjective Value for $200 at 3 years	0-200
21. SV_1yr_200	Subjective Value for $200 at 1 year	0-200
22. SV_5yr_200	Subjective Value for $200 at 5 years	0-200
23. SV_10yr_200	Subjective Value for $200 at 10 years	0-200
24. SV_1mo_40K	Subjective Value for $40,000 at 1 month	0-40000
25. SV_6mo_40K	Subjective Value for $40,000 at 6 months	0-40000
26. SV_1yr_40K	Subjective Value for $40,000 at 1 year	0-40000
27. SV_3yr_40K	Subjective Value for $40,000 at 3 years	0-40000
28. SV_5yr_40K	Subjective Value for $40,000 at 5 years	0-40000
29. SV_10yr_40K	Subjective Value for $40,000 at 10 years	0-40000
30. AUC_200	Area Under the Curve for Discounting of $200	0.0-1.0
31. AUC_40K	Area Under the Curve for Discounting of $40,000	0.0-1.0
Instrument: Spatial Orientation (Variable Short Penn Line Orientation Test)		
32. VSPLOT_TC	Penn Line Orientation: Total Number Correct	0-24
33. VSPLOT_CRTE	Penn Line Orientation: Median Reaction Time Divided by Expected Number of Clicks for Correct Trials	Typical range: 640…2800
34. VSPLOT_OFF	Penn Line Orientation: Total Positions Off for All Trials	0-165
Instrument: Sustained Attention (Short Penn Continuous Performance Test)		
35. SCPT_TP	Short Penn CPT True Positives = Sum of CPN_TP and CPL_TP	0-60
36. SCPT_TN	Short Penn CPT True Negatives = Sum of CPN_TN and CPL_TPN	0-120
37. SCPT_FP	Short Penn CPT False Positives = Sum of CPN_FP and CPL_FP	0-120

38. SCPT_FN	Short Penn CPT False Negatives = Sum of CPN_FN and CPL_FN	0-60
39. SCPT_TPRT	Short Penn CPT Median Response Time for True Positive Responses	0-1000 ms
40. SCPT_SEN	Short Penn CPT Sensitivity = SCPT_TP/(SCPT_TP + SCPT_FN)	Typical range: 0.8-1.0
41. SCPT_SPEC	Short Penn CPT Specificity = SCPT_TN/(SCPT_TN + SCPT_FP)	Typical range: 0.8-1.0
42. CPT_LRNR	Short Penn CPT Longest Run of Non-Responses)	5-16
Instrument: Verbal Episodic Memory (Penn Word Memory Test)		
43. IWRD_TOT	Penn Word Memory: Total Number of Correct Responses	0-40
44. IWRD_RTC	Penn Word Memory: Median Reaction Time for Correct Responses	Typical range: 1100-3200
Instrument: Working Memory (List Sorting)		
45. List Sorting Unadjusted	NIH Toolbox List Sorting Working Memory Test Unadjusted Scale Score	
46. List Sorting Adjusted	NIH Toolbox List Sorting Working Memory Test Adjusted Scale Score	
Category: Emotion		
Variable Name	Description	Values
Instrument: Emotion Recognition (Penn Emotion Recognition Test)		
47. ER40_CR	Penn Emotion Recognition: Number of Correct Responses	0-40
48. ER40_CRT	Penn Emotion Recognition: Correct Responses Median Response Time (ms)	Typical range: 1435-2746
49. ER40ANG	Penn Emotion Recognition: Correct Anger Identifications	0-8
50. ER40FEAR	Penn Emotion Recognition: Correct Fear Identifications	0-8
51. ER40HAP	Penn Emotion Recognition: Correct Happy Identifications	0-8
52. ER40NOE	Penn Emotion Recognition: Correct Neutral Identifications	0-8
53. ER40SAD	Penn Emotion Recognition: Correct Sad Identifications	0-8
Instrument: Negative Affect		
54. Anger-Affect	NIH Toolbox Anger-Affect Survey	
55. Anger-Hostility	NIH Toolbox Anger-Hostility Survey	
56. Anger-Aggression	NIH Toolbox Anger-Physical Aggression Survey	
57. Fear-Affect	NIH Toolbox Fear-Affect Survey	
58. Fear-Somatic	NIH Toolbox Fear-Somatic Arousal Survey	
59. Sadness	NIH Toolbox Sadness Survey	

Instrument: Psychological Well-being		
60. Life Satisfaction	NIH Toolbox General Life Satisfaction Survey	
61. Meaning and Purpose	NIH Toolbox Meaning and Purpose Survey	
62. Positive Affect	NIH Toolbox Positive Affect Survey	
Instrument: Social Relationships		
63. Friendship	NIH Toolbox Friendship Survey	
64. Loneliness	NIH Toolbox Loneliness Survey	
65. Perceived Hostility	NIH Toolbox Perceived Hostility Survey	
66. Perceived Rejection	NIH Toolbox Perceived Rejection Survey	
67. Emotional Support	NIH Toolbox Emotional Support Survey	
68. Instrumental Support	NIH Toolbox Instrumental Support Survey	
Instrument: Stress and Self Efficacy		
69. Perceived Stress	NIH Toolbox Perceived Stress Survey	
70. Self-Efficacy	NIH Toolbox Self-Efficacy Survey	
Category: Personality		
Variable Name	Description	Values
Instrument: Five-Factor Model (NEO-FFI)		
71. NEOFAC_A	NEO-FFI Agreeableness	Typical range: 19-44
72. NEOFAC_O	NEO-FFI Openness	14-42
73. NEOFAC_C	NEO-FFI Conscientiousness	23-46
74. NEOFAC_N	NEO-FFI Neuroticism	4-36
75. NEOFAC_E	NEO-FFI Extroversion	11-45

A.4 Paths with Most and Least MTSTs

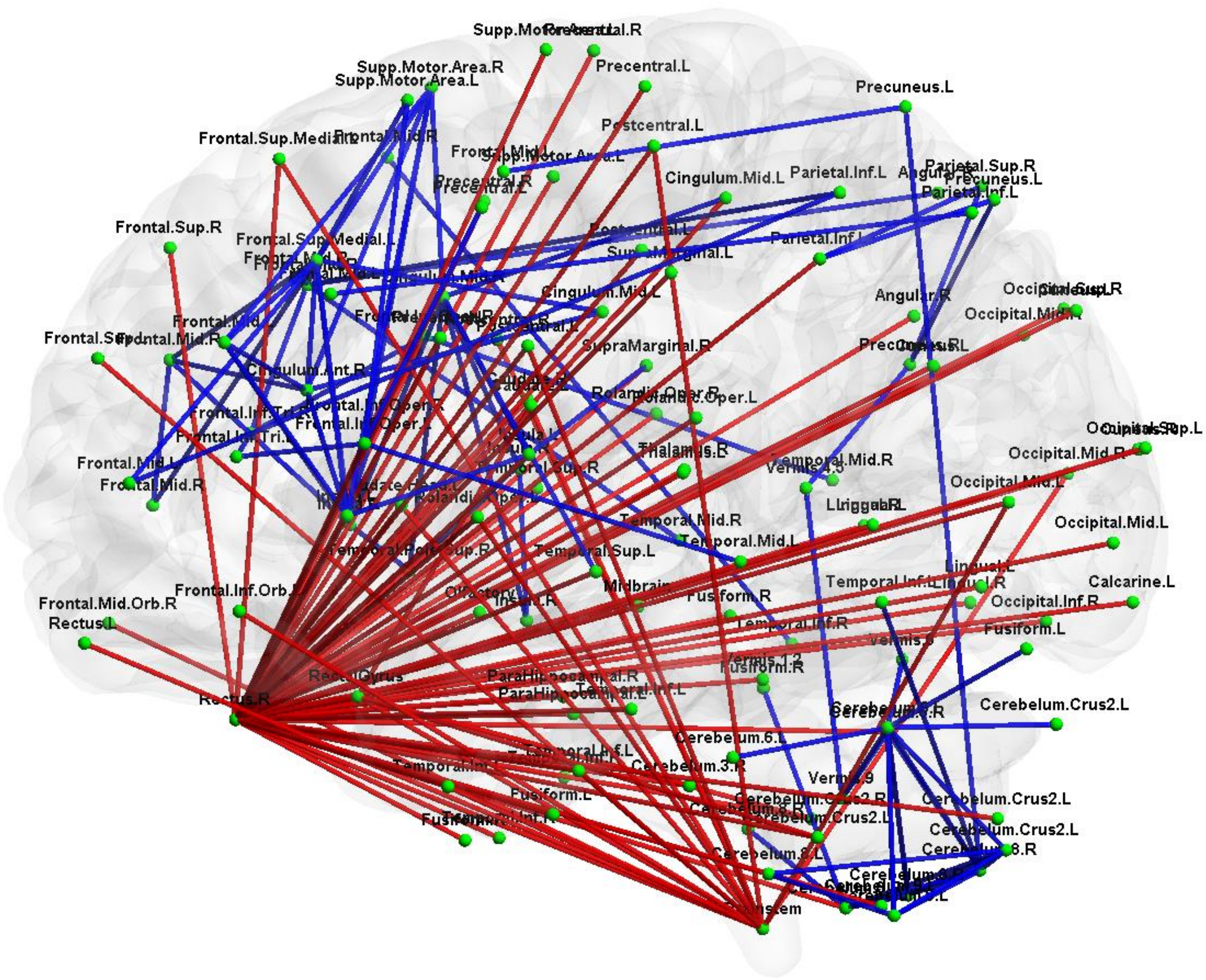

Figure A1 Paths with top and bottom 0.5% MTSTs. The red paths represent interregional MTSTs whose values are among the top 0.5% of all MTSTs, and blue paths represent interregional MTSTs whose values are among the bottom 0.5% of all MTSTs. The MTSTs mentioned here have been averaged over all runs.

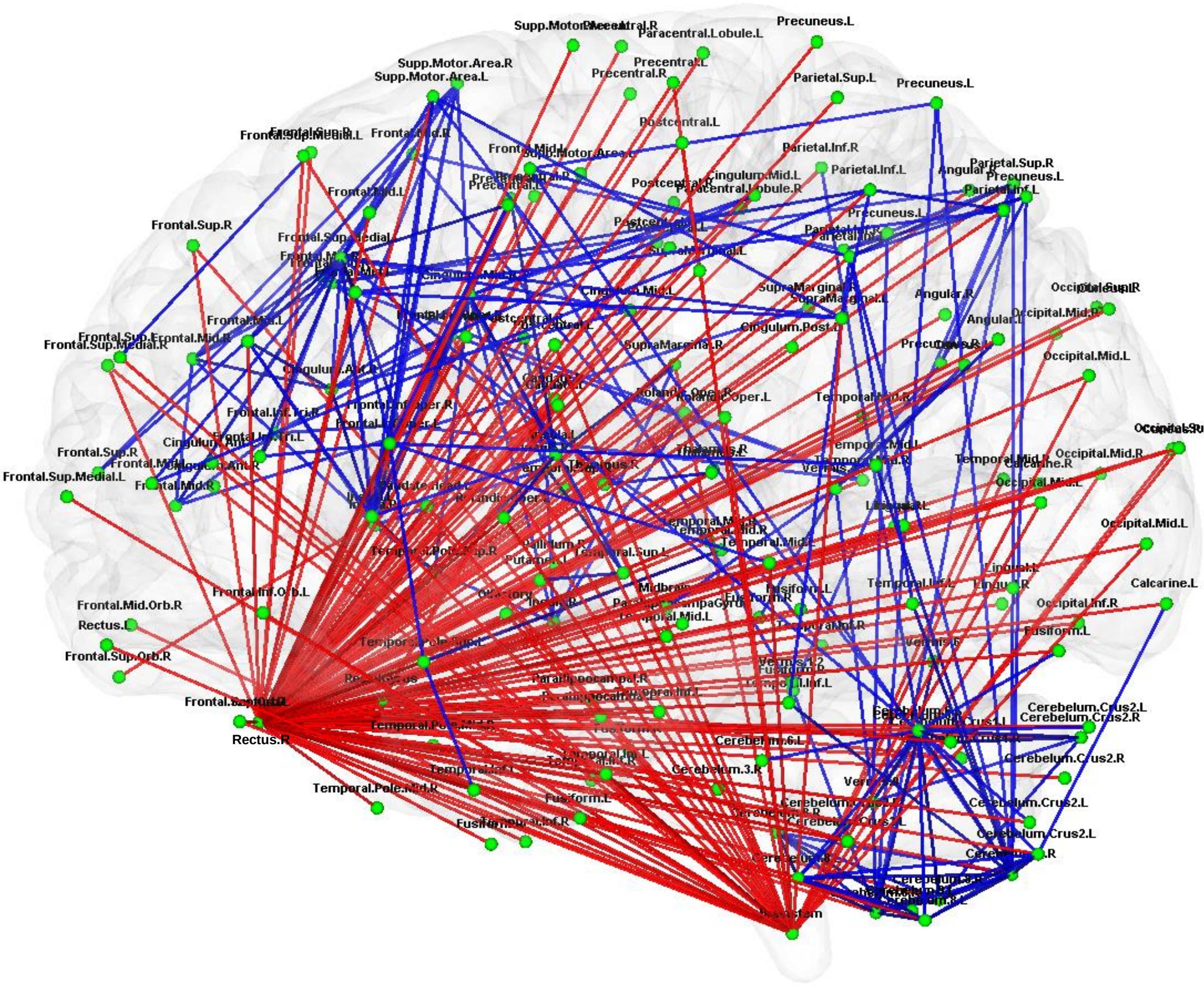

Figure A2 Paths with top and bottom 1% MTSTs. The red paths represent interregional MTSTs whose values are among the top 1% of all MTSTs, and blue paths represent interregional MTSTs whose values are among the bottom 1% of all MTSTs. The MTSTs mentioned here have been averaged over all runs.

A.5 Regions with Top and Bottom 20% rMTST and rCFP

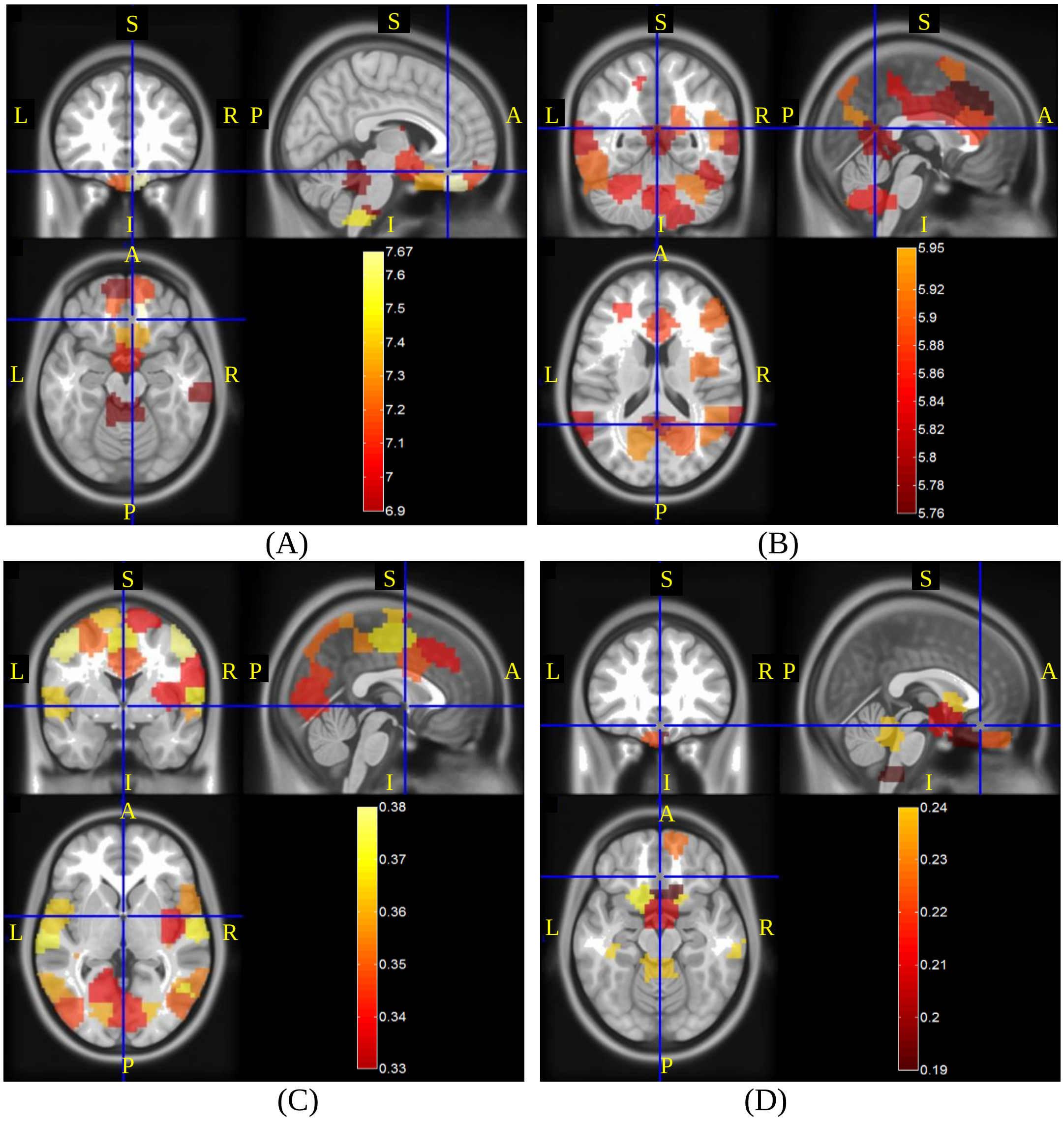

(A) (B)

(C) (D)

Figure A3 Regions with top and bottom 20% rMTST and rCFP. Each brain region has 189 paths associated with it and hence the same number of MTSTs and CFPs. We define metrics, regional MTST (rMTST) and regional CFP (rCFP), by finding the mean MTST/CFP of all paths associated with a given region. Regions within top 20% of all rMTSTs are shown in (A) and within bottom 20% of all rMTSTs are shown in (B).Corresponding maps for top and bottom 20% rCFPs are shown in (C) and (D), respectively. Hot colormap is used to represent the numeric value of corresponding metric for each region shown. (A: anterior, P: posterior, S: superior, I: inferior, L: left, R: right)

Compared with Fig.4.8 in main text, there are fewer regions highlighted in Fig.A3. It is noteworthy that some important resting state networks are even missing, like visual network in Fig.4.8 (A) in main text and so do some important regions like anterior cingulate cortex (ACC) in Fig.4.8 (A) and posterior cingulate cortex (PCC) in (C) in main text. This implies that with proportions of only top and bottom 20%, Fig.A3 is not as informative as Fig.4.8, missing some important regional information. On the other hand, if more than 30% of rMTSTs and rCFPs are shown, the amount of regions will be too numerous for any meaningful visualization. Thus we choose to illustrate top and bottom 30% of rMTSTs and rCFPs in Fig.4.8 of the main text.

A.6 Paths with MTSTs Significantly Correlating with Selected Behavioral Measures

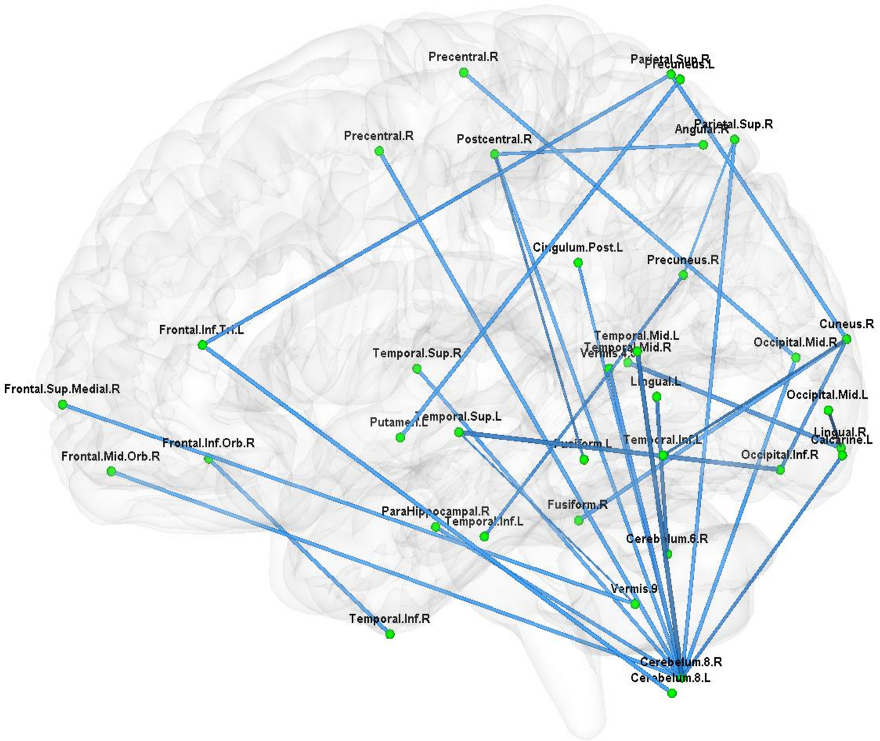

(A) Episodic memory (picture sequence unadjusted)

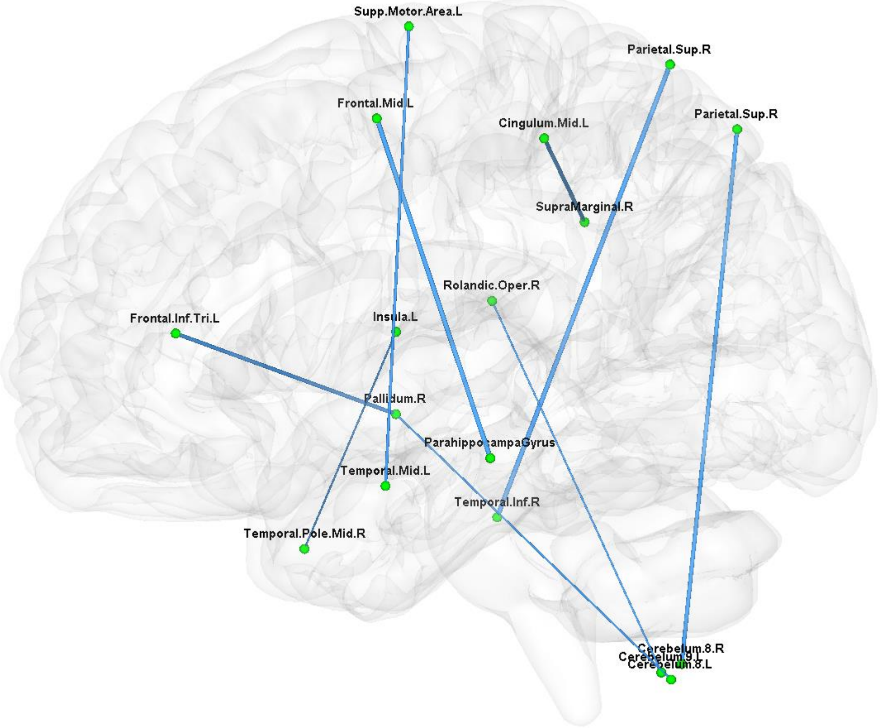

(B) Fluid intelligence (PMAT24_A_CR)

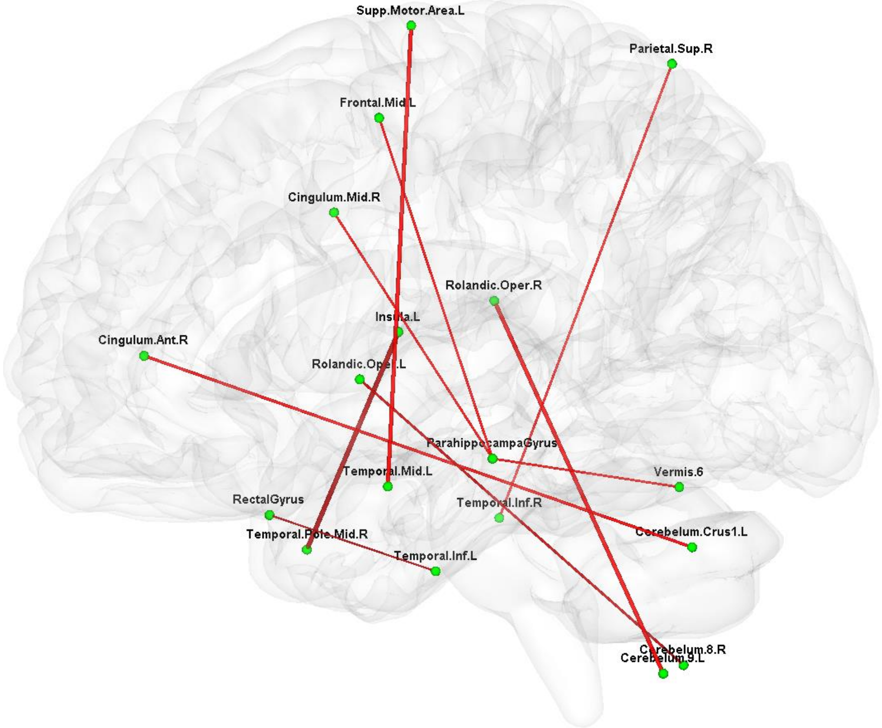

(C) Fluid intelligence (PMAT24_A_SI)

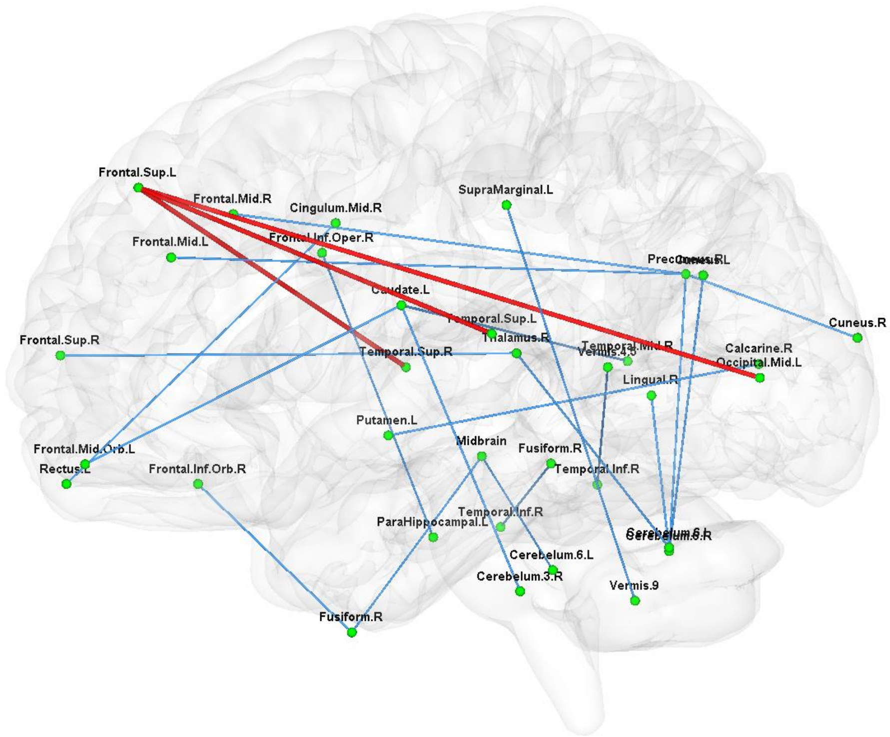

(D) Self-regulation/impulsivity (AUC_200)

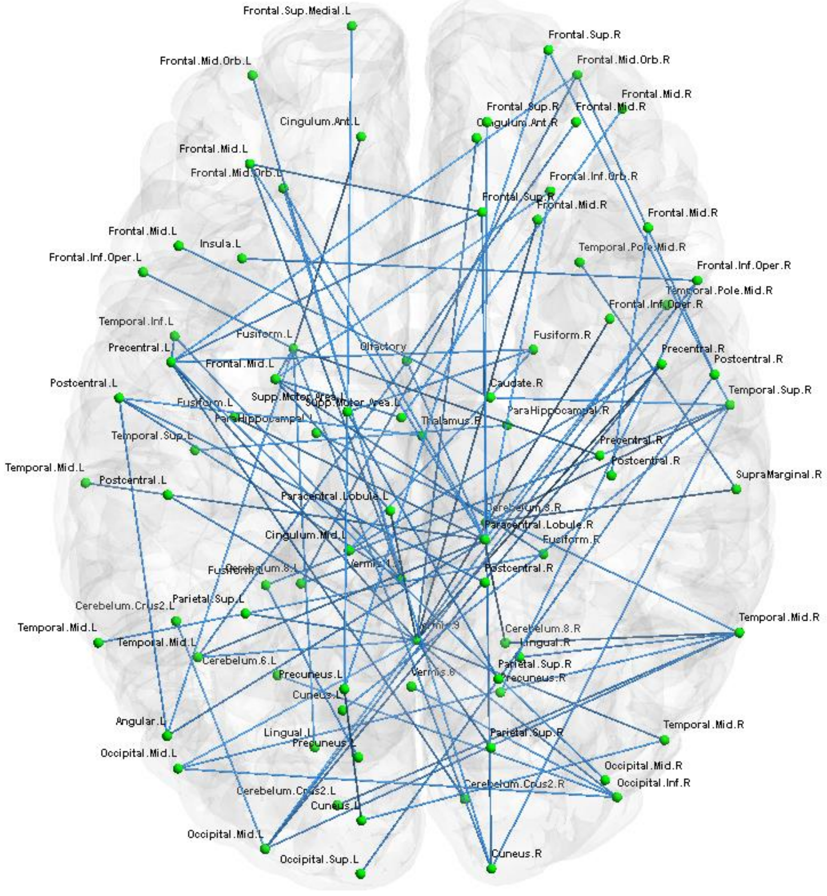

(E) Sustained attention (SCPT_TP)

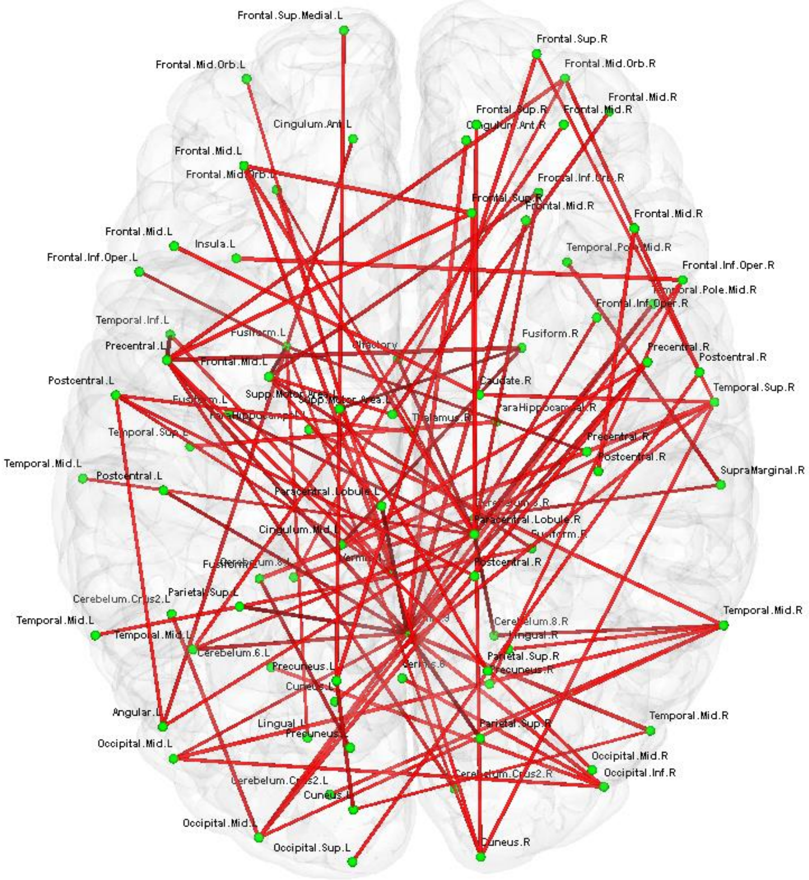

(F) Sustained attention (SCPT_FN)

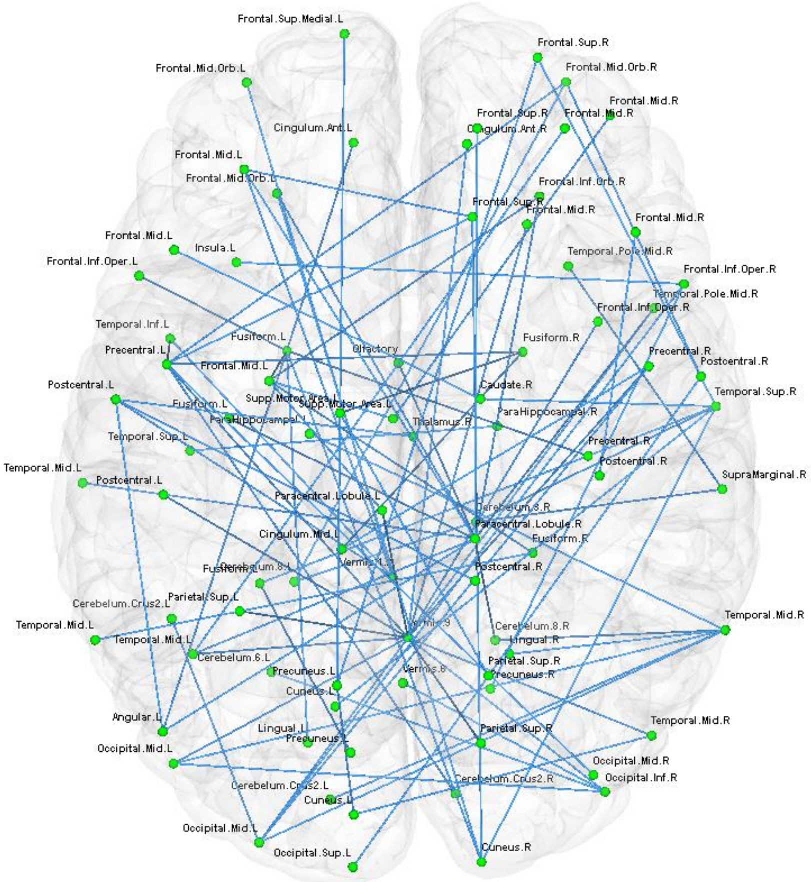

(G) Sustained attention (SCPT_SEN)

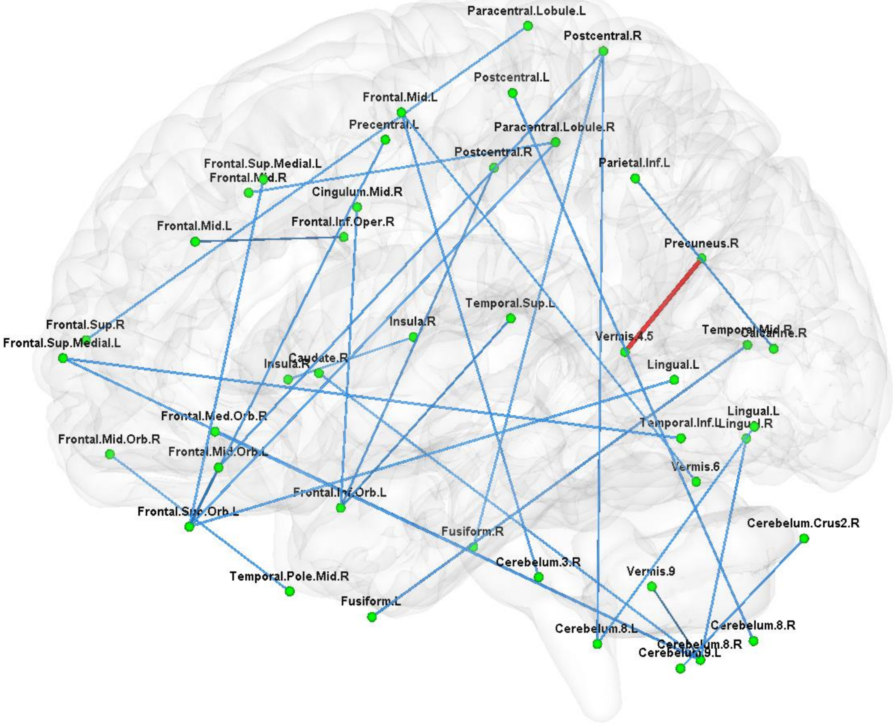

(H) Sustained attention (SCPT_SPEC)

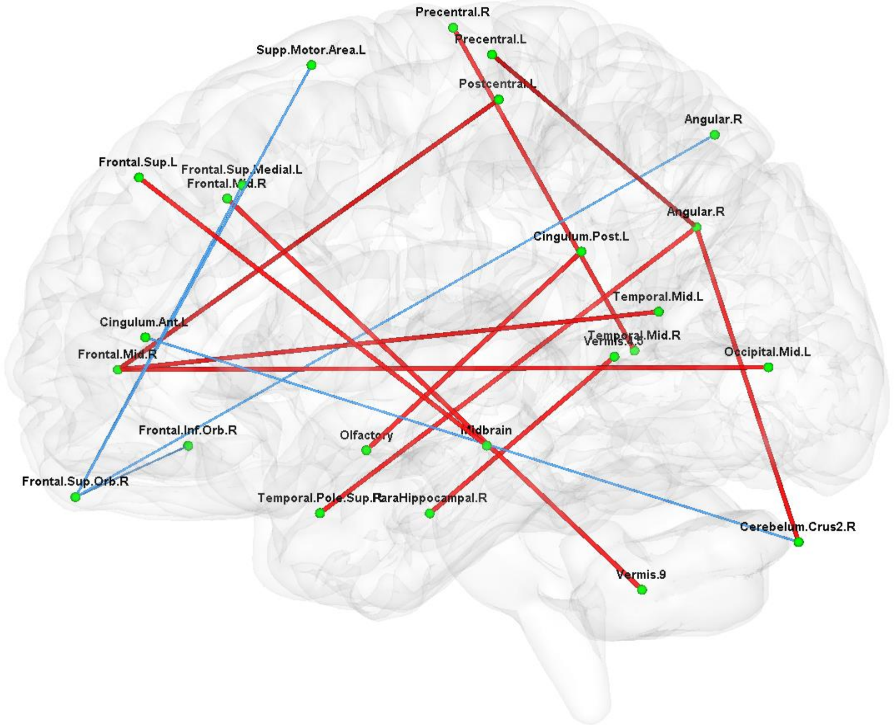

(I) Sustained attention (CPT_LRNR)

Figure A4 Paths with MTSTs significantly predicting variability in selected behavioral measures. The predictive ability is quantified by regression coefficient α for each MTST in the GLM shown in Eq.4.3 of the Methods section in the main text. The coefficient α is passed through a z-test and Bonferroni corrected for multiple comparisons (corrected p=0.05/75=0.00067, where 0.05 is uncorrected p value, and 75 is number of behavioral tests). In each subfigure, cobalt blue paths have negative α values, and red paths have positive α values. The behavior tests for subfigures are: (A) episodic memory (picture sequence test, unadjusted). (B) Fluid intelligence (PMAT24_A_CR). (C) Fluid intelligence (PMAT24_A_SI). (D) Self-regulation/impulsivity (AUC_200). (E) Sustained attention (SCPT_TP). (F) Sustained attention (SCPT_FN). (G) Sustained attention (SCPT_SEN). (H) Sustained attention (SCPT_SPEC). (I) Sustained attention (CPT_LRNR).

A.7 Schematic of Distance Measure Calculation in Second Level Clustering

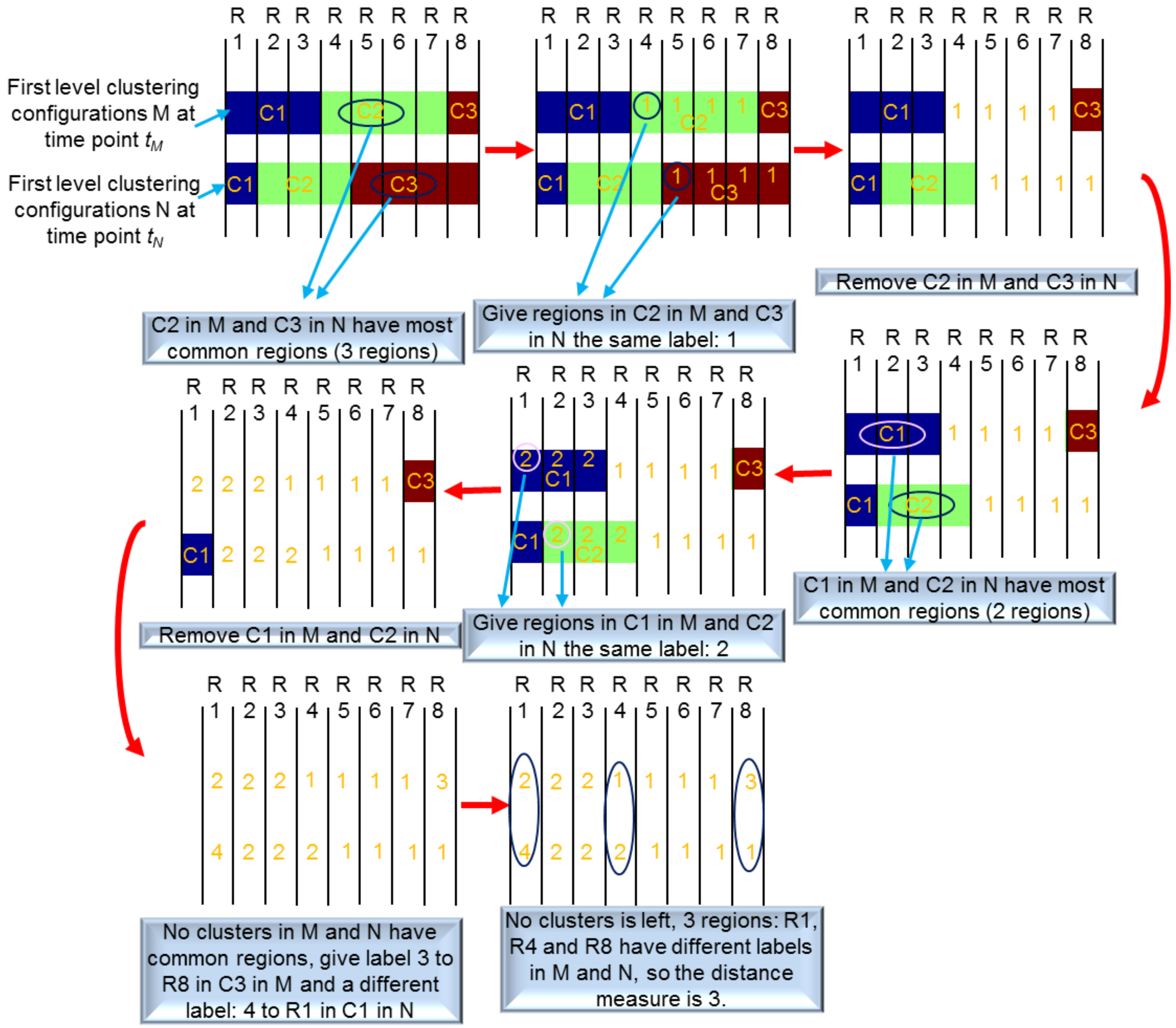

C2 in M and C3 in N have most common regions (3 regions)

Give regions in C2 in M and C3 in N the same label: 1

Remove C2 in M and C3 in N

C1 in M and C2 in N have most common regions (2 regions)

Give regions in C1 in M and C2 in N the same label: 2

Remove C1 in M and C2 in N

No clusters in M and N have common regions, give label 3 to R8 in C3 in M and a different label: 4 to R1 in C1 in N

No clusters is left, 3 regions: R1, R4 and R8 have different labels in M and N, so the distance measure is 3.

Figure A5 A schematic of distance measure calculation in second level clustering. The schematic starts with any two first level clustering configurations at different time points as shown on the upper left corner. Red arrows indicate the direction of the procedure. (R1,…, R8 denote region#1 to region#8, and C1, C2, C3 denote cluster#1, cluster#2, and cluster#3)

A.8 An Illustrative Example of the Calculation of Metrics: MTST, SDTST, CFP.

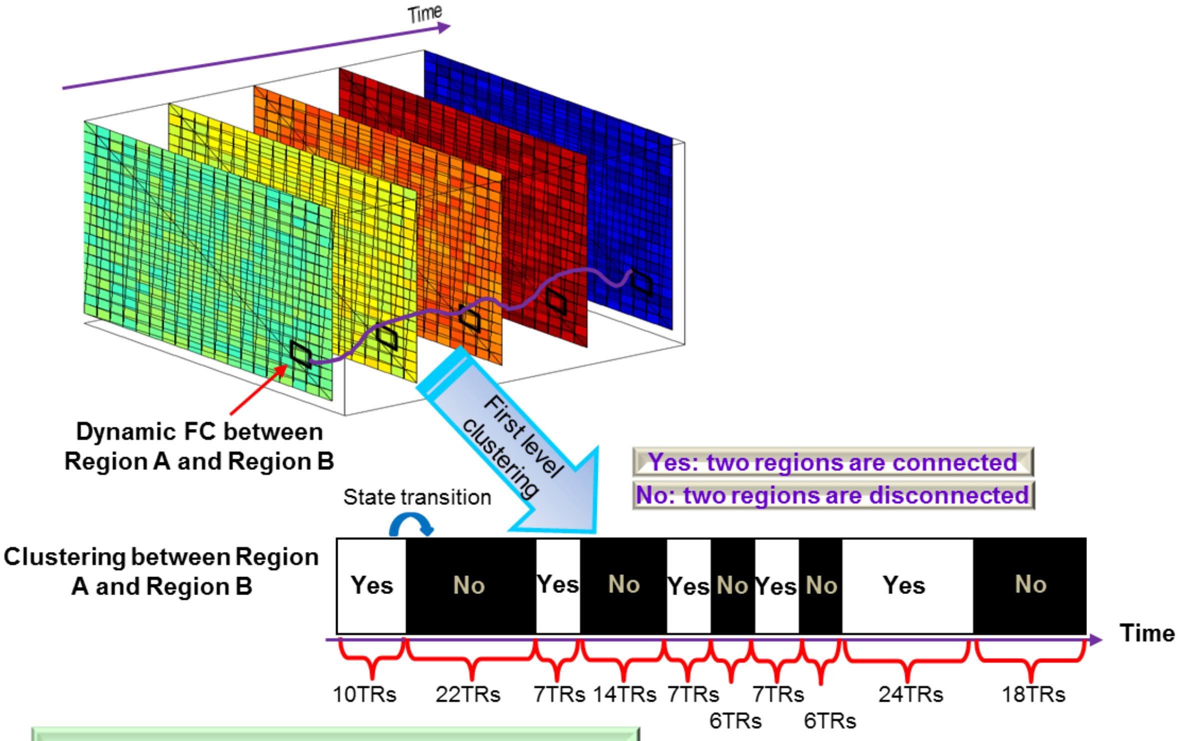

MTST: $(10+22+7+14+7+6+7+6+24+18)/10=12.1(\mathrm{TR})$

SDTST: $\mathrm{sqrt}(((10-12.1)^2+(22-12.1)^2+(7-12.1)^2+(14-12.1)^2+(7-12.1)^2+(6-12.1)^2+(7-12.1)^2+(6-12.1)^2+(24-12.1)^2+(18-12.1)^2)/(10-1))=6.95\ (\mathrm{TR})$

CFP: $(10+7+7+7+24)/\ (10+22+7+14+7+6+7+6+24+18)=0.45$

Figure A6 An illustrative example of the calculation of three metrics: MTST, SDTST, CFP. The first level clustering result leads to a series of state transitions for every pair of regions between clustered and unclustered states. Specifically, two regions either belong to the same cluster (connected, clustered state) or different clusters (disconnected, un-clustered state), and switch between these two states, as reflected in the black-and-white bar with “Yes” and “No” indicating whether they are clustered or not. Then the three metrics: MTST, SDTST, CFP are calculated as in corresponding boxes. Note the fourth metric: SFC is widely known and thus not illustrated here.

Appendix B

Table B1. AAL labels, MNI co-ordinates, and statistical summary of DEC and SEC paths associated of the CC200 regions having at least one path connected

Variance of DEC, healthy controls<PTSD				
AAL name of region centroids	MNI coordinates of centroid x y z	Inflow degree	Outflow degree	Sum of connecting paths' weights
Cerebelum_8_R	18.95 -55.38 -57.68	3	1	4.090
Pons	-2.59 -25.20 -37.88	2	0	2.327
Precentral_L	-46.96 0.03 48.80	0	1	1.323
Supp_Motor_Area_L	-1.54 -10.90 53.54	0	1	1.055
Cinglulum_Post_L	0.40 -42.74 7.41	0	1	1.024
Precentral_R	37.56 -18.39 65.54	0	1	1.007
Variance of DEC, healthy controls>PTSD				
Cerebelum_Crus2_R	51.31 -50.19 -44.12	10	0	11.524
Temporal_Mid_R*	70.74 -30.26 -1.79 65.09 -53.34 7.39 50.35 -74.53 7.56	0	4	5.999
Postcentral_R	14.95 -43.44 74.55 34.70 -44.88 66.60	3	1	4.850
Precentral_R	37.56 -18.39 65.54 16.09 -17.07 72.69	3	0	4.712
Frontal_Mid_R	34.76 14.33 56.50 47.11 26.56 37.07 42.05 50 3.54	1	3	4.504
Lingual_L	-16.00 -59.48 0.57	2	2	4.402
Cerebelum_Crus2_L	-34.43 -78.48 -44.10 -45.96 -51.08 -46.94	1	2	3.844
Fusiform_R	43.93 -42.84 -24.22	3	0	3.664
Temporal_Inf_L	-52.45 -42.24 -26.11	0	2	3.233
Postcentral_L	-47.64 -26.20 58.17	2	0	2.753
Cingulum_Mid_L	-11.88 -37.10 50.28	0	2	2.750
Parietal_Inf_R	52.80 -47.15 54.41	0	2	2.639
Cerebelum_6_R	27.25 -61.78 -30.95	0	2	2.450
Parietal_Inf_L	-49.33 -54.47 51.09	2	0	2.377
Frontal_Sup_L	-12.54 45.79 42.41 -15.71 58.38 25.89	0	2	2.282
Fusiform_L	-28.28 -43.98 -12.04	0	2	2.037
Precuneus_L	-10.08 -77.95 50.04 -11.90 -46.47 73.35	1	1	1.970
Precuneus_R	17.96 -65.15 24.97	1	1	1.965
Brainstem	1.60 -42.77 -60.82	0	1	1.556

Temporal_Mid_L	-41.72 -58.20 15.26	0	1	1.431
ParaHippocampal_L	-18.26 -13.95 -28.16	0	1	1.355
Cerebelum_8_R	32.05 -40.52 -45.65	1	0	1.353
Insula_R	38.0 -5.77 9.15	0	1	1.349
Temporal_Inf_R	63.34 -47.21 -17.55	0	1	1.334
Paracentral_Lobule_L	-3.72 -29.33 71.68	1	0	1.312
Angular_L	-47.75 -73.73 28.59	0	1	1.023
Temporal_Sup_L	-42.28 -17.34 -6.55	0	1	1.021
Calcarine_R	1.01 -79.9 5.81	1	0	0.997
Precentral_L	-46.96 0.03 48.80	1	0	0.995
Rolandic_Oper_L	-55.53 0.62 1.72	0	1	0.994
SEC, healthy controls<PTSD				
Caudate_R	14.71 13.69 1.91 15.97 -6.95 19.68	0	10	14.536
Frontal_Mid_R	42.05 50 3.54 25.30 28.13 38.15	10	0	12.111
Temporal_Inf_R	62.82 -27.60 -26.10 63.34 -47.21 -17.55	0	7	10.799
Thalamus_R	19.64 -30.83 8.98 2.58 -14.49 6.76	0	6	9.019
Postcentral_R	34.70 -44.88 66.60 39.87 -22.35 43.17	5	0	8.003
Temporal_Inf_L	-39.13 -22.77 -27.44 -52.85 -60.85 -11.17 -52.45 -42.24 -26.11	1	5	7.938
Insula_R	38.08 -5.77 9.15	3	0	4.548
Frontal_Inf_Oper_R	56.83 16.15 15.70	1	2	4.346
Rolandic_Oper_R	42.75 -26.59 17.49	3	0	4.257
SupraMarginal_R	64.52 -25.08 24.80	3	0	3.969
Thalamus_L	-16.41 -30.63 8.50	0	3	3.875
Temporal_Mid_R	46.27 -53.41 16.87	2	0	3.521
Parietal_Inf_L	-49.33 -54.47 51.09 -33.183 -74.54 48.03	2	0	3.482
Cingulum_Ant_R	2.14 26.57 21.06	0	2	2.943
Postcentral_L	-37.63 -24.31 42.38	2	0	2.877
Frontal_Inf_Orb_L	-46.14 36.88 -12.56	0	2	2.730
Fusiform_R	26.47 -37.83 -13.28	0	2	2.520
Insula_L	-35.12 -7.20 11.28	2	0	2.437
Cerebelum_6_L	-29.18 -38.20 -34.81 -25.93 -61.76 -30.25	1	1	2.411
Temporal_Mid_L	-57.99 -39.32 -5.05	1	0	1.738
Cerebelum_Crus1_L	-47.83 -66.58 -32.01	1	0	1.719
Precentral_L	-28.74 -24.84 67.26	1	0	1.438
Cerebelum_Crus2_R	10.93 -86.19 -31.32	1	0	1.346
Supp_Motor_Area_R	14.86 7.67 67.07	1	0	1.292

Temporal_Sup_L	-61.82 -25.83 12.92	1	0	1.283
Frontal_Inf_Tri_R	49.15 35.12 14.47	1	0	1.260
Frontal_Inf_Tri_L	-44.94 37.29 10.94	1	0	1.253
Occipital_Sup_R	15.33 -88.55 33.41	1	0	1.230
Temporal_Pole_Sup_L	-42.34 12.70 -19.94	0	1	1.210
ParaHippocampal_R	19.36 -12.39 -25.52	0	1	1.206
Cerebelum_8_L	-31.00 -62.73 -58.85	0	1	1.197
Precuneus_L	-12.80 -64.47 64.14	0	1	1.193
Lingual_R	21.29 -74.31 -11.23	1	0	1.186
Cerebelum_6_R	27.25 -61.78 -30.95	0	1	1.185
SEC, healthy controls>PTSD				
Temporal_Inf_L	-52.45 -42.24 -26.11	2	0	2.677
ParahippocampaGyrus	-20.96 -26.24 -14.20	2	0	2.543
Frontal_Mid_R	32.92 47.43 25.66	0	2	2.536
Cerebelum_6_R	27.25 -61.78 -30.95	0	1	1.352
Cerebelum_6_L	-25.93 -61.76 -30.25	0	1	1.325
Paracentral_Lobule_R	14.90 -35.03 48.29	0	1	1.245
Fusiform_L	-28.28 -43.98 -12.04	1	0	1.239

Table B2. AAL labels, MNI co-ordinates, and statistical summary of DFC and SFC paths associated of the CC200 regions having at least one path connected

Variance of DFC, healthy controls<PTSD			
AAL name of region centroids	MNI coordinates of centroid x y z	connectivity degree	Sum of connecting paths' weights
None			
Variance of DFC, healthy controls>PTSD			
Postcentral_L	-37.63 -24.31 42.38 -57.19 -7.03 27.78 -47.64 -26.20 58.17	7	18.733
Caudate_R	15.97 -6.95 19.68	7	17.619
Frontal_Mid_L	-45.47 22.97 35.66 -31.43 39.14 28.32 -26.41 -3.30 54.27 -32.82 53.61 6.90	6	15.912
Precentral_L	-46.96 0.03 48.80 -28.74 -24.84 67.26	6	14.701
Vermis_1.2	-1.59 -42.74 -22.95	4	10.470
Occipital_Mid_R	34.59 -89.14 8.39	4	10.391
Temporal_Inf_R	63.34 -47.21 -17.55 55.82 -12.56 -37.76	4	9.321
Putamen_L	-24.75 -4.85 -7.63	3	8.699
Frontal_Sup_R	14.36 29.64 56.74 27.43 61.62 8.53	3	7.716
Cerebelum_Crus2_L	-34.43 -78.48 -44.10	3	7.213

Rectus_L	-8.66 60.41 -17.42	2	6.238
SupraMarginal_L	-59.12 -28.81 38.92	2	6.013
Cerebelum_Crus2_R	10.93 -86.19 -31.32	2	5.879
Occipital_Mid_L	-28.43 -96.04 -2.15 -45.62 -80.15 4.03	2	5.843
Cerebelum_6_L	-25.93 -61.76 -30.25	2	5.724
Parietal_Inf_R	34.32 -50.54 42.06	2	5.417
Cerebelum_8_L	-21.37 -43.64 -52.50	2	5.289
Fusiform_L	-34.50 -10.84 -43.47	2	5.118
Parietal_Inf_L	-49.33 -54.47 51.09	2	5.022
Fusiform_R	26.47 -37.83 -13.28	2	4.729
SupraMarginal_R	64.52 -25.08 24.80	2	4.718
Caudate_L	-14.24 -7.50 18.68	2	4.525
Temporal_Sup_L	-61.82 -25.83 12.92	1	3.287
Paracentral_Lobule_L	-3.72 -29.33 71.68	1	3.008
Temporal_Pole_Sup_R	28.48 9.58 -25.46	1	2.808
Insula_R	42.49 -6.88 -13.98	1	2.803
Pallidum_R	23.97 -7.16 -5.32	1	2.718
Frontal_Mid_R	47.11 26.56 37.07	1	2.710
Frontal_Mid_Orb_R	33.15 56.72 -14.39	1	2.702
Cerebelum_8_R	32.05 -40.52 -45.65	1	2.636
Insula_L	-35.12 -7.20 11.28	1	2.479
Occipital_Inf_R	41.00 -85.82 -14.07	1	2.473
Temporal_Pole_Sup_L	-42.34 12.70 -19.94	1	2.445
Vermis_6	0.42 -63.99 -19.92	1	2.430
Cerebelum_Crus1_L	-47.83 -66.58 -32.01	1	2.347
Precentral_R	49.75 -0.38 49.78	1	2.329
Postcentral_R	39.87 -22.35 43.17	1	2.304
Frontal_Sup_Medial_R	10.33 60.23 24.68	1	2.244
Calcarine_L	-8.37 -99.02 -11.19	1	2.217
SFC, healthy controls<PTSD			
Vermis_1.2	-1.59 -42.74 -22.95	9	18.765
Brainstem	1.60 -42.77 -60.82	10	17.705
Lingual_L	-18.66 -75.95 -8.83 -16.00 -59.48 0.57	7	12.652
Lingual_R	21.80 -58.16 0.46 19.34 -98.75 -9.67 21.29 -74.31 -11.23	6	12.160
Midbrain	0.05 -23.79 -11.82	5	10.420
Vermis_9	1.42 -54.85 -40.97	5	9.719
Parietal_Inf_L	-49.33 -54.47 51.09 -31.61 -51.45 41.04	4	8.182
SupraMarginal_R	62.81 -45.26 33.38	4	7.266
Vermis_6	0.42 -63.99 -19.92	4	6.919
SupraMarginal_L	-58.22 -50.21 31.77	4	6.906

Postcentral_L	-37.63 -24.31 42.38 -47.64 -26.20 58.17	4	6.825
Calcarine_R	3.01 -79.95 6.81	4	6.762
Fusiform_R	26.47 -37.83 -13.28	3	6.202
Occipital_Mid_L	-28.43 -96.04 -2.15 -30.29 -87.38 23.13	3	6.023
Fusiform_L	-28.28 -43.98 -12.04	2	4.428
Temporal_Mid_R	50.35 -74.53 7.56	2	4.338
Temporal_Pole_Sup_L	-42.34 12.70 -19.94	2	4.104
Temporal_Inf_R	55.82 -12.56 -37.76 42.46 -2.63 -47.00	2	3.828
Cerebelum_6_R	27.25 -61.78 -30.95	2	3.738
Precuneus_R	17.96 -65.15 24.97	2	3.621
Precentral_R	37.56 -18.39 65.54 49.75 -0.38 49.78	2	3.604
Precentral_L	-28.74 -24.84 67.26	2	3.203
Temporal_Pole_Sup_R	28.48 9.58 -25.46	1	2.853
Cerebelum_9_L	-7.22 -60.78 -57.42	1	2.390
Cuneus_R	16.20 -99.93 12.08	1	2.026
ParahippocampaGyrus	-20.96 -26.24 -14.20	1	2.013
Frontal_Mid_L	-32.82 53.61 6.90	1	2.011
Occipital_Sup_R	15.33 -88.55 33.41	1	1.991
Angular_R	39.76 -69.40 51.04	1	1.965
Cingulum_Mid_L	0.35 -18.33 32.96	1	1.806
Insula_R	42.49 -6.88 -13.98	1	1.657
Cuneus_L	-13.14 -68.67 24.72	1	1.654
Cerebelum_6_L	-25.93 -61.76 -30.25	1	1.637
Occipital_Mid_R	38.64 -82.44 29.50	1	1.572
SFC, healthy controls>PTSD			
None			

*: When more than one centroid is indicated for a given AAL regions, it means that multiple CC200 regions are associated with the same AAL label. Since CC200 regions are functionally homogeneous and AAL labels can span a large anatomical region, it is to be expected that multiple CC200 regions would be associated with a single AAL label.